ISSN 1983-4195

IBRACON Structures and Materials Journal

Revista IBRACON de Estruturas e Materiais

Volume 15, Number 4
August 2022

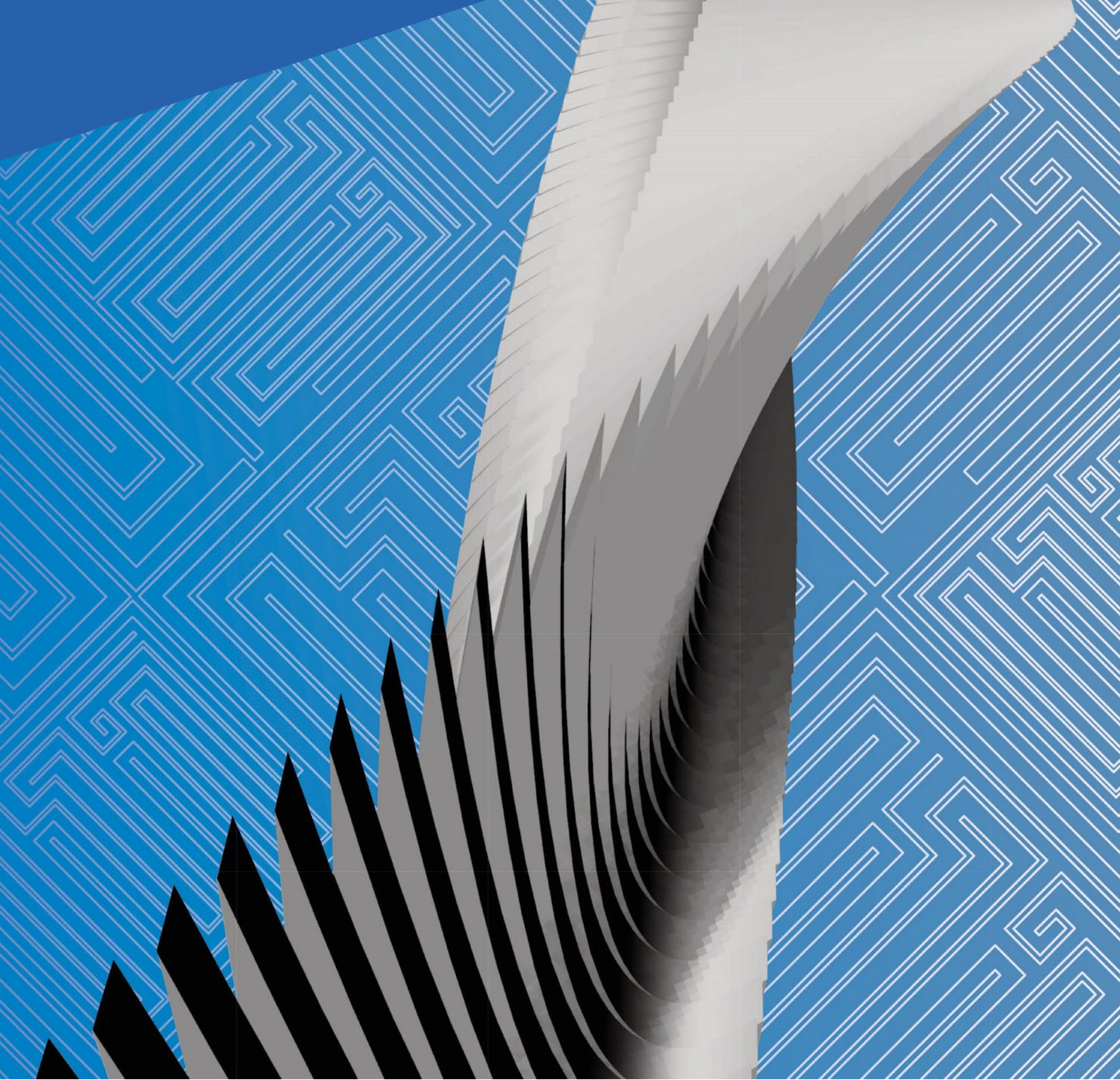

ISSN 1983-4195
Volume 15, Number 4
August 2022

IBRACON

Editorial

First, I would like to thank Editor-in-Chief very much, Prof. Guilherme Parsekian, for his invitation to write this issue's editorial of *IBRACON Structures and Materials Journal (ISMJ)*. 2022 is a year of just celebration for IBRACON (Brazilian Concrete Institute). In this June 23rd, the Institute celebrated its fifty years of important accomplishments for the Brazilian concrete community.

Among the important IBRACON's activities, the following can be cited: publication of the technical journal *Concreto & Construções*, of our scientific journal *IBRACON Structures and Materials Journal (ISMJ)* and also of a numerous list of books and other important technical publications; annually promoting the *CBC*, Brazilian Concrete Conference , the most important Brazilian technical conference of our concrete industry; active participating in elaboration the Brazilian Standards of ABNT (Brazilian Association of Technical Standards); promoting of other several activities, such as technical certification and post-graduated courses.

One of the most important missions of IBRACON is to congregate researchers, professors and concrete designers and contractors in a unique community, with a single purpose, which is of improving the quality of the concrete industry. IBRACON's journals and conferences provide a particular opportunity of join academic and professional communities.

With respect to our *IBRACON Structures and Materials Journal (ISMJ)*, of which I am proud of being part as Associated Editor, among a Pleiades of internationally recognized researchers, it should be acknowledged its impressive development in the last few years, under the enthusiastic leadership of Prof. Guilherme Parsekian. The journal publishes papers and has the formal recognition of institutions such as SCIELO – Scientific Electronics Library Online. This, on the other hand, attracts the best of our researchers for publishing the results of their work in our journal. Recently, ISMJ Journal conquered an important international position, because of the quality of the published papers.

In these fifty years, the dreams of IBRACON founders, past leaders and community members became reality, building an increasing strong and active institution.

We are certain that of every one of us, members, and admirers of IBRACON, are looking forward for our *CBC* in Brasilia, next October, meeting our friends again, from which we were sadly separated in the pandemic times.

As part of the 2022 celebrations, we announce now one more issue of our *IBRACON Structures and Materials Journal (ISMJ)*.

Sergio Hampshire de Carvalho Santos
Associate Editor
Full Professor, Federal University of Rio de Janeiro

ISSN 1983-4195
Volume 15, Number 4
August 2022

IBRACON Structures and Materials Journal
Revista IBRACON de Estruturas e Materiais

Contents

Evaluation of formulations for predicting the shear strength of concrete filled circular holes in steel plates 15401
L. G. J. MIRANDA, O. P. AGUIAR, P. E. C. SILVÉRIO and R. B. CALDAS

Probabilistic chloride diffusion modelling in cracked concrete structures by transient BEM formulation 15402
V. B. SOUZA and E. D. LEONEL

Elaboration of fracture prediction map using 2D digital image correlation - 2D CID 15403
L. S. ASSIS, J. T. ASSIS, J. R. C. PESSOA and A. D. TAVARES JR.

Analysis of cementitious matrices self-healing with bacillus bacteria 15404
V. MULLER, F. PACHECO, C. M. CARVALHO, F. FERNANDES, V. H. VALIATI, R. C. E. MODOLO, H. Z. EHRENBRING and B. F. TUTIKIAN

Exploratory study for the alkaline activation of basalt powder as a supplementary cementitious matrix 15405
R. GHELLER, L. L. SILVA, M. A. FIORI and E. R. BATISTON

Nonlinear analysis method of concrete structures under cyclic loading based on the generalized secant modulus 15406
L. R. S. PEREIRA and S. S. PENNA

Nonlinear analysis of reinforced concrete structures using thin flat shell elements 15407
J. R. B. SILVA and B. HOROWITZ

Numerical analysis of piled rafts with short bored piles 15408
E. A. S. OLIVEIRA, M. O. JUSTINO and J. R. GARCIA

Evaluation of the reliability of optimized reinforced concrete beams 15409
R. S. CORREIA, G. F. F. BONO and C. M. PALIGA

A method for considering the influence of distinct casting stages in the flexural design of prestressed concrete cross sections 15410
E. V. W. TRENTINI, G. A. PARSEKIAN and T. N. BITTENCOURT

Cover: Parametric Tower

Courtesy: Marcela Noronha P. de O. e Sousa

IBRACON

Ibracon Structures and Materials Journal is published bimonthly
(February, April, June, August, October, and December) by IBRACON.

IBRACON
Instituto Brasileiro do Concreto Founded in 1972

Av. Queiroz Filho, nº 1700 — sala 407/408
Torre D — Villa Lobos Office Park
CEP 05319-000 — São Paulo, SP — Brazil
Phone: +55 11 3735-0202
Fax: +55 11 3733-2190
E-mail: riem@ibracon.org.br
Website: http://www.ibracon.org.br

Cover design & Layout: Editora Cubo
www.editoracubo.com.br

Aims and Scope

Aims and Scope

The IBRACON Structures and Materials Journal (in Portuguese: Revista IBRACON de Estruturas e Materiais) is a technical and scientific divulgation vehicle of IBRACON (Brazilian Concrete Institute), published every two months. Each issue has 12 to 15 articles and, possibly, a technical note and/or a technical discussion regarding a previously published paper. All contributions are reviewed and approved by professionals with recognized scientific competence in the area. The IBRACON Structures and Materials Journal is an open access Journal, free of charges for authors and readers.

Objectives

The IBRACON Structures and Materials Journal´s main objectives are:

- Present current developments and advances in concrete structures and materials.
- Make possible the better understanding of structural concrete behavior, supplying subsidies for a continuous interaction among researchers, producers, and users.
- Stimulate the development of scientific and technological research in the areas of concrete structures and materials, through papers peer-reviewed by a qualified Editorial Board.
- Promote the interaction among researchers, constructors and users of concrete structures and materials and the development of Civil Construction.
- Provide a vehicle of communication of high technical level for researchers and designers in the areas of concrete structures and materials.

Submission Procedure

The procedure to submit and revise the contributions, as well as the formats, are detailed in the Journal Website (ismj.org).

The papers and the technical notes are revised by at least two reviewers indicated by the editors. Discussions and replies are accepted for publication after a review by the editors and at least one member of the Editorial Board. In case of disagreement between the reviewer and the authors, the contribution will be sent to a specialist in the area, not necessarily linked to the Editorial Board. Conflict of interests is carefully handled by the Editors.

Contribution Types

The Journal will publish original papers, short technical notes, and paper discussions. Original papers will be accepted if they are in accordance with the objectives of the Journal and present quality of information and presentation. A technical note is a brief manuscript. It may present a new feature of research, development, or technological application in the areas of Concrete Structures and Materials, and Civil Construction. This is an opportunity to be used by industries, companies, universities, institutions of research, researchers, and professionals willing to promote their works and products under development.

A discussion is received no later than 3 months after the publication of the paper or technical note. The discussion must be limited to the topic addressed in the published paper and must not be offensive. The right of reply is granted to the Authors. The discussions and the replies are published in the subsequent issues of the Journal.

The submission file should be in accordance with the paper template available at the Journal Website. It is recommended that the length of the papers does not exceed 25 pages. Where available, URLs for the references should be provided.

The IBRACON Structures and Materials Journal will conduct the review process for manuscripts submitted in English. Titles, abstracts, and keywords are presented in English, and in Portuguese or Spanish. Articles and technical notes are peer-reviewed and only published after approval of the reviewers and the Editorial Board.

Once accepted, an article is typeset according to the journal layout. The author will be required to review and approve the galleys before publishing. At this stage only typesetting errors will be considered.

Internet Access

The IBRACON Structures and Materials Journal Webpage is available at http://ismj.org.

Sponsors

The funds for the maintenance of the Journal are currently obtained from the IBRACON. The Journal is not supposed to be maintained with funds from private sponsorship, which could diminish the credit of the publications.

Photocopying

Photocopying in Brazil. Brazilian Copyright Law is applicable to users in Brazil. IBRACON holds the copyright of contributions in the journal unless stated otherwise at the bottom of the first page of any contribution. Where IBRACON holds the copyright, authorization to photocopy items for internal or personal use, or the internal or personal use of specific clients, is granted for libraries and other users registered at IBRACON.

Copyright

All rights, including translation, reserved. Under the Brazilian Copyright Law Nº. 9610 of 19th February 1998, apart from any fair dealing for the purpose of research or private study, or criticism or review, no part of this publication may be reproduced, stored in a retrieval system, or transmitted in any form or by any means, electronic, mechanical, photocopying, recording or otherwise, without the prior written permission of IBRACON. Requests should be directed to IBRACON:

IBRACON

Av. Queiroz Filho, 1700 – sala 407/408 – Torre D
Villa Lobos Office Park
05319-000 – Vila Hamburguesa
São Paulo – SP
Phone: +55 (11) 3735-0202
E-mail: riem@ibracon.org.br

Disclaimer

Papers and other contributions and the statements made, or opinions expressed therein are published on the understanding that the authors of the contribution are the only responsible for the opinions expressed in them and that their publication does not necessarily reflect the views of IBRACON or of the Journal Editorial Board.

Editorial Board

Editor-in-chief emeritus

José Luiz Antunes de Oliveira e Sousa, Universidade Estadual de Campinas - UNICAMP, Campinas, SP, Brazil, jls@fec.unicamp.br
https://orcid.org/0000-0002-1108-4356

Editor-in-chief

Guilherme Aris Parsekian, Universidade Federal de São Carlos - UFSCar, São Carlos, SP, Brazil, parsekian@ufscar.br
https://orcid.org/0000-0002-5939-2032

Associate Editors

Antonio Carlos dos Santos, Universidade Federal de Uberlândia - UFU, Uberlândia, MG, Brazil, acds@ufu.br
https://orcid.org/0000-0001-9019-4571

Bernardo Horowitz, Universidade Federal de Pernambuco - UFPE, Recife, PE, Brazil, bernardo.horowitz@ufpe.br
https://orcid.org/0000-0001-7763-7112

Bernardo Tutikian, Universidade do Vale do Rio dos Sinos - UNISINOS, São Leopoldo, RS, Brazil, bftutikian@unisinos.br
https://orcid.org/0000-0003-1319-0547

Bruno Briseghella, Fuzhou University, Fujian, China, bruno@fzu.edu.cn
https://orcid.org/0000-0002-8002-2298

Carmen Andrade, Universitat Politècnica de Catalunya, Spain, candrade@cimne.upc.edu
https://orcid.org/0000-0003-2374-0928

Diogo Rodrigo Ribeiro, Universidade do Porto - FEUP, Portugal, drr@isep.ipp.pt
https://orcid.org/0000-0001-8624-9904

Edna Possan, Universidade Federal da Integração Latino Americana - UNILA, Foz do Iguaçu, PR, Brazil, edna.possan@unila.edu.br
https://orcid.org/0000-0002-3022-7420

Fernando Pelisser, Universidade Federal de Santa Catarina - UFSC, Florianópolis, SC, Brazil, f.pelisser@ufsc.br
https://orcid.org/0000-0002-6113-5473

José Marcio Fonseca Calixto, Universidade Federal de Minas Gerais - UFMG, Belo Horizonte, MG, Brazil, calixto@dees.ufmg.br
https://orcid.org/0000-0003-2828-0967

José Tadeu Balbo Universidade de São Paulo - USP, São Paulo, SP, Brazil, jotbalbo@usp.br
https://orcid.org/0000-0001-9235-1331

Leandro Mouta Trautwein, Universidade Estadual de Campinas - UNICAMP, Campinas, SP, Brazil, leandromt@fec.unicamp.br
https://orcid.org/0000-0002-4631-9290

Lia Lorena Pimentel, Pontifícia Universidade Católica de Campinas - PUCCAMP, Campinas, SP, Brazil, lialp@puc-campinas.edu.br
https://orcid.org/0000-0001-5146-0451

Luís Oliveira Santos, Laboratório Nacional de Engenharia Civil, Lisboa, Portugal, luis.osantos@lnec.pt
https://orcid.org/0000-0003-2591-2842

Mark G Alexander, University of Cape Town, Cape Town, South Africa, mark.alexander@uct.ac.za
https://orcid.org/0000-0002-0986-3529

María Josefina Positieri, Universidad Tecnológica Nacional, Argentina, mpositieri@gmail.com
https://orcid.org/0000-0001-6897-9946

Mário Jorge de Seixas Pimentel, Universidade do Porto - FEUP, Porto, Portugal, mjsp@fe.up.pt
https://orcid.org/0000-0001-8626-6018

Maurício de Pina Ferreira, Universidade Federal do Pará - UFPA, Belém, PA, Brazil, mpina@ufpa.br
https://orcid.org/0000-0001-8905-9479

Mauro de Vasconcellos Real, Universidade Federal do Rio Grande - FURG, Rio Grande, RS, Brazil, mauroreal@furg.br
https://orcid.org/0000-0003-4916-9133

Nigel G. Shrive, University of Calgary, Calgary, Canada, ngshrive@ucalgary.ca
https://orcid.org/0000-0003-3263-5644

Osvaldo Luís Manzoli, Universidade Estadual Paulista "Júlio de Mesquita Filho" - UNESP, Bauru, SP, Brazil, osvaldo.l.manzoli@unesp.br
https://orcid.org/0000-0001-9004-7985

Pedro Castro Borges, CINVESTAV, Mérida, Mexico, castro@cinvestav.mx
https://orcid.org/0000-0001-6983-0545

Rebecca Gravina, RMIT University, Melbourne, Australia, rebecca.gravina@rmit.edu.au
https://orcid.org/0000-0002-8681-5045

Editorial Board

Ricardo Carrazedo, Universidade de São Paulo - USP, São Carlos, SP, Brazil, carrazedo@sc.usp.br
https://orcid.org/0000-0002-9830-7777

Samir Maghous, Universidade Federal do Rio Grande do Sul - UFRGS, Porto Alegre, RS, Brazil, samir.maghous@ufrgs.br
https://orcid.org/0000-0002-1123-3411

Sérgio Hampshire de C. Santos, Universidade Federal do Rio de Janeiro - UFRJ, Rio de Janeiro, RJ, Brazil, sergiohampshire@gmail.com
https://orcid.org/0000-0002-2930-9314

Túlio Nogueira Bittencourt, Universidade de São Paulo - USP, São Paulo, SP, Brazil, tbitten@usp.br
https://orcid.org/0000-0001-6523-2687

Vladimir Guilherme Haach, Universidade de São Paulo - USP, São Carlos, SP, Brazil, vghaach@sc.usp.br
https://orcid.org/0000-0002-9501-4450

Yury Villagrán Zaccardi, Universidad Tecnológica Nacional Facultad Regional La Plata, Buenos Aires, Argentina, yuryvillagran@gmail.com
https://orcid.org/0000-0002-0259-7213

Former Editors

Américo Campos Filho, Universidade Federal do Rio Grande do Sul - UFRGS, Porto Alegre, RS, Brazil

Denise C. C. Dal Molin Universidade Federal do Rio Grande do Sul - UFRGS, Porto Alegre, RS, Brazil

Eduardo Nuno Brito Santos Júlio, Instituto Superior Técnico - IST, Lisboa, Portugal

Emil de Souza Sánchez Filho, Universidade Federal Fluminense - UFF, Rio de Janeiro, RJ, Brazil

Fernando Soares Fonseca, Brigham Young University – BYU, Provo, UT, USA

Geraldo Cechella Isaia, Universidade Federal de Santa Maria - UFSM, Santa Maria, RS, Brazil

Gonzalo Ruiz, Universidad de Castilla-La Mancha - UCLM, Ciudad Real, Spain

Guilherme Sales Melo, Universidade de Brasília - UnB, Brasilia, DF, Brazil

Leandro Francisco Moretti Sanchez, University of Ottawa, Ottawa, ON, Canada

Luiz Carlos Pinto da Silva Filho, Universidade Federal do Rio Grande do Sul - UFRGS, Porto Alegre, RS, Brazil

Mounir Khalil El Debs, Universidade de São Paulo - USP, São Carlos, SP, Brazil

Nicole Pagan Hasparyk, Eletrobras Furnas, Aparecida de Goiânia, GO, Brazil

Paulo Helene, Universidade de São Paulo - USP, São Paulo, SP, Brazil

Paulo Monteiro, University of California Berkeley, Berkeley, CA, USA

Roberto Caldas de Andrade Pinto, Universidade Federal de Santa Catarina - UFSC, Florianópolis, SC, Brazil

Ronaldo Barros Gomes, Universidade Federal de Goiás - UFG, Goiânia, GO, Brazil

Romilde Almeida de Oliveira, Universidade Católica de Pernambuco - UNICAP, Recife, PE, Brazil

Romildo Dias Toledo Filho, Universidade Federal do Rio de Janeiro - UFRJ, Rio de Janeiro, RJ, Brazil

Rubens Machado Bittencourt, Eletrobras Furnas, Aparecida de Goiânia, GO, Brazil

Vladimir Antonio Paulon, Universidade Estadual de Campinas - UNICAMP, Campinas, SP, Brazil

Direction

Board of Direction 2021/2023 Biennium

President
Paulo Helene
1st Vice-President Director
Júlio Timerman
2nd Vice-President Director
Enio José Pazini Figueiredo
Presidency Advisors
Arnaldo Forti Battagin
Eduardo Antonio Serrano
Gilberto Antonio Giuzio
Iria Lícia Oliva Doniak
Jaques Pinto
João Luis Casagrande
Jorge Batlouni Neto
José Marques Filho
Mario William Esper
Ronaldo Tartuce
Rubens Machado Bittencourt
Selmo Chapira Kuperman
Simão Priszkulnik
Túlio Nogueira Bittencourt
Wagner Roberto Lopes
1st Director-Secretary
Cláudio Sbrighi Neto
2nd Director-Secretary
Carlos José Massucato
1st Treasurer Director
Júlio Timerman
2nd Treasurer Director
Hugo S. Armelin
Marketing Director
Alexandre Britez
Marketing Director Advisor
Guilherme Covas
Publications Director
Guilherme Parsekian
Publications Director Advisor
Túlio Nogueira Bittencourt
Event Director
Rafael Timerman
Event Director Advisor
Luis César De Luca
Technical Director
Carlos Britez
Technical Director Advisor
Emílio Takagi
Institutional Relations Director
César Henrique Daher
Institutional Relations Director Advisor
José Vanderley de Abreu
Course Director
Jéssica Pacheco
Course Director Advisor
André Mendes
Student Activities Director
Jéssica Andrade Dantas
Student Activities Director Advisor
Patrícia Bauer
Personnel Certification Director
Adriano Damásio Soterio
Personnel Certification Director Advisor
Paula Baillot
Research and Development Director
Bernardo Tutikian
Research and Development Director Advisor
Roberto Christ

Council 2021/2023 Biennium

Individual Members
Alio Ernesto Kimura
Antônio Carlos dos Santos
Antônio Domingues de Figueiredo
Arnaldo Forti Battagin
Bernardo Fonseca Tutikian
Carlos José Massucato
César Henrique Sato Daher
Claudio Sbrighi Neto
Enio José Pazini Figueiredo
Geraldo Cechella Isaia
Iberê Martins da Silva
Inês Laranjeira da Silva Battagin
Iria Lícia Oliva Doniak
Jéssika Mariana Pacheco Misko
José Tadeu Balbo
Leandro Mouta Trautwein
Luiz Prado Vieira Júnior (*in memoriam*)
Mário William Esper
Rafael Timerman
Rubens Curti
Vladimir Antonio Paulon

Past President Members
Eduardo Antônio Serrano
José Marques Filho
Júlio Timerman
Paulo Roberto do Lago Helene
Ronaldo Tartuce
Rubens Machado Bittencourt
Selmo Chapira Kuperman
Simão Priszkulnik
Túlio Nogueira Bittencourt

Corporate Members
ABCIC - Associação Brasileira da Construção Industrializada de Concreto – Iria Lícia Oliva Doniak

ABCP - Associação Brasileira de Cimento Portland – Paulo Camilo Penna

ABECE - Associação Brasileira de Engenharia e Consultoria Estrutural – João Alberto de Abreu Vendramini

ABESC - Associação Brasileira das Empresas de Serviços de Concretagem – Wagner Roberto Lopes

EPUSP - Escola Politécnica da Universidade de São Paulo – Túlio Nogueira Bittencourt

IPT - Instituto de Pesquisas Tecnológicas do Estado de São Paulo – José Maria de Camargo Barros

MC-BAUCHEMIE BRASIL INDÚSTRIA E COMÉRCIO LTDA – Jaques Pinto

PhD Engenharia Ltda – Douglas de Andreza Couto

TQS Informática Ltda – Nelson Covas

VOTORANTIM Cimentos S/A – Mauricio Bianchi

IBRACON Structures and Materials Journal
Revista IBRACON de Estruturas e Materiais
ISSN 1983-4195 ismj.org

ORIGINAL ARTICLE

Evaluation of formulations for predicting the shear strength of concrete filled circular holes in steel plates

Avaliação de fórmulas para obtenção da capacidade resistente dos furos circulares em chapa de aço preenchidos com concreto

Larice Gomes Justino Miranda[a]
Otávio Prates Aguiar[a]
Paulo Estevão Carvalho Silvério[a]
Rodrigo Barreto Caldas[a]

[a]Universidade Federal de Minas Gerais – UFMG, Departamento de Engenharia de Estruturas, Belo Horizonte, MG, Brasil

Received 21 October 2020
Accepted 02 March 2021

Abstract: Since the development of perforated plate shear connectors, different formulations have been proposed to predict their shear strength. Most of these formulations were derived from standard push-tests on multiple concrete filled holes (CFH) specimens simulating specific steel-concrete composite beam applications. Aiming at a more general application of these connectors in composite structures and the understanding of the physical and geometric parameters that influence their shear strength, the present work evaluated the use of 12 different formulations to predict 92 test results of single-hole specimens extracted from the literature. Such tests were chosen because the single-hole configuration allows better isolation of the connection behavior which facilitates comparative analysis. The predictions were statistically evaluated, and it was considered that the best formulations were those that showed lower scatter of data and a correction factor closer to one. Also, it was investigated if the individual terms that constitute the formulations adequately describe or show relation to the mechanics that govern the connection. It was verified that the best statistically rated formulations were also the ones showing clearer relation to the connector mechanical behavior. Among the evaluated formulations, three were significantly better than the others for strength prediction, however, it was noted that they can be further improved by considering the influence of concrete confinement and plate thickness on the hole's strength.

Keywords: composite structures, shear connectors, concrete filled circular holes in steel plates, push tests, statistical evaluation.

Resumo: Desde o desenvolvimento de conectores de cisalhamento em chapa contínua com furos circulares, diferentes formulações foram propostas para o cálculo da capacidade resistente dos mesmos. A maior parte dessas formulações foi desenvolvida com base no ensaio *push-out* padrão de protótipos com múltiplos furos simulando a aplicação desses conectores em vigas mistas de aço e concreto. Visando a aplicação mais geral desses conectores em estruturas mistas e o entendimento dos parâmetros físicos e geométricos que influenciam em sua capacidade resistente, avaliou-se, no presente trabalho, a aplicação de 12 dessas formulações a 92 resultados de ensaio. Esses ensaios extraídos da literatura têm em comum o fato de apresentarem apenas um furo solicitado. Escolheram-se ensaios com essa característica por permitirem isolar melhor o comportamento da conexão, facilitando análises comparativas. Os resultados extraídos foram avaliados estatisticamente, sendo consideradas as melhores formulações aquelas que apresentaram menor dispersão de dados e fator de correção próximo à unidade. Além disso, foi investigado se os termos individuais que constituem as formulações descrevem adequadamente ou mostram relação com a mecânica que rege a conexão. Verificou-se que as formulações mais bem avaliadas estatisticamente foram também as que apresentaram uma relação mais clara com o comportamento mecânico do conector. Dentre as formulações avaliadas, três se mostraram significativamente melhores que as demais para previsão da capacidade resistente, contudo, observou-se que ainda é possível aprimorá-las se levada em consideração a influência do confinamento e espessura da chapa na capacidade resistente do furo.

Palavras-chave: estruturas mistas, conector de cisalhamento, chapa contínua com furos circulares, ensaios de cisalhamento direto, avaliação estatística.

Corresponding author: Larice Gomes Justino Miranda. E-mail: laricejustino@yahoo.com.br
Financial support: None.
Conflict of interest: Nothing to declare.
Data Availability: The data that support the findings of this study are available from the corresponding author, LGJM, upon reasonable request.
This is an Open Access article distributed under the terms of the Creative Commons Attribution License, which permits unrestricted use, distribution, and reproduction in any medium, provided the original work is properly cited.

How to cite: L. G. J. Miranda, O. P. Aguiar, P. E. C. Silvério, and R. B. Caldas, “Evaluation of formulations for predicting the shear strength of concrete filled circular holes in steel plates,” *Rev. IBRACON Estrut. Mater.*, vol. 15, no. 4, e15401, 2022, https://doi.org/10.1590/S1983-41952022000400001

1 INTRODUCTION

Concrete filled circular holes in steel plates (CFH) with or without a transverse rebar are applied frequently in composite connections. Initially, the CFH were observed only in composite beams, as a constituent part of shear connectors, called Perfobond [1]. However, several other applications have emerged over the years (Figure 1) [2]–[5].

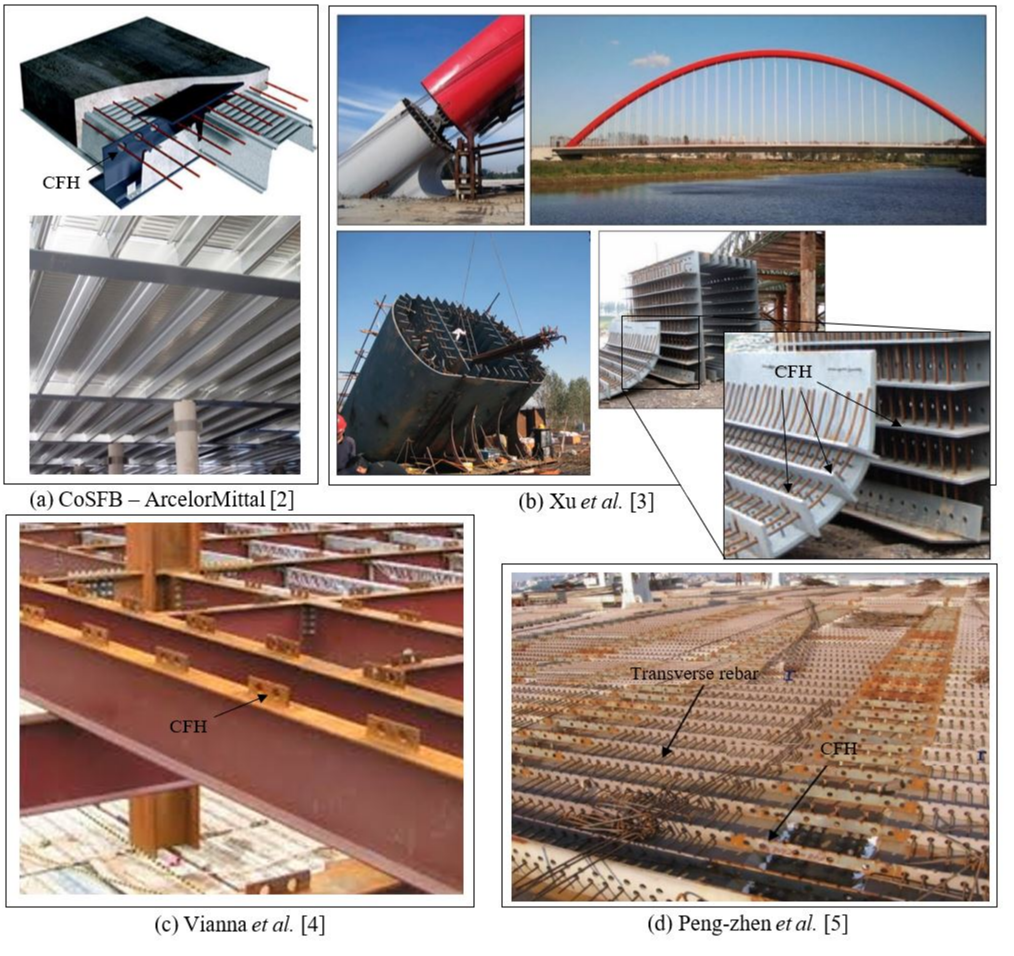

Figure 1. Examples of CFH applications: a) slim-floor beams; b) composite bridge transitions; c) composite beam (original conception of Perfobond); d) composite bridge decks.

Although there are several applications of CFH in civil construction, it is noted that a large part of the research that involve these elements was dedicated to studying not the CFH itself, but some structural arrangement (most often Perfobond connectors in composite beams) in which the CFH is a constituent part. Therefore, although there are several formulations designed to predict the shear strength of connections composed by CFH, it is observed that part of them present high errors if applied to predict the resistance of a single CFH. This is due to the fact that these formulations are mostly associated with failure modes that are specific of the studied structural arrangement and not of the CFH itself.

Therefore, this work proposes to study the CFH regardless of various applications already proposed for this element, through an investigation to identify, among the main equations of literature, those that best express the behavior of CFH and can predict its shear strength with greater precision.

In this investigation it was evaluated the use of 12 different formulations to predict 92 test results of single CFH. The predictions were statistically compared based on Annex D of EN 1990: 2002 [6] and the best formulations were those that showed lower scatter of data, a correction factor closer to one and their constituent terms better adjusted to the connector's mechanical behavior.

Tests with single-hole specimens were chosen because, by focusing the analysis on one hole, that is, the aspect common to any application or variation of CFH, it is possible to better isolate the fundamental mechanisms that govern the connection and the geometric and material parameters that influence them, thus reducing the number of parameters that influence the test results and facilitating the comparison among the 12 formulations. In doing so, it was possible to dissociate the behavior of the hole from other variables such as the end bearing resistance (contact between the edge of the steel plate and the concrete), that occur in some applications of the connector, and the distance between consecutive holes, which relates to the overlapping of stress fields in the concrete [7], as shown in Figure 2.

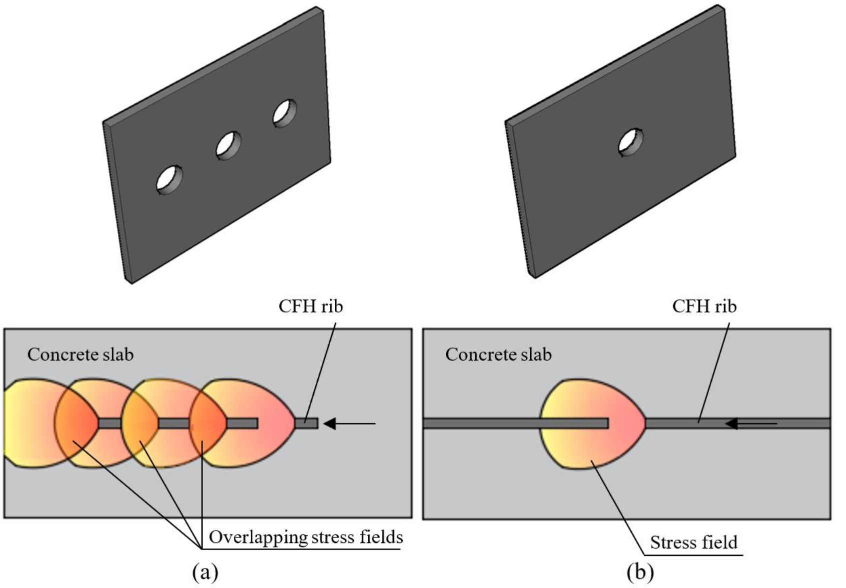

Figure 2. Representation of stress fields in a concrete slab for a) CFH rib with end bearing resistance and multiple holes and b) continuous CFH rib with a single hole.

It was considered in this work that if a formulation, though conceived for a given CFH application with specific geometric settings, can predict with enough accuracy the strength of a single hole, it may be considered suitable to express the fundamental mechanisms that govern the connection. Therefore, with some adaptations, it may be possible to extrapolate it to predict the strength of any application or variation of CFH, for example, ensuring an adequate distance between the centers of the holes, greater than 2.25 times the diameter of the hole [7]. However, if the formulation fails to predict the strength of a single hole, it can be concluded that it is not properly based on the physics that governs the connection and can not be extrapolated for CFH applications that differ from the one for which it was proposed.

2 LITERATURE REVIEW

2.1 Shear tests on CFH

2.1.1 General

Since the development of the CFH, several researches have been conducted for assessing its behavior in different structural application, mainly through push-test tests, standardized in Annex B of EN 1994-1-1:2004 [8]. The standard push test specimen consists of two small concrete slabs connected to a steel profile by the shear connectors. A vertical compression load is applied to the top of the steel profile, which slides in relation to the slabs. By measuring both the applied load and the vertical relative displacement between steel and concrete, the connector's load × slip curve is obtained.

Su et al. [9] states that the standard push test, also referred as push-out test, brings a deviation angle between the direction of resultant shear force of connector and the direction of applied force (Figure 3), which induces a pull-out force component in the connector and an increase in the friction between the steel profile and the slab. The deviation angle magnitude varies according to the specimen dimensions, which is one of the reasons why different results are often observed among tests of similar connectors by different researchers. Moreover, push-out tests are mostly directed to shear connectors in shallow applications, *i.e.*, where the connectors are near the concrete surface, as the standard specimen is designed to simulate the interaction of steel beams with typical concrete slabs.

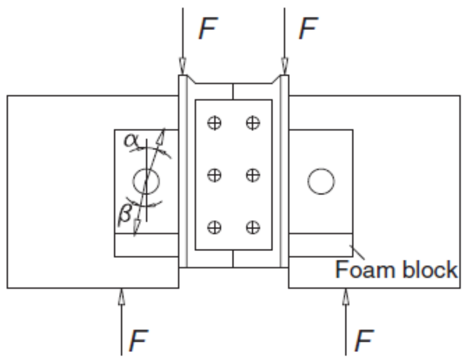

Figure 3. Conventional push-out test layout and deviation angle [9].

As an alternative to the push-out test, some researchers have proposed a new shear test setup, called plug-in test [9]–[12], in which the typical specimen consists of a single perforated steel plate embedded in a reinforced concrete block. A vertical compression load is applied directly to the top of the perforated steel plate, which slides inside the concrete block (Figure 4). This setup eliminates the deviation angle as the load is centered and vertically aligned with the connector and allows simulating situations where the connector is deeply embedded in the concrete.

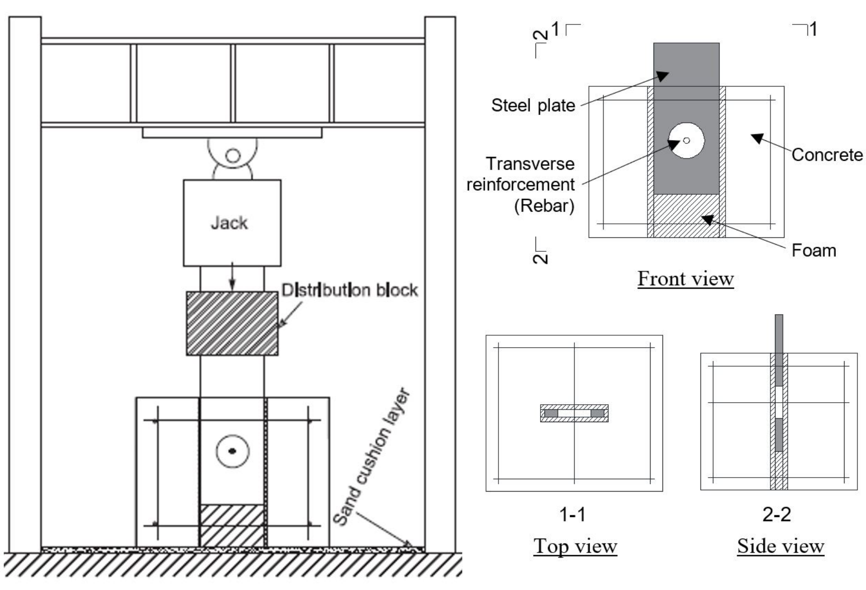

a) b)

Figure 4. Plug-in test a) setup and b) specimen details (adapted from [9]).

2.1.2 Shear tests with single-hole specimens

The CFH shear strength is determined by the combination of the individual contributions of the transverse rebar in the hole, the concrete dowel formed by the concrete that fills the hole, the bond and friction between the steel plate and the concrete. The end bearing resistance of the CFH rib (Figure 2a) is not present in every application and will not be addressed in this paper. In order to study each of these contributing factors and, aiming at the application of CFH in different design applications, different authors performed shear tests with single CFH in push-out [12], [13] and plug-in [9]–[12] configurations.

Su et al. [9] carried out 15 plug-in shear tests with single CFH specimens, in which the influence of the hole diameter and the presence of transverse reinforcement on the strength of the connector were evaluated. Reinforcement failure was observed in the tests, which rarely occurs in conventional push-out tests. From the test results, it was concluded that the plug-in shear test can eliminate the influence of friction and the deviation angle on the performance of the connector, and that the CFH has higher stiffness than stud-bolts.

He et al. [10] performed 12 plug-in tests divided into six specimen groups, each one of them varied in presenting steel-concrete bond, transverse rebar in the hole and concrete dowel (there were specimens without hole in the steel plate). From the test results, it was possible to determine the contribution of each strength component (concrete dowel, transverse rebar and bond) in the connector's overall strength, as shown in Figure 5.

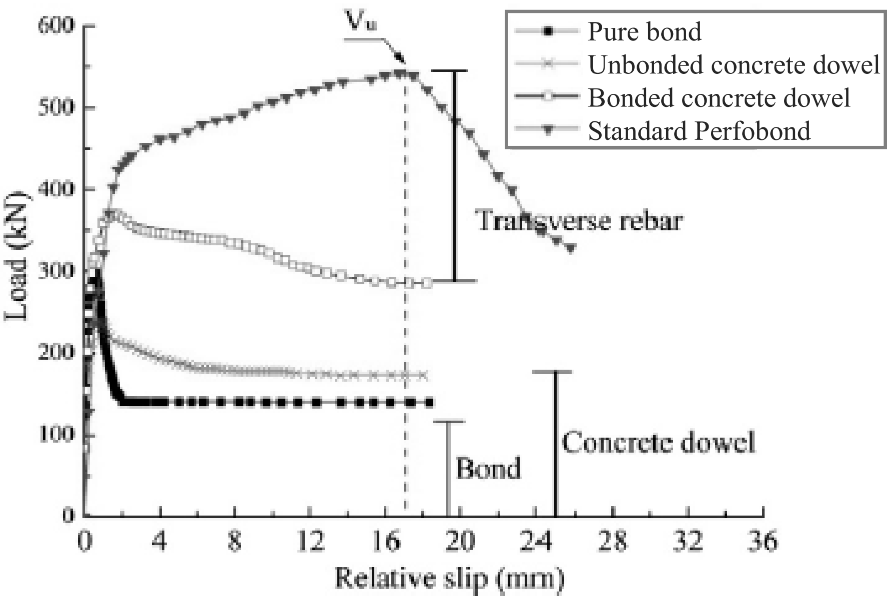

Figure 5. Analytical diagram of strength components of the CFH [10].

Zheng et al. [13] performed 9 push-out shear tests with single CFH specimens with transverse rebar in the hole, in which the influence of the hole diameter on the behavior of the CFH was evaluated. It was observed that both strength and stiffness of the connector increase as the hole diameter is enlarged, though the strength grows at a decreasing rate as the confinement effect of transverse rebar on concrete becomes weaker when the hole gets larger.

Nakajima and Nguyen [11], conducted 34 plug-in shear tests in order to evaluate the influence of the transverse reinforcement in the CFH strength. The specimens varied in transverse rebar diameter, hole diameter, plate thickness and material properties. It was observed that the transverse rebar in the hole contributes to the strength of the CFH by suppressing the opening of the shear fracture surface and by the dowel action. However, when the transverse rebar diameter is large relative to the hole diameter, it moves through the concrete within the hole which reduces the shear surface of the concrete dowel. To prevent this effect, the rebar bending stiffness must be adjusted to the compressive stiffness of its surrounding concrete.

Xiao et al. [12] performed 12 push-out and 12 plug-in tests to compare the mechanical behavior of CFH in conventional composite beams with that in a steel-concrete hybrid bridge transition, where the holes are deeply embedded in concrete. In these tests, the thickness of the steel plate and the compressive strength of the concrete were varied. It was observed that the failure mode is related to concrete spalling in the push-out tests and to the transverse rebar rupture in the plug-in tests, with plug-in tests show significantly higher strength than push-out tests. It was also observed that the test configuration has little influence on the initial stiffness, however, the degradation of the stiffness is associated with the concrete slab cracking in the push-out tests and the steel yielding of the transverse rebar in the plug-in tests.

From these 5 authors, 92 single-hole shear tests were extracted, totaling 30 variations of the connector. Their main characteristics are presented in Table 1.

2.2 Predicting formulations for CFH shear strength

Since the development of steel plate connectors with holes, different analytical models have been proposed to calculate the shear capacity of CFH (Table 2). Oguejiofor and Hosain [7], [14]; Hosaka et al. [15]; Medberry and Shahrooz [16]; Veríssimo [17]; Al Darzi et al. [18]; Ahn et al. [19] and Zheng et al. [13] derived regression analysis equations, evaluating the shear strength of CFH, obtained by means of push-out tests. He et al. [10] and Nakajima and Nguyen [11] proposed analytical models based on plug-in tests results, Zhao and Liu [20] based their formulation both push-out and plug-in test results and Braun [21] proposed a formulation for the case of application of the CFH in composite slim floor beam (CoSFB).

Table 1. Main geometric and material properties of the experimental specimens.

Author	Specimen	Test setup	Concrete strength, f_c (MPa)	Hole diameter, d (mm)	Plate thickness, t (mm)	Diameter of the transverse rebar, d_s (mm)	Average ultimate load, P_u (kN)
Su et al. [9]	SCP-50	Plug-in	47.12	50	20	0	206.64
	SCP-60	Plug-in	47.12	60	20	0	314.09
	SCP-75	Plug-in	47.12	75	20	0	386.82
	SBP-24	Plug-in	47.12	24	20	22	316.75
	SBP-60	Plug-in	47.12	60	20	22	411.51
He et al. [10]	C-b0r0d1	Plug-in	46.1	60	25	0	246.5
	C-b1r0d1	Plug-in	46.1	60	25	0	370
	C-b1r1d0	Plug-in	46.1	21	25	20	325.5
	C-b0r1d1	Plug-in	46.1	60	25	20	449
	C-b1r1d1	Plug-in	46.1	60	25	20	547
Zheng et al. [13]	CP-1	Push-out	59.5	50	20	20	388.77
	CP-2	Push-out	59.5	60	20	20	426.17
	CP-3	Push-out	59.5	75	20	20	514.23
Nakajima and Nguyen [11]	D30T12R10	Plug-in	32.15	30	12	10	90.27
	D40T12R13	Plug-in	29	40	12	13	177.96
	D40T12R16	Plug-in	29	40	12	16	238.64
	D60T12R10	Plug-in	32.27	60	12	10	250.18
	D60T12R13	Plug-in	32.5	60	12	13	238.21
	D60T12R16	Plug-in	33.3	60	12	16	246.57
	D60T19R16	Plug-in	34.1	60	19	16	242.28
	D60T25R16	Plug-in	34.1	60	25	16	269.53
	D70T12R13	Plug-in	29	70	12	13	279.59
	D70T12R16	Plug-in	29	70	12	16	301.24
	D90T12R10	Plug-in	32.15	90	12	10	413.72
Xiao et al. [12]	ST16	Push-out	41.68	60	20	16	222.9
	ST16C	Push-out	26.56	60	20	16	159.6
	ST16T	Push-out	41.68	60	8	16	158.35
	PT16	Plug-in	41.68	60	20	16	396.93
	PT16C	Plug-in	26.56	60	20	16	328.08
	PT16T	Plug-in	41.68	60	8	16	246

Table 2. Some formulations for predicting the strength of CFH.

Authors	Predicting models
Oguejiofor and Hosain [7]	$q = 0.590 A_{cc}\sqrt{f_c} + 1.233 A_{tr} f_y + 2.871 nd^2 \sqrt{f_c}$
Oguejiofor and Hosain [14]	$q = 4.50 htf_c + 3.31 nd^2 \sqrt{f_c} + 0.91 A_{tr} f_y$
Hosaka et al. [15]	$Q = 3.38 d^2 \sqrt{t/d} f_c - 39$, without transverse rebars*
	$Q = 1.45\left[\left(d^2 - d_s^2\right) f_c + d_s^2 f_u\right] - 26.1$, with transverse rebars*
Medberry and Shahrooz [16]	$P = 0.747 bh_{ecs}\sqrt{f_c} + 0.413 b_f L_c + 1.304 nd^2 \sqrt{f_c} + 0.9 A_{tr} f_y$
Veríssimo [17]	$q = 3.68\sqrt{h/b}\, htf_c + 2.60 nd^2 \sqrt{f_c} + 0.13 A_{cc}\sqrt{f_c} + 34.3\times10^6 \left(A_{tr}/A_{cc}\right)$
Al-Darzi et al. [18]	$q = 255309 + 0.762 htf_c - 7.59\times10^{-4} A_{tr} f_y + 3.97 nd^2 \sqrt{f_c}$
Ahn et al. [19]	$q = 3.14 htf_c + 2.98 nd^2 \sqrt{f_c} + 1.21 A_{trp} f_y$, for single CFH rib $q = 2.76 htf_c + 2.61 nd^2 \sqrt{f_c} + 1.06 A_{trp} f_y$, for twin CFH rib
Zhao and Liu [20]	$Q = 1.38\left(d^2 - d_s^2\right) f_c + 1.24 d_s^2 f_y$
He et al. [10]	$q = \tau_b A_b + 1.06 A_c f_{cu} + 2.09 A_s f_y$; $\tau_b = -0.022 f_{cu} + 0.306\sqrt{f_{cu}} - 0.573$
Zheng et al. [13]	$Q = 1.76\alpha_A\left(A - A_s\right) f_c + 1.58 A_s f_y$; $\alpha_A = 3.80\left(A_s / A\right)^{2/3}$
Nakajima and Nguyen [11]	$q = 0.15 A f_c^{0.65} A_l^{0.43} t^{-0.5}$, without transverse rebars*
	$q = 0.15\alpha\left(A - A_s\right) f_c^{0.65} A_l^{0.43} t^{-0.5} + 0.84 d_s f_y d^{0.1} t^{0.8}$; $\alpha = 6.9 d_s^{0.4} d^{-0.7}$, with transverse rebars*
Braun [21]	$q = 36.919\left(f_c td\times10^{-3}\right)^{0.287} + \left(\pi d_s^2 f_y / 2\sqrt{3}\right)\times10^{-3}$

Notation:

A is the hole area (mm²);
A_b is the area of the contact surface between the steel plate and the concrete (mm²);
A_c is the section area of the concrete dowel, $A_c = \pi(d^2 - d_s^2)/4$;
A_{cc} is the shear area of concrete per connector (mm²), which is the longitudinal slab area minus the connector area;
A_l is the side area of the concrete block (mm²);
A_s is the section area of the transverse rebar in one hole (mm²);
A_{tr} is the total area of transverse reinforcement (mm²);
A_{trp} is the area of the transverse rebars in the rib holes (mm²);
L_c is the contact length between the steel and the concrete per flange (mm);
P is the shear capacity per slab using CFH (N);
Q is the shear capacity per hole of CFH (N);
b is the concrete slab thickness (mm);
b_f is the steel beam flange width (mm);
d is the hole diameter (mm);
d_s is the diameter of the transverse rebar that passes through the hole (mm);
f_c is the compressive concrete strength - cylinder (MPa);
f_{cu} is the compressive concrete strength - cube (MPa);
f_u is the tensile strength of the transverse rebar (MPa);
f_y is the yield of reinforcement (MPa);
h is the connector height (mm);
h_{ecs} is the concrete slab height below the CFH (mm);
n is the number of holes of the connector;
q is the shear capacity per rib of CFH (N);
t is the connector thickness (mm).
(*) transverse rebar passing through the holes

The range of values of the geometric and material parameters for which the formulations were derived can be observed in Table 3.

Table 3. Range of values and test setup from which the formulations were derived.

Author	Test setup	f_{cu} (MPa)	f_c (MPa)	d (mm)	t (mm)	d_s (mm)
Oguejiofor and Hosain [7]	Push-out	-	20.91 - 41.43	50	13	10
Oguejiofor and Hosain [14]	Push-out	-	20 - 40	35; 50	6; 13	-
Hosaka et al. [15]	Push-out	-	23.8 - 57.6	35 - 80	8 - 22	5.1 - 28.6
Medberry and Shahrooz [16]	Push-out	-	39.6 - 45.5	50	12.7; 19	-
Veríssimo [17]	Push-out	-	20.91 - 41.43	50	13	10
Al-Darzi et al. [18]	Push-out	54.6	-	50	-	-
Ahn et al. [19]	Push-out	-	28.1 - 52.6	55	6	16
Zhao and Liu [20]	Push-out and plug-in	20 - 70	-	35 - 90	-	10-25
He et al. [10]	Plug-in	58.1	46.1	21; 60	25	20

Table 3. Continued...

Author	Test setup	f_{cu} (MPa)	f_c (MPa)	d (mm)	t (mm)	d_s (mm)
Zheng et al. [13]	Push-out	70.3	59.5	50; 60; 75	20	20
Nakajima and Nguyen [11]	Plug-in	-	29 - 34.1	30; 40; 60; 70; 90	12; 19; 25	10; 13; 16
Braun [21]	Slim Floor	30 - 67	25 - 55	25; 40	7.5; 15.5	12

Notation:
d is the hole diameter (mm);
d_s is the diameter of the transverse rebar that passes through the hole (mm);
f_c is the compressive concrete strength - cylinder (MPa);
f_{cu} is the compressive concrete strength - cube (MPa);
t is the connector thickness (mm).

2.3 Statistical evaluation

Annex D from EN 1990:2002 [6] presents a standard procedure to derive design equations based on statistical evaluations. Part of this method, used in this work, involves a number of discrete steps which must be followed until good compatibility between the equation and experimental data is achieved:

- Step 1: develop a design model for the theoretical resistance that cover the basic variables that affect the resistance at relevant limit state;
- Step 2: substitute the measured properties into the resistance function so as to obtain theoretical values r_{ti} to form the basis of a comparison with the experimental values r_{ei} from the tests, and plot the points representing pairs of corresponding values (r_{ti}, r_{ei}), as indicated in Figure 6;
- Step 3: Estimate the mean value correction factor b (Equation 1)

$$b = \frac{\sum r_e r_t}{\sum r_t^{\,2}} \tag{1}$$

where r_e is the experimental resistance value and r_t is the theoretical resistance determined from the resistance function.

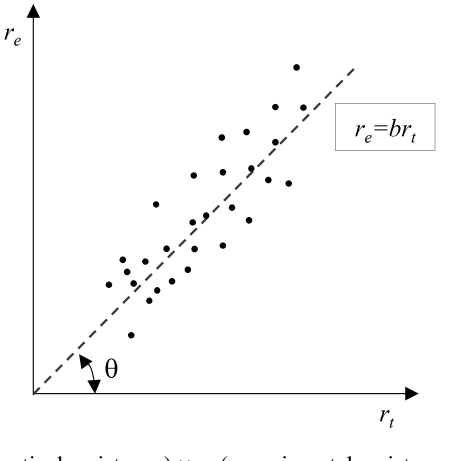

Figure 6. r_t (theoretical resistance) × r_e (experimental resistance) diagram [6].

- Step 4: Estimate the coefficient of variation of the errors V_δ (Equation 6), based on log-normal distribution

$$r_{ei} = b\, r_{ti}\, \delta_i \rightarrow \delta_i = \frac{r_{ei}}{b\, r_{ti}} \tag{2}$$

$$\Delta_i = \ln\left(\delta_i\right) \quad (3)$$

$$\overline{\Delta} = \frac{1}{n}\sum_{i=1}^{n}\Delta_i \quad (4)$$

$$s_\Delta{}^2 = \frac{1}{n-1}\sum_{i=1}^{n}\left(\Delta_i - \overline{\Delta}\right)^2 \quad (5)$$

$$V_\delta = \sqrt{\exp\left(s_\Delta{}^2\right) - 1} \quad (6)$$

where r_{ei} is the experimental resistance for specimen i, r_{ti} is the theoretical resistance determined from the resistance function, δ_i is the error term, Δ_i is the logarithm of the error term, $\overline{\Delta}$ is the mean value of the logarithm of the error term, n is the number of experimental results and $s_\Delta{}^2$ is the estimate value of variance of the term Δ.

- Step 5: Analyze compatibility of the test population with the resistance function analyzed, based on the scatter of the (r_{ei}, r_{ti}) values.

If the scatter values are too high to give an economical design, the design model can be modified taking into account parameters which has previously been ignored or modifying the parameters b and V_δ by the analysis of population subsets.

3 METHODOLOGY

The test results presented in 2.1.2, excluding the specimens with no hole by He et al. [10], were gathered and their geometric and material parameters were extracted from the specimens' descriptions (Table 1). These parameters were then applied to the 12 formulations presented in 2.2 (Table 2).

The concrete compressive strength obtained with cubic specimens was assumed to be 1.25 times that obtained with cylindrical specimens [22]. The bond between steel and concrete was only considered when authors did not use means to eliminate it, such as grease, oil and foam. For those formulations that consider an end bearing resistance, the equation term related to this contribution was discarded as none of the specimens in this work have this feature. For formulations with parameters referring specifically to slab geometry (A_{cc}, b, h_{ecs}), the concrete block of plug-in specimens was converted into slab by taking the block dimension that runs parallel to the steel plate width as corresponding to the slab thickness.

With the results obtained, the standard evaluation procedure in 2.3 was applied and, based on the correction factor (b) and coefficient of variation (V_δ) values, the formulations were evaluated. The final aim of this analysis was to determine the formulations that can best predict the CFH shear strength for the different studied shear test setups and application possibilities.

4 RESULTS AND DISCUSSIONS

Figure 7 shows the ordered pairs of strength values obtained from the formulations (r_t) and from the shear tests (r_e), where plug-in test results are denoted by circles and push-out test results by triangles. Then, the statistical analysis was performed, resulting in correction factors (b) and coefficients of variation (V_δ) for each formulation, which are presented in Table 4 and Figure 8. Based on the statistical analysis and experimental observations of the CFH behavior, critical analysis and discussion of the constituting terms of the formulations were also carried out.

Additionally, it was done an evaluation of the sensitivity of the formulations' terms to variations in the concrete's compressive strength (f_c), hole diameter (d), thickness of the connector plate (t) and diameter of the transverse rebar (d_s) when the other parameters are kept constant, as shown in Figure 9. For this, only the sets of shear tests in which the author kept constant all the parameters that could influence the result while varying one parameter of interest were selected. The results of these test sets are presented by points in graphs that relate the parameter of interest (f_c, d, t and d_s) to the obtained strength value (q). Overlaying these experimental points and the curves $q \times f_c$, d, t and d_s provided by the formulations when inputted the same parameters kept constant in the shear tests, it is possible to evaluate if the formulations adequately capture the trends observed experimentally.

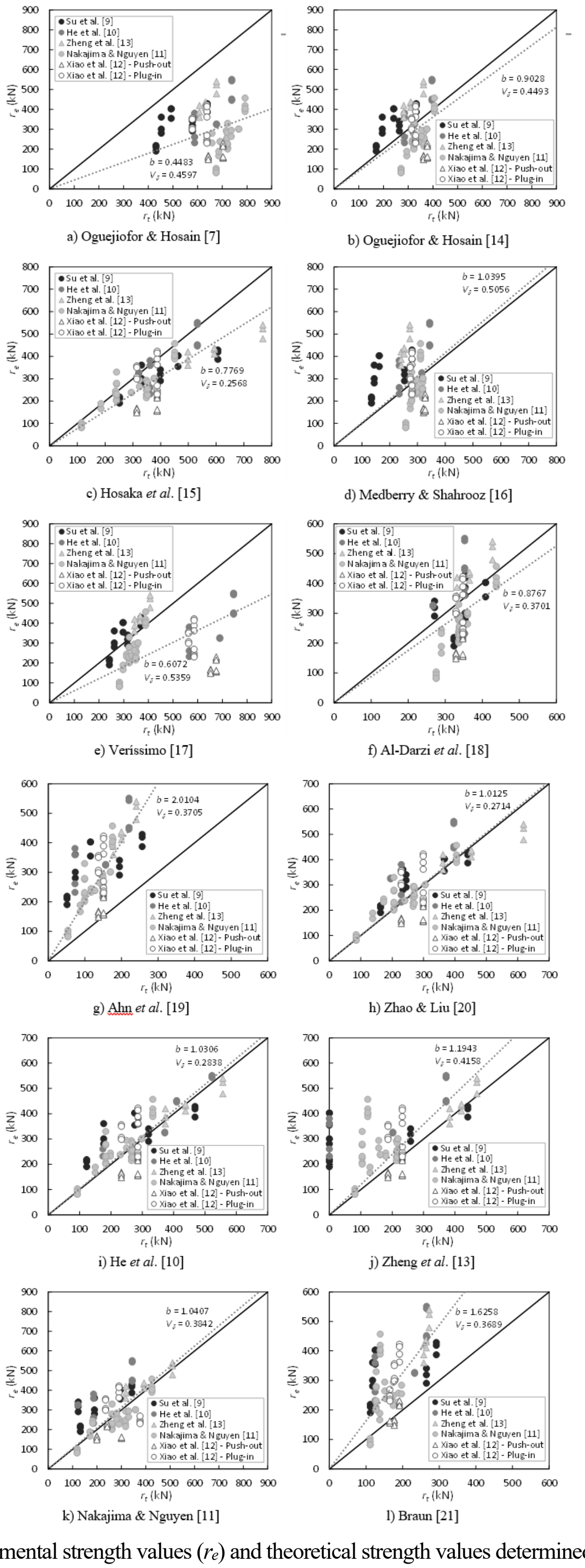

a) Oguejiofor & Hosain [7]
b) Oguejiofor & Hosain [14]
c) Hosaka *et al*. [15]
d) Medberry & Shahrooz [16]
e) Veríssimo [17]
f) Al-Darzi *et al*. [18]
g) Ahn *et al*. [19]
h) Zhao & Liu [20]
i) He *et al*. [10]
j) Zheng *et al*. [13]
k) Nakajima & Nguyen [11]
l) Braun [21]

Figure 7. Relation between experimental strength values (r_e) and theoretical strength values determined from analyzed formulations (r_t).

Given the small number of experimental points available for this analysis (Figure 9), the trend evaluation of the curves was done simply by comparing the average slope of each curve with the slope of a line connecting the first to the last experimental point, within the experimental values interval. The average slopes of the curves are given in Table 5 as a factor of the slope defined by the experimental points.

Table 4. Statistical analysis of the formulations: equations ranked by coefficient of variation (V_δ).

Formulation	V_δ	b
Hosaka et al. [15]	0.2568	0.7769
Zhao and Liu [20]	0.2714	1.0125
He et al. [10]	0.2838	1.0306
Braun [21]	0.3689	1.6258
Al-Darzi et al. [18]	0.3701	0.8767
Ahn et al. [19]	0.3705	2.0104
Nakajima and Nguyen [11]	0.3842	1.0407
Zheng et al. [13]	0.4158	1.1943
Oguejiofor and Hosain [14]	0.4493	0.9028
Oguejiofor and Hosain [7]	0.4597	0.4483
Medberry and Shahrooz [16]	0.5056	1.0395
Veríssimo [17]	0.5359	0.6072

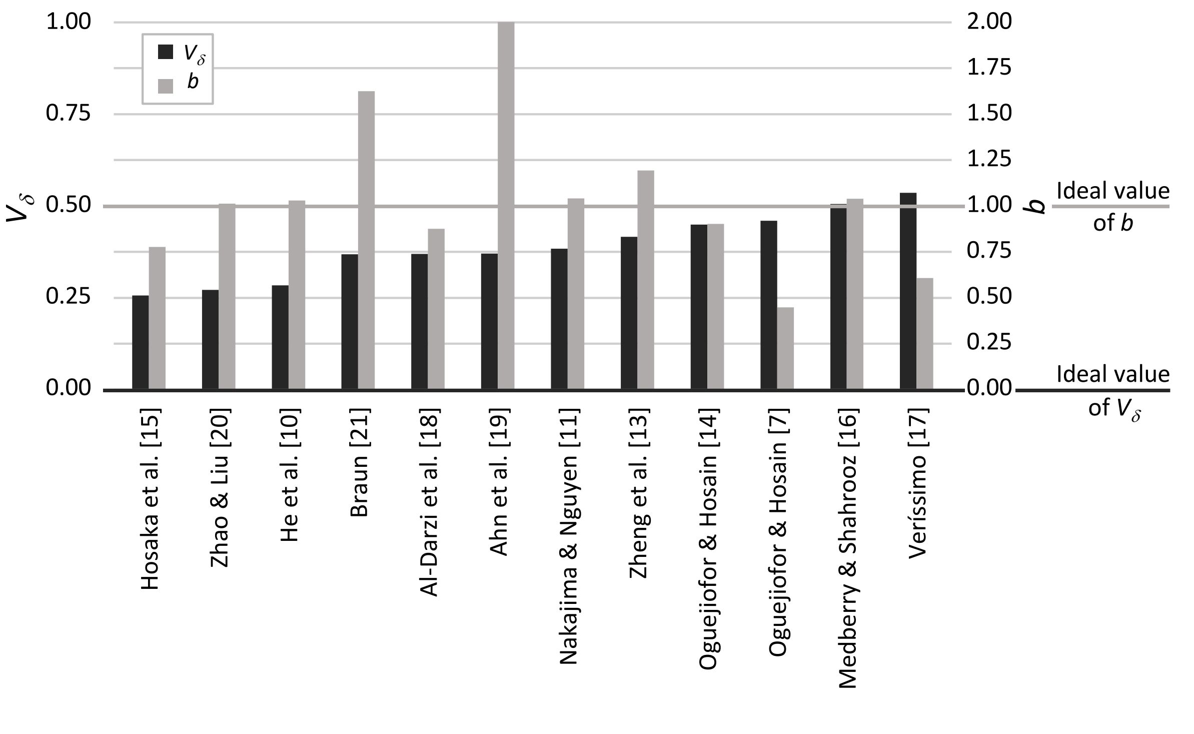

Figure 8. Statistical analysis result: formulations in order of coefficient of variation (V_δ).

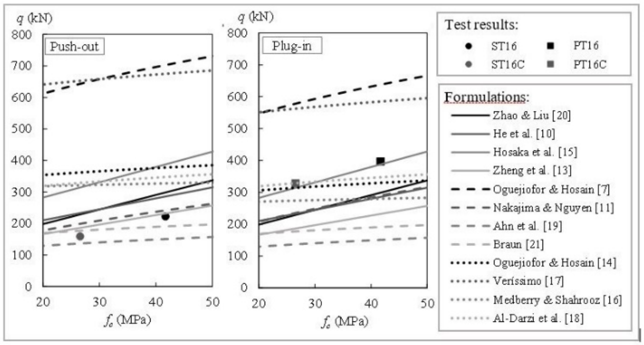

a) variation of compressive concrete strength (f_c)

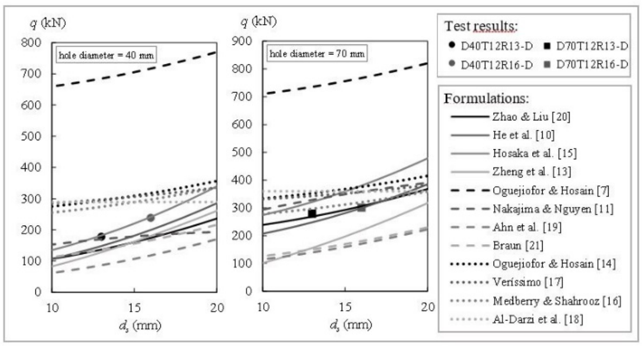

b) variation of diameter of the transverse rebar (d_s)

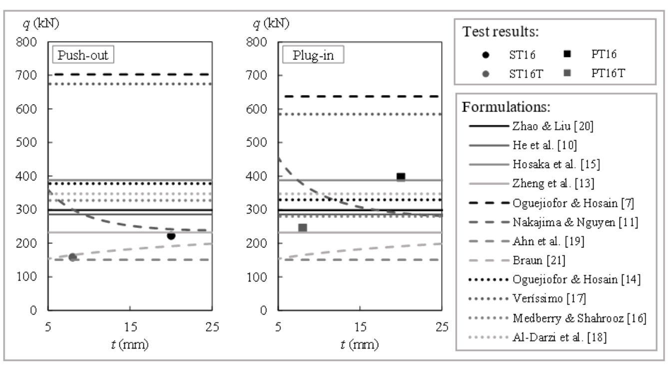

c) variation of Perfobond connector thickness (t)

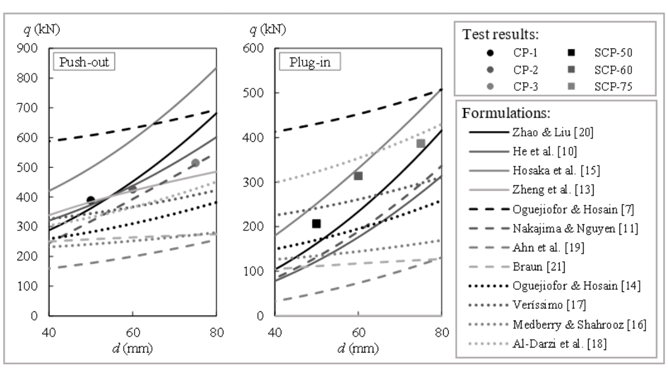

d) variation of hole diameter (d)

Figure 9. Strength values (q) obtained in shear tests and predicted by formulations observing the variation of a) compressive concrete strength, b) diameter of the transverse rebar that passes through the hole, c) CFH rib thickness and d) hole diameter.

Table 5. Formulations ranked by approximation of average slope of $q \times f_c$, d, t and d_s curves in relation to the slope defined by experimental points.

Formulation	Variation of compressive concrete strength		Variation of diameter of the transverse rebar		Variation of plate thickness		Variation of hole diameter		Average
	push-out	plug-in	*d*=40	d=70	push-out	plug-in	push-out	plug-in	
Zhao and Liu [20]	1.10	1.01	0.62	1.73	0.00	0.00	2.05	1.13	0.95
He et al. [10]	0.83	0.76	0.85	2.38	0.00	0.00	1.46	0.85	0.89
Hosaka et al. [15]	1.16	1.06	0.98	2.74	0.00	0.00	2.15	1.17	1.16
Zheng et al. [13]	0.72	0.66	0.87	2.93	0.00	0.00	0.69	-	0.84
Oguejiofor and Hosain [7]	0.94	0.87	0.53	1.48	0.00	0.00	0.55	0.34	0.59
Nakajima and Nguyen [11]	0.67	0.79	0.21	1.36	-0.91	-0.57	1.52	0.91	0.50
Ahn et al. [19]	0.22	0.20	0.52	1.45	0.00	0.00	0.50	0.35	0.41
Braun [21]	0.22	0.20	0.49	1.38	0.41	0.17	0.12	0.08	0.38
Oguejiofor and Hosain [14]	0.25	0.23	0.39	1.09	0.00	0.00	0.64	0.39	0.37
Veríssimo [17]	0.35	0.32	0.24	0.67	0.00	0.00	0.50	0.31	0.30
Medberry and Shahrooz [16]	0.10	0.09	0.38	1.08	0.00	0.00	0.25	0.16	0.26
Al-Darzi et al. [18]	0.29	0.27	0.00	0.00	0.00	0.00	0.76	0.47	0.23

4.1 Statistical analysis of the formulations

From the results of the statistical analysis, it can be observed that the formulations that shown lower values of coefficient of variation (V_δ), therefore, lower scatter of data, were those by Hosaka et al. [15], Zhao and Liu [20] and He et al. [10], in that order.

Although the formulation by Hosaka et al. [15] presented the lowest coefficient of variation, its correction factor (*b*) was 22.31% lower than one, evidencing the need to adjust the parameters of the formulation.

The formulations by Zhao and Liu [20] and He et al. [10] also shown low coefficients of variation when compared to the other formulations and a correction factors very close to one, *i.e.*, $\theta \approx 45°$ (Figure 6), which characterizes them as the best formulations. The better compatibility of such formulations with the experimental data is due to the fact that He et al. [10] performed a comparative analysis that effectively isolated the influence of each strength component (concrete dowel, transverse rebar in the hole and bond) from single-hole plug-in tests (Figure 5) and that Zhao and Liu [20] derived their formulation from 168 test results, both plug-in and push-out.

The other formulations presented higher scatter of the data even though in some cases [11], [16] the correction factor was close to one, as desired.

4.2 Analysis of the terms that constitute the formulations

Although some formulations may at times provide predictions close to the experimental results, the terms that constitute their equations may not consistently represent the mechanical behavior of the connection [10], [13]; therefore, it was conducted in this work an analysis of the terms that constitute these formulations.

It is noted that the constituting terms of some formulations are specifically related to the test configuration from which they were derived [7], [13], [16]; making it difficult to apply them in certain design applications. Regarding the formulations by Oguejiofor and Hosain [7] and Medberry and Shahrooz [16], because they were derived from push-out tests, these authors specified a term to address the splitting of the concrete slab observed in the tests, however, this failure mode does not occur in plug-in tests and, in composite beam applications, it is usually resisted by the slab's transverse reinforcement (see item 6.6.6 of EN 1994.1.1:2004 [8]), not by the connector itself. Regarding the formulation by Zheng et al. [13], it is valid only when there is transverse rebar passing through the hole, in the absence of this, such formulation provides null values, which had to be discarded in the statistical analysis.

Observing the points referring to the experimental results of Xiao et al. [12] in Figure 7, it is noted that for most formulations the results of the push-out (triangles) and plug-in (circles) tests laid vertically aligned in the diagrams, indicating that these formulations are unable to predict a strength increase as the depth of the connection increases. Only the formulation by Nakajima and Nguyen [11] was able to predict higher strength values for plug-in shear tests. The Oguejiofor and Hosain [7], [14]; Medberry and Sharooz [16] and Veríssimo [17] formulations showed the opposite trend, *i.e.*, they incorrectly predicted higher strength for push-out tests.

In Figure 9c, it is noted a trend of strength increase as the thickness of the steel plate is increased, which was addressed only by Braun [21]. In the formulation by Nakajima and Nguyen [11] the plate thickness parameter (*t*) has an exponential power of -0.5 in the first term of the equations which caused the hole's strength to decrease with an increase of plate thickness. The other formulations show no relation between the hole's strength and the plate thickness.

By combining the analysis of the terms of the formulations with the statistical analysis, it is observed that, despite showing low scatter the formulation by Hosaka et al. [15] has constant terms to which no physical meaning has been attributed. The same happens with the formulation by Al-Darzi et al. [18], where in some cases the constant terms even exceed the expected strength value. Also, in this formulation [18] the transverse rebar in the hole contributes negatively to the connector strength, which was not observed in any other formulation and doesn't agree with the experimental observations in 2.1.2.

As for the two best ranked formulations in the statistical analysis (Zhao and Liu [20] and He et al. [10]), it is observed that they are basically constituted of a term regarding the contribution of the concrete dowels and another regarding the transverse rebar in the hole, thus defining the strength of the CFH as the sum of these two main strength components.

The sensitivity evaluation of the formulations' terms (Figure 9 and Table 5) showed that the three best ranked formulations in the statistical evaluation (Zhao and Liu [20], He et al. [10] and Hosaka et al. [15]) were also the ones that best captured the trends observed experimentally, as they resulted in curves with average slopes closer to those defined by the experimental points. This indicates that these equations showed better correlation with experimental data in 4.1 because they better describe the mechanical behavior of the connection and the influence of each isolated parameter.

However, it should be noted that none of the formulations adequately captured the influence that the plate thickness and depth of the connection have on hole strength. Therefore, it is suggested that, in addition to the geometric parameters already addressed by Zhao and Liu [20] and He et al. [10], plate thickness and depth of the connection should also be considered for predicting CFH shear strength. Also, a series of new push tests should be conducted in order to obtain more detailed curves relating of each of these parameters with the connector's strength. By doing so, according to Annex D of EN 1990: 2002 [6] (item D8.2.2.5 Step 5), a formulation with lower coefficient of variation could be obtained which would allow a more economical design.

5 CONCLUSIONS

In this work 12 formulations were evaluated for predicting the strength of CFH in 92 shear tests with single-hole specimens. It was considered that a formulation that adequately predicts the strength of a single hole, *i.e.*, the fundamental aspect of CFH connections, is more suitable to be adapted and extrapolated to the various structural applications of this type of connection. From statistical and critical analysis, it was concluded that:

- the formulation proposed by Hosaka et al. [15] presented the lowest scatter of data, but its correction factor was the fifth furthest from one. Also, it has constant terms to which no physical meaning has been attributed, this makes it difficult to adapt this equation to different design conditions, since these terms cannot be related to the physical and geometric settings of a given situation;
- the formulations that presented lower scatter and correction factor value closer to one were the ones by Zhao and Liu [20] and He et al. [10], thus being considered the best formulations for obtaining the strength of CFH, both in plug-in and push-out tests. These formulations are basically constituted of a term referring to the contribution of concrete dowels and another referring to the contribution of the transverse rebars that passes through the hole;
- other formulations presented higher scatter, evidencing the need to review the parameters considered for deriving these formulations;
- among the formulations studied in this paper, it is suggested that the best three for predicting the strength of CFH are those by Zhao and Liu [20], He et al. [10] and Hosaka et al. [15], in that order;
- none of the formulations adequately expressed the influence that plate thickness and depth of the connection have on the hole strength. Moreover, there were few single-hole test results from which to draw curves relating the strength of the connector to its geometric and material parameters. Therefore, it is suggested to conduct further shear tests on the CFH so that the plate thickness and depth of the connector are included in the set of parameters that constitutes the formulations. Thus, more detailed curves relating of each individual parameter with the CFH strength can be drawn.

ACKNOWLEDGEMENTS

The authors wish to acknowledge the Coordenação de Aperfeiçoamento de Pessoal de Nível Superior (CAPES), Conselho Nacional de Desenvolvimento Científico e Tecnológico (CNPq), Fundação de Amparo à Pesquisa do Estado de Minas Gerais (FAPEMIG) and Universidade Federal de Minas Gerais (UFMG) for their support for the realization and dissemination of this study.

REFERENCES

[1] F. Leonhardt, W. Andrä, H. P. Andrä, and W. Harre, "Neues, vorteilhaftes verbundmittel für stahlverbund-tragwerke mit hoher daurfestigkeit," *Beton Stahlbetonbau*, vol. 82, no. 12, pp. 325–331, Dec 1987, http://dx.doi.org/10.1002/best.198700500.

[2] ArcelorMittal Europe. "Slim floor: an innovative concept for floors, design guide." http://constructalia.arcelormittal.com (accessed Apr. 24, 2017).

[3] F. Xu, Z. Zhang, D. Wang, and W. Hulil, "Application of a perfobond rib shear connector group in a beam-arch hybrid bridge," *Struct. Eng. Int.*, vol. 25, no. 4, pp. 414–418, 2015, http://dx.doi.org/10.2749/101686615X14355644770974.

[4] J. Vianna, L. F. Costa-Neves, P. C. G. S. Vellasco, and S. A. L. Andrade, "Structural behaviour of T-Perfobond shear connectors in composite girders: An experimental approach," *Eng. Struct.*, vol. 30, no. 9, pp. 2381–2391, Sep 2008, http://dx.doi.org/10.1016/j.engstruct.2008.01.015.

[5] L. Peng-Zhen, C. Lin-feng, L. Yang, L. Zheng-lun, and S. Hua, "Study on mechanical behavior of negative bending region based design of composite bridge deck," *Int. J. Civ. Eng.*, vol. 16, pp. 489–497, 2018, http://dx.doi.org/10.1007/s40999-017-0156-0.

[6] European Committee for Standardization, *Basis of Structural Design*, EN 1990:2002, 2002.

[7] E. C. Oguejiofor and M. U. Hosain, "A parametric study of perfobond rib shear connectors," *Can. J. Civ. Eng.*, vol. 21, no. 4, pp. 614–625, 1994, http://dx.doi.org/10.1139/l94-063.

[8] European Committee for Standardization, *Design of Composite Steel and Concrete Structures – Part 1-1: General Rules and Rules for Buildings*, EN 1994-1-1:2004, 2004.

[9] Q. T. Su, W. Wang, H. W. Luan, and G. T. Yang, "Experimental research on bearing mechanism of perfobond rib shear connectors," *J. Construct. Steel Res.*, vol. 95, pp. 22–31, Apr 2014, http://dx.doi.org/10.1016/j.jcsr.2013.11.020.

[10] S. He, Z. Fang, Y. Fang, M. Liu, L. Liu, and A. S. Mosallam, "Experimental study on perfobond strip connector in steel-concrete joints of hybrid bridges," *J. Construct. Steel Res.*, vol. 118, pp. 169–179, Mar 2016, http://dx.doi.org/10.1016/j.jcsr.2015.11.009.

[11] A. Nakajima and M. H. Nguyen, "Strain behavior of penetrating rebar in perfobond strip and its evaluation of shear resistance," *J. JSCE*, vol. 4, no. 1, pp. 1–18, 2016, http://dx.doi.org/10.2208/journalofjsce.4.1_1.

[12] L. Xiao, X. Li, and Z. J. Ma, "Behavior of perforated shear connectors in steel–concrete composite joints of hybrid bridges," *J. Bridge Eng.*, vol. 22, no. 4, pp. 1–15, Apr 2017, http://dx.doi.org/10.1061/(ASCE)BE.1943-5592.0001020.

[13] S. Zheng, Y. Liu, T. Yoda, and W. Lin, "Parametric study on shear capacity of circular-hole and long-hole perfobond shear connector," *J. Construct. Steel Res.*, vol. 117, pp. 64–80, Feb 2016, http://dx.doi.org/10.1016/j.jcsr.2015.09.012.

[14] E. C. Oguejiofor and M. U. Hosain, "Numerical analysis of push-out specimens with perfobond rib connectors," *Comput. Struc.*, vol. 62, no. 4, pp. 617–624, Feb 1997, http://dx.doi.org/10.1016/S0045-7949(96)00270-2.

[15] T. Hosaka, K. Mitsuki, H. Hiragi, Y. Ushijima, Y. Tachibana, and H. Watanabe, "An experimental study on shear characteristics of perfobond strip and its rational strength equations," *J. Struct. Eng.*, vol. 46, pp. 1593–1604, 2000.

[16] S. B. Medberry and B. M. Shahrooz, "Perfobond shear connector for composite construction," *Eng. J. (N.Y.)*, vol. 39, no. 1, pp. 2–12, 2002.

[17] G. S. Veríssimo, "Desenvolvimento de um conector de cisalhamento em chapa dentada para estruturas mistas de aço e concreto e estudo do seu comportamento," D.Sc. thesis, Dept. Eng. Estruturas, Univ. Fed. Minas Gerais, Belo Horizonte, 2007.

[18] S. Y. K. Al-Darzi, A. R. Chen, and Y. Q. Liu, "Finite element simulation and parametric studies of perfobond rib connector," *Am. J. Appl. Sci.*, vol. 4, no. 3, pp. 122–127, Mar 2007.

[19] J. H. Ahn, C. G. Lee, J. H. Won, and S. H. Kim, "Shear resistance of the perfobond-rib shear connector depending on concrete strength and rib arrangement," *J. Construct. Steel Res.*, vol. 66, no. 10, pp. 1295–1307, Oct 2010, http://dx.doi.org/10.1016/j.jcsr.2010.04.008.

[20] C. Zhao and Y. Q. Liu, "Experimental study of shear capacity of perfobond connector," *Eng. Mech.*, vol. 29, no. 12, pp. 349–354, 2012.

[21] M. Braun, "Investigation of the load-bearing behavior of CoSFB-dowels," Ph.D. dissertation, Fac. Sci. Technol. Commun., Univ. Luxembourg, Luxembourg, 2018.

[22] C. T. Tam, S. B. Daneti, and W. Li, "EN 206 conformity testing for concrete strength in compression," *Procedia Eng.*, vol. 171, pp. 227–237, 2017, http://dx.doi.org/10.1016/j.proeng.2017.01.330.

Author contributions: Otávio Prates Aguiar was the idealizer of this paper and contributed to the conclusions and translation of the text; Larice Gomes Justino Miranda developed the study and wrote the paper; Paulo Estevão Carvalho Silvério assisted in obtaining literature test data. All work was supervised and reviewed by Rodrigo Barreto Caldas.

Editors: Leandro Trautwein, Guilherme Aris Parsekian.

IBRACON Structures and Materials Journal
Revista IBRACON de Estruturas e Materiais
ISSN 1983-4195 *ismj.org*

ORIGINAL ARTICLE

Probabilistic chloride diffusion modelling in cracked concrete structures by transient BEM formulation

Modelagem probabilística da difusão de cloreto em estruturas de concreto fissurado pela formulação transiente do MEC

Vinícius de Barros Souza[a]
Edson Denner Leonel[a]

[a]Universidade de São Paulo – USP, Escola de Engenharia de São Carlos, Departamento de Engenharia de Estruturas, São Carlos, SP, Brasil

Received 17 August 2021
Accepted 29 October 2021

Abstract: Reinforcement corrosion is a concern in the structural engineering domain, since it triggers several pathological manifestations, reducing the structural service life. Chloride diffusion has been considered one of main causes of reinforcements' corrosion in reinforced concrete. Corrosion starts when the chloride concentration at the reinforcements interface reaches the threshold content, leading to depassivation, whose assessment of its time of starts is a major challenge. This study applied the transient Boundary Element Method (BEM) approach for modelling chloride diffusion in concrete pores. The subregion BEM technique effectively represented the cracks inherent to the material domain, and environmental effects were also considered. Because of the inherent randomness of the problem, the service life was evaluated within the probabilistic context; therefore, Monte Carlo Simulation (MCS) assessed the probabilistic corrosion time initiation. Three applications demonstrated the accuracy and robustness of the model, in which the numerical results achieved by BEM were compared against numerical, analytical, and experimental responses from the literature. The probabilistic modelling substantially reduced the structural service life when the cracks length was longer than half of concrete cover thickness in highly aggressive environments.

Keywords: boundary element method, chloride diffusion, corrosion, structural durability, probabilistic analysis.

Resumo: A corrosão das armaduras é uma preocupação no domínio da engenharia estrutural, uma vez que este fenômeno desencadeia diversas manifestações patológicas, reduzindo a vida útil estrutural. A difusão do cloreto tem sido considerada uma das principais causas da corrosão das armaduras em concreto armado. A corrosão começa quando a concentração de cloreto na interface das armaduras atinge o teor limite, levando à despassivação, cuja avaliação do seu tempo de início é um grande desafio. Este estudo aplicou a abordagem transiente do Método dos Elementos de Contorno (MEC) para modelar a difusão de cloretos em poros do concreto. A técnica de sub-região do MEC possibilitou a representação de fissuras no domínio de forma eficaz, sendo também considerados efeitos ambientais. Por causa da inerente aleatoriedade do problema, a vida útil foi avaliada dentro do contexto probabilístico; portanto, a Simulação de Monte Carlo (SMC) avaliou o tempo de iniciação da corrosão probabilisticamente. Três aplicações demonstraram a precisão e robustez do modelo, no qual os resultados numéricos obtidos pelo MEC foram comparados com respostas numéricas, analíticas e experimentais da literatura. A modelagem probabilística reduziu substancialmente a vida útil estrutural quando o comprimento das fissuras superou a metade da espessura do cobrimento de concreto em ambientes altamente agressivos.

Palavras-chave: método dos elementos de contorno, difusão de cloreto, corrosão, durabilidade estrutural, análise probabilística.

How to cite: V. B. Souza and E. D. Leonel, "Probabilistic chloride diffusion modelling in cracked concrete structures by transient BEM formulation", *Rev. IBRACON Estrut. Mater.*, vol. 15, no. 4, e15402, 2022, https://doi.org/10.1590/S1983-41952022000400002

Corresponding author: Vinícius de Barros Souza. E-mail: vbarros@usp.br
Financial support: Coordenação de Aperfeiçoamento de Pessoal de Nível Superior - Brasil (CAPES) – Finance Code 001.
Conflict of interest: Nothing to declare.
Data Availability: The computational codes written in FORTRAN are stored in digital media and fully available in the "Laboratório de Informática e Mecânica Computacional do SET/EESC/USP". The authors share these files kindly on demand.

This is an Open Access article distributed under the terms of the Creative Commons Attribution License, which permits unrestricted use, distribution, and reproduction in any medium, provided the original work is properly cited.

1 INTRODUCTION

Structural durability is a concern in the engineering domain, particularly in civil engineering, which largely employs reinforced concrete (RC) structures. The coupling of steel and concrete leads to effective structural systems and provides alternatives for magnificent architectural designs, chemical and thermal protection, and complementary mechanical behaviour. The service life concept frequently assesses the durability of RC structures and comprehends the time span for adequate material and structural performance [1]. Because RC is a porous-cracked composite material often exposed to environmental actions, the prediction of service life is a complex task and requires the development of robust and accurate frameworks despite the time span values suggested by design codes.

Pathological manifestations such as cover cracking, leaching, spalling, and reinforcement corrosion substantially reduce the durability of RC structures - the latter is the main mechanism, affecting approximately 58% of such structures and leading to 1% to 5% economic loss in the gross domestic product [2]–[5]. Chloride ingress is one of the main triggering causes of reinforcements corrosion, whose nature is often electrochemical in RC structures [6]. Chloride ions (Cl^-) penetrate the concrete pores by diffusion, and the reinforcements corrosion starts when the chloride concentration at the concrete/reinforcement interface reaches the threshold content [7], eliminating the passivation layer. Therefore, an accurate prediction of the time of corrosion initiation enables adequate assessments of structural durability.

The chloride diffusion process can be modelled by analytical approaches such as Fick's law [8]–[13]; however, analytical solutions account for inherent simplifications (e.g., time-independent boundary conditions, inert materials, body's geometry, material homogeneity, and dimensionality domain). Since structural materials in general do not satisfy such hypotheses, those approaches are non-robust for real-world applications.

On the other hand, numerical methods offer strategies for a proper modelling of the diffusion phenomenon. The Finite Element Method (FEM) and its extended version (XFEM) have been largely adopted for this purpose [14]–[21]; however, they both require domain mesh, which introduces domain approximations. Besides, an accurate assessment of domain variables leads to refined spatial and temporal discretisation, hence, a high number of degrees of freedom and large systems of algebraic equations [22]. These approaches may also lead to large computational time-consuming techniques, which make recursive or even parametric modelling prohibitive.

BEM effectively models the diffusion phenomenon and because this approach enables a boundary integral representation of the problem, the mesh required has a one-order dimensionality reduction. Moreover, discretisation is at the body's boundary and no domain mesh is needed. The latter aspect enables an accurate assessment of internal fields, which is attractive in diffusion problems with geometric details such as cracks, and relevant in durability assessments, which require a precise determination of the chloride concentration at the concrete/reinforcements interface. Discretisation solely at the boundary provides a solution with few degrees of freedom in comparison to domain methods. Therefore, BEM is adequate for parametric or even recursive analyses, as those required in probabilistic modelling [23]–[25].

Despite its accuracy, BEM has been marginally applied for solving corrosion time initiation and durability problems. Yang et al. [26], [27] adopted it for the diffusion modelling of chloride ions into cover thickness of concrete structures, and Chen et al. [28] analysed chloride diffusion in high-performance concretes, in which the BEM performance was compared against experimental results. Pellizzer and Leonel [29] modelled chloride ingress in concrete pores using the time-dependent BEM approach for diffusion, and later [30] proposed a Reliability-Based Design Optimisation (RBDO) formulation for the probabilistic optimisation of cover thickness in concrete structures subjected to chloride penetration. The present study contributes to the field applying the transient BEM approach for the time-dependent diffusion modelling of chlorides in concrete structures. The novelty involves the cracks influence modelling, which are preferential ingress paths. Such material discontinuities inherent to the concrete microstructure were discretely accounted, thus extending the state-of-the-art of the problem and enabling a realistic diffusion modelling in concrete pores.

Huge uncertainties influence the chloride diffusion processes and, since this phenomenon depends upon temperature, moisture, concrete mechanical integrity, structural loadings, concrete topology microstructure, among others, deterministic approaches fail in accurately predicting the chloride concentration and its evolution along time [31]–[33]. Consequently, the phenomenon can be handled solely in the probabilistic framework. For such purpose, First Order Reliability Method (FORM) or even Second Order Reliability Method (SORM) might be utilised; however, the inherent phenomenon complexities do not enable the process description by a single set of equations. The robust problem description requires numerical methods and implicit representations, as those adopted in this study. This aspect leads to numerical derivatives within FORM and SORM procedures, which may introduce a lack of convergence in several cases. Besides, the design point cannot be accurately determined in high nonlinear probabilistic problems, such as those handled herein, which make those solution techniques non-effective. Monte Carlo Simulation (MCS) is an adequate approach for assessing the probability of failure for the problems considered in this study. Since it requires a large range of simulations for an accurate probability of failure assessment, its computation cost is a concern. Nevertheless, the computational effectiveness of BEM enables a probabilistic description via MCS. Very few studies have adopted this coupling scheme [29], [30], [34], thus motivating this research, which deals with the probabilistic modelling of chloride ingress in concrete pores.

The transient BEM formulation for diffusion handles the phenomenon description, whereas its coupling with MCS accounts for the uncertainties modelling. High-order boundary elements perform spatial approximations and the constant interpolation scheme approximates the temporal variables. BEM model accounts the presence of cracks and their influence upon the chloride flux velocity, which is the novelty in this study. Because concrete is cracked by loading and cure actions, the cracks representation enables an accurate and realistic problem modelling. Environmental effects such as chloride binding, temperature, and loadings were included in the modelling, which is a contribution of the study. Three applications demonstrated the accuracy and robustness of the proposed framework. The BEM results were compared against numerical, analytical, and experimental responses from the literature in applications one and two. The third application described the probabilistic modelling for tidal zones and highly aggressive environments.

2 TRANSIENT FORMULATION

2.1 Integral equations and BEM formulation

The following differential equation governs the transient diffusion problem (Equation 1):

$$\nabla^2 u - \frac{1}{k}\frac{\partial u}{\partial t} = 0 \tag{1}$$

where u represents the potential, t is time and k denotes the diffusion coefficient.

The solution of the differential equation requires boundary conditions regarding potential (u) and flux (q), as in Equations 2-3:

$$u(x,t) = \overline{u}(x,t) \;\; x \in \Gamma_1, \tag{2}$$

$$q(x,t) = \overline{q}(x,t) \;\; x \in \Gamma_2, \tag{3}$$

and initial conditions (Equation 4):

$$u(x,t_0) = u_0(x) \;\; x \in \Omega \tag{4}$$

where u_0 represents the potential conditions enforced along the domain (Ω) at the initial time (t_0), and $\overline{u}$ and $\overline{q}$ denote prescribed potential values in Γ_1 and prescribed flux values in Γ_2, respectively, where $\Gamma = \Gamma_1 \cup \Gamma_2$ is the body boundary. Flux is the directional derivative of u in relation to the outward normal vector to the boundary (η), i.e. $q = \partial u / \partial \eta$. In the present study, the potential represents the chloride concentration at a given point x for time t and q chloride flux.

Wrobel [35] demonstrated Equation 1 provides a boundary integral representation applying one of the following approaches: Laplace Transformation, Dual Reciprocity Method, or Time-Dependent Fundamental Solution. This study has adopted the latter; therefore, Green's second identity is applied to Equation 1 towards the boundary integral representation. The application of weighted residual technique, the integration of the resulting kernels by parts, and the classical limit process lead to the following integral equation:

$$c(\xi)u(\xi,t_F)+\int_{t_0}^{t_F}\int_{\Gamma}u(x,t)\ q^*(\xi,x,t_F,t)k\ d\Gamma\ dt=\int_{t_0}^{t_F}\int_{\Gamma}q(x,t)\ u^*(\xi,x,t_F,t)k\ d\Gamma\ dt+\int_{\Omega}u_0(x)\ q^*(\xi,x,t_F,t_0)k\ d\Omega \tag{5}$$

where x indicates the field points and ξ denotes the source points, t_0 is the initial time and t_F is the observation time, u^* and q^* are the time-dependent fundamental solutions to potential and flux, respectively, and c is the BEM free term. The free term value depends upon the source point position; it equals 0.5 for source point on smooth boundaries, such as those used here.

Equation 5 contains a domain integral, which can be transformed into a boundary integral by the Dual Reciprocity Method. Nevertheless, for the sake of simplicity, this term has been assumed nil, and Equation 5 can be rewritten as Equation 6.

$$c(\xi)u(\xi,t_F)+k\int_{t_0}^{t_F}\int_{\Gamma}u(x,t)\ q^*(\xi,x,t_F,t)d\Gamma\ dt=k\int_{t_0}^{t_F}\int_{\Gamma}q(x,t)\ u^*(\xi,x,t_F,t)d\Gamma\ dt. \tag{6}$$

For two-dimensional problems, the time-dependent fundamental solutions in Equation 6 are as follows (Equations 7-8) [35]:

$$u^*(\xi,x,t_F,t)=\frac{1}{4\pi k\tau}\exp\left(-\frac{r^2}{4k\tau}\right), \tag{7}$$

$$q^*(\xi,x,t_F,t)=-\frac{r\dfrac{\partial r}{\partial \eta}}{8\pi k^2\tau^2}\exp\left(-\frac{r^2}{4k\tau}\right), \tag{8}$$

where $\tau=t_F-t$ (t_F is analysis time), r indicates the distance between the source ξ and field x points, and $\dfrac{\partial r}{\partial \eta}=r_{,k}\,\eta_k$.

2.2 Algebraic representation

The numerical solution of Equation 6 requires spatial and temporal discretisation. Dividing boundary Γ into N_e boundary elements and time span t_F-t_0 into NT time steps, and inverting the order of integration in Equation 6, the following discretised equation can be obtained:

$$c_i\ u_i^{NT}=k\sum_{j=1}^{Ne}\sum_{n=1}^{NT}\int_{\Gamma_\mathrm{j}}\int_{t_0^n}^{t_F^n}q^n\ u^*dt\ d\Gamma_\mathrm{j}-k\sum_{j=1}^{Ne}\sum_{n=1}^{NT}\int_{\Gamma_\mathrm{j}}\int_{t_0^n}^{t_F^n}u^n\ q^*dt\ d\Gamma_\mathrm{j} \tag{9}$$

where u_i^{NT} is the potential value in source point i at time step NT, and t_0^n and t_F^n are initial and final times at time step n, respectively.

Equation 9 can be rewritten assuming a constant approximation along time and the positioning of collocation points at smooth boundaries. Therefore,

$$\sum_{n=1}^{NT}\sum_{j=1}^{Ne} H_{ij}^{n}\ u_{j}^{n} = \sum_{n=1}^{NT}\sum_{j=1}^{Ne} G_{ij}^{n}\ q_{j}^{n}, \tag{10}$$

where:

$$G_{ij}^{n} = k\int_{\Gamma_{\mathrm{j}}} U_{n}^{*}\ d\Gamma_{\mathrm{j}}, \tag{11}$$

$$H_{ij}^{n} = \begin{cases} k\int_{\Gamma_{j}} Q_{n}^{*}\ d\Gamma_{j} + 0.5\, if\ n = 1\, and\ i = j, \\ \quad k\int_{\Gamma_{j}} Q_{n}^{*}\ d\Gamma_{j}\ otherwise. \end{cases} \tag{12}$$

Equation 10 provides the algebraic system of equations for each boundary node. Therefore, the integration of U^{*} and Q^{*} leads to classical BEM influence matrices *G* and *H*, respectively. Because the problem is transient, the process solution requires a time-marching scheme [35], solved here as

$$\sum_{n=1}^{NT}\left[H\right]^{NT-n+1}\left\{u\right\}^{n} = \sum_{n=1}^{NT}\left[G\right]^{NT-n+1}\left\{q\right\}^{n}. \tag{13}$$

Since half of the quantities at the boundary are unknown, Equation 13 can be solved by

$$\left[A\right]\left\{x\right\}^{NT} = \left[B\right]\left\{y\right\}^{NT} + \sum_{n=1}^{NT-1}\left(\left[G\right]^{NT-n+1}\left\{q\right\}^{n} - \left[H\right]^{NT-n+1}\left\{u\right\}^{n}\right), \tag{14}$$

where $\left[A\right]$ and $\left[B\right]$ contain columns from *G* and *H* matrices evaluated at the first time step. More specifically, $\left[A\right]$ contains the influence terms associated with unknown variables, and $\left[B\right]$ contains the influence terms related to prescribed variables. Vectors $\left\{y\right\}^{NT}$ and $\left\{x\right\}^{NT}$ contain, respectively, the prescribed and unknown quantities at the boundary for the NT time step.

The singular kernels in Equations 11 and 12 were regularized by the semi-analytical method known as Singularity Subtraction Technique [36], whereas the non-singular ones were integrated by the Gauss-Legendre quadrature.

Equation 9 also assesses the chloride concentration at the domain. In such case, the free term equals unity since the collocation point is positioned at the domain. Thus, the chloride concentration can be evaluated by the following algebraic representation:

$$\left\{u_{i}\right\}^{NT} = \sum_{n=1}^{NT}\left(\sum_{j=1}^{Ne} G_{ij}^{\prime n}\ q_{j}^{n} - \sum_{j=1}^{Ne} H_{ij}^{\prime n}\ u_{j}^{n}\right), \tag{15}$$

where $G_{ij}^{\prime n} = k\int_{\Gamma_{\mathrm{j}}} U_{n}^{*}\ d\Gamma_{\mathrm{j}}$ and $H_{ij}^{\prime n} = k\int_{\Gamma_{j}} Q_{n}^{*}\ d\Gamma_{j}$.

Equation 15 can be solved by the time-marching process previously addressed, providing the chloride concentration at internal points (u_{int}):

$$\left\{u_{int}\right\}^{NT}=\sum_{n=1}^{NT}\left(\left[G'\right]^{NT-n+1}\left\{q\right\}^{n}-\left[H'\right]^{NT-n+1}\left\{u\right\}^{n}\right). \tag{16}$$

3 SUBREGION BEM TECHNIQUE

The transient BEM formulation enables the diffusion modelling of homogeneous domains, i.e., with a single diffusion coefficient. Nevertheless, the formulation represents the diffusion in non-homogeneous materials when coupled to the classical subregion BEM technique, which discretises the non-homogeneous domain into homogeneous piecewise regions where the compatibility of potentials and equilibrium of fluxes are enforced along the materials interfaces, as depicted in Figure 1.

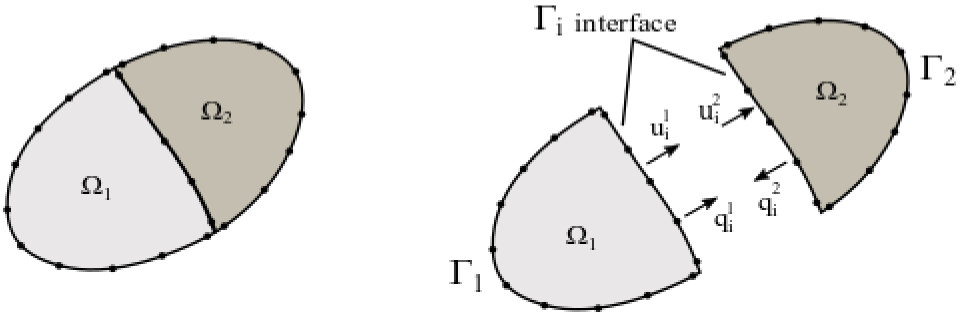

Figure 1. Discretisation in subregions and imposition of continuity on materials interfaces.

The algebraic operations required in the subregion BEM technique can be performed straightforwardly in a two-domain problem (Figure 1). In this case, Equations 11 and 12 lead to the following algebraic representation:

$$\begin{bmatrix} H^{1} & H_{i}^{1} & 0 & 0 \\ 0 & 0 & H^{2} & H_{i}^{2} \end{bmatrix}\begin{Bmatrix} u^{1} \\ u_{i}^{1} \\ u^{2} \\ u_{i}^{2} \end{Bmatrix}=\begin{bmatrix} G^{1} & G_{i}^{1} & 0 & 0 \\ 0 & 0 & G^{2} & G_{i}^{2} \end{bmatrix}\begin{Bmatrix} q^{1} \\ q_{i}^{1} \\ q^{2} \\ q_{i}^{2} \end{Bmatrix}, \tag{17}$$

where the superscript index indicates the domain and i denotes the material interface.

Since potentials and fluxes are indeterminate along the material interfaces, Equation 17 requires the following compatibility and equilibrium conditions for a proper solution (Equations 18-19):

$$u_{i}^{1}=u_{i}^{2}, \tag{18}$$

$$q_{i}^{1}=-q_{i}^{2}. \tag{19}$$

The coupling of Equations 17-19 leads to the following system:

$$\begin{bmatrix} H^1 & H_i^1 & 0 \\ 0 & H_i^2 & H^2 \end{bmatrix} \begin{Bmatrix} u^1 \\ u_i^1 \\ u^2 \end{Bmatrix} = \begin{bmatrix} G^1 & G_i^1 & 0 \\ 0 & -G_i^2 & G^2 \end{bmatrix} \begin{Bmatrix} q^1 \\ q_i^1 \\ q^2 \end{Bmatrix}. \tag{20}$$

Equation 20 can be solved by simply enforcing the boundary conditions, which triggers the classical columns change procedure of BEM. The subregion BEM technique provides generality to the numerical technique because non-homogeneous materials can be properly handled, and can also be applied for representing cracks. For such a purpose, the material interfaces contain the crack surfaces. Therefore, the entire domain requires a division into subregions, where the compatibility of potentials and equilibrium of fluxes must not be enforced along the crack surfaces, which become ordinary boundaries. The subregion approach does not require hypersingular integral equations, thus simplifying the integration process, and its application is straightforward when the kernels formulations are known.

4 DETERMINISTIC APPLICATIONS

4.1 Transient diffusion modelling in a square domain

A concrete column of square cross-section is exposed to an environment whose chloride ions (Cl^-) concentration is 1% of the concrete weight, as illustrated in Figure 2a. For the sake of simplicity, the problem symmetry properties were used. Therefore, a quarter of the domain was modelled and the symmetry boundary conditions assured the domain continuity (Figure 2b). The chloride diffusion coefficient is 10^{-12} m²/s (0.3154 cm²/year).

The application assesses the corrosion time initiation at the point depicted in Figure 2b, whose cover thickness is 5 cm for 20 years' structural lifetime. The analytical solution presented by Bitaraf and Mohammadi [13] and the numerical responses based on FEM, Finite Difference Method (FDM), Element-Free Galerkin (EFG), and Finite Point Method (FPM) are references herein and enable the verification of the BEM formulation accuracy.

The BEM mesh is composed of 40 isoparametric lagrangian elements with linear approximation, which leads to 44 collocation points (Figure 2c). The FPM modelling required a grid with 185 nodes, and the FEM employed 328 triangular elements with 185 nodes - the same number of nodes was used by the EFG method. The FDM results were provided by a 11x11 grid with 121 nodes [13], [37].

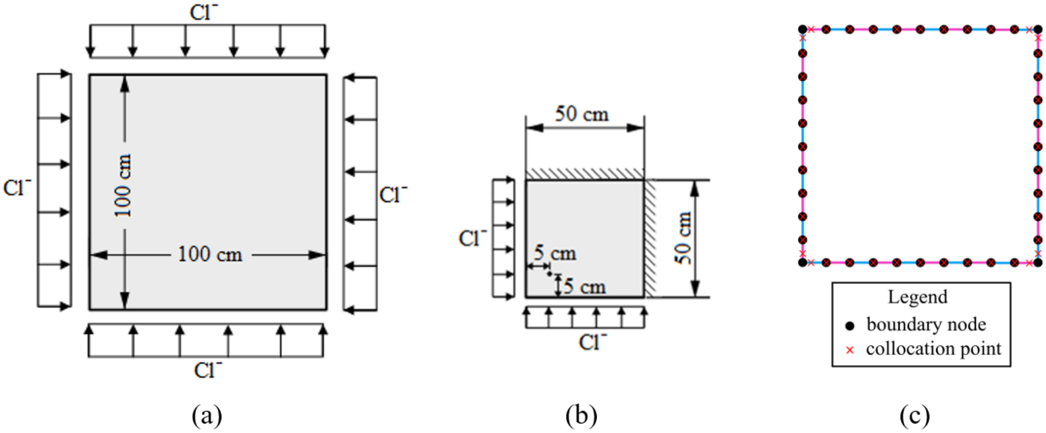

Figure 2. (a) Cross-section geometry and boundary conditions, (b) Symmetry boundary conditions, (c) BEM mesh.

The threshold chloride content for reinforcement depassivation is 0.10% of the concrete weight [13]. Figure 3 shows the results achieved by BEM, whose time was discretised within 20 time steps and the space kernels were integrated by 10 integration points, and the reference responses.

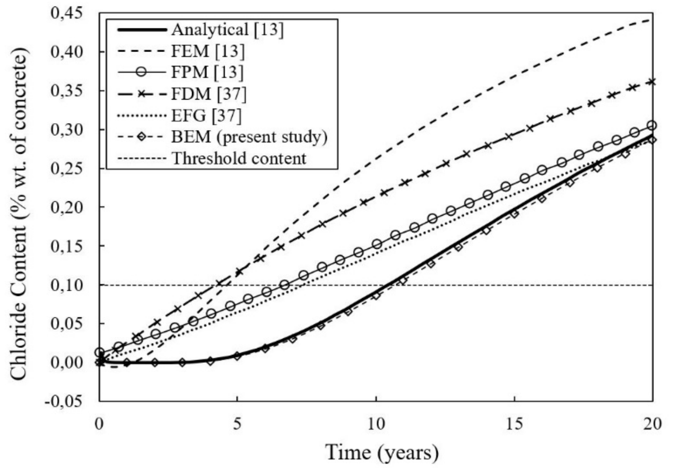

Figure 3. Chloride content evolution along time at 5 cm concrete cover.

The results in Figure 3 show the superior performance of BEM over other numerical approaches; its responses are in excellent agreement with the analytical predictions. BEM achieved such results with the coarsest mesh among the considered numerical methods, which demonstrates its accuracy.

BEM also accurately predicted the corrosion time initiation, i.e., the time span in which the chloride concentration at 5 cm cover is equal to the threshold content. The structural lifetime assessed by the analytical approach was 10.50 years. BEM predicted 10.65 years, showing a 1.4% difference in relation to the reference. The predictions of EFG, FPM, FEM, and FDM were, respectively, 7.58 years, 6.70 years, 4.67 years, and 4.33 years [13], highlighting the accuracy of BEM in diffusion modelling.

4.2 Diffusion modelling in a cracked material

The application deals with the chloride diffusion modelling in a cracked material. The responses provided by BEM were compared against the experimental results of Şahmaran [38], who conducted tests in prismatic specimens (355.6 x 50.8 x 76.2 mm) molded with mortar (w/c = 0.485) and reinforced with three levels of a 1 mm diameter steel reinforcement mesh in a 6 mm grid. After 43 days' curing in water, the specimens were pre-cracked using a 4-point bending test, which led to a single crack in the mortar samples. The unloaded specimens were immersed in a 3% NaCl solution for 30 days, after which their chloride concentration along the cracked area was quantified.

According to Şahmaran [38], the widths (w) of the cracks were narrower at a deeper level of the specimens than at the surface (V-shaped). An optical microscope measured such widths at five different points, providing a 29.4 μm average width and an 18.7 mm crack depth.

BEM used a two dimensional specimen of 356.0 mm x 76.0 mm cross-section for numerically reproducing the experiment. The crack was positioned at the cross-section centre and modelled by the subregion technique as a straight one parallel to the specimen's height (Figure 4a). The chloride content along the specimen's lower surface was 0.51% (per weight of cementitious materials), as suggested by Du et al. [39], who analysed the experimental data presented in [38]. The chloride concentration at the upper surface was nil, whereas the vertical surfaces were sealed with resin, leading to nil flux values. Therefore, such boundary conditions were enforced in the numerical modelling. The chloride diffusion coefficient in the mortar was $4.746x10^{-12}$ m²/s (0.41 mm²/day), considering ratio w/c = 0.485 [39].

Two subregions discretised the cross-section, requiring 150 isoparametric lagrangian elements of quadratic approximation and 320 nodes. The crack discretisation was composed of 7 nodes and positioned at the subregions interface. Figure 4b illustrates the boundary mesh.

Because of the capillarity effect along the crack surfaces, which appear due to their V-shape, the chloride concentration prescribed along the crack surfaces started with 0.51% at the crack mouth and reduced progressively at a 0.07% rate for each node, finishing with 0.09% at the crack tip. For the sake of simplicity, the reinforcements were not represented in the numerical model.

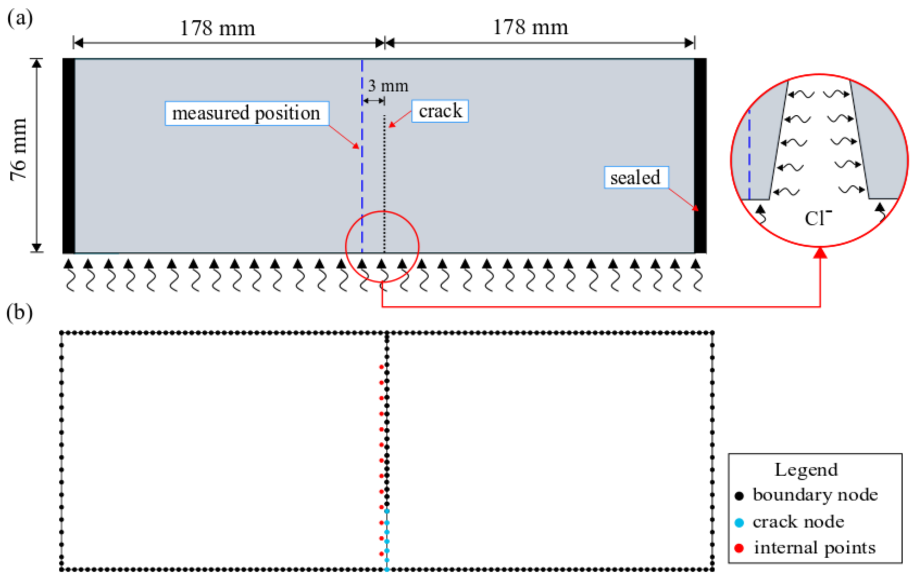

Figure 4. (a) Specimen geometry, (b) BEM mesh.

The red dots in Figure 4b represent the measuring points, which are equally spaced by 5 mm along the cross-section. The experimental analysis accounted for an uncracked specimen (w=0), which served as testimonial; the case was considered in the numerical modelling. The same BEM mesh was used in the testimonial modelling, in which both compatibility of chlorides concentration and equilibrium of fluxes were enforced along the crack nodes. Figure 5 displays the experimental results of Şahmaran [35] and the numerical responses achieved by BEM. The numerical modelling required 10 integration points for spatial integrations and 30 time steps in a 30-day time exposure to the NaCl solution.

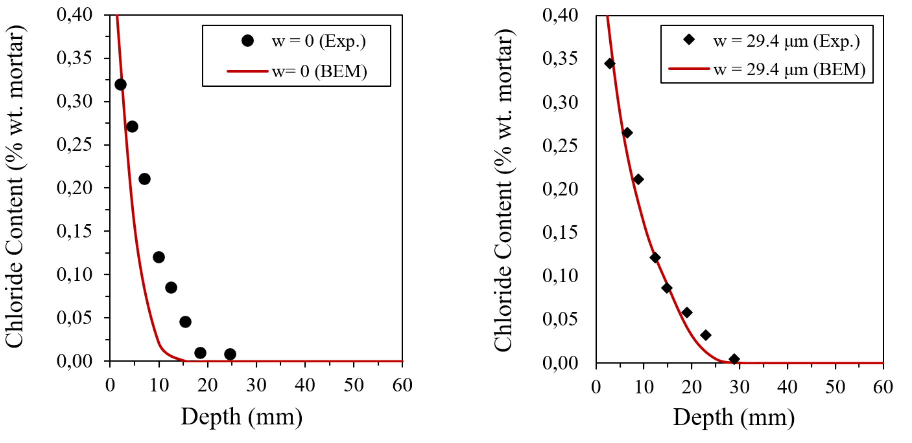

Figure 5. Comparison of results: Experimental (Exp.) [35] and numerical (BEM).

The numerical results provided by BEM are in good agreement with the experimental responses of Şahmaran [35] for the cracked specimen, although they underestimated the chloride concentration values for the $5 < \text{depth} < 15$ mm cover range in the non-cracked specimen. Nevertheless, the numerical modelling represented the crack influence on the chloride concentration distribution along the material domain, and the non-requirement of domain mesh by BEM provided high accuracy for the internal fields assessment.

5 PROBABILISTIC MODELLING: MONTE CARLO SIMULATION

Monte Carlo Simulation (MCS) is a numerical simulation technique developed by Metropolis and Ulam [40] that uses random numbers and limit state function simulations for uncertainty quantification purposes. In structural engineering applications, it usually assesses the probability of failure (P_f) of complex structures and structural systems subject to randomness. The probability of failure of a system can be determined by the integral of the joint probability density function (f_X) evaluated over the failure domain (Ω_f). However, the f_X function is implicit in complex engineering problems, hampering an explicit evaluation of the probability of failure, which can be assessed by simulation techniques that evaluate limit states punctually. In MCS, the simplest simulation technique, an indicator function $I[x]$ indicates if a simulated condition belongs to failure or safe conditions. The function is unitary when the simulated point belongs to the failure domain, and nil otherwise. Therefore, the probability of failure can be assessed by the following integral:

$$P_f = \int_{\Omega_f} f_X(x)\,dx = \int_{\Omega} I[x]\, f_X(x)\,dx\,. \tag{21}$$

Equation 21 can be estimated by a finite number of samples, n_s, according to:

$$P_f \approx \hat{P}_f = \frac{1}{n_s}\sum_{j=1}^{n_s} I\left[x_j\right] = \frac{n_f}{n_s}\,, \tag{22}$$

in which n_f is the number of samples in the failure domain and $\hat{P}_f$ is the estimated probability of failure.

Each evaluation of the indicator function involves a simulation of the limit state function, which defines the frontier between failure and safe domains. In the present study, the mechanic-probabilistic modelling is based on the limit state of corrosion initiation (G), defined by the difference between the threshold chloride content (C_{th}) and the chloride concentration (C) on the reinforcement interface, at point x and time t, as follows:

$$G(x,t) = C_{th} - C(x,t). \tag{23}$$

The chloride threshold has been often represented by deterministic values accounting for the class of environmental aggressiveness and concrete composition. Since the quantity displays an important randomness behaviour, C_{th} was modelled as a random variable in this study.

The probabilistic modelling performed here accounts for the environmental influence (e.g., temperature and chloride binding) on the concrete, as well as that of loads on the structure. Such effects were considered in the evaluation of the diffusion coefficient of concrete (k_0) by introducing penalization factors corresponding to chloride binding (F_1), temperature (F_2), and acting loads (F), as follows [41]:

$$k_0 = k_{\text{ref}}.F_1\left(C_b\right).F_2\left(T\right).F\left(\varepsilon,d\right), \tag{24}$$

where:

$k_{\text{ref}} =$ chloride diffusivity in saturated concrete at 28 days (m^2/s);

$C_b =$ bound chloride concentration (kg/m^3);

$T =$ reference temperature (K);

$\varepsilon =$ concrete compressive strain (‰);
$d =$ damage variable.

Diffusion coefficient k_{ref} is a parameter related to water cement ratio, *w/c*, and can be determined by the empirical expression proposed by Bentz et al. [42]:

$$k_{\text{ref}} = 10^{-10+4.66(w/c)}\ cm^2 / s. \tag{25}$$

The factors in Equation 24 are detailed in Equations 26-29.

• Chloride binding factor

$$F_1(C_b) = \left[1 + \frac{\alpha}{\omega_e\left(1+\beta C_f\right)^2}\right]^{-1}, \tag{26}$$

where:
$\alpha, \beta =$ Langmuir constant values;
$\omega_e =$ evaporable water content;
$C_f =$ free chloride concentration (kg/m^3).

• Temperature factor

$$F_2(T) = \exp\left[\frac{U}{R}\left(\frac{1}{T_{\text{ref}}} - \frac{1}{T}\right)\right], \tag{27}$$

where:
$U =$ activation energy of the diffusion process (J. mol^{-1});
$R =$ gas constant (8.31 J. $\text{K}^{-1}.\text{mol}^{-1}$);
$T_{\text{ref}} =$ current temperature (K).

• Acting loads factor

$$F(\varepsilon, d) = 1 + B\varepsilon + \frac{k_{\max}}{k_0}\left\{1 + C_1 d - \left[1 + \left(\frac{1}{d_{cr}}\right)^n\right]^{-1}\right\}, \tag{28}$$

where:
$B =$ parameter related to the concrete material irrespective of damage levels;
$k_{\max} =$ diffusion coefficient in completely damaged concrete (m^2/s);
$k_0 =$ diffusion coefficient in sound concrete (m^2/s);
$C_1, n, d_{\text{cr}} =$ model parameters.

When the concrete strain reaches the ultimate value (ε_u), damage variable d corresponds to 1 and the concrete is assumed completely damaged [41]. In this case, $C_1 = -Bk_s\varepsilon_u / k_{\max}$ and the loading factor can be simplified to Equation 29.

$$F\left(\varepsilon_u,1\right)=1+\frac{k_{\max}}{k_0}-\frac{k_{\max}}{k_0}\left[1+\left(\frac{1}{d_{cr}}\right)^n\right]^{-1}. \tag{29}$$

5.1. Probabilistic scenarios of chloride diffusion in a typical bridge beam

The application assesses the probability of reinforcement depassivation accounting for the influence of climatic conditions (temperature), chloride binding capacity, and effects of acting loads on an I shape cross-section commonly employed in bridge beams. It considers the beam a part of reinforced concrete structures exposed to tidal splashes.

The cross-sections largest dimensions are 90 cm x 40 cm, reinforced by eight 20 mm diameter rebars. Because of the high environmental aggressiveness, the concrete cover is 50 mm [43]. The beam connects the structural system by its upper boundary, which composes the structure deck; therefore, the chloride flux at this boundary is nil. The remaining cross-section boundaries, i.e., the lower and vertical are exposed to the chloride attack (Cl^-).

The subregion BEM technique represents the macrocracks in the numerical modelling. Their lengths are h and h $\sqrt{2}$, idealized as perfectly straight. For the sake of simplicity, the chloride concentration at the macrocrack surfaces equals that at the beam surface (C_0). Figure 6 illustrates the cross-section dimensions and macrocracks positions.

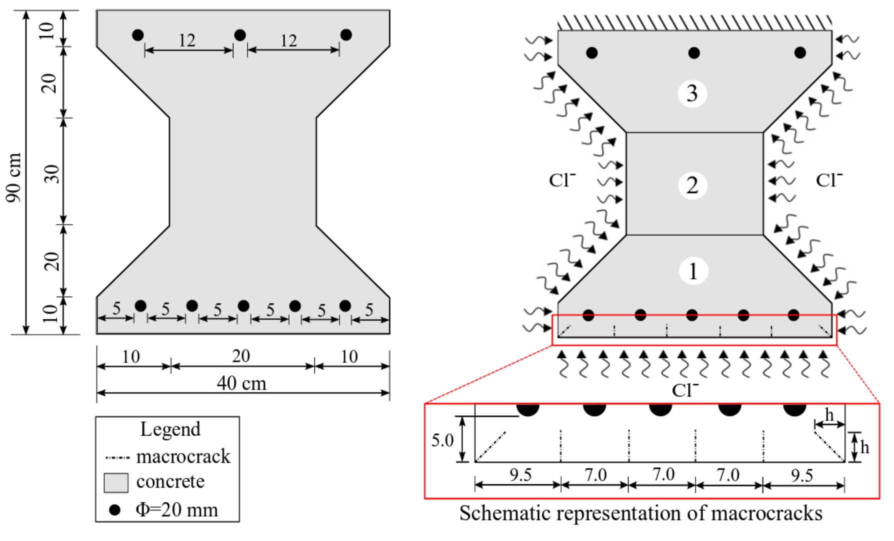

Figure 6. Cross-section geometry (measured in cm) and boundary conditions.

The cracks were positioned at the lower cross-section boundary towards representing the mechanical degradation in the concrete caused by tensile stress. The diffusion coefficient in region 1 accounts for the load factor (Equation 29); therefore, the analysed beam can be considered simply supported. The other effects (temperature and chloride binding) are equally considered in the diffusivity of regions 1, 2 and 3.

The probabilistic modelling accounts for three random variables. The *w/c* ratio data were adopted from Stewart et al. [44], who suggested 0.40 as the mean value for exposure to tidal or splash zones based on maximum *w/c* ratio specified in AS 5100.5. The coefficient of variation (C.O.V) assumed was 10% for concrete manufactured under controlled conditions, and the mean and C.O.V values of the surface chloride concentration (C_0) for splash zones were established by Val and Stewart [45], from data on offshore and onshore RC structures along the Australia coast reported by Collins and Grace [46] and McGee [47]. The chloride threshold content (C_{th}) was based on data provided by Vassie [48], who studied the percentage of corrosion cases in UK bridges in relation to the total chloride concentration at the reinforcement level [45]. Table 1 shows the input parameters of the model.

Table 1. Model input parameters.

Parameter	Mean	C.O.V	Distribution	Reference
C_0	7.35 kg/m^3	0.700	Lognormal	[45]
C_{th}	3.35 kg/m^3	0.375	Normal	[45]
w/c	0.40	0.040	Lognormal	-
C_f [1]	1.50 kg/m^3	-	Deterministic	[49]
U	44,600 J/mol	-	Deterministic	[50]
T_{ref}	296,15 K	-	Deterministic	[50]
T	300,30 K	-	Deterministic	-
$k_{\max} / k_0$ [2]	4.00	-	Deterministic	-

[1] Value correlated to $\omega_e = 0.6$, $\alpha = 11.8$ e $\beta = 4.0$ [49], [51]; [2] Model parameters: $n = 5$, $d_{cr} = 0.4$ [52].

The numerical modelling adopts the transient BEM approach, whose mesh at the external boundaries is composed of 172 isoparametric lagrangian elements of quadratic approximation, leading to 384 collocation points. Since the reinforcements are assumed non-porous media, the nil flux condition is enforced along their boundaries. Eight isoparametric boundary elements with quadratic approximation discretise each reinforcement boundary and 10 Gauss-Legendre points perform the space integrations, whereas 15 time steps discretise the analysis time.

Eight probabilistic scenarios enabled the assessment of isolated and joint influences of the environment and loadings on the chloride diffusion in concrete pores. Table 2 shows the scenarios considered, where dots indicate the presence of effect in the modelling. The even scenarios account for crack length with h=2 cm.

Table 2. Effects considered in each scenario.

Effect	Scenario							
	1	2	3	4	5	6	7	8
Chloride binding			•	•	•	•	•	•
Temperature					•	•	•	•
Acting load							•	•
Macrocracks		•		•		•		•

MCS performed the probabilistic simulations, in which 20,000 samples for each random variable describe safe and failure domains. Figure 7 shows the evolution of the probability of failure along time for a 75-year structural service-life.

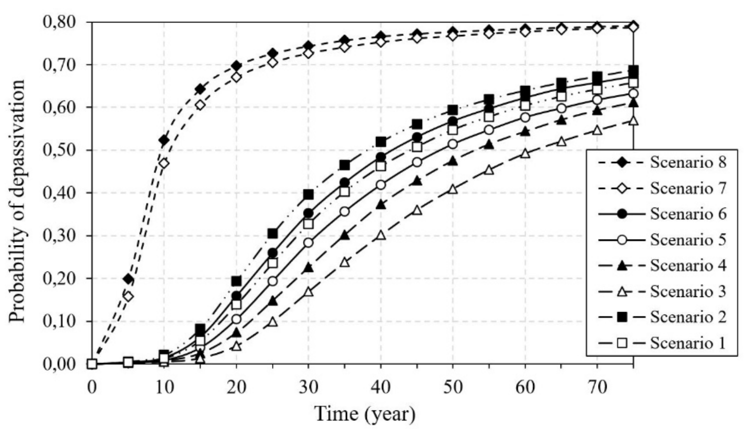

Figure 7. Probability of depassivation as a function of time for different scenarios.

Scenario 1, which disregards the influence of the effects, overestimates the probability of reinforcement depassivation when compared to scenarios that include the chloride binding capacity isolated and jointly with the influence of temperature or macrocracks on the concrete. At 50 years, the overestimation is 33%, 15%, and 6% for scenarios 3, 4, and 5, respectively, which is expected, since the effects of cracks and temperature accelerate the chloride diffusion, whereas chloride binding reduces the process, although in different proportions. The results also show the importance of representing environmental and mechanical influences on the diffusion process of chlorides in concrete for avoiding overestimation or underestimation of the design service life. Realistic frameworks such as those proposed here are fundamental for an accurate structural service life assessment.

The probability of failure significantly increases when the modelling accounts for the chloride binding capacity (see the curves for scenarios 1 and 3). This effect represents the concrete capacity for binding the free chlorides into its pores, and can be explained by the approximately 30% reduction in the F_1 factor (Equation 26). On the other hand, the temperature growth increases 28% the concrete diffusivity, whereas acting loads penalize this variable by 396%. Such environmental actions increase the probability of failure, as observed in scenario 5 in comparison to scenario 3, and scenario 7 in comparison to scenarios 3 and 5. The loading effects influenced the diffusion phenomenon more strongly than the temperature in the simulations, since the damage was complete. Nevertheless, different behaviours can be displayed if usual structural service loads are considered.

The loading effects assume a major importance in the diffusion modelling (see Figure 7), since they uniformly penalize the concrete diffusivity along the cross-section domain. However, cracks also increase the chloride diffusion velocity. Because their discontinuities introduce preferential ingress paths, the probability of failure increases when cracks are considered. The presence of 2 cm long cracks reduces 20% of the probabilistic structural service, which demonstrates their importance in the modelling.

The cracks influence can be further investigated. For this purpose, scenario 5 (h=0) are compared against scenario 6, in which the probabilistic modelling accounts for crack lengths increasing progressively with $1 \leq h \leq 4$ cm. Figure 8 displays the numerical responses provided by the transient BEM approach.

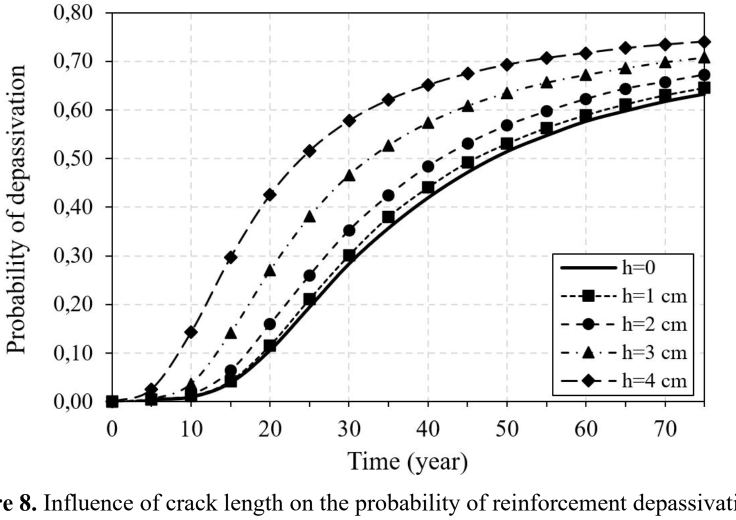

Figure 8. Influence of crack length on the probability of reinforcement depassivation.

The numerical results in Figure 8 show cracks with h equals 1 cm and 2 cm exert a small influence on the evolution of the probability of failure. However, the probability of failure significantly increases when h assumes 3 cm and 4 cm, which are higher than half of the cover thickness. Obviously, this behaviour accounts for severe environmental aggressiveness and 5 cm cover thickness. For 50-year time span, the probability of failure for 4 cm long crack is 35% higher than the case in which cracks are disregarded. Fib Bulletin 34 [53] recommends an 10% maximum depassivation probability for exposition to seawater. In such a context, the avoidance of cracks would extend the structural service life by 10 years, on average.

5 CONCLUSIONS

This study applied the transient BEM formulation for the chloride diffusion modelling in concrete pores. The approach was coupled to MCS for a probabilistic assessment of the structural service life, thus enabling a probabilistic assessment of durability in RC structures. Tidal zones were considered for an environmental aggressiveness description, and the numerical responses have led to the following conclusions:

1. BEM provided accurate results in comparison to other numerical techniques, such as FEM, EFG, FDM, and FPM, achieving superior performance with fewer degrees of freedom, which is an advantage when repetitive analyses are required, as in MCS.

2. The environment is fundamental in diffusion modelling. The chloride binding effect reduces the concrete diffusivity and, consequently, extends the structural service life by binding the free chlorides in the concrete pores. However, temperature and loading effects increase diffusivity and reduce structural durability, which is a concern, especially regarding global warming, since temperatures are expected to rise in the near future. Therefore, an accurate structural durability modelling must consider such effects.

3. The structural service life can be considerably reduced by cracks. Because cracks enable a preferential chloride ingress path, their length play a major role in the problem. The application considered herein suggests cracks length longer than half of the concrete cover thickness significantly reduces the probabilistic service life.

The model proposed herein is general and, for the sake of completeness, the authors adopted data from the literature for the applications. Nevertheless, the model can be applied for any geographical region if the required data are available.

ACKNOWLEDGEMENTS

The authors acknowledge Universidade de São Paulo (EESC/USP/Brazil) for their support and the research grant financed by Coordenação de Aperfeiçoamento de Pessoal de Nível Superior – Brasil (CAPES) – Finance Code 001.

REFERENCES

[1] E. Possan, “Modelagem da carbonatação e previsão de vida útil de estruturas de concreto em ambiente urbano,” Ph.D. dissertation, UFRGS, Porto Alegre, 2010.

[2] A. A. Nince and J. C. T. S. Clímaco “Levantamento de dados sobre deterioração de estruturas na Região Centro-Oeste do Brasil,” *Anais do Congress on High-Performance and Quality of Concrete Structures,* Florianópolis, SC, 1996.

[3] O. T. Rincón, A. R. Carruyo, C. Andrade, P. R. L. Helene, and I. Díaz, *Manual de Inspección, Evaluación y Diagnóstico de Corrosión en Estructuras de Hormigón Armado.* Rio de Janeiro: Iberoam Program Sci. Technol. Dev., 1998.

[4] M. Grochoski and P. R. L. Helene, *Sistemas de Reparo para Estruturas e Concreto com Corrosão de Armaduras* (USP Polytechnic School Technical Bulletin), São Paulo: USP, 2008, pp. 1–23.

[5] Grandes Construções, “Brasil perde 4% do PIB com corrosão,” *Aço na Construção*, May 17, 2017. [Online]. Available: https://www.grandesconstrucoes.com.br/Materias/Exibir/brasil-perde-4-do-pib-com-corrosao

[6] V. Gentil, *Corrosão*, 3th ed. Rio de Janeiro: Livros Técnicos e Científicos, 1996.

[7] K. Tuutti, "Service life of structures with regard to corrosion of embedded steel," *Spec. Publ.*, vol. 65, pp. 223–236, 1980.

[8] L. Collepardi, A. Marcialis, and R. Turriziani, "La cinetica di penetrazione degli ioni cloruro nel calcestruzzo," *Cemento*, vol. 67, no. 4, pp. 157–164, 1970.

[9] P. S. Mangat and B. T. Molloy, "Prediction of long term chloride concentration in concrete," *Mater. Struct.*, vol. 27, no. 6, pp. 338–346, 1994., http://dx.doi.org/10.1007/BF02473426.

[10] L. Mejlbro, “The complete solution of Fick’s second law of diffusion with time-dependent diffusion coefficient and surface concentration,” in *Durability Concr. Saline Environ.*, Lund, Sweden, 1996, pp. 127–158.

[11] M. K. Kassir and M. Ghosn, "Chloride-induced corrosion of reinforced concrete bridge decks," *Cement Concr. Res.*, vol. 2, no. 1, pp. 139–143, 2002, http://dx.doi.org/10.1016/S0008-8846(01)00644-5.

[12] M. Bitaraf and S. Mohammadi, "Analysis of chloride diffusion in concrete structures for prediction of initiation time of corrosion using a new meshless approach," *Constr. Build. Mater.*, vol. 22, no. 4, pp. 546–556, 2008, http://dx.doi.org/10.1016/j.conbuildmat.2006.11.005.

[13] S. Zhou, "Analytical model for square root increase of surface chloride concentration and decrease of chloride diffusivity," *J. Mater. Civ. Eng.*, vol. 28, no. 4, pp. 04015181, 2016, http://dx.doi.org/10.1061/(ASCE)MT.1943-5533.0001483.

[14] Y. Zeng, "Modeling of chloride diffusion in hetero-structured concretes by finite element method," *Cement Concr. Compos.*, vol. 29, no. 7, pp. 559–565, 2007, http://dx.doi.org/10.1016/j.cemconcomp.2007.04.003.

[15] C. Fu, X. Jin, and N. Jin, "Modeling of chloride ions diffusion in cracked concrete," in *Earth and Space 2010: Eng. Sci. Constr. Oper. Challenging Environ.*, Honolulu, Hawaii, 2010, pp. 3579–3589, http://dx.doi.org/10.1061/41096(366)343.

[16] J. Xiao, J. Ying, and L. Shen, "FEM simulation of chloride diffusion in modeled recycled aggregate concrete," *Constr. Build. Mater.*, vol. 29, pp. 12–23, 2012, http://dx.doi.org/10.1016/j.conbuildmat.2011.08.073.

[17] R. Duddu, "Numerical modeling of corrosion pit propagation using the combined extended finite element and level set method," *Comput. Mech.*, vol. 54, no. 3, pp. 613–627, 2014, http://dx.doi.org/10.1007/s00466-014-1010-8.

[18] X.-Y. Wang and L.-N. Zhang, "Simulation of Chloride Diffusion in Cracked Concrete with Different Crack Patterns," *Adv. Mater. Sci. Eng.*, vol. 2016, pp. 1075452, 2016, http://dx.doi.org/10.1155/2016/1075452.

[19] H. S. Al-Alaily, A. A. A. Hassan, and A. A. Hussein, "Use of extended finite element method and statistical analysis for modelling the corrosion-induced cracking in reinforced concrete containing metakaolin," *Can. J. Civ. Eng.*, vol. 45, no. 3, pp. 167–178, 2018, http://dx.doi.org/10.1139/cjce-2017-0298.

[20] Y. Wu and J. Xiao, "The multiscale spectral stochastic finite element method for chloride diffusion in recycled aggregate concrete," *Int. J. Comput. Methods*, vol. 15, no. 1, pp. 1750078, 2018, http://dx.doi.org/10.1142/S0219876217500785.

[21] J. Peng, S. Hu, J. Zhang, C. S. Cai, and L. Li, "Influence of cracks on chloride diffusivity in concrete: a five-phase mesoscale model approach," *Constr. Build. Mater. Elsevier*, vol. 197, pp. 587–596, 2019, http://dx.doi.org/10.1016/j.conbuildmat.2018.11.208.

[22] L. F. Yang, Z. Chen, Q. Gao, and J. W. Ju, "Compensation length of two-dimensional chloride diffusion in concrete using a boundary element model," *Acta Mech.*, vol. 224, no. 1, pp. 123–137, 2013, http://dx.doi.org/10.1007/s00707-012-0721-1.

[23] L. C. Wrobel and D. B. Figueiredo, "Numerical analysis of convection-diffusion problems using the boundary element method," *Int. J. Numer. Methods Heat Fluid Flow*, vol. 1, no. 1, pp. 3–18, 1991, http://dx.doi.org/10.1108/eb017470.

[24] G. F. Dargush and P. K. Banerjee, "Application of the boundary element method to transient heat conduction," *Int. J. Numer. Methods Eng.*, vol. 31, no. 6, pp. 1231–1247, 1991, http://dx.doi.org/10.1002/nme.1620310613.

[25] E. D. Leonel, A. Chateauneuf, W. S. Venturini, and P. Bressolette, "Coupled reliability and boundary element model for probabilistic fatigue life assessment in mixed mode crack propagation," *Int. J. Fatigue*, vol. 32, no. 11, pp. 1823–1834, 2010, http://dx.doi.org/10.1016/j.ijfatigue.2010.05.001.

[26] L. F. Yang et al., "Analysis of chloride diffusion in concrete by the boundary element method," *J. Concr.*, pp. 25–28, 2008.

[27] L. F. Yang, Z. Chen, Y. Wang, W. Meng, L. Song, and Q. Feng, "Boundary element method for analysis of two-dimensional chloride diffusion in concrete," *J. Chin. Ceram. Soc.*, vol. 7, pp. 1110–1117, 2009.

[28] Z. Chen et al., "Analysis of chloride diffusion in high-performance concrete and its service life by the boundary element method," *J. Build. Mater*, vol. 13, pp. 97–103, 2010.

[29] G. P. Pellizzer and E. D. Leonel, "Probabilistic corrosion time initiation modelling in reinforced concrete structures using the BEM," *Rev. IBRACON Estrut. Mater.*, vol. 13, no. 4, e13409, 2020, http://dx.doi.org/10.1590/s1983-41952020000400009.

[30] G. P. Pellizzer and E. D. Leonel, "The cover thickness design of concrete structures subjected to chloride ingress from RBDO solution technique," *Rev. IBRACON Estrut. Mater.*, vol. 13, no. 5, e13502, 2020, http://dx.doi.org/10.1590/s1983-41952020000500002.

[31] D. V. Val and P. A. Trapper, "Probabilistic evaluation of initiation time of chloride-induced corrosion," *Reliab. Eng. Syst. Saf.*, vol. 93, no. 3, pp. 364–372, 2008, http://dx.doi.org/10.1016/j.ress.2006.12.010.

[32] B. Saassouh and Z. Lounis, "Probabilistic modeling of chloride-induced corrosion in concrete structures using first-and second-order reliability methods," *Cement Concr. Compos.*, vol. 34, no. 9, pp. 1082–1093, 2012, http://dx.doi.org/10.1016/j.cemconcomp.2012.05.001.

[33] U. M. Angst, "Predicting the time to corrosion initiation in reinforced concrete structures exposed to chlorides," *Cement Concr. Res.*, vol. 115, pp. 559–567, 2019, http://dx.doi.org/10.1016/j.cemconres.2018.08.007.

[34] Q. M. Jiang, L. F. Yang, and Z. Chen, "Stochastic analysis of chloride profiles in concrete structures," *Adv. Mat. Res.*, vol. 163-167, pp. 3364–3368, 2010, http://dx.doi.org/10.4028/www.scientific.net/AMR.163-167.3364.

[35] L. C. Wrobel, *The Boundary Element Method – Applications in Thermo-Fluids and Acoustics, vol. 1.* United Kingdom: John Wiley & Sons, 2002.

[36] M. Guiggiani and P. Casalini, "Direct computation of Cauchy principal value integrals in advanced boundary elements," *Int. J. Numer. Methods Eng.*, vol. 24, no. 9, pp. 1711–1720, 1987, http://dx.doi.org/10.1002/nme.1620240908.

[37] A. Farahani and H. Taghaddos, "Prediction of service life in concrete structures based on diffusion model in a marine environment using mesh free, FEM and FDM approaches," *J. Rehabil. Civ. Eng.*, vol. 8, no. 4, pp. 1–14, 2020., http://dx.doi.org/10.22075/jrce.2020.19189.1380.

[38] M. Şahmaran, "Effect of flexure induced transverse crack and self-healing on chloride diffusivity of reinforced mortar," *J. Mater. Sci.*, vol. 42, no. 22, pp. 9131–9136, 2007, http://dx.doi.org/10.1007/s10853-007-1932-z.

[39] X. Du, L. Jin, R. Zhang, and Y. Li, "Effect of cracks on concrete diffusivity: a meso-scale numerical study," *Ocean Eng. Elsevier*, vol. 108, pp. 539–551, 2015, http://dx.doi.org/10.1016/j.oceaneng.2015.08.054.

[40] N. Metropolis and S. Ulam, "The Monte Carlo method," *J. Am. Stat. Assoc.*, vol. 44, no. 247, pp. 335–341, 1949.

[41] C. Fu, X. Jin, H. Ye, and N. Jin, "Theoretical and experimental investigation of loading effects on chloride diffusion in saturated concrete," *J. Adv. Concr. Technol.*, vol. 13, no. 1, pp. 30–43, 2015, http://dx.doi.org/10.3151/jact.13.30.

[42] D. P. Bentz, J. R. Clifton, and K. A. Snyder, "Predicting service life of chloride-exposed reinforced concrete," *Concr. Int.*, vol. 18, no. 12, pp. 42–47, 1996.

[43] Associação Brasileira de Normas Técnicas, *Projeto de Estruturas de Concreto – Procedimento*, ABNT NBR 6118:2014, 2014.

[44] M. G. Stewart, X. Wang, and M. N. Nguyen, "Climate change impact and risks of concrete infrastructure deterioration," *Eng. Struct.*, vol. 33, no. 4, pp. 1326–1337, 2011, http://dx.doi.org/10.1016/j.engstruct.2011.01.010.

[45] D. V. Val and M. G. Stewart, "Life-cycle cost analysis of reinforced concrete structures in marine environments," *Struct. Saf.*, vol. 25, no. 4, pp. 343–362, 2003, http://dx.doi.org/10.1016/S0167-4730(03)00014-6.

[46] F. G. Collins and W. R. Grace, "Specifications and testing for corrosion durability of marine concrete: the Australian perspective," *Spec. Publ.*, vol. 170, pp. 757–776, 1997.

[47] R. McGee, "Modelling of durability performance of tasmanian bridges," in *ICASP8 Appl. Stat. Probab. Civ. Eng., vol. 1*, R. E. Melchers and M. G. Stewart, Eds., Rotterdam: Balkema, pp. 297–306, 1999.

[48] P. R. Vassie, "Reinforcement corrosion and the durability of concrete bridges," *Proc. Inst. Civ. Eng. Part 1*, vol. 76, no. 8, pp. 713–723, 1984, http://dx.doi.org/10.1680/iicep.1984.1207.

[49] E. Zacchei and C. G. Nogueira, "Chloride diffusion assessment in RC structures considering the stress-strain state effects and crack width influences," *Constr. Build. Mater.*, vol. 201, pp. 100–109, 2019, http://dx.doi.org/10.1016/j.conbuildmat.2018.12.166.

[50] D. Vieira, A. Moreira, J. Calmon, and W. Dominicini, "Service life modeling of a bridge in a tropical marine environment for durable design," *Constr. Build. Mater. Elsevier*, vol. 163, pp. 315–325, 2018, http://dx.doi.org/10.1016/j.conbuildmat.2017.12.080.

[51] T. Ishida, P. Iqbal, and H. Anh, "Modeling of chloride diffusivity coupled with non-linear binding capacity in sound and cracked concrete," *Cement Concr. Res. Elsevier*, vol. 39, no. 10, pp. 913–923, 2009, http://dx.doi.org/10.1016/j.cemconres.2009.07.014.

[52] B. Gerard, G. Pijaudier-Cabot, and C. Laborderie, "Coupled diffusion-damage modelling and the implications on failure due to strain localization," *Int. J. Solids Struct.*, vol. 35, no. 31–32, pp. 4107–4120, 1998, http://dx.doi.org/10.1016/S0020-7683(97)00304-1.

[53] Fédération Internationale Du Béton, *Model Code for Service Life Design*, FIB Bulletin 34:2006, 2006.

Author contributions: VBS: conceptualization, literature review, methodology, computational implementation & validation, formal analysis, written, illustration and editing. EDL: conceptualization, literature review, methodology, formal analysis, supervision, layout, writing-review.

Editors: Bruno Briseghella, Guilherme Aris Parsekian.

IBRACON Structures and Materials Journal
Revista IBRACON de Estruturas e Materiais
ISSN 1983-4195 ismj.org

ORIGINAL ARTICLE

Elaboration of fracture prediction map using 2D digital image correlation - 2D CID

Elaboração de mapa de previsão de fratura utilizando correlação de imagens digital 2D – CID 2D

Leandro Silva de Assis[a]
Joaquim Teixeira de Assis[b]
José Renato de Castro Pessoa[c]
Armando Dias Tavares Júnior[d]

[a]Instituto Federal da Bahia – IFBA, Ilhéus, BA, Brasil
[b]Laboratório de Ensaios Físicos – LEFI, Instituto Politécnico do Rio de Janeiro / Universidade do Estado do Rio de Janeiro, Nova Friburgo, RJ, Brasil
[c]Laboratório de Ensaios Mecânicos e Resistência dos Materiais – LEMER/Universidade Estadual de Santa Cruz, Ilhéus, BA, Brasil
[d]Laboratório de Ótica do Instituto de Física Armando Dias Tavares – IFADT/Universidade do Estado do Rio de Janeiro, Rio de Janeiro, RJ, Brasil

Received 06 September 2021
Accepted 10 November 2021

Abstract: This work aims to present a methodology for the elaboration of a deformation map in a Portland cement concrete specimen to predict fractures caused by axial compression stresses, using the technique of Digital Image Correlation - DIC 2D. For this purpose, 5 concrete specimens with compressive strength expected at 28 days fck of 40 MPa were analyzed, which were tested in the ABNT NBR 5739/2018 standard - compression test of cylindrical concrete specimens. During the test, the necessary digital images were acquired in the DIC-2D array. These images were subsequently processed, and the results interpreted statistically. According to the result of the correlation of images obtained, it was found that 67% of the specimens had regions of accumulation of stresses that indicated in advance the location of the rupture, which enabled the development of a fracture prediction map. The results obtained in the research showed that the methodology used by means of the DIC-2D arrangement was able to predict the place where the rupture in the specimens occurred.

Keywords: fracture, deformation, concrete, image.

Resumo: Este trabalho tem como objetivo apresentar uma metodologia para elaboração de um mapa de deformação em um corpo de prova de concreto de cimento Portland de modo a prever fraturas provocadas por tensão de compressão axial, utilizando técnica de Correlação Digital de Imagem - CID 2D. Para alcançar este objetivo, foram analisados 5 corpos de prova de concreto com resistência à compressão esperada aos 28 dias fck de 40 MPa que foram ensaiados por meio da norma da ABNT NBR 5739/2018 - ensaio de compressão de corpos de prova cilíndricos de concreto. Durante o ensaio foram adquiridas as imagens digitais necessárias no arranjo CID-2D. Posteriormente essas imagens foram processadas e os resultados interpretados estatisticamente. De acordo com o resultado de correlação de imagens obtido, constatou-se que 67% dos corpos de prova possuíam regiões acumuladoras de tensão que indicaram antecipadamente o local da ruptura, o que permitiu a elaboração de um mapa de previsão de fratura. Os resultados obtidos na pesquisa mostraram que a metodologia utilizada por meio do arranjo CID-2D conseguiu prever o local onde houve ruptura no corpo de prova.

Palavras-chave: fratura, deformação, concreto, imagem.

How to cite: L. S. Assis, J. T. Assis, J. R. C. Pessoa, and A. D. Tavares Jr.“Elaboration of fracture prediction map using 2D digital image correlation - 2D CID,” Rev. IBRACON Estrut. Mater., vol. 15, no. 4, e15403, 2022, https://doi.org/10.1590/S1983-41952022000400003

Corresponding author: Leandro Silva de Assis. E-mail: leandro.assis@ifba.edu.br
Financial support: None.
Conflict of interest: Nothing to declare.
Data Availability: The data that support the findings of this study are available from the corresponding author, LSA, upon reasonable request.
This is an Open Access article distributed under the terms of the Creative Commons Attribution License, which permits unrestricted use, distribution, and reproduction in any medium, provided the original work is properly cited.

1 INTRODUCTION

The use of concrete in habitable constructions imply the need for rigorous processes to monitor the integrity of the structure, in particular eventual flaws that may lead to collapse [01], [02].

The microstructure of the concrete is heterogeneous and complex, making it difficult to develop realistic models of its microstructure that predict its behavior when deformed. This microstructure explains the great difference in values of tensile and compressive strength. [03]

One of the techniques that aid the interpretation and decision making with automatic analysis by computers is called DIC - 2D - Digital Image Correlation. The evolution of computers and improvement in the resolutions of digital cameras, made possible the analysis and quantification of small displacements caused by different stress levels from the overlapping of images [04], [05].

Thus, it is possible to map defects in concrete structures in service without necessarily having contact with them, facilitating the inspection of difficult-to-access structures with greater precision. [06]

According to Metha & Monteiro [03], the strength of the concrete is associated with the movement of macropores inside the hardened paste, which start in capillary voids greater than 50 ηm, reaching its fracture with displacements in the order of 2000 µm.

Considering that the tests used in diagnostic engineering are mostly limited to the heterogeneous condition of the concrete, and the human eye lower limit of accuracy in the order of 200 µm when in its perfect's faculties, in addition to being subject to gross errors of reading and interpretation [07]. The revolution of digital images has boosted the possibilities of observation bringing with it resolutions that can reach 20 µm / pixel, and when associated with computational algorithms, they become a powerful tool combined with non-destructive diagnostic engineering. [08]

This work presents a methodology to the elaboration of a deformation map in a Portland cement concrete specimen to predict fractures caused by axial compression loading, using DIC - 2D technique.

The following steps were performed to the analyses:

i) Relevant characteristics for the acquisition / manufacture of the specimen were evaluated for proper application in the DIC - 2D test and representation of a structure in service;
ii) Parameters of the DIC - 2D arrangement were defined for the acquisition of digital images with a resolution compatible with the displacements to be measured;
iii) The deformation of the specimen was analyzed using digital image correlation algorithms that process the images of the specimens acquired by the DIC - 2D arrangement;
vi) A deformation map was elaborated and superimposed on the digital image of the specimen to check if the occurrence of the crack matches the prediction found in the DIC - 2D.

2 MATERIALS AND EXPERIMENTAL PROGRAM

2.1 Preparation of the specimens

Five 10x20 cm cylindrical concrete specimens were modeled according to ABNT NBR 5738/2015 [09], using type CP V Portland cement, washed sand, and gravel 1, with an expected compressive strength of 40 MPa, according to the mix proportion shown in Table 1.

Table. 1 – Mix proportion of the concrete

CEMENT %	FINE AGGREGATE%	COARSE AGGREGATE%	SLUMP (cm)	W/C
1	1.7	1.27	3.04	0.36

After 24 hours the specimens were unmolded and kept in an immersion tank for 28 days to perform the wet cure and then removed and dried at an ambient temperature of approximately 25 ° C, protected from direct sunlight.

Before tested to compression, the specimens were rectified. A lateral strip area of 8.5 cm in width and 20 cm in length, received superficial treatment.

The superficial treatment consisted of, spraying a matte black spray paint forming a stochastic pattern (speckle). In the respective strip, powdered flowering pigment with a particle size ranging from 10-60µm was applied, formed by inorganic compounds based on natural mica and metallic oxides of iron and titanium, according to the manufacturer's information (company MASTERBATCH PIGMENTOS). This pigment can emit brightness when illuminated with ultraviolet (UV) radiation [10], helping the digital correlation, as seen in the Figure 1a, b.

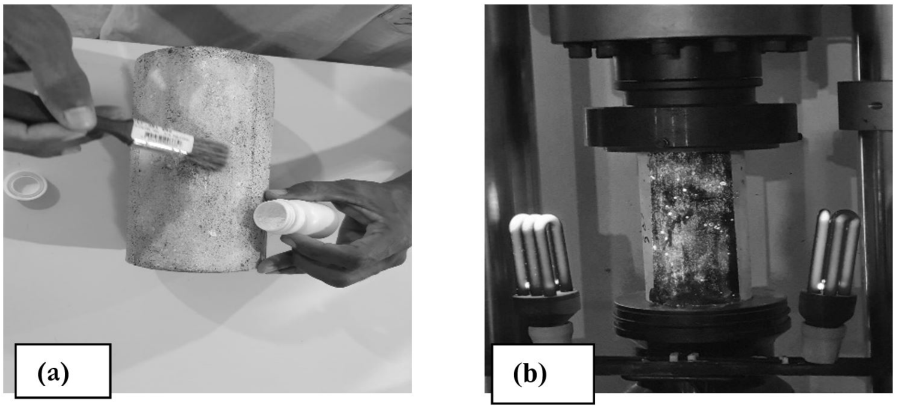

Figure 1: a) application of the contrast with flourishing powder b) Enhancement of the contrast with UV light [11]

2.3 Mechanical test

Each specimen was submitted to the axial compression loading according to NBR 5739/2018 [12], in a universal mechanical testing machine / model EMIC / PC200, applying progressive load at a constant rate of 0.5 MPa / s, until failure.

2.4 Acquisition of images in the 2D DIC array

The images were acquired by a DIC - 2D arrangement, composed of: (a) a load application system capable of causing deformation in the specimen due to the axial compression load, (b) a set of artificial lighting in which two 27W UV lamps are used to prevent shadows in the image, and, (c) a Canon / EOS model 70D digital camera with 18 - 55 mm lens, mounted on a tripod at a distance of 1.0 m from the target for which it formed an angle of 90 ° with center line of the specimen.

The sensor was connected to a I5 laptop, 2.7Ghz, 4GB of RAM, as shown in Figure 2, which shows the DIC - 2D array assembled in the laboratory.

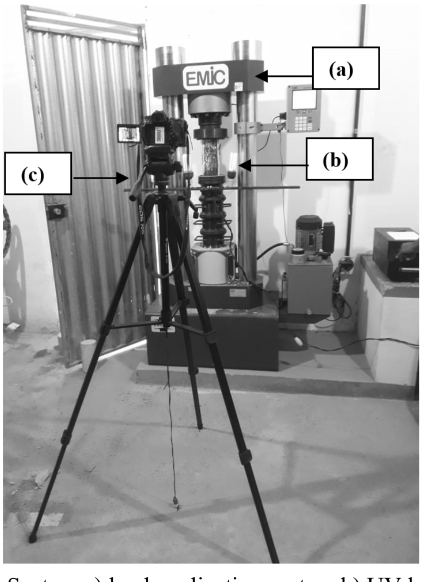

Figure 2: Assembly of the DIC-2D System a) load application system b) UV lamps c) a sensor digital camera [11]

2.3 Processing of images

The acquired images were processed at NCORR, a set of algorithms developed by the Technological Institute of Georgia, operated through MATLAB®.

The initial image is divided into two sections called blocks or subsets of 10 pixels in radius and spacing between them by 2 pixels and these blocks are searched for in the next image. (Figure 3)

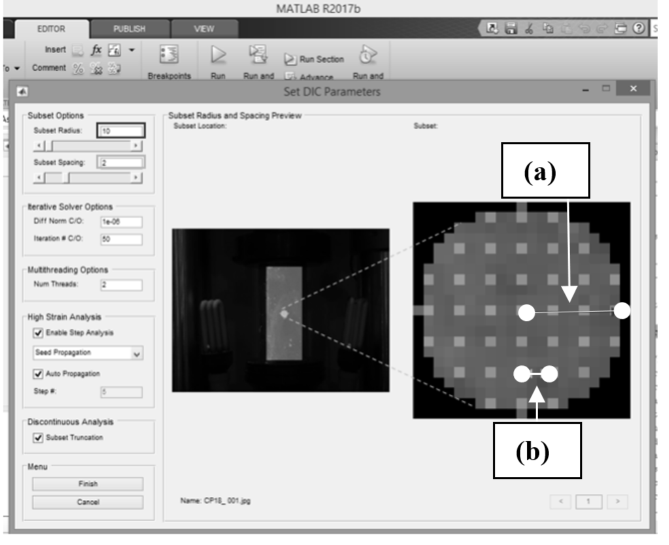

Figure 3: subsets of the region of interest (a) radius of the subset 10 pixels, (b) spacing of the subset 2 pixels [11]

Each block is a set of pixels and the objective of the algorithm is to determine its new position through the normalized cross-correlation cost function NCC (Eq. 1) [13], which indicates the closest likelihood, when analysing the intensity values of these pixels. The algorithm calculates the movement that the block made from one configuration to another, within an area (which is the search area of the algorithm) called Region of Interest (ROI), thus obtaining the displacements and, through these, later calculates the stresses [14].

$$NCC = 1 - \frac{\sum_{i=1}^{N} \sum_{j=1}^{N} f_{ij}\, g_{ij}}{\sqrt{\sum_{i=1}^{N} \sum_{j=1}^{N} fij^{2} - \sum_{i=1}^{N} \sum_{j=1}^{N} gij^{2}}} \tag{1}$$

Where:

NCC = Normalized cross-correlation cost function

$\sum_{i=1}^{N}$ = Sum of intensities in the reference image

$\sum_{j=1}^{N}$ = Sum of intensity in the deformed image

$f_{ij}\, g_{ij}$ = Likelihood function operators f (reference image) g (deformed image)

$\sqrt{\sum_{i=1}^{N} \sum_{j=1}^{N} fij^{2} - \sum_{i=1}^{N} \sum_{j=1}^{N} gij^{2}}$ = Distance between operators in the reference image and the deformed image

2.4 Propagation of Displacement and Deformation Fields

To assist in the evaluation of deformations in the specimens, the images were divided into quadrants and sub-quadrants, as shown in Figure 4, in order to observe the position where the maximum and minimum values of the displacements occurred, enabling the mapping of the trajectory of the fractures while increasing loading.

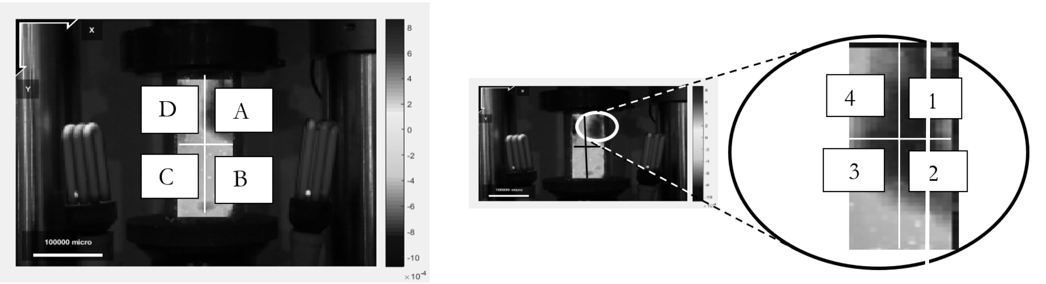

Figure 4 - Indication of quadrants A, B, C, D - Quadrants, 1,2,3,4 - Sub-squares [11]

3 RESULTS AND DISCUSSIONS

From the methodology represented in Figure 4, the map shown in Figure 5 was developed, which describes the location where the largest and smallest deformations occurred, evidencing the recurrent changes in direction in the fracture propagation front, as the load increased.

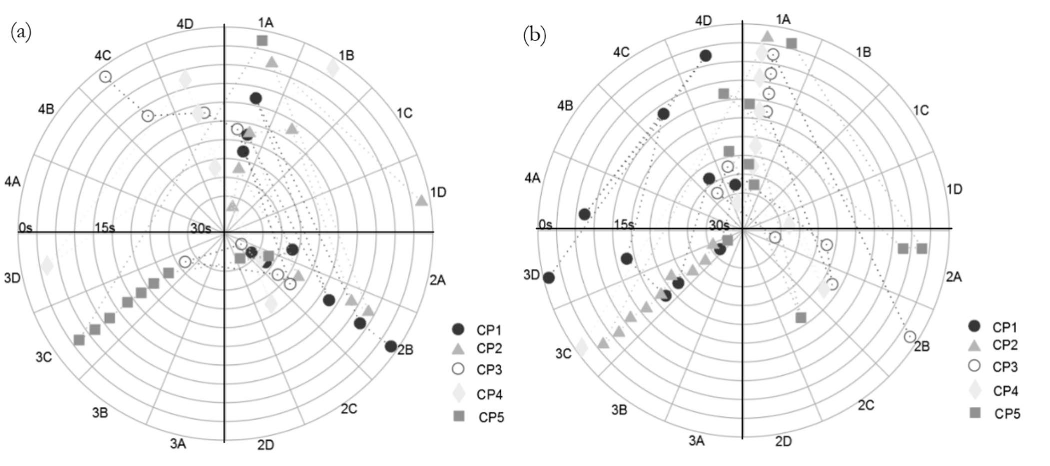

Figure 5 - Graphic map - a) spatial occurrence of maximum deformation on the x axis, b) spatial occurrence of minimum deformation on the x axis [11]

The concentric circles in graph represent the time (30s before the interval), decreasing from the center to the edges (time 30s in the center, less load and time 0s on the edge, greater load), that is, they were compared with the reference image (without deformation). All images acquired with loading in relation to 30s, 27s, 24s, 21s, 18s, 15s, 12s, 9s, 6s, 3s, 0s, where 30s corresponds to the lowest deformation load and 0s corresponds to the maximum deformation load in the ultimate limit state (rupture).

The orthogonal lines, represent the quadrants of the specimen, while the consecutive lines that cut the origin, represent the sub-squares, as indicated in the methodology (Figure 4).

The dotted lines indicate the trajectory of the deformation perceived by the proposed image correlation methodology for fracture prediction.

The distribution of the deformations presented by the map / graph (Figure 5a, b) suggests a non-linearity in the concrete deformation, and the main fracture propagation front can change its location when it finds stress concentrators, associated with fragility points in other regions of the studied PC, as stated by Corr [15].

To clarify the information brought by the maps / graphs, we highlight CP4, to make a detailed analysis of the occurrences of the displacement fields and their deformations in the x axis.

3.1 Exclusive deformation signature

When analyzing the relative deformations on the x-axis, of CP4 in Figure 5a, it can be seen that the frequency of occurrence of the maximum deformation values was concentrated in the region between the 1st and 4th quadrant, however when observing the frequency of occurrence of the minimum values Figure 4b, a change of direction is observed for the 3rd quadrant, suggesting the regions of CP4, which will suffer stress relief, possibly with crack propagation.

In a general analysis of Figure 5a, b, it is observed that each specimen has a different design of the regions of occurrence of the maximum and minimum values of deformation, suggesting that the property of heterogeneous and non-linear concrete determines an exclusive deformation signature. Depending on the studies by Metha and Monteiro [03], which indicate the difficulty in developing models that describe this behavior in concrete. The elaboration of a fracture prediction map can prove experimentally the complexity of the specimen deformation.

3.2 XY interdependence - POISSON coefficient

When statistically observing the deformation planes ε_x and ε_y, the Chi-square test revealed the interdependence of these variables with 95% significance, when accepting the H0 hypothesis (Figure 6 and Table 2), suggesting that the deformation in the x plane is dependent on the deformation in the y plane, according to the Poisson's ratio cited by Araújo [16].

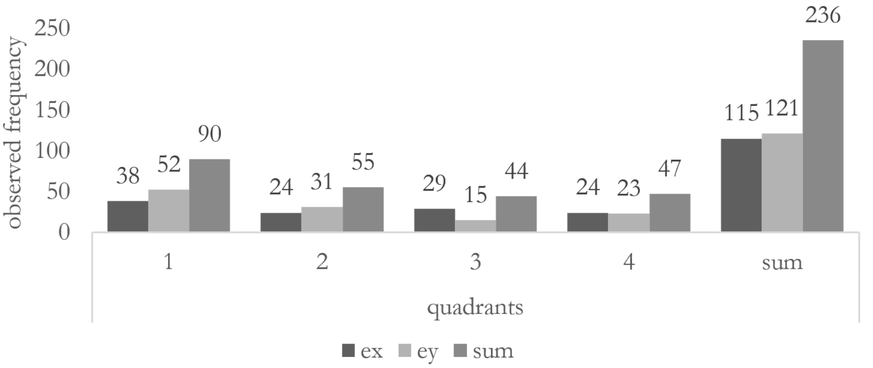

Figure 6 - Observed frequency of deformation ε_x and ε_y by quadrants.

Table 2 - On the left, deformation frequency ε_x and ε_y by quadrants A, B, C and D, on the right the parameters ANOVA, X^2- standard deviation, G.L - degree of freedom, H0 - chi-square hypothesis.

	Quadrants				
	A	B	C	D	X^2 = 7.40
εx	38	24	29	24	G.L = 3
εy	52	31	15	23	error = 5%
					Critical value = 7.82
					H0 = Acepted

3.2 Fracture prediction map

According to Mascia [17] the largest deformations are expected in the direction perpendicular to the application of the force, which for this experiment of axial compression test, it was observed that the largest deformations were perceived along the x axis, which in fact was observed. By superimposing in the images, the frequency of the maximum and minimum values of deformation of the x-axis, according to its quadrant of occurrence extracted from the map / graph, the indication of the places of beginning of possible fractures, with magnitudes of 800μm, was observed, according to the scale of the image acquired in the test. (Table 2)

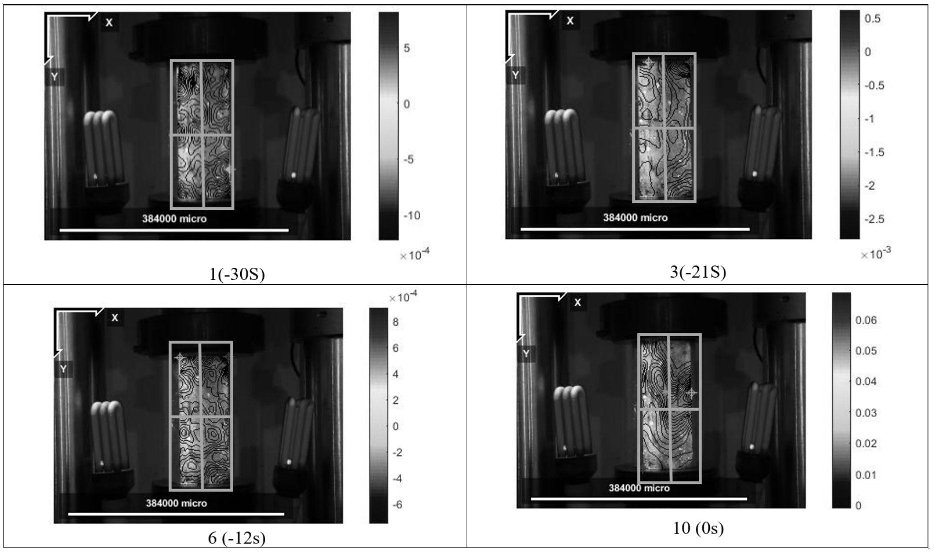

Frame 1 - Isoline map of deformations along the x-axis.

The isoline map (Frame 1) represents the regions of specimen deformation perceived by the proposed DIC test methodology along the x-axis, bringing us a perception of how the crack propagates during the test, in addition to the agglutination of the stress concentration points, demonstrating the phenomenon of “stress smoothing” mentioned by Carpinteri [18].

It is possible to observe through the isolines that the points of tension accumulation, tend to remain in their places, being able to agglutinate as the demands increase and the structure organizes itself for the new state of tension.

Standard 5739/2018, classifies the fracture of the specimen in seven types (Figure 7) and analyzing the distribution of the discontinuity of a PC it is possible to suggest the points of weakness.

The analysis of the deformations added to the knowledge of the type and direction of the stresses responsible for the studied deformation, arrived at the perception of the fracture prediction that will assist in a preventive action with the dynamic structural analysis including in the construction site.

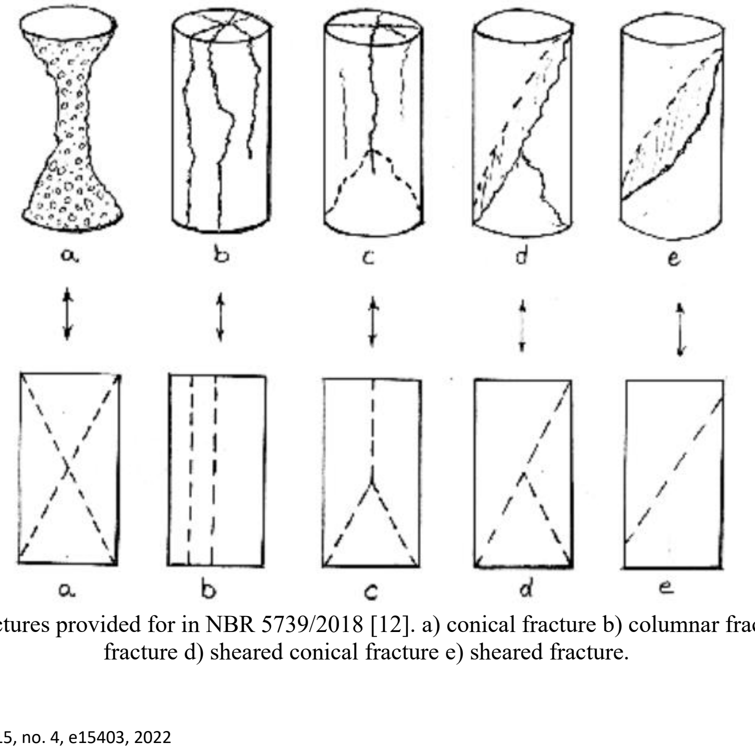

Figure 7 – Types of fractures provided for in NBR 5739/2018 [12]. a) conical fracture b) columnar fracture c) split columnar fracture d) sheared conical fracture e) sheared fracture.

As shown in Figure 8, the indication of the region with fracture prediction in fields of distribution of plane x deformation was observed in approximately 67% of the test specimens tested.

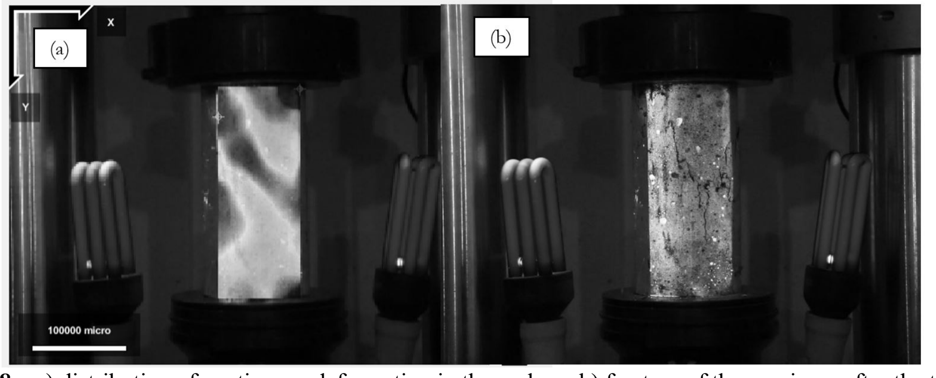

Figure 8 – a) distribution of continuous deformation in the x plane, b) fracture of the specimen after the test

5 CONCLUSIONS

In the presentation of the results, it was possible to elaborate a fracture prediction map in 67% of the analyzed specimens. In the specimens where it was not possible to predict the fracture, it was observed in the images acquired when being processed, that they undergo de-correlation due to the inefficiency of the random pattern, vibrations or shading that were not controlled in the laboratory.

The map / graph prepared in this research shows that crack propagation in specimen concrete is not linear.

In the test of comparison of means of the maximum frequency observed in this test, it was possible to perceive the interdependence of transverse and axial deformations, as demonstrated by the Poisson's ratio.

The test also suggests regions of possible discontinuities through alternating points shown on the deformation map of the plane perpendicular to the application of the force.

It is also possible to notice the multiple crack propagation fronts, which change direction depending on the stress concentration points.

6 ACKNOWLEDGEMENTS

Author thank the State University of Santa Cruz, the Postgraduate Program in Sciences, Innovation and Modeling of Materials - PROCIMM / UESC, the Federal Institute of Bahia / Ilhéus, the Institute of Physics Armando Dias Tavares of UERJ / Rio de Janeiro, UFF / Niterói Department of Optics, UFF / Niterói Department of Mechanical Engineering, Polytechnic Institute of Rio de Janeiro - IPRJ / UERJ Nova Friburgo and AXIS Engineering.

7 REFERENCES

[01] M. H. F. Medeiros, J. J. O. Andrade, and P. Helene, "Durabilidade e vida útil das estruturas de concreto," in *Concreto: Ciência e Tecnologia*, C. Isaia, Ed., São Paulo: IBRACON, 2011.

[02] R. J. C. Ribeiro and D. R. C. Oliveira, "O colapso do edifício Real Class," *Rev. IBRACON Estrut. Mater.*, vol. 11, no. 2, Mar/Apr 2018., http://dx.doi.org/10.1590/s1983-41952018000200008.

[03] K. Mehta and P. J. M. Monteiro, *Concreto: Estrutura, Propriedades e Materiais*, 3. ed. São Paulo: IBRACON, 2014.

[04] M. Koster, C. Kenel, W. J. Lee, and C. Leinenbach, "Digital image correlation for the characterization of fatigue damage evolution in brazed steel joints. 2014 Procedia," *Mater. Sci.*, vol. 3, pp. 1117–1122, Mar. 2016.

[05] B. Pan, "Reliability-guided digital image correlation for image deformation measurement," *Appl. Opt.*, vol. 48, pp. 1535–1542, 2009.

[06] Y. M. Picoy, "Correlação digital de imagens para medições de deslocamentos em vigas em balanço," M.S. dissertation, Engenharia de Sistemas e Automação - UFLA, Lavras, 2016.

[07] A. H. A. Santos, R. L. S. Pitangueira, G. O. Ribeiro, and R. B. Caldas, "Estudo do efeito de escala utilizando correlação de imagem digital de Imagem," *Rev. IBRACON Estrut. Mater.*, vol. 8, no. 3, pp. 323–340, Jun 2015., http://dx.doi.org/10.1590/S1983-41952015000300005.

[08] O. Marques Fo. and H. Vieira No., *Processamento Digital de Imagens*. Rio de Janeiro: Brasport, 1999.

[09] Associação Brasileira de Normas Técnicas, *NBR 5738: Moldagem e Cura de Corpos-de-Prova Cilíndricos ou Prismáticos de Concreto*, 2015.

[10] W. D. Callister, *Ciência e Engenharia de Materiais: Uma Introdução*, 9. ed. Rio de Janeiro: John Wiley & Sons, 2016.

[11] L. S. Assis, "Elaboração de mapa de previsão de fratura em concreto através de correlação digital de imagens DIC- 2D," Dissertação de mestrado, Universidade Estadual de Santa Cruz, Ilhéus, 2020.

[12]Associação Brasileira de Normas Técnicas, *NBR 5739 Concreto - Ensaio de Compressão de Corpos de Prova Cilíndricos*, 2018.

[13]F. Bárnik et al. "Measurement and comparison study of deformation using extensometer and 2D DIC technology," in *24th Slovak-Polish International Scientific Conference on Machine Modelling and Simulations*, Sep. 2019.

[14] J. Blaber, B. Adair, and A. Antoniou, "Ncorr: Open-Source 2D digital image correlation matlab software," *SEM*, vol. 55, no. 6, pp. 1105-1122, Mar. 2015.

[15] D. Corr, M. Accardi, L. Graham-Brady, and S. Shaha, "Digital image correlation analysis of interfacial debonding properties and fracture behavior in concrete," *Eng. Fract. Mech.*, vol. 74, no. 1-2, pp. 109–121, Jan 2007.

[16]J. M. Araújo, *Curso de Concreto Armado*, 4. ed. Rio Grande: Dunas, 2014.

[17] N. T. Mascia, *Teoria das Deformações*. Campinas: Universidade Estadual de Campinas, 2017.

[18] A. Carpinteri and F. Accornero, "Multiple snap-back instabilities in progressive microcracking coalescence," *Eng. Fract. Mech.*, vol. 187, pp. 272–281, Jan 2017., http://dx.doi.org/10.1016/j.engfracmech.2017.11.034.

Author contributions: JTA: conceptualization, supervision, writing; JRCP: conceptualization, supervision, writing; ADTJ: conceptualization

Editors: Lia Pimentel, Guilherme Aris Parsekian.

IBRACON Structures and Materials Journal
Revista IBRACON de Estruturas e Materiais
ISSN 1983-4195 ismj.org

ORIGINAL ARTICLE

Analysis of cementitious matrices self-healing with *bacillus* bacteria

Análise de matrizes cimentícias autocicatrizantes com bactéria Bacillus

Vinicius Muller[a]
Fernanda Pacheco[a]
Caroline Macedo Carvalho[b]
Franciele Fernandes[a]
Victor Hugo Valiati[b]
Regina Celia Espinosa Modolo[c]
Hinoel Zamis Ehrenbring[a]
Bernardo Fonseca Tutikian[c]

[a]Universidade do Vale do Rio do Sinos – UNISINOS, itt Performance; Graduação em Engenharia Civil, São Leopoldo, RS, Brasil
[b]Universidade do Vale do Rio do Sinos – UNISINOS, Programa de Pós-graduação em Ciências Biológicas, São Leopoldo, RS, Brasil
[c]Universidade do Vale do Rio do Sinos – UNISINOS, , Programa de Pós-graduação em Engenharia Civil, São Leopoldo, RS, Brasil

Received 05 July 2021
Accepted 01 December 2021

Abstract: Bacterial solutions have been studied to promote self-healing of cementitious matrices, however, the concentration of this solutions varied between studies. Consequently, the objective of this study was to evaluate the self-healing potential of different concentrations of *Bacillus subtilis* AP91 encapsulated in expanded perlite (EP). Visual examination and capillary absorption of water was measured over time. Test samples were also subjected to strength resistance tests. The physiochemical properties of EP and his distribution on the matrix was evaluated. There was no observable trend in the effect of solution concentration on the width of crack healed. However, concentration affected the quantity and length of the fissures healed. Capillary absorption decreased as fissures were healed while no significant changes were measured in strength resistance regardless of the concentration. Results indicated that EP provided suitable encapsulation to the bacterial solution and there is an adequate distribution of the capsules in the cementitious matrix.

Keywords: bacteria, concrete, durability, cracking, mortar, self-healing.

Resumo: Soluções bacterianas têm sido estudadas para promover a autocura de matrizes cimentícias, entretanto, a concentração dessas soluções variou entre os estudos. Consequentemente, o objetivo deste estudo foi avaliar o potencial de autocura de diferentes concentrações de *Bacillus subtilis* AP91 encapsulado em perlita expandida (PE). O exame visual e a absorção capilar de água foram medidos ao longo do tempo. As amostras de teste também foram submetidas a testes de resistência de força. Foram avaliadas as propriedades físico-químicas do EP e sua distribuição na matriz. Não houve tendência observada no efeito da concentração da solução na largura da fissura cicatrizada. No entanto, a concentração afetou a quantidade e o comprimento das fissuras cicatrizadas. A absorção capilar diminuiu conforme as fissuras foram curadas, enquanto nenhuma mudança significativa foi medida na resistência da força, independentemente da concentração. Os resultados indicaram que a EP proporcionou encapsulamento adequado à solução bacteriana e que há uma distribuição adequada das cápsulas na matriz cimentícia.

Palavras-chave: bactéria, concreto, durabilidade, fissura, argamassas, autorregenerantes.

How to cite: V. Muller et al. "Analysis of cementitious matrices self-healing with *bacillus* bacteria," *Rev. IBRACON Estrut. Mater.*, vol. 15, no. 4, e15404, 2022, https://doi.org/10.1590/S1983-41952022000400004

Corresponding author: Regina Célia Espinosa Modolo. E-mail: reginaem@unisinos.br
Financial support: The authors would like to thank Unisinos, Performance Technological Institute (itt) and CNPq for the financial support granted to Regina Célia Espinosa Modolo (Grant # 307755 / 2018-5).
Conflict of interest: Nothing to declare.
Data Availability: The data that support the findings of this study are openly available in [Unisinos repository] at [http://www.repositorio.jesuita.org.br/handle/UNISINOS/9376], reference number [9376].

This is an Open Access article distributed under the terms of the Creative Commons Attribution License, which permits unrestricted use, distribution, and reproduction in any medium, provided the original work is properly cited.

1 INTRODUCTION

Worldwide, concrete is the material most used material [1] due to several advantages [2]–[4]. However, it has been noted that Portland cement production accounts for 9.5% of global carbon dioxide emissions [5]. Besides these environmental considerations, additional costs are accrued when dealing with interventions in reinforced concrete. In developed countries, costs with repair, maintenance and reconstruction of structures is higher than new ones [6]. In developing countries, concrete structures tend to deteriorate ahead of their expected life cycle [3]. In monetary terms, one-third of the budget of large construction projects in the Netherlands is designated for interventions while in Great Britain, 45% of all activities are repair and maintenance [7]. Complementing, Gardner et al. [8] highlight the problem of maintenance costs, citing the United Kingdom as an example and thus justifying the need for such expenses to be minimized. The demolition/construction cycle of a project results in severe environmental costs [9] which are also believed to be associated with repair work [6].

Fissure formation and the resulting entry of harmful agents is one of the main causes of damage to reinforced concrete [10]–[16]. Thus, mitigating the occurrence and the size of fissures reduces concrete deterioration due to environmental factors [17], [18]. Fissure recovery usually involves the use of chemical products that are expensive and potentially harmful to health and the environment [16]. Consequently, new techniques to extend the durability of structures, such as self-healing concrete, are needed [19]. Self-healing can be obtained from higher cement use [20], [21], addition of pozzolans[21], [22], chemical solution encapsulation in light and porous aggregates [23] and bacterial solutions in concrete [16], [24]–[27].

Bacterial solutions inserted in cementitious compounds promote microbiologically induced calcite precipitation (MICP). Species of the *Bacillus* genus are capable of metabolizing MICP while at the same time being resistant to aggressive environments [28]. This bacterial genus has been widely studied and cultivated in alkaline mediums and its dormant endospores are able to survive centuries in chemically aggressive environments [29]–[32]. Like other chemoorganotrophic bacteria, this genus extracts energy from the oxidation of organic compounds [29]. The MICP reaction in cementitious compounds occurs through calcium lactate oxidation (Equation 1 and Equation 2), and calcium acetate oxidation (Equation 3 and Equation 4) [33], [34].

$$CaC_6H_{10}O_6 + 6O_2 \rightarrow CaCO_3 + 5CO_2 + 5H_2O \tag{1}$$

$$5CO_2 + 5Ca(OH)_2 \rightarrow 5CaCO_3 + 5H_2O \tag{2}$$

$$Ca(C_4H_6O_4) + 4O_2 \rightarrow CaCO_3 + 3CO_2 + 3H_2O \tag{3}$$

$$3CO_2 + 3Ca(OH)_2 \rightarrow 3CaCO_3 + 3H_2O \tag{4}$$

In Equation 1, calcium lactate ($CaC_6H_{10}O_6$) oxidates into calcium carbonate ($CaCO_3$) with carbon dioxide (CO_2) and water (H_2O) as leftover products. As shown in Equation 2, CO_2 produced from Equation 1 reacts with calcium hydroxide ($Ca(OH)_2$) present in large quantities in concrete as a product of cement hydration to precipitate additional $CaCO_3$. Similarly, Equation 3 shows that calcium acetate ($Ca(C_4H_6O_4)$) oxidates into $CaCO_3$, H_2O and CO_2, with the latter undergoing the same reaction with ($Ca(OH)_2$) as seen in Equation 4. It has been noted that MICP through oxidation of organic compounds occurs primarily with bacteria of the genera *Bacillus pseudofirmus, Bacillus cohnii, Bacillus alkalinitrilicus and Bacillus* sp., which may be further complemented with other MICP-inducing metabolic processes [31].

As noted in Equation 1 and Equation 3, calcic nutrients are needed for the bacteria to perform MICP. Most studies make use of calcium lactate [10], [15], [27], [33], [35]–[37] calcium nitrate [25], [38], [39] calcium chloride [40], [41] and calcium acetate [33], [40], [42]. In addition to calcic nutrients, other more complex nutrients have been used such as yeast extract [15], [25], [33], [38], [39], [43], [44], meat extract [45] and peptone [33], [45]. However, these nutrients are known to have lower efficiency since their exact composition is unknown, especially with respect to calcium content [31]. The effect of different nutrients on strength resistance has been tested in cement pastes aged over time [33]. Results demonstrated that calcium lactate yielded the best results, with a strength increase comparing with control samples.

Studies conducted in Brazil have obtained positive results of MICP with *Bacillus subtilis* AP91 [46]. Surface treatment of pre-existing concretes has also been performed with *Bacillus sphaericus* and resulted in water absorption, gas permeability and chromatic aspect values similar to the application of commercial hydrophobic additives [40].

Surface treatment also reduced water absorption with beneficial effects on concrete durability [47]. Visual investigation of healed fissures confirmed the great potential of this technique with healing of fissures as wide as 0.79 mm [15]. Testing variations in general, each with distinct concentrations, led to an overall increase in strength resistance of cementitious compounds [45], [30]. *Bacillus, Sporosarcina* and *Shewanella* genera were tested in concentrations varying from 5 x 10^4 cells/mL to 2.8 x 10^8 cells/ mL and a concentration of 3 x 10^6 measured in colony-forming units/mL (CFU/mL).

Bacterial solution used in substitution to mixing water resulted in an increase of 13% in strength resistance and 8.5% reduction in permeability [47]. However, bacteria may be damaged over time, cause its metabolic activity decreases in environments with pH above 12 [43]. In extreme cases, bacteria may not survive the alkaline environment, mechanical stresses of concrete mixing or cement hydration since matrix pores have dimensions of less than 0.5 μm while bacteria have dimensions between 1 μm and 3 μm [10], [25], [33], [36]. Consequently, micro-organisms encapsuled in light or porous aggregates have been tested [15], [27], [34]. Fissuring ruptures the capsules and releases the healing agent, which seeps into the matrix though capillary penetration [48].

Bacteria of the specie *B. cohnii* were tested encapsulated in expanded clay (EC) and expanded perlite (EP) in the 2 mm to 4 mm granulometric range [15] and found healing to be more effective with EP. A bacterial solution of *B. pseudofirmus* DSM 8715 encapsulated in EP was successfully used in 20% substitution by volume of sand in concrete [34]. In order to prevent premature release of the healing agent, higher resistance coatings are recommended for the capsules in order to ensure light aggregate integrity during the mixing process [48]. Some types of coatings commonly used are geopolymers [15] and cement [49]. As for the effects of curing, self-healing mortars were tested in submerged curing and wet/dry cycles [37]. It was determined that the underwater cure form ~~of curing~~ yielded better results, probably due to the higher availability of oxygen.

Despite the use of coatings and the use of capsules for bacterial solutions, as mentioned before, it is also noted that studies evaluated the bacterial solution concentration, considering its relevance in the process of healing. Vijay, Murmu and Deo [30], for example, presented several studies with the authors choice for the bacterial concentration. Sidiq, Gravina and Giustozzi [50], considering specifically the specie *B. subtilis* pointed out the use of 10^5 cell/ml. It is noted that the concentration must be selected for each specie, considering the characteristics of the microorganisms.

This study conducted mechanical and visual analyses of mortars with the addition of *B. subtilis* AP91 solutions in CFU/mL concentrations of 3 x 10^6, 3 x 10^7 and 3 x 10^8 encapsulated in EP, aiming to analyze if this concentration has effect on mechanical performance of the samples and its potential to promote self-healing. The encapsulating potential of the EP aggregate was also evaluated through void space measurements in a scanning electronic microscope (SEM) and the EP distribution in the mortar matrix was evaluated with micro-computed tomography (μCT).

EP capsules were chosen among other options due to their availability in the study region, and for their compatibility with concrete matrix in self-healing concretes [15]. Other systems can be used, such as superabsorbent polymers [51] or vascular networks however [52], with complex preparation procedures.

Several research have been carried out in the study of self-healing of cementitious materials, however, when it comes to self-healing promoted by biological agents, little is discussed about the influence of the concentration of these agents in this process. Still, there is a lack of published studies using microorganisms cataloged in Brazil. It is hoped that this study will contribute to the development of self-healing Brazilian cementitious materials, as well as bringing to discussion not only the different varieties of microorganisms used to promote self-healing, but also the concentration in which they are inserted in matrices.

2 EXPERIMENTAL PROCEDURES

2.1 Mixing ratio and characterization of materials

The bacteria used in this study was the same as Schwantes-Cezario, Nogueira and Toralles [53] and Schwantes-Cezario et al. [54]. Consequently, the same mixing ratio of 1:1 (cement: sand) in mass was used in the mortar. Expanded perlite (EP) with grain sizes between 2.4 mm and 4.8 mm was used to encapsulate the micro-organisms as in Zhang et al. [15]. It should be noted that granulometry of the EP used in Zhang et al. [15] yielded sizes between 2 mm to 4 mm. Since the sieve sizes were defined according to ASTM C33 [55], an adaptation to the diameters was necessary for this study. Fine EP aggregate was used in a substitution of 30% in volume for sand so that the final adapted mixing ratio was defined as 1:0.7:0.084 (cement: sand: EP). While the amount of EP substitute remained constant, the concentrations of bacterial solution varied throughout this study. Table 1 presents the mixing ratio of materials for each sample with respect to a 1 kg consumption of cement.

Table 1 – Materials and mixing ratio of samples studied

Sample	Cement, kg	Sand, kg	EP, kg	*B. subtilis* AP91 concentration, UFC/ml	Water/cement ratio
BAC.6	1	0.7	0.084	3×10^6	0.37
BAC.7	1	0.7	0.084	3×10^7	0.37
BAC.8	1	0.7	0.084	3×10^8	0.37

Cement used was of Type IL(10) as defined in ASTM C595 [56] with no pozzolanic addition. Laser granulometry, surface area and density tests were conducted on the cement. Laser granulometry was performed in a Microtrac model S3500 apparatus with isopropyl alcohol as fluid. Surface area tests were conducted with Brunauer, Emmett and Taller (BET) isotherms and MicroActive TriStar II Plus 2.02 software. Density was measured in a helium gas pycnometer following ASTM D5550 [57] procedures. Results were a surface area of 2.0474 ± 0.0085 m^2/g and density of 3.0049 g/cm^3, while granulometry results are presented in Figure 1. Sand granulometry was obtained with ASTM C33 [55] and density was obtained with ASTM C128 [58] and ASTM C29 [59]. The sand used was quartz-based and locally sourced from a river. Similar procedures were followed to obtain EP granulometry and apparent density. The apparent density of EP was measured for the natural original as well as the bacterial solution-impregnated and coated materials. Sand and EP characterizations are shown in Table 2 while granulometries are shown in Figure 2.

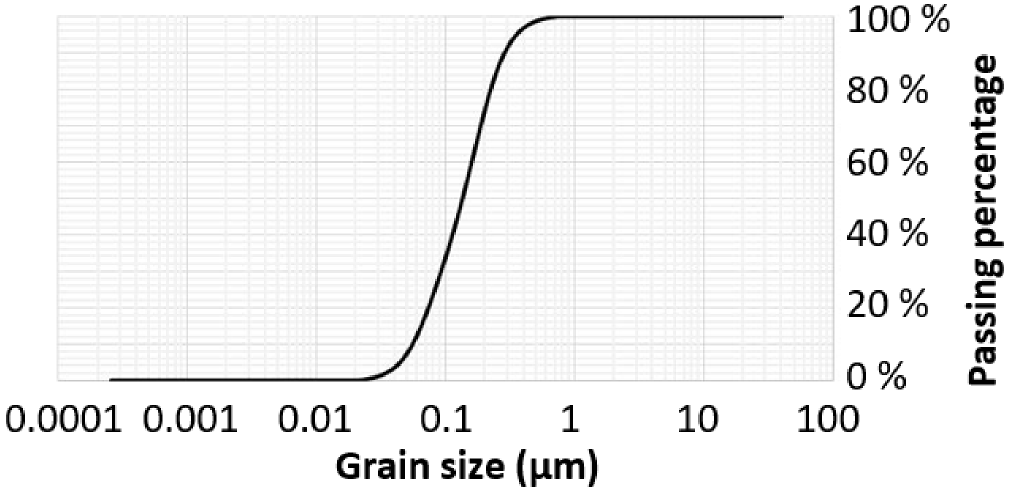

Figure 1 – Cement particle size distribution.

Table 2 – Density and apparent density of aggregates

Aggregate		Apparent Density kg/m³	Density kg/m³	Maximum characteristic dimension, mm	Fineness modulus
Sand		1,734.33	2,700	3.26	3.01
EP	Natural	94.36	-	4.75	4.14
	Treated	475.50	-		

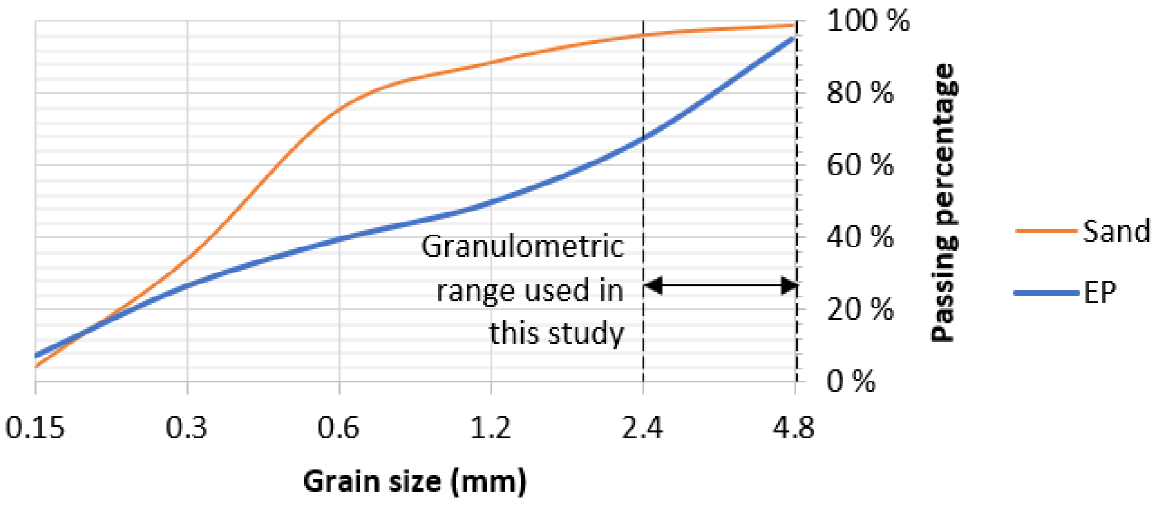

Figure 2 – Aggregate granulometry

It should be noted that despite sand not having the same granulometric distribution, a limited EP granulometric range was used in this study. This was defined in order to match sizes used in other studies [15], [27], and to allow direct comparison of the results between them. The chemical composition of EP is shown in Table 3, according to data provided by the producer.

Table 3 – Chemical composition of EP

SiO_2		Al_2O_3		Fe_2O_3		TiO_2		CaO		MgO	
Min	Max	Min	Max	Min	Max	Min	Max	Min	Max	Min	Max
71	78	8.5	15	0.3	1.2	0.01	0.01	0.3	1.2	0.1	0.3
Na_2O		**K_2O**		**SO_3**		**P_2O_5**		**MnO**		**Loss of Ignition**	
Min	Max	Min	Max	Min	Max	Min	Max	Min	Max	Min	Max
2.5	4.2	3.00	7.00	0.01	0.01	0.01	0.03	0.01	0.04	0.10	2.00

2.2 Growth curve, cultivation and bacterial encapsulation

The *B. subtilis* AP91 strain used was provided by the Campinas branch of Empresa Brasileira de Pesquisa Agropecuária – EMBRAPA. Cultivation in vitro was conducted in Luria Bertani (LB) broth containing 10g/L of tryptone 5g/L of yeast extract and 5g/L sodium chloride in deionized water. This broth has been used to adequately cultivate *B. subtilis* [48], [53]. A volume of 100 mL of LB broth was placed in two 250 mL Erlenmeyers flasks each and sterilized in an autoclave at 121° C for 15 min. Following sterilization, each flask was inoculated, and the cultures were incubated in an orbital shaker at 165 rpm and 37º C (98.6ºF) for 24 h. The growth curve was obtained by taking samples over the incubation period. The cultivation absorbance was analyzed in a Kazuaki model IL-226-NM spectrophotometer of 600 nm wavelength. Simultaneously to the absorption measurement, each sample was ten-fold serially diluted in saline solution (0.9% sodium chloride) and each dilution was pour-plated in agar LB for colony forming unit (CFU) counting. It should be noted that not all bacteria exist as isolated cells and bacterial agglomerates and groups also generate a single colony. Due to this fact, colony-counting cannot be taken as the absolute number of cells and, thus, CFU was selected [60]. Plated samples were placed in an incubator at 36 ºC for 48 h, at which point colonies were counted for the corresponding absorption value. The procedure adopted is shown in Figure 3 and described in detail in Swanson et al. [60]. Figure 4 shows the species spectrophotometric behavior relating the absorbance and concentration of each sample.

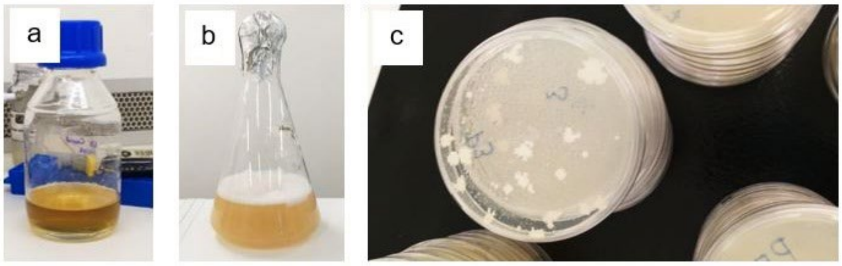

Figure 3 – Procedures for spectrophotometry of *B. subtilis* AP91: (a) sterile LB Broth, (b) LB broth with bacterial growth and (c) colonies 48h after in an incubator

The figure allows the determination of the cultivation level of *B. subtilis* AP91 based on its absorbance. In the equation, shown overlaid in Figure 4, the absorbance (A_{600}) is dimensionless and concentration (C) is given in CFU/mL. The figure allows the determination of the cultivation level of *B. subtilis* AP91 based on its absorbance. In the equation, shown overlaid in Figure 4, the absorbance (A_{600}) is dimensionless and concentration (C) is given in CFU/mL.

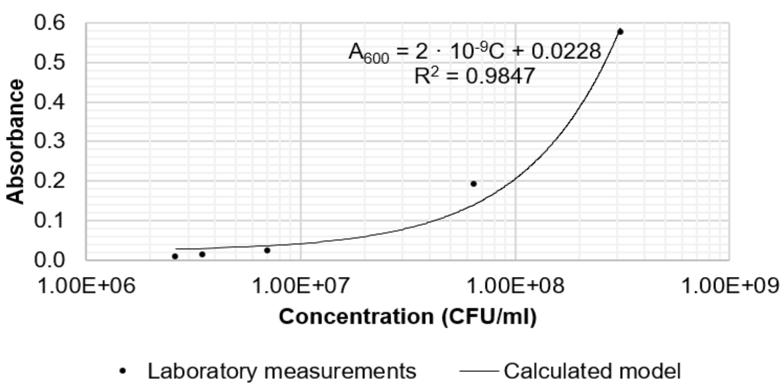

Figure 4 – Spectrophotometric behavior of B. subtilis AP91

A sterile buffer solution containing 1.06 g/L of sodium phosphate (anhydrous dibasic), 0.36 g/L sodium phosphate (monobasic) and 8.17 g/L sodium chloride in deionized water was used as dilutant for the bacteria for the purpose of encapsulation and later insertion in the cementitious mixture. In parallel, the bacteria were inoculated in 2 L Erlenmayer flasks with 1 L of sterile BL broth and incubated in an orbital shaker for 24 h. Following the 24 h growth period, the solutions were centrifuged in an Eppendorf AG model 5430 R centrifuge at 4,000 rpm and 23 ºC for 3 min to precipitate the cells. The supernatant was discarded, and the cells washed 4 more times with the sterile phosphate buffer solution, each time following the same previous centrifugation and supernatant discarding procedures. This was done in order to remove any organic matter present in the cultivation solution. The progressive changes in visual appearance of the solution are shown in Figure 5. The buffer solution and washing procedures followed the methodology of Schwantes-Cezario et al. [53].

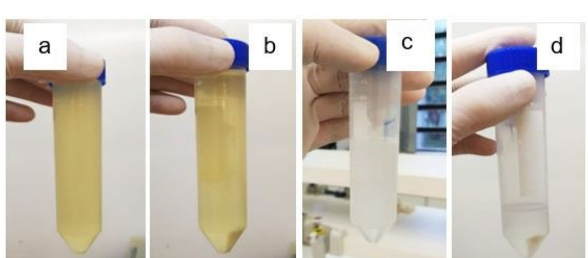

Figure 5 – LB broth (a) before (b) and after centrifugation; (c) buffer solution before (d) and after centrifugation

After washing, cells were re-suspended in phosphate buffer solution and its absorbance was measured to define the initial concentration. Then, the solution was diluted to the target concentration. The solutions were refrigerated at 8 ºC for 2 days in order to promote sporulation [53] and slows down cellular multiplication [29], ensuring that concentrations are kept constant.

Impregnation of EP with bacterial solution was accomplished by submerging the aggregate for 3 hours in different concentration solutions. After soaking, the EP was placed in a vacuum desiccator for the 30 min necessary to achieve maximum impregnation [49]. Following impregnation, excessive liquid was drained, and EP dried in an incubator at 45 ºC for 48 h. After drying, EP was sprayed with a calcium lactate solution containing 8 g/L of calcium lactate, 1 g/L of yeast extract and deionized water and further incubated at 45 ºC for 48 h. This procedure followed the methodology of Zhang et al. [15]. As a protective coating, the same cement used in the mortar was sprinkled on the aggregate following the procedure of Sisomphon et al. [49]. Although not mentioned in other studies, a further spraying of the calcium lactate solution prior to coating with cement was necessary to promote hydration and improve adhesiveness. Once the encapsulation process was completed, the aggregate was kept at rest for 7 days to cure the cement coating prior to molding the test samples as per the methodology of Zhang et al. [15].

2.3 Molding of samples

Cylindrical (50 mm x 100 mm or 1.96in x 3.93in) and prismatic (40 mm x 40 mm x 160 mm) samples were molded and cured in a climate-controlled chamber (humidity and temperature) for 7 days [61]. Fissures were induced in prismatic samples with a bending test following ASTM C348 [62]. To prevent total sample rupture, a 5 mm diameter CA 60 steel bar was inserted ¼ into the base of the samples in a similar procedure as Alghamri et al. [63]. After fissuring, samples were returned to the chamber to promote oxygenation to the bacteria and induce the bio-mineralization reaction.

2.4 Visual analysis of healing, capillary absorption of water and strength resistance tests

After fissuring, visual analyses were conducted at 7, 14, 28 and 42 days to inspect for signs of healing and monitor its evolution. A Motic SMZ-168 stereo zoom microscope was used for inspection and measurements were taken with AutoCAD™ software. A capillary absorption test was conducted at 42 days following the procedure of RILEM TC 116-PCD [64] to obtain the mass of absorbed water relative to exposed area. The sample was leached with hydrochloric acid to remove any calcium carbonate precipitation and return the samples to their pre-healing state. The absorptivity test was then repeated, and the results allowed comparison of absorption pre and post-healing. Strength resistance tests were conducted following ASTM C39 [65] procedures at 7 days, 28 days and 54 days after demolding.

2.5 Complementary analyses

Scanning electronic microscopy (SEM) with a Zeiss brand apparatus was used in EP samples embedded in the cementitious matrix in order to determine their internal microstructure and suitability as capsule for *B. subtilis*. Along with SEM, an energy dispersion spectroscopy (EDS) was performed to evaluate EP chemical composition before and after calcium lactate spraying in order to determine its effective presence on the surface of the structure. Since EP is extremely porous, density variations allowed micro-computed tomography (μCT) to determine its distribution in the cementitious matrix. For these complementary analyses, fragments of sample BAC.7 were used from which planes were sliced with a circular saw. Exceptionally, pre-spraying samples of EP were taken for EDS analysis from the natural aggregate as supplied by the manufacturer. The samples were dried at 50ºC until mass constant and then metallized with gold.

3. RESULTS AND DISCUSSION

3.1 Compressive strength and capillary absorption of water

Figure 6 demonstrates that the average strength resistance remained at around the same level for the samples over the time periods of this study.

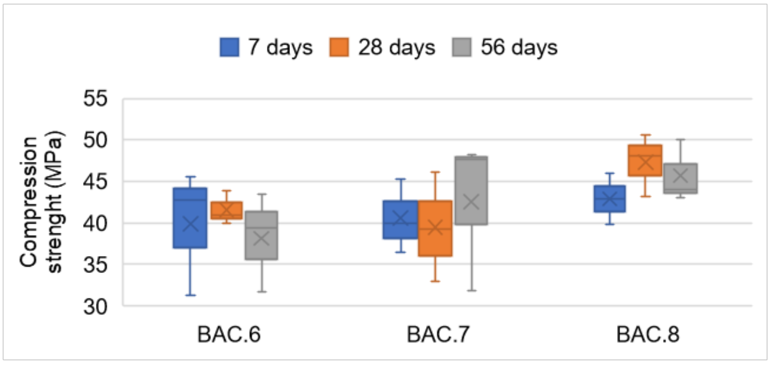

Figure 6 – Compression resistance results at 7 days, 28 days and 56 days

The largest variation was measured at 4.4 MPa, or 10.26% with respect to the smallest value, for sample BAC.8 between 7 days and 28 days. The fact that there was little variance from 7 days to 56 days could be attributed to the type of cement used, which contained an elevated percentage of clinker [56] and resulted in considerable strength from an early age. The largest difference in strength between mixing ratios for the same period was measured between BAC.7 and BAC.8 at 28 days: 7.9 MPa, or 20% with respect to the smallest value. The relatively low variance in strength between mixing ratios could be attributed to the identical cement: sand: EP ratio and water/cement relation between samples, of which only bacterial concentration varied. These results indicated that bacterial addition had no impact in the uncracked specimens despite the possibility of naturally occurring micro-fissures being formed in the cementitious matrices. Even if these micro-fissures were present, they were likely in small quantities and size since the samples themselves were of small size and have a high degree of freedom, thus minimizing fissuring from retractions.

Comparisons with Schwantes-Cezario et al. [53], which provided the mixing ratio, denoted that there was a decrease in strength. While strengths for the samples of this study were measured in the approximate range of 35 MPa to 50 MPa, Schwantes-Cezario et al. [53] obtained strengths in the range of 55 MPa to 75 MPa. This decrease was likely due to inserted EP being a lighter aggregate in the cementitious matrix as noted by Jonkers [35]. On the other hand, Afifudin et al. [24] observed that the same mixing ratio but with *B. subtilis* inserted directly in the matrix in different concentrations yielded more significant differences. It should be noticed that the authors did not use capsules, and thus, the bacterial solution may have contributed with the formation of the crystals along the sample, achieving better strength results.

The low variation in strength due to concentration observed in the samples of this study were likely the result of EP preventing bacterial activity in the uncracked samples. This was in agreement with the expectation that healing agents would only become active after the capsules were ruptured [63], [66].

Figure 7 shows the average water absorption of all samples before and after leaching with hydrochloric acid. It should be noted that it was not possible to compare absorption between samples because the fissures did not have the same geometry. At the 24 h mark, it could be seen that all samples had higher absorption after leaching with increases of 18.76%, 8.62% and 43.45% for samples BAC.6, BAC.7 and BAC.8, respectively. Although there was no proportional relationship between bacterial concentration and decrease in absorption, it could be stated that BAC.8 presented a higher efficiency in healing.

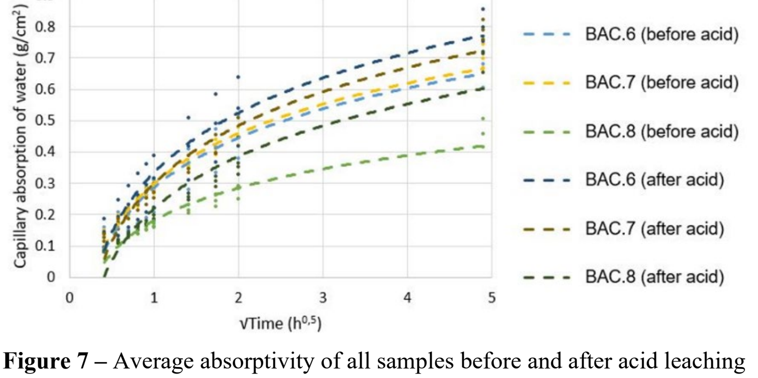

Figure 7 – Average absorptivity of all samples before and after acid leaching

Results obtained in this study, especially with BAC.8, were in-line with Alghamri et al. [63], which obtained a decrease of about 50% in absorption with a sodium silicate solution encapsulated when compared to control samples. Additionally, Siddique et al. ~~[62]~~ [67] inserted a bacterial solution in the matrix with no encapsulation and obtained absorption reductions between 50% and 70%. In this case, the direct insertion of bacteria had a more efficient impact in absorption since their action was not conditioned to capsule rupturing.

3.2 Visual surface analysis, SEM analysis and Micro-computed tomography

A total of 9 samples were molded for visual analysis and all presented evidence of at least 1 or more surface healing locations.

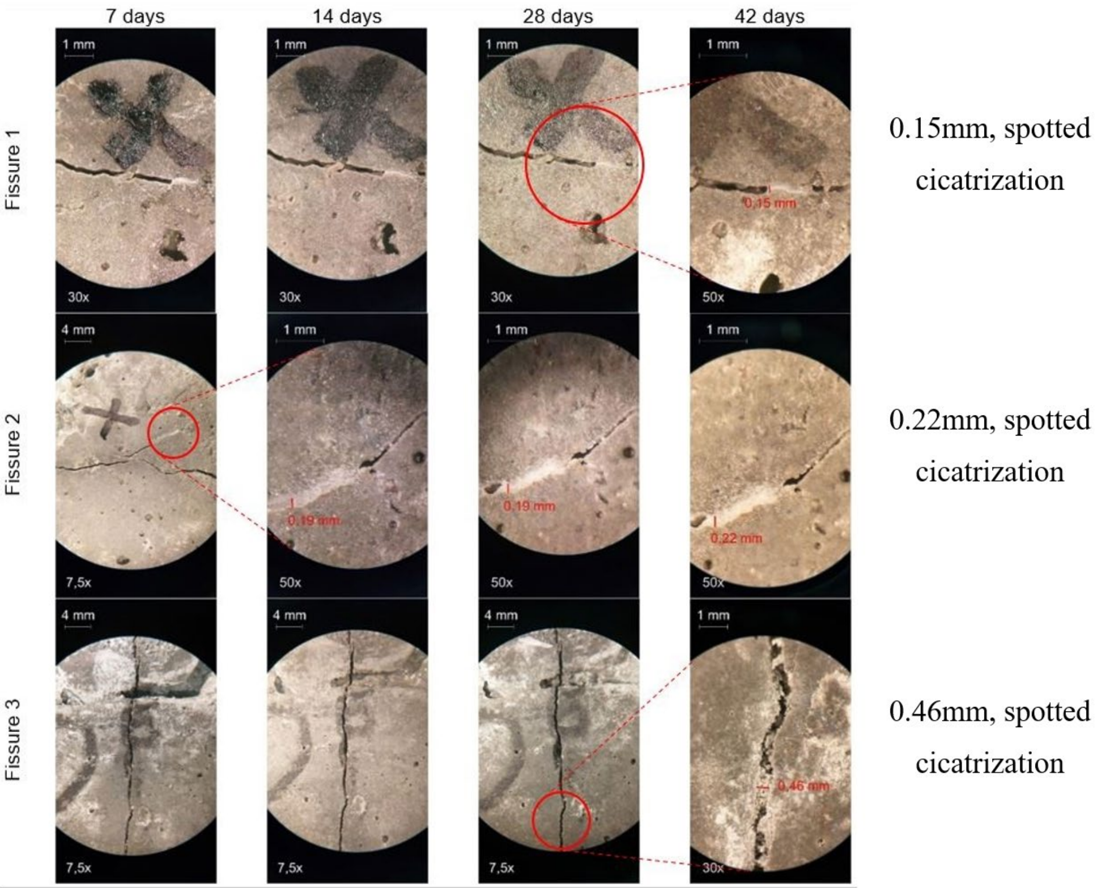

Figure 8 – Self-healing activity of sample BAC.6 at several ages

Figure 8 shows the results for sample BAC.6 at several ages, designated fissure 1 through 3. In Figure 8, fissures 1 and 2 were healed at 7 days and no further major healing products were formed at older ages. However, fissure 3 presented a different coloration healing which healed further between 28 days and 42 days. For sample BAC.6, the maximum healing width was of 0.46 mm and healing occurred in spots rather than along the extent of the fissure. Spotted healing similar to fissure 1 and fissure 2 was also observed in others studies ~~[63]~~ [68]. Wall-bound healing presented in fissure 3, which could further evolve and result in complete healing at later ages, was also annotated by Khaliq and Ehsan [69]. Whether spotted or wall-bound, healing could be attributed to the local availability of EP releasing products for self-healing. It should be noted that, regardless of the type of healing, the visual aspect observed in the samples were of a whitish product, referred to in other works as calcite formed from bacterial solutions [21], [70]. Figure 9 shows the results from sample BAC.7, designated fissure 4 through 7.

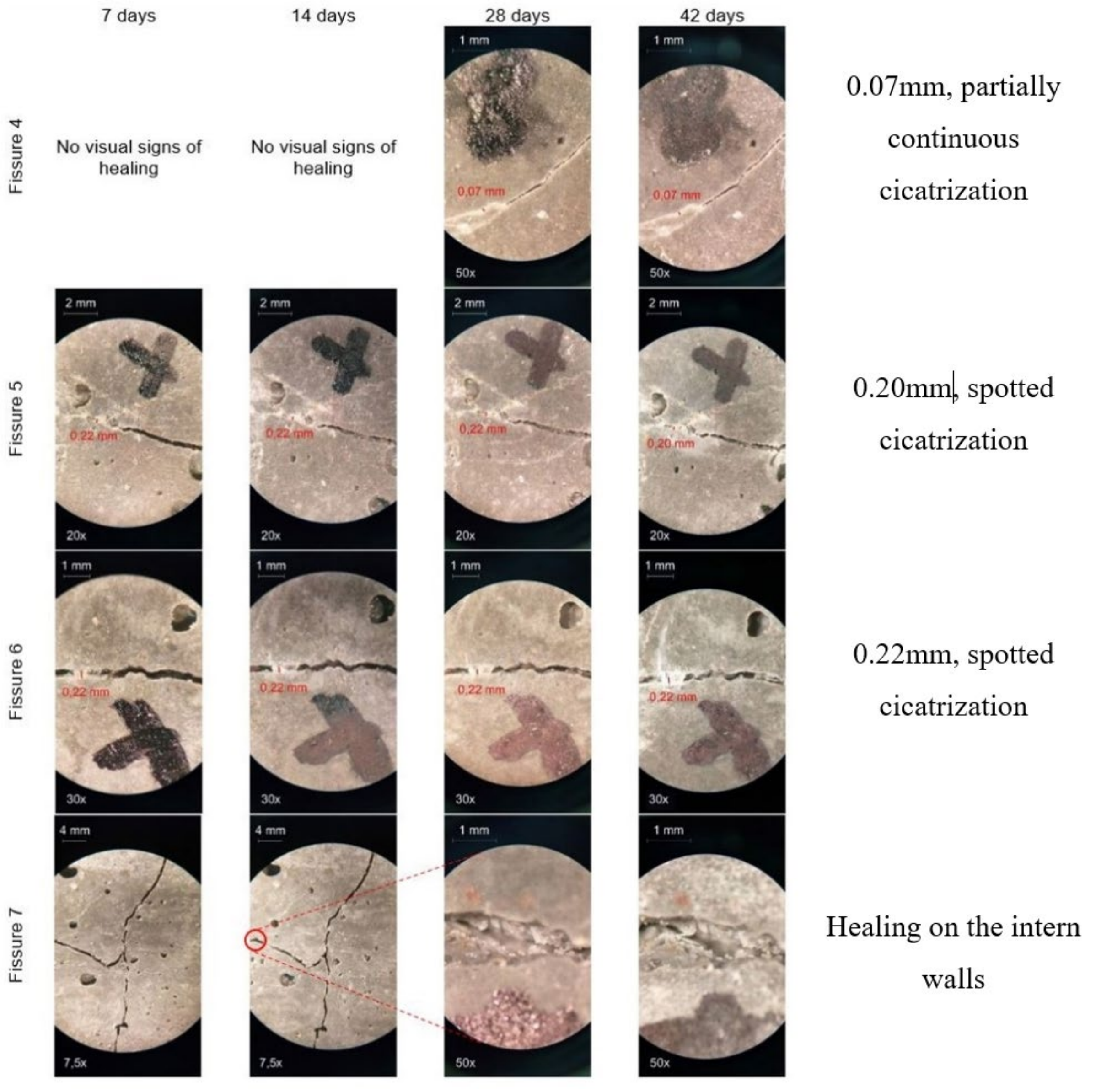

Figure 9 – Self-healing activity of sample BAC.7 at several ages

Fissure 4 did not present evidence of healing at 7 days and 14 days so there are no images associated with these ages. The healing in sample BAC.7 occurred in a similar fashion to sample BAC.6: namely, there were observable appearances of products in the fissures but, after a certain age, no further healing evolution. Figure 10 shows the results from sample BAC.8, designated fissure 8 through 11.

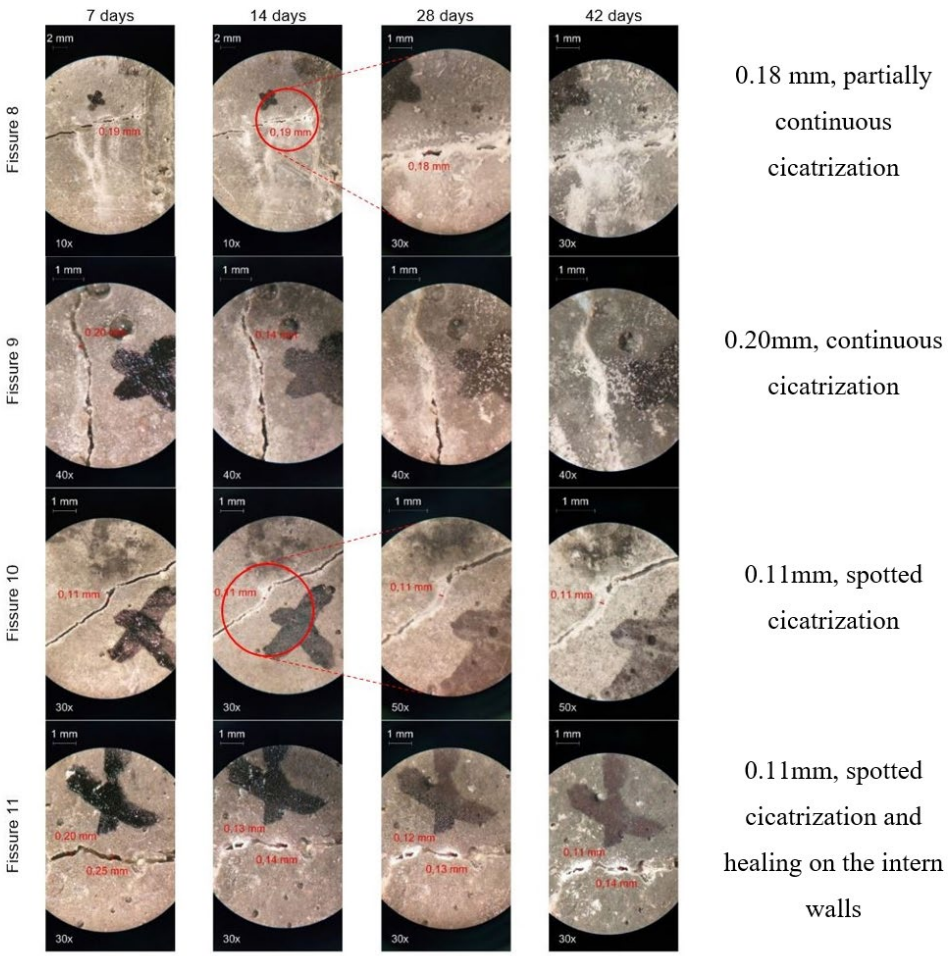

Figure 10 – Self-healing activity of sample BAC.8 at several ages

Unlike previous samples, BAC.8 presented an expressive healing evolution from 7 days to 42 days. Similar evolutions were observed in other studies [15], [27]. Healing was also observed to appear along the entire length of the fissure, which made the BAC.8 sample the most efficient of the samples tested in this study, with a maximum width of fissure healed of 0.20 mm. It should also be noted that not only concentrations of healing product were detected in the fissure but further calcite deposits were observed on the surface – a behavior observed by Zhang et al. [15]. Table 4 presents the results of the visual analysis.

Table 4 – Synthesis of visual analysis results

Sample	Fissure	Maximum healed width, mm	Type of healing
BAC.6	1	0.15	Spotted
	2	0.22	Spotted
	3	0.46	Spotted
BAC.7	4	0.07	Partially continuous
	5	0.22	Spotted
	6	0.22	Spotted
	7	0.00	Starting healing on the walls
BAC.8	8	0.19	Partially continuous
	9	0.20	Continuous
	10	0.11	Spotted
	11	0.11	Spotted*

*There was no total closure of the fissure width. The reported value is the difference between the initial and final widths.

The maximum fissure width healed was 0.46 mm for BAC.6, which was an exceptional value with respect to the other samples. The remaining samples had maximum healed fissure widths between 0.20 mm and 0.22 mm regardless of the composition. Comparing the results of this study with reference works, encapsulated in EP and coated in cement obtained a maximum healing width of 0.4 mm *B. cohnii* but most healed fissures were below 0.3 mm [27]. Similarly, *B. cohnii* encapsulated in EP but coated in geopolymer obtained a maximum healing width of 0.8 mm while also presenting higher efficiency for fissures up to 0.3 mm in width [15]. The differences observed between the studies may be related to the genus of bacteria or the type of coating. In the case of Jiang et al. [27], an alternative coating of magnesium potassium phosphate cement was able to heal a fissure 1.24 mm wide.

Besides differences in composition between samples, an aspect of extreme importance for healing to occur was the EP distribution inside the matrix. Accordingly, visual analysis of this study did not indicate a relation between the aspect of the fissure and the type of healing, further reinforcing that aggregate dispersion may be the single most relevant factor. This consideration was also postulated in De Koster et al. [71]. Scanning electronic microscopy (SEM) was used to obtain the EP and micro-structure shown in Figure 11.

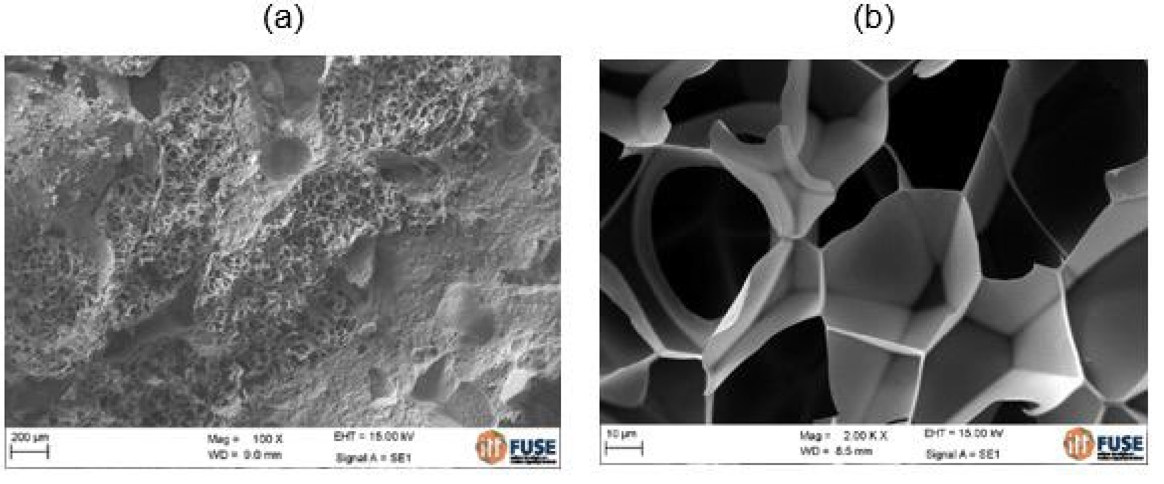

Figure 11 – SEM of a slice of EP at magnifications of (a) 100x and (b) 2,000x

It could be observed that a great quantity of void spaces was present inside the aggregate, in opposite contrast to a compact cementitious matrix. Pores were measured to have dimensions in the order of 10 µm to 40 µm. Since *B. subtilis* AP91 spores had known approximate diameters of 1 µm [35] this demonstrated that the aggregate had sufficient space for encapsulation. However, bacterial spores were not seen inside EP in Figure 11. This could be explained as: (a) the EP cut used for SEM was too far from the surface of the aggregate at a depth at which bacteria might not have been absorbed (b) sample preparation required cutting and water from the cutting disk inevitably reached the test sample and may washing away of the micro-organisms from the EP.

Scanning electronic microscopy of EP impregnated with *B. cohnii* was also conducted by Jiang et al. [27] and bacterial spore were observed. Spore distribution, however, was not homogeneous within the aggregate. This result highlighted the need of more studies to determine the total bacterial impregnation effectiveness. Otherwise, bacteria would be limited to void spaces located around the external part of the aggregate with considerable impact on the chosen EP granulometry to be used. To this end, an energy dispersion spectroscopy (EDS) was performed in the samples of this study before and after spraying of calcium lactate. Results are shown in Figures 12a and 12b and the percentage of elements detected is shown in Table 5.

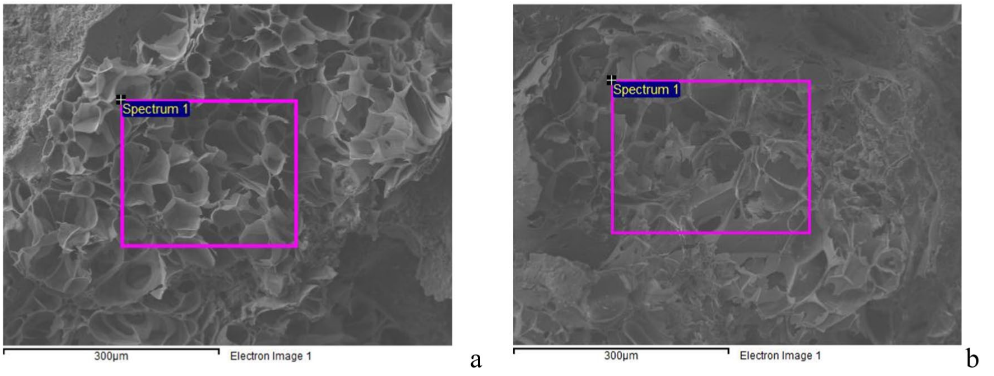

Figure 12 – Target region analysed (a) EP capsule in mortar for EDS analysis (b) EP grain without impregnation with bacterial solution or coating for EDS analysis

Table 5 – Percentage of elements found through EDS in the samples

Element	EP with calcium lactate, %		EP without bacterial solution or coating, %	
	Weight	Atomic	Weight	Atomic
O	41.91	57.85	43.05	57.65
Na	1.96	1.88	2.27	2.12
Al	5.79	4.74	7.18	5.70
Si	33.41	26.27	40.70	31.04
K	8.57	4.84	4.76	2.61
Ca	7.09	3.91	0.62	0.33
Fe	1.26	0.50	1.41	0.54
Total	100.00		100.00	

Table 5 allows a chemical comparison between samples. It was clear that the EP sample sprayed with calcium lactate yielded a percentage of calcium 11x higher in its composition compared with the untreated EP grain. This indicated a successful absorption of the bacterial solution in the light aggregate.

Figure 13 displays images from micro-computed tomography (μCT) at the sample.

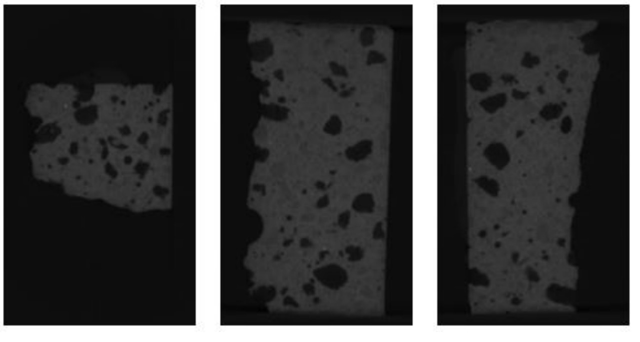

Figure 13 – μCT images of all 3 planes of a sample

It could be seen that EP distribution inside the cementitious matrix was fairly homogeneous. Despite the differences in mass percentage of each material, there were no large accumulations or lack of aggregates throughout the planes. This EP distribution was significant since, in the case of a fissure, there should be a higher probability of rupture of capsules and subsequent release of healing product [6], [72], [73].

4. CONCLUSIONS

Strength resistance of the samples of this study denoted that the concentration of the bacterial solution encapsulated in the cementitious matrix did not affect performance. This was probably due to the lack of micro-organism activity since the samples were not fissured and no capsule rupture likely. Capillary absorption of water comparison across samples with varying levels of healing agent yielded a reduction in absorption after 42 days of healing. Sample BAC.8 obtained the largest reduction in absorption, 43.45%, while also presenting the highest visual efficiency with healing along the length of fissures, and thus, it is noticed its superior performance among others, considering the durability potential due to low absorption and its efficiency related to healing product formation. However, the width of fissure healed was equivalent in all samples with a maximum value of 0.22 mm and a single outlier result of 0.46 mm. Microanalysis of EP inserted in the cementitious matrix observed void spaces with adequate dimensions to hold bacterial spores. Further SEM/EDS analysis confirmed effective EP impregnation with calcium lactate spraying. Samples presented a uniform EP distribution within the matrix which increased the probability that, upon formation of a fissure, capsule rupturing would be likely and healing agent released.

Overall, it could be concluded that the concentration of *B. subtilis* AP91 bacterial solution encapsulated in EP and coated in Portland cement did not affect the width of fissure healed. However, concentration did appear to have an effect in the length of fissure healed. It was unclear if the lower effectiveness of lower concentration samples was a result of the number of cells present lack of nutrients for bio-mineralization of calcium carbonate or uneven EP distribution in the cementitious matrix.

For this material to become viable on a large scale, both in financial and executive terms, conditions of use of bacterial solutions with less preparation must be evaluated, for example, invest in encapsulating the solution only by immersion, or analyze its use directly in the mixture water.

REFERENCES

[1] P. Patel, "Helping concrete heal itself," *ACS Cent. Sci.*, vol. 1, no. 9, pp. 470–472, 2015, http://dx.doi.org/10.1021/acscentsci.5b00376.

[2] A. Carmona Fo. and T. G. Carmona, *Fissuração nas Estruturas de Concreto*. Mérida, México: ALCONPAT, 2013.

[3] M. Chemrouk, "The deteriorations of reinforced concrete and the option of high performances reinforced concrete," *Procedia Eng.*, vol. 125, pp. 713–724, 2015, http://dx.doi.org/10.1016/j.proeng.2015.11.112.

[4] V. M. John, "Concreto sustentável," in *Concreto: Ciência e Tecnologia*, G. C. Isaia, Ed. São Paulo, Brasil: IBRACON, 2011, pp. 1843–1869.

[5] J. G. J. O. Olivier, G. Janssens-Maenhout, M. Muntean, and J. A. H. W. Peters, *Trends in Global CO_2 Emissions: 2014 Report.* Hague, Netherlands: PBL, 2014.

[6] V. C. Li and E. Herbert, "Robust self-healing concrete for sustainable infrastructure," *J. Adv. Concr. Technol.*, vol. 10, pp. 207–218, 2012., http://dx.doi.org/10.3151/jact.10.207.

[7] S. Sangadji, "Porous network concrete a bio-inspired building component o make concrete structures self-healing," Ph.D. dissertation, Institut Teknologi Bandung, Bandung, Indonesia, 2015.

[8] D. Gardner, R. Lark, T. Jefferson, and R. Davies, "A survey on problems encountered in current concrete construction and the potential benefits of self-healing cementitious materials," *Case Stud. Constr. Mater.*, vol. 8, pp. 238–247, 2018, http://dx.doi.org/10.1016/j.cscm.2018.02.002.

[9] W. Celadyn, "Durability of buildings and sustainable architecture," *Czas. Tech.*, vol. 7A, pp. 17–26, 2014.

[10] V. Wiktor and H. M. Jonkers, "Quantification of crack-healing in novel bacteria-based self-healing concrete," *Cement Concr. Compos.*, vol. 33, pp. 763–770, 2011, http://dx.doi.org/10.1016/j.cemconcomp.2011.03.012.

[11] H. Huang, G. Ye, C. Qian, and E. Schlangen, "Self-healing in cementitious materials: materials, methods and service conditions," *Mater. Des.*, vol. 92, pp. 499–511, 2016, http://dx.doi.org/10.1016/j.matdes.2015.12.091.

[12] J. Timerman, "Reabilitação e reforço de estruturas de concreto," in *Concreto: Ciência e Tecnologia*, G. C. Isaia, Ed., São Paulo, Brasil: IBRACON, 2011, pp. 1175–1209.

[13] K. van Breugel "Is there a market for self-healing cement-based materials?," *First Int. Conf. Self Heal. Mater*. Noordwijk aan Zee, The Netherlands, April 2007, pp. 1–9.

[14] L. Ferrara et al., "Experimental characterization of the self-healing capacity of cement based materials and its effects on the material performance: a state of the art report by COST Action SARCOS WG2," *Constr. Build. Mater.*, vol. 167, pp. 115–142, 2018, http://dx.doi.org/10.1016/j.conbuildmat.2018.01.143.

[15] J. Zhang et al., "Immobilizing bacteria in expanded perlite for the crack self-healing in concrete," *Constr. Build. Mater.*, vol. 148, pp. 610–617, 2017, http://dx.doi.org/10.1016/j.conbuildmat.2017.05.021.

[16] S. Krishnapriya, D. L. V. Babu, and G. P. Arulraj, "Isolation and identification of bacteria to improve the strength of concrete," *Microbiol. Res.*, vol. 174, pp. 48–55, 2015, http://dx.doi.org/10.1016/j.micres.2015.03.009.

[17] P. K. Mehta and P. J. M. Monteiro, *Concreto Microestrutura, Propriedades e Materiais*, 2nd ed. São Paulo: IBRACON, 2014.

[18] H. W. Reinhardt and M. Jooss, "Permeability and self-healing of cracked concrete as a function of temperature and crack width," *Cement Concr. Res.*, vol. 33, no. 7, pp. 981–985, 2003, http://dx.doi.org/10.1016/S0008-8846(02)01099-2.

[19] M. S. Reddy, V. Achal, and A. Mukherjee "Microbial concrete, a wonder metabolic product that remediates the defects in building structures," in *Microorganisms in Environmental Management: Microbes and Environment*, T. Satyanarayana, B. N. Johri and A. Prakash, Eds., Dordrecht: Springer Netherlands, 2012, pp. 547–568.

[20] E. Schlangen, N. ter Heide, and K. van Breugel "Crack healing of early age cracks in concrete," in *Measuring, Monitoring and Modeling Concrete Properties*, M. S. Konsta-Gdoutos, Ed., Dordrecht: Springer Netherlands, 2007, p. 273–284.

[21] A. Alyousif, "Self-healing capability of engineered cementitious composites incorporating different types of pozzolanic materials," Ph.D. dissertation, Ryerson University, Toronto, Canada, 2016.

[22] M. Şahmaran and V. C. Li, "Durability properties of micro-cracked ECC containing high volumes fly ash," *Cement Concr. Res.*, vol. 39, no. 11, pp. 1033–1043, 2009, http://dx.doi.org/10.1016/j.cemconres.2009.07.009.

[23] R. Alghamri, A. Kanellopoulos, and A. Al-Tabbaa, "Impregnation and encapsulation of lightweight aggregates for self-healing concrete," *Constr. Build. Mater.*, vol. 124, pp. 910–921, 2016., http://dx.doi.org/10.1016/j.conbuildmat.2016.07.143.

[24] H. Afifudin, W. Nadzarah, M. S. Hamidah, and H. Noor Hana, "Microbial participation in the formation of Calcium Silicate Hydrated (CSH) from Bacillus subtilis," *Procedia Eng.*, vol. 20, pp. 159–165, 2011, http://dx.doi.org/10.1016/j.proeng.2011.11.151.

[25] J. Y. Wang, D. Snoeck, S. Van Vlierberghe, W. Verstraete, and N. De Belie, "Application of hydrogel encapsulated carbonate precipitating bacteria for approaching a realistic self-healing in concrete," *Constr. Build. Mater.*, vol. 68, pp. 110–119, 2014, http://dx.doi.org/10.1016/j.conbuildmat.2014.06.018.

[26] S. Gupta, S. D. Pang, and H. W. Kua, "Autonomous healing in concrete by bio-based healing agents: a review," *Constr. Build. Mater.*, vol. 146, pp. 419–428, Aug 2017, http://dx.doi.org/10.1016/j.conbuildmat.2017.04.111.

[27] L. Jiang, G. Jia, C. Jiang, and Z. Li, "Sugar-coated expanded perlite as a bacterial carrier for crack-healing concrete applications," *Constr. Build. Mater.*, vol. 232, 2020, http://dx.doi.org/10.1016/j.conbuildmat.2019.117222.

[28] S. A. K. Zai and M. K. Murthy, "Self healing concrete," *J. Civ. Eng. Environ. Technol.*, vol. 2, no. 16, pp. 27–33, 2015.

[29] M. T. Madigan, J. M. Martinko, K. S. Bender, D. H. Buckley, and D. A. Stahl *Microbiologia de Brock*, 14th ed. Porto Alegre: Grupo A Educação S.A., 2016.

[30] K. Vijay, M. Murmu, and S. V. Deo, "Bacteria based self healing concrete: a review," *Constr. Build. Mater.*, vol. 152, pp. 1008–1014, 2017, http://dx.doi.org/10.1016/j.conbuildmat.2017.07.040.

[31] V. Müller, F. Pacheco, and B. Tutikian, "Técnicas e metodologias de biomineralização na cicatrização de fissuras do concreto," *Rev. Arquitetura IMED*, vol. 8, no. 2, pp. 164–182, 2019, http://dx.doi.org/10.18256/2318-1109.2019.v8i2.3679.

[32] F. Pacheco, "Análise da eficácia dos mecanismos de autocicatrização do concreto," Ph.D. dissertation, Universidade do Vale do Rio dos Sinos, São Leopoldo, Brasil, 2020.

[33] H. M. Jonkers, A. Thijssen, G. Muyzer, O. Copuroglu, and E. Schlangen, "Application of bacteria as self-healing agent for the development of sustainable concrete," *Ecol. Eng.*, vol. 36, no. 2, pp. 230–235, 2010, http://dx.doi.org/10.1016/j.ecoleng.2008.12.036.

[34] M. Alazhari, T. Sharma, A. Heath, R. Cooper, and K. Paine, "Application of expanded perlite encapsulated bacteria and growth media for self-healing concrete," *Constr. Build. Mater.*, vol. 160, pp. 610–619, Jan 2018, http://dx.doi.org/10.1016/j.conbuildmat.2017.11.086.

[35] H. M. Jonkers, "Bacteria-based self-healing concrete," *Frankfurter Afrikanistische Blatter*, vol. 8, no. 1, pp. 49–79, 2011.

[36] H. M. Jonkers and A. Thijssen "Bacteria mediated remediation of concrete strutures," in *2nd Int. Symp. Serv. Life Des. Infrastruct.*, October 2010, pp. 833–840.

[37] E. Tziviloglou, V. Wiktor, H. M. Jonkers, and E. Schlangen, "Bacteria-based self-healing concrete to increase liquid tightness of cracks," *Constr. Build. Mater.*, vol. 122, pp. 118-125, 2016, http://dx.doi.org/10.1016/j.conbuildmat.2016.06.080.

[38] J. Wang, J. Dewanckele, V. Cnudde, S. Van Vlierberghe, W. Verstraete, and N. De Belie, "X-ray computed tomography proof of bacterial-based self-healing in concrete," *Cement Concr. Compos.*, vol. 53, pp. 289–304, 2014, http://dx.doi.org/10.1016/j.cemconcomp.2014.07.014.

[39] J. Y. Wang, H. Soens, W. Verstraete, and N. De Belie, "Self-healing concrete by use of microencapsulated bacterial spores," *Cement Concr. Res.*, vol. 56, pp. 139–152, 2014, http://dx.doi.org/10.1016/j.cemconres.2013.11.009.

[40] W. De Muynck, K. Cox, N. De Belie, and W. Verstraete, "Bacterial carbonate precipitation as an alternative surface treatment for concrete," *Constr. Build. Mater.*, vol. 22, no. 5, pp. 875–885, 2008, http://dx.doi.org/10.1016/j.conbuildmat.2006.12.011.

[41] R. Pei, J. Liu, S. Wang, and M. Yang, "Use of bacterial cell walls to improve the mechanical performance of concrete," *Cement Concr. Compos.*, vol. 39, pp. 122–130, 2013, http://dx.doi.org/10.1016/j.cemconcomp.2013.03.024.

[42] M. Alazhari, T. Sharma, A. Heath, R. Cooper, and K. Paine, "Application of expanded perlite encapsulated bacteria and growth media for self-healing concrete," *Constr. Build. Mater.*, vol. 160, pp. 610–619, 2017, http://dx.doi.org/10.1016/j.conbuildmat.2017.11.086.

[43] J. Wang, K. Van Tittelboom, N. De Belie, and W. Verstraete, "Use of silica gel or polyurethane immobilized bacteria for self-healing concrete," *Constr. Build. Mater.*, vol. 26, no. 1, pp. 532–540, 2012, http://dx.doi.org/10.1016/j.conbuildmat.2011.06.054.

[44] J. Wang, H. M. Jonkers, N. Boon, and N. De Belie, "Bacillus sphaericus LMG 22257 is physiologically suitable for self-healing concrete," *Appl. Microbiol. Biotechnol.*, vol. 101, no. 12, pp. 5101–5114, 2017, http://dx.doi.org/10.1007/s00253-017-8260-2.

[45] J. Xu and X. Wang, "Self-healing of concrete cracks by use of bacteria-containing low alkali cementitious material," *Constr. Build. Mater.*, vol. 167, pp. 1–14, 2018, http://dx.doi.org/10.1016/j.conbuildmat.2018.02.020.

[46] N. Schwantes-Cezario, L. P. Medeiros, A. G. De Oliveira, G. Nakazato, R. Katsuko Takayama Kobayashi, and B. M. Toralles, "Bioprecipitation of calcium carbonate induced by Bacillus subtilis isolated in Brazil," *Int. Biodeterior. Biodegradation*, vol. 123, pp. 200–205, 2017., http://dx.doi.org/10.1016/j.ibiod.2017.06.021.

[47] A. F. Alshalif, J. M. Irwan, N. Othman, and L. H. Anneza "Isolation of Sulphate Reduction Bacteria (SRB) to improve compress strength and water penetration of bio-concrete," *MATEC Web Conf.*, vol. 47, July 2016, pp. 01016.

[48] G. Souradeep and H. W. Kua, "Encapsulation technology and techniques in self-healing concrete," *J. Mater. Civ. Eng.*, vol. 25, pp. 864–870, October 2016, http://dx.doi.org/10.1061/(ASCE)MT.1943-5533.

[49] K. Sisomphon, O. Copuroglu, and A. Fraaij, "Application of encapsulated lightweight aggregate impregnated with sodium monofluorophosphate as a self-healing agent in blast furnace slag mortar," *Heron*, vol. 56, no. 1–2, pp. 17–36, 2011.

[50] A. Sidiq, R. Gravina, and F. Giustozzi, "Is concrete healing really efficient? A review," *Constr. Build. Mater.*, vol. 205, pp. 257–273, 2019, http://dx.doi.org/10.1016/j.conbuildmat.2019.02.002.

[51] K. Van Tittelboom et al., "Comparison of different approaches for self-healing concrete in a large-scale lab test," *Constr. Build. Mater.*, vol. 107, pp. 125–137, 2016, http://dx.doi.org/10.1016/j.conbuildmat.2015.12.186.

[52] R. Davies, T. Jefferson, and D. Gardner, "Development and testing of vascular networks for self-healing cementitious materials," *J. Mater. Civ. Eng.*, vol. 33, no. 7, pp. 1–15, 2021, http://dx.doi.org/10.1061/(asce)mt.1943-5533.0003802.

[53] N. Schwantes-Cezario, G. S. F. Nogueira, and B. M. Toralles, "Biocimentação de compósitos cimentícios mediante adição de esporos de Bacillus subtilis AP91," *Rev. Eng. Civ. IMED*, vol. 4, no. 2, pp. 142–158, 2017, http://dx.doi.org/10.18256/2358-6508.2017.v4i2.2072.

[54] N. Schwantes-Cezario, M. F. Porto, G. F. B. Sandoval, G. F. N. Nogueira, A. F. Couto, and B. M. Toralles, "Effects of Bacillus subtilis biocementation on the mechanical properties of mortars," *Rev. IBRACON Estrut. Mater.*, vol. 12, no. 1, pp. 31–38, 2019, http://dx.doi.org/10.1590/s1983-41952019000100005.

[55] American Society for Testing and Materials, *ASTM C33/C33M - Standard Specification for Concrete Aggregates*, 2018.

[56] American Society for Testing and Materials, *ASTM C595/C595M - Standard Specification for Blended Hydraulic Cements*, 2020.

[57] American Society for Testing and Materials, *ASTM D5550 - Standart Test Method for Specific Gravity of Soil Solids by Gas Pycnometer*, 2014.

[58] American Society for Testing and Materials, *ASTM C128 - Standard Test Method for Relative Density (Specific Gravity) and Absorption of Fine Aggregate*, 2015.

[59] American Society for Testing and Materials, *ASTM C29/C29M - Standard Test Method for Bulk Density ('Unit Weight') and Voids in Aggregate*, 2017.

[60] K. M. J. Swanson, R. L. Petran, and J. H. Hanlin "Culture methods for enumeration of microorganisms," in *Compendium of Methods for the Microbiological Examination of Foods*, 4th ed., F. P. Downes and K. Ito, Eds. Washington, DC, United States: APHA, 2001, pp. 53–62.

[61] American Society for Testing and Materials, *ASTM C31/C31M - Standard Practice for Making and Curing Concrete Test Specimens in the Field* 2019.

[62] American Society for Testing and Materials, *ASTM C348 - Standard Test Method for Flexural Strength of Hydraulic-Cement Mortars*, 2020.

[63] R. Alghamri, A. Kanellopoulos, and A. Al-Tabbaa, "Impregnation and encapsulation of lightweight aggregates for self-healing concrete," *Constr. Build. Mater.*, vol. 124, pp. 910–921, 2016, http://dx.doi.org/10.1016/j.conbuildmat.2016.07.143.

[64] RILEM TC 116-PCD, "Permeability of concrete as a criterion of its durability," *Mater. Struct.*, vol. 32, pp. 174–179, 1999.

[65] American Society for Testing and Materials, *ASTM C39/C39M - Standard Test Method for Compressive Strength of Cylindrical Concrete Specimens*, 2020.

[66] M. M. Pelletier, R. Brown, A. Shukla, and A. Bose, "Self-healing concrete with a microencapsulated healing agent," *Cement Concr. Res.*, 2011.

[67] R. Siddique et al., "Effect of bacteria on strength, permeation characteristics and micro-structure of silica fume concrete," *Constr. Build. Mater.*, vol. 142, pp. 92–100, 2017, http://dx.doi.org/10.1016/j.conbuildmat.2017.03.057.

[68] B. Hilloulin, D. Hilloulin, F. Grondin, A. Loukili, and N. De Belie, "Mechanical regains due to self-healing in cementitious materials: Experimental measurements and micro-mechanical model," *Cement Concr. Res.*, vol. 80, pp. 21–32, 2016, http://dx.doi.org/10.1016/j.cemconres.2015.11.005.

[69] W. Khaliq and M. B. Ehsan, "Crack healing in concrete using various bio influenced self-healing techniques," *Constr. Build. Mater.*, vol. 102, pp. 349–357, 2016, http://dx.doi.org/10.1016/j.conbuildmat.2015.11.006.

[70] J. Parks, M. Edwards, P. Vikesland, and A. Dudi, "Effects of bulk water chemistry on autogenous healing of concrete," *J. Mater. Civ. Eng.*, vol. 22, no. 5, pp. 515–524, 2010, http://dx.doi.org/10.1061/(ASCE)MT.1943-5533.0000082.

[71] S. A. L. De Koster, R. M. Mors, H. W. Nugteren, H. M. Jonkers, G. M. H. Meesters, and J. R. Van Ommen, "Geopolymer coating of bacteria-containing granules for use in self-healing concrete," *Procedia Eng.*, vol. 102, pp. 475–484, 2015, http://dx.doi.org/10.1016/j.proeng.2015.01.193.

[72] A. Al-Tabbaa, C. Litina, P. Giannaros, A. Kanellopoulos, and L. Souza, "First UK field application and performance of microcapsule-based self-healing concrete," *Constr. Build. Mater.*, vol. 208, pp. 669–685, 2019., http://dx.doi.org/10.1016/j.conbuildmat.2019.02.178.

[73] D. Snoeck, J. Dewanckele, V. Cnudde, and N. De Belie, "X-ray computed microtomography to study autogenous healing of cementitious materials promoted by superabsorbent polymers," *Cement Concr. Compos.*, vol. 65, pp. 83–93, 2016, http://dx.doi.org/10.1016/j.cemconcomp.2015.10.016.

Author contributions: VM: experimental procedure, materials characterization, writing; FP: experimental procedure, writing, revising; CMC: experimental procedure, materials characterization; FF: experimental procedure, materials characterization; VHV: writing, revising; RCEM: writing, revising; HZE: writing, revising ; BFT: supervision, revising, formal analysis.

Editors: Mark Alexander, Guilherme Aris Parsekian.

Rev. IBRACON Estrut. Mater., vol. 15, no. 4, e15405, 2022

IBRACON Structures and Materials Journal
Revista IBRACON de Estruturas e Materiais
ISSN 1983-4195 ismj.org

ORIGINAL ARTICLE

Exploratory study for the alkaline activation of basalt powder as a supplementary cementitious matrix

Estudo exploratório para ativação alcalina de pó basáltico como uma matriz cimentícia suplementar

Rafael Gheller[a]
Luciano Luiz Silva[a]
Márcio Antônio Fiori[a]
Eduardo Roberto Batiston[a]

[a]Universidade Comunitária da Região de Chapecó – UNOCHAPECÓ, Department of Civil Engineering, Chapecó, SC, Brasil

Received 26 July 2021
Accepted 02 December 2021

Abstract: Portland cement remains the main material of choice in construction due to its thermal, mechanical and durability properties. However, there is growing concern about the large amount of energy consumed and the environmental pollution generated during its production. The objective of this study, therefore, was to evaluate the potential of the fine residual material produced by crushing basalt rocks to form a supplementary cementitious matrix through alkaline activation. Basalt powder with a particle size of less than 53µm was prepared and activated with a sodium hydroxide solution, with a sodium silicate solution as an adjuvant. The curing process of the material was also carried out at 5 temperature levels, 75, 85, 100, 115, 125°C, according to the experimental design. The paste was dry curing at a standard digital laboratory oven for 24 hours. After curing, the compressive strength of the material was evaluated, reaching a mean value of 10.21 MPa for the H5S15T125 mixture at 28 days. The microstructure analysis was performed by X-ray microtomography, presenting the reconstruction of the internal pores and cracks, leading to the conclusion that higher curing temperatures formed more porous matrices, although with more strength. Based on the collected data, the statistical analysis of the design was performed showing that sodium hydroxide and temperature have a statistically significant effect on the response variable compressive strength. As such, the alkali-activation of basalt powder can potentially produce a cementitious material of moderate strength, giving purpose to the residue and reducing the emission of harmful particles into the atmosphere.

Keywords: basalt, geopolymer, alkali-activated materials, cement.

Resumo: O cimento Portland continua sendo o principal material de escolha na construção civil, devido às suas propriedades térmicas, mecânicas e de durabilidade. No entanto, há uma crescente preocupação com a grande quantidade de energia consumida e a poluição ambiental gerada durante sua produção. Dessa forma, a presente pesquisa buscou avaliar o potencial do material residual fino produzido pela britagem de rochas basálticas através da ativação alcalina, para formar uma matriz cimentícia suplementar. O pó do basalto com tamanho de partículas menor que 53µm foi preparado e ativado com solução de hidróxido de sódio, tendo como coadjuvante a solução silicato de sódio. O material também teve o processo de cura realizado em 5 níveis de temperatura, 74,8, 85, 100, 115, 125,2°C conforme o delineamento experimental. Depois de curado o material teve a resistência à compressão avaliada, atingindo valor médio de 10,21 MPa para a mistura H5S15T125. A análise da microestrutura foi realizada através da microtomografia de raios X, apresentando a reconstrução dos poros e fissuras presentes internamente, concluindo que temperaturas de cura mais altas formaram matrizes mais porosas, embora com mais resistência. A partir dos dados coletados foi realizada a análise estatística do planejamento apresentando que hidróxido de sódio e a temperatura apresentam efeito estatisticamente significativo na variável resposta resistência à compressão. Portanto, é possível através da

Corresponding author: Rafael Gheller. E-mail: gheller@unochapeco.edu.br
Financial support: Institutional scholarship offered by the Universidade Comunitária da Região de Chapecó - Unochapecó.
Conflict of interest: Nothing to declare.
Data Availability: The data that support the findings of this study are available from the corresponding author, [RG], upon reasonable request."SciELO Data" is available at https://data.scielo.org/ if the authors wish to deposit Data at this multidisciplinary repository.

This is an Open Access article distributed under the terms of the Creative Commons Attribution License, which permits unrestricted use, distribution, and reproduction in any medium, provided the original work is properly cited.

álcali-ativação do pó de basalto produzir um material cimentício de resistência moderada, dando finalidade ao resíduo e diminuído a emissão de partículas nocivas à atmosfera.

Palavras-chave: basalto, geopolímero, materiais álcali-ativados, cimento.

How to cite: R. Gheller, L. L. Silva, M. A. Fiori, and E. R. Batiston, "Exploratory study for the alkaline activation of basalt powder as a supplementary cementitious matrix," *Rev. IBRACON Estrut. Mater.*, vol. 15, no. 4, e15405, 2022, https://doi.org/10.1590/S1983-41952022000400005

1 INTRODUCTION

Civil construction uses several natural resources of the most varied types, and it generates great environmental impacts. However, it is a sector with room for technological innovation, be it in modern construction techniques or – especially - in high-performance materials. As such, new sources of raw material must be studied and used, was they could improve results in relation to performance and returns, consequently contributing to environmental issues.

From the perspective of reducing environmental impacts, it is known that Portland Cement is a major generator of harmful particles during its production. There is growing concern, therefore, about the large amount of energy consumed and the environmental pollution generated during its production. Research data from Rashad and Zeedan [1] reveal that for every ton of cement produced, approximately 0.8 tons of carbon dioxide are generated. The search for alternative cement materials that can reduce energy consumption and pollution has therefore become an important focus in several studies on this topic [2].

Unlike Portland cement, geopolymers are binders produced by the alkaline activation of aluminosilicate. These geopolymers tend to have similar performance as Portland cement and they are considered the most promising alternative for its replacement [3].

Alkaline activation is the synthesis reaction of the geopolymers. It is the hydration of aluminosilicates with alkaline or alkaline-earth substances, and there may be several aluminosilicate materials susceptible to this type of reaction [4]. Currently, most studies involving geopolymers look at materials such as blast furnace slag, fly ash and metakaolin [5]. However, new materials have been gaining attention in the research of new precursors, such as basalt [6]–[8].

In this sense, basalt is considered a potential raw material for the production of geopolymers, with essential elements for the alkali-activation process, the presence of silica and alumina in high levels, and, in some cases, with considerable amounts of vitreous material [6]–[10].

Basalts constitute the most common type of rock found on the Earth's surface. It is a volcanic igneous rock that covers about 70% of the planet's surface, and it's considered an industrial raw material with high potential due to its large-scale availability, high homogeneity, low impurities, high chemical stability, recyclability and non-toxic reactivity with water and air [11].

This material is widely consumed in civil construction, mainly as aggregate in concretes and for the foundation formation in pavements. Its processing, however, produces fine material residues that end up limiting some parameters of its use based on the Brazilian NBR 7211 standard [12], turning the powdery material into an unwanted waste for mining operations.

Studies by Drago et al. [13] have estimated that the amount of powdery material with a diameter of less than 0.075 mm in industrial sand is 7% to 20%, and this material is extracted in the washing method and generally goes unused in the crushing plant operation. These values represent a significant volume of fine material that could be susceptible to new applications.

In addition, the particle size reduced by grinding increases the reactivity of basalt due to the increase in its surface area. This makes basalt a promising material for the production of special cements by means of the alkali-activation process [6], [7], [11].

The improvement of a cementitious matrix is closely related to the microstructure of the material. Tortuous microstructures with narrow, isolated pores inhibit the diffusion of aggressive substances through the matrix, especially acids, carbonates or chlorides. Understanding the microstructural characteristics of the binder is therefore of vital importance to enable the incorporation of the alkali activation technology on a commercial scale [14]. The main microstructural properties of a binder include porosity, tortuosity, and the extent of pore network percolation [15], [16].

According to this problem definition, data from the National Association of Aggregate-Producing Entities for Construction (*Associação Nacional das Entidades de Produtores de Agregados para Construção*) [17] for the aggregates market reveal that in 2014 Brazil consumed the largest volume of aggregates ever, with an estimated consumption of 741 million tons of aggregates for concrete. And of this total, 302 million tons correspond to gravel, extracted mainly from magmatic rocks. This means one must think about the amount of fine material waste generated, which often ends up being deposited in the yards of the crushing units.

Although non-toxic, the fine material ends up being carried by the water due to its fineness, carrying suspended debris, causing the silting of rivers and effluents, and it can also be carried by air. Resolution No. 307 [18] allowed instruments to move towards overcoming this reality, defining responsibilities and duties and making waste management mandatory in order to mitigate the environmental impacts arising from the uncontrolled activities related to the generation, transport and destination of these materials. It also determines that generators should adopt measures to reduce the generation of waste or to look for sources of reuse or recycling.

After the precursor element, alkaline activators are the essential component in the development of alkaline cement. In general terms, the activators used in aluminosilicate-based cement materials to generate high alkalinity are alkaline hydroxides, alkaline silicates or mixtures of both. The most commonly-used alkaline reagent solutions are based on a mixture of sodium hydroxides (NaOH) or potassium hydroxide (KOH) and silicate, sodium (Na2SiO3) or potassium (K2SiO3) solutions.

Geopolymerization then occurs in alkaline solutions with aluminosilicate oxides and silicates (solid or liquid) as reagents. Synthesis occurs through a mechanism that involves the dissolution of aluminum and silicon species from the surfaces of the base materials, as well as the surface hydration of the undissolved particles. Subsequently, the polymerization of active surface groups and soluble species occurs to form a gel, which then generates a hardened geopolymer structure. In most cases, only a small amount of the silica and alumina present in particles needs to dissolve and take part in the reaction for the entire mixture to solidify [19].

The objective of this work was to contribute to an alternative use of the fine material waste extracted from basalt, making it applicable as building material by forming a cement compound through its alkali-activation, transforming it into a product that can have some added value, reducing the environmental impact and developing innovative materials for civil construction. In addition, the interaction of three variables within the experiment was evaluated to achieve a reasonable compressive strength and seek an adequate characterization routine, after which the microstructural analysis using the X-ray microtomography technique was performed.

2 MATERIALS AND EXPERIMENTAL PROGRAM

The material used was established by basalt quarry waste, from the process of comminution of aggregates for civil construction in the western region of Santa Catarina, Brazil.

From Table 1, it is possible to observe some main chemical compounds for its mineral formation.

Table 1- Chemical composition of the basalt powder

Chemical composition, in oxides (%)	
SiO2	51,553
Fe2O3	13,906
Al2O3	13,091
CaO	8,846
MgO	4,159
TiO2	3,360
Na2O	2,537
K2O	1,583
P2O5	0,435
MnO	0,190
Loss on ignition	<0,39

All the tests were carried out in controlled environments within the laboratories, evaluating the characteristics of the materials to optimize the strength of the materials, and analyzing their macro and micro structural characteristics to ensure the reliability of the experiment, following pre-established parameters to obtain the data.

Therefore, this is a 2^3 factorial design, and response surface methodology (RSM) was used to obtain the optimal mixing proportions. Geometrically, the design is a cube, with 8 different treatments. This designs allows 3 main effects (A,B,C) to be estimated together with the second-order interactions (AB, AC, BC) and one third-order interaction (ABC) [20]. Three factors were defined in the study: the cure temperature, the molarity of the NaOH solution, and the percentage of Na2SIO3 present in the alkaline solution.

The levels that each factor should be studied were specified to begin developing the research. Since it is a full 2^3 composite factorial design, it will have eight tests that make up the factorial system, six axial points and one central point.

In the experimental design, the levels of each factor are represented by codes, which alternate until all possible combinations are formed.

To form the axial points of the design, the values of "∝" are established as follows in Equation 1:

$$\propto = (2^k)^{\frac{1}{4}} => \propto = (2^3)^{\frac{1}{4}} => \propto = 1{,}681 \quad (1)$$

Where ∝= the distance, in coded units, from each axial point in the factorial design, and k= number of factors involved in the experiment.

Values +1 and -1 represent the levels of each factor and make up the factorial system. The level encoded with the numeral 0 represents intermediate values of +1 and -1, and finally +∝ and -∝ will make up the axial points of the factors addressed in the study.

As can be seen in Table 1, a specific nomenclature is given to each mixture. This code has the function of helping in the identification of the material and can be explained as follows: for example, the mixture H5S15T125 is initially represented by the letter "H", assigned to sodium hydroxide, followed by the numeral "5", used to demonstrate the molarity of the solution. Next, " S15 "represents the addition of 15% of the sodium silicate solution to the volume of the alkaline solution, and, finally, "T125" refers to the temperature, which was 125°C for this example.

A test design matrix had to be developed for the logical development of the study, so that mathematical models were applied with the collection of the results to evaluate the effects of the different mixtures established in the study. Table 2 presents the design matrix.

Table 2. Design Matrix $2^{k=3}$

Tests	Sodium hydroxide (Mol/L)	Proportion of the NaSiO solution (%)	Temperature (°C)	Point	Nomenclature
1(1)	3 (-1)	9 (-1)	85 (-1)	Factorial	H3S9T85
2 (a)	7 (1)	9 (-1)	85 (-1)	Factorial	H7S9T85
3 (b)	3 (-1)	21 (1)	85 (-1)	Factorial	H3S21T85
4 (ab)	7 (1)	21 (1)	85 (-1)	Factorial	H7S21T85
5 (c)	3 (-1)	9 (-1)	115 (1)	Factorial	H3S9T115
6 (ac)	7 (1)	9 (-1)	115 (1)	Factorial	H7S9T115
7 (bc)	3 (-1)	21 (1)	115 (1)	Factorial	H3S21T115
8 (abc)	7 (1)	21 (1)	115 (1)	Factorial	H7S21T115
9	1,6 (+α)	15 (0)	100 (0)	Star	H1,6S15T100
10	8,3 (-α)	15 (0)	100 (0)	Star	H8, 3S15T100
11	5 (0)	25 (+α)	100 (0)	Star	H5S5T100
12	5 (0)	5 (-α)	100 (0)	Star	H5S25T100
13	5 (0)	15 (0)	75 (+α)	Star	H5S15T75
14	5 (0)	15 (0)	125(-α)	Star	H5S15T125
15	5 (0)	15 (0)	100 (0)	Central	H5S15T100

The experiment based on factorial schemes involves combinations between the levels of two or more factors. The proposed model considers the effect of a constant, the linear and quadratic effect of each of the independent variables, in addition to the effect of the interaction between them, which is presented later in the table of estimated effects.

The basalt powder with each alkaline solution proposed in the statistical model were mixed for 120 seconds, the period necessary for complete homogenization of the paste. Then, the filling of the molds took place in three layers, where for each layer, 20 compression movements with a socket were applied to improve the densification and then the excess material was flattened.

All mixtures underwent thermal curing for 24 hours, at a standard digital laboratory oven, hermetically insulated so that there is no rapid loss of water, posteriorly remained at room temperature until 28 days at room temperature, at which age they were ruptured, and their compressive strength was evaluated. For each mixture, at least 4 specimens were tested to collect compressive strength data.

2.1 X-ray Microtomography

X-ray microscopy (μCT) is a recent technique that can be used in the three-dimensional reconstitution of solid materials to study crystallization processes, the origins of cracks and fissures, and the arrangement of pores and voids [21].

For this test, the samples of hardened basalt paste were prepared as disks with 5 mm thickness and 25 mm diameter and arranged in a container with silica gel and sealed to avoid moisture absorption. They were then sent to the Technological Characterization Laboratory (LCT) linked to the Department of Mining and Petroleum Engineering of the Polytechnic School of the University of São Paulo (USP).

The equipment used was the Zeiss Xradia Versa microtomograph, model XRM-510. This equipment uses the combination of a micrometric focus beam and image magnification in two stages: in the first step, the images are magnified through geometric magnification as in a conventional microtomograph; in the second step, a scintillator converts the X-rays to visible light and then magnifies the image optically through high contrast lenses, further enhancing the resolution of the sample's microstructure.

It is worth highlighting here that according to [22] it is possible to evaluate the pores through the three-dimensional reconstruction of the sample. These pores can be classified as open or closed, according to their disposition to an external fluid. Each type of pore is of influence on permeability, mechanical properties, density and conductivity. Pores can also be interconnected, further increasing the volume of voids and brittleness of the piece. In addition, surface roughness can also be considered as porosity.

In addition to the microtomography, analyzing the microstructure of the material is essential to reach conclusions about the material.

2.2. Mechanical Tests

The compressive strength test provides data on the strength of the material when subjected to controlled loads. In addition, it is possible to analyze the rupture interface and obtain data on the modulus of elasticity of the sample. The procedure of this test is adapted according to the Brazilian standard NBR 7215 [23], but since the cylindrical specimens have smaller dimensions (25 mm in diameter and 50 mm in length), the test speed and the applied force will be proportionally smaller.

The equipment used for this test was the Shimadzu Autograph AGX-Plus. For the test, a rotary joint was used to correct possible angular differences between the ends of the cylindrical specimen. A load at a constant speed of 0,03 kN/s was applied until the rupture of the geopolymer specimen. The age evaluated in the study was 28 days after molding.

Based on these data, the results were applied in the software STATISTICA, to validate the reliability of the study, presenting mathematical calculations to reveal which factors collaborated for a better performance of the material, and which levels and factors could be negligible in future research.

3 RESULTS AND DISCUSSION

3.1 Compressive Strength

The mean values for the compressive strength of each sample are presented in Table 3 for the tests in the first round and duplicate tests of the experimental design.

Table 3. Compressive strength results at 28 days

Tests	Nomenclature	Compressive strength in MPa (1st round)	Compressive strength in MPa (2nd round)
1(1)	H3S9T85	1,789	0,651
2 (a)	H7S9T85	1,759	1,959
3 (b)	H3S21T85	1,137	1,312
4 (ab)	H7S21T85	2,192	2,629
5 (c)	H3S9T115	3,190	5,567
6 (ac)	H7S9T115	7,473	6,997
7 (bc)	H3S21T115	4,441	8,292
8 (abc)	H7S21T115	7,946	5,639
9	H1,6S15T100	0,344	0,415
10	H8, 3S15T100	2,228	0,699
11	H5S5T100	4,432	2,447
12	H5S25T100	7,136	2,771
13	H5S15T75	5,431	3,504
14	H5S15T125	8,208	10,215
15	H5S15T100	4,781	2,395

The average values of compressive strength observed both in the first experiment and in the duplicate reveal that the molar variation presents maximum resistance values within the proposed range. Analytically, it is also possible to note that the increase in temperature in the two rounds of tests, contributing to the replicability and reliability of the experiment.

Using the response surface methodology to present the results, Figure 1 shows the tendency in the two-dimensional plane that - with increasing concentrations of sodium hydroxide or temperature - an increase in the compressive strength will occur, as represented by the color scale of the image.

The level curves represent the variation of compressive strength as a function of the independent variables that presented statistical significance in the study. As can be seen, the variables maintain their encoding of the design matrix and vary from -∝ up to +∝ for the evaluated points, indicated by blue circumferences.

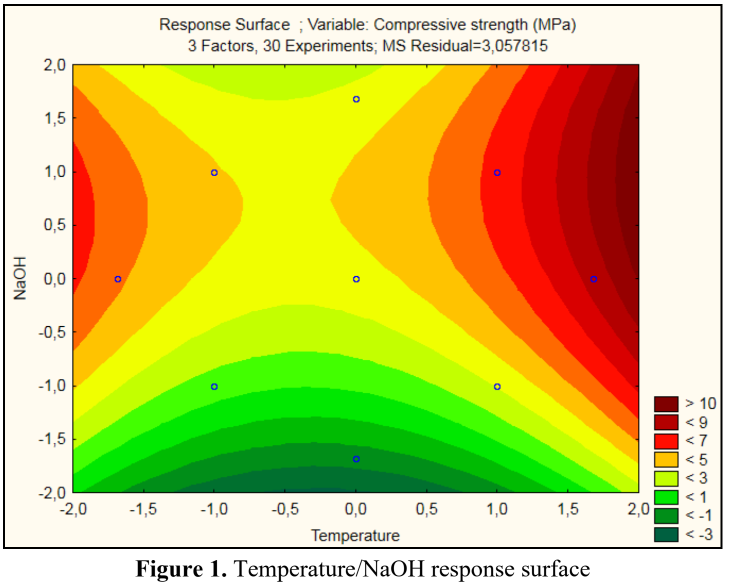

Figure 1. Temperature/NaOH response surface

Since there was no interaction between the independent variables, it is possible to make an analysis through the response surface methodology (RSM) according to each factor.

Figure 2 represents the surface three-dimensionally, where it is possible to see the curvature of the experiment effects using the quadratic equation that describes the experiment. The influence of NaOH concentration is worth highlighting at this point, which had a negative estimated effect for the quadratic effect. This phenomenon is visible on the response surface through the formation of a curvature that reaches a maximum point of the NaOH factor and soon after the strength values decrease as a function of the increase in the molarity of sodium hydroxide.

For the independent variable temperature, on the other hand, a positive or proportional correlation to compressive strength was revealed according to the proposed model and the calculation of estimated effects [6].

The variable sodium silicate did not correlate with compressive strength, so this phenomenon may be related to the chemical nature of basalt, and its subsequent use may be dispensed with.

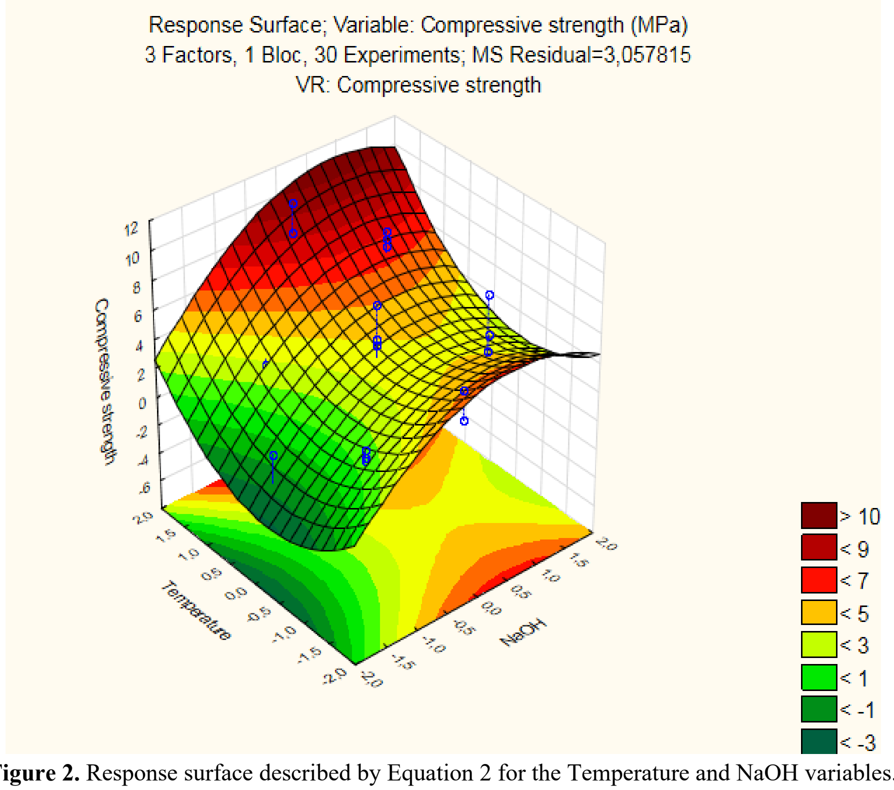

Figure 2. Response surface described by Equation 2 for the Temperature and NaOH variables.

3.2 X-ray Microtomography (µCT)

For the microstructural imaging test performed through microtomography, samples of the mixtures were chosen that showed prominence in terms of compressive strength, since they encompass different levels of independent variables. The mixtures chosen were H7S9T85, H7S9T115, H5S15T125 and H5S15T100.

The advantage of this test is to evaluate the internal microstructure of the geopolymer and the arrangement of pores and cracks through a non-destructive method with minimal need for sample preparation.

The colors indicate the groups of interconnected pores and cracks, and distinct colors are not in communication with each other within the spatial distribution.

Figure 3 reconstructs the sample and distribution of voids in a 3D space of the quantified volume of sample H7S9T85 and the pixel size at acquisition corresponds to 19 µm. The colors indicate the groups of interconnected pores and cracks, and distinct colors are not in communication with each other within the spatial distribution.

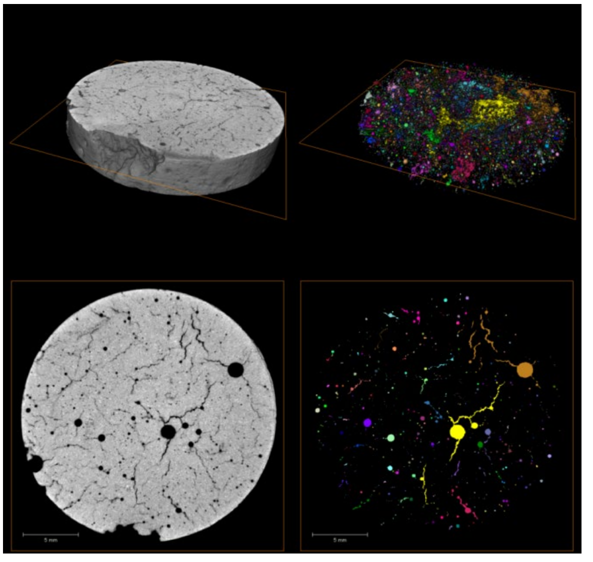

Figure 3. Generated images showing sample reconstitution and the distribution of voids in a 3D space of the quantified volume of sample H7S9T85.

The evaluation of sample H5S15T100 shows the image referring to the central point of the experiment. This experiment had an increase in the curing temperature, but a reduction in the concentration of the sodium hydroxide solution.

The 3D reconstruction reveals quite dispersed pores with voids and cracks that do not connect in large areas of the material, as can be ascertained through the color variation in the image.

The porosity of this sample was 3% of the volume and fewer cracks can be seen in the 2D plane, which may be related to a decrease in the amount of sodium hydroxide, an effect that is illustrated by Figure 4.

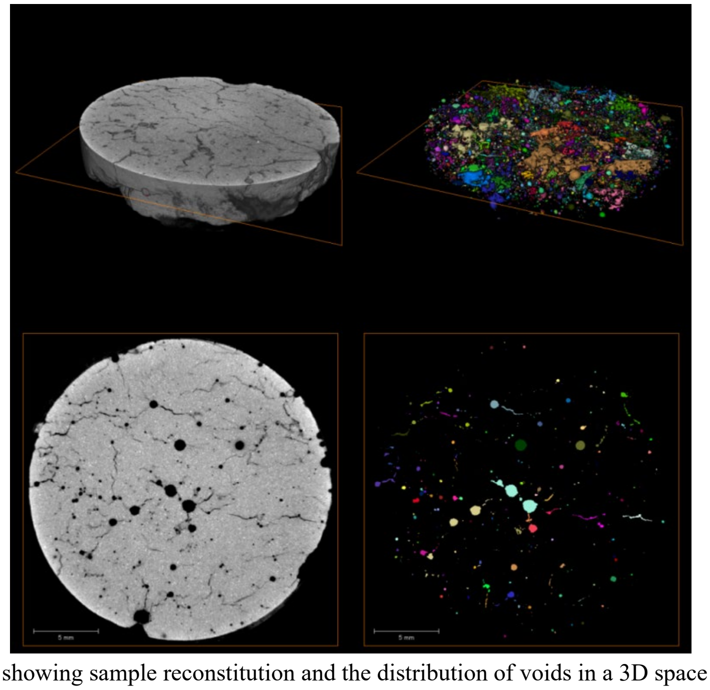

Figure 4. Generated images showing sample reconstitution and the distribution of voids in a 3D space of the quantified volume of sample H5S15T100.

Figure 5, on the other hand, visually demonstrates a significant increase in porosity, totaling a pore volume of 7%. Its compressive strength, however, was higher compared to the samples treated with lower temperatures.

Areas can be seen with larger volumes of interconnected pores represented by the same color, and on the 2D surface there is an increase in the presence of microcracks.

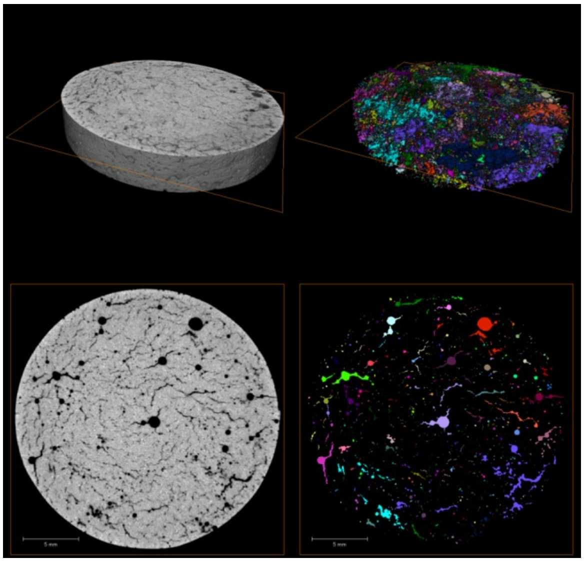

Figure 5. Generated images showing sample reconstitution and the distribution of voids in a 3D space of the quantified volume of sample H7S9T115.

And finally, sample H5S15T125, which is represented in Figure 6, had the highest amount of porosity, 9%. This representation reveals that the red color predominates in almost the entire porous fraction of the material, which shows that the voids are connected to each other within the geopolymeric matrix. In the 2D plane, the cracks show the retraction of the material due to heating and the loss of moisture with segmented voids throughout the sample.

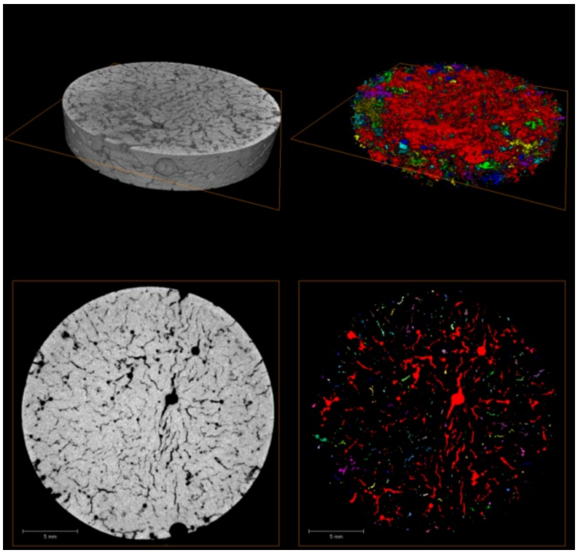

Figure 6. Generated images showing sample reconstitution and the distribution of voids in a 3D space of the quantified volume of sample H5S15T125.

But despite having a more porous material, this mixture was the one that showed the greatest compressive strength, reaching the mean value of 10.21 MPa. This phenomenon is linked to a synergy between temperature and molar concentration of the activator, presented on the response surface, mainly occurring in the first 24 hours.

The creation of bubbles can be associated with the reaction of reactive metal chemical elements (Al, Zn or Si) with the activation alkaline solution, releasing hydrogen gas bubbles and forming a complex network of pores [2]. Through the visual analysis, it is possible to identify a large variation in pore size, with micropores, mesopores and macropores at the interface, but it is necessary to focus on the reduction of macropores, since this has high relevance in relation to compressive strength.

The microstructural variability in the formation of the hardened material is affected by the variation of the factors under study, where the bond between the particles is affected by the physical and chemical properties of each mixture, or even by the electrostatic condition of the particle surface [24].

This study, therefore, provided the first systematic three-dimensional analysis of alkali-activated binder structures by X-ray microtomography and it provides an understanding of the distribution and geometry of the internal and external pore network in the sample, in a way that is not achievable using two-dimensional techniques such as scanning electron microscopy.

Thus, the obtained dataset provided information on porosity and pore geometry within the representative samples of the experiment. The three-dimensional reconstruction reveals primarily an interpretation of the pore chains, signaling that a greater thickening of the geopolymer in the curing process will bring more mechanical strength due to improvements in the transition zone and greater formation of binding gels. A denser matrix associated with temperature may have a beneficial synergic result for the geopolymer matrix.

On the other hand, when looking for a lighter and insulating material, it is important that the volume of voids remains or even increases. And in this regard, μCT provides data on the homogeneity of the material so that future developments in this area are understood based on its microstructure.

As with most analytical techniques, μCT has some significant limitations. Perhaps its biggest disadvantage is the compensation between resolution and sample size [15], [25].

Products with thermal curing at higher temperatures had an increase in porosity but their mechanical strength also increased significantly. Sample H5S15T125 is an example. It had a compressive strength of 8.20 MPa and 10.251 MPa in each round of the experiment, respectively, while its porosity was 9%. Table 4 shows the total volume of the samples and the volume of voids and their porosity as a percentage.

Table 4. Total pore volume measured by the complementary μCT test and porosities as % of volume.

Sample	total vol (μm3)	pore vol (μm3)	porosity (%)
H7S9T85	1638300058968	60588942927	4%
H7S9T115	1737570000000	122993393055	7%
H5S15T125	1594880065183	137415146409	9%
H5S15T100	1584490150696	49512614886	3%

This behavior of the H5S15T125 sample is explained by the evaporation of water and the chemical changes of the hydration products resulting from the temperature rise, causing an increase in the porosity and pore size of the paste [26]. Although the increase in temperature potentiates the geopolymerization effect, the rapid exudation creates a thickening of the porous structure and the mechanical strength properties end up being affected [27].

It is estimated that the hardened binders contain pores with characteristic diameters that vary below the resolution used in the test, from 19 μm up to approximately 10 nm, which can lead to significant complexities in the geometry and distribution of the pores [28], [29]. However, in this research they presented crystallization even in samples with greater porosity, pointing out that a better thickening of the paste will improve mechanical strength.

4 CONCLUSIONS

Basalt rocks show potential for the development of alternative cements through the alkali-activation process. Although the compressive strength results were not high, it is possible to use this material in the addition of more reactive materials or even as a porous material for sound and thermal insulation purposes.

The statistical mathematical evaluation of the results revealed the existence of two independent variables (NaOH concentration and temperature) with a statistical significance in the strength gain of the material. Future research could expand the experimental design and obtain increases in mechanical strength.

In addition, due to the low emission of harmful gases and the composition of raw materials that cause less environmental impact compared to Portland cement, the product of this research has aspects of a promising material in civil construction.

The X-ray microtomography imaging revealed that the increase in curing temperature caused an increase in the porosity and number of cracks of the material, but higher temperatures formed a product of the basalt powder reaction with a material that was more resistant to axial compression.

Therefore, even with compressive strength values falling far short of the values obtained for other geopolymers based on metakaolin, blast furnace slag and some types of ash, the great advantage of the development of cementing materials with basalt rocks is the ease of obtaining the powdery material present in the aggregates, the abundance of raw material, and the aptitude for the alkali-activation process.

As this is an exploratory study, the study area was delimited to seek data on the mechanical strength and microstructure of the material. Future research should stipulate optimal proportions for alkaline reagents and additions so that maximum material performance is achieved, in addition to proposing an increase in the scale of production from laboratory to industrial scale.

Thus, the development of a matrix with additional cementitious materials from basalt powder is environmentally less aggressive due to low CO2 emissions and economically viable, giving utility to a product of low added value, which is often discarded by mining companies in the region.

ACKNOWLEDGMENTS

The authors would like to thank the financial support offered by the Community University of the Region of Chapecó - Unochapecó.

REFERENCES

[1] A. M. Rashad and S. R. Zeedan, "The effect of activator concentration on the residual strength of alkali-activated fly ash pastes subjected to thermal load," *Constr. Build. Mater.*, vol. 25, no. 7, pp. 3098–3107, 2011, http://dx.doi.org/10.1016/j.conbuildmat.2010.12.044.

[2] H. Y. Zhang, V. Kodur, S. L. Qi, L. Cao, and B. Wu, "Development of metakaolin-fly ash based geopolymers for fire resistance applications," *Constr. Build. Mater.*, vol. 55, pp. 38–45, 2014, http://dx.doi.org/10.1016/j.conbuildmat.2014.01.040.

[3] J. Davidovits, *Geopolymer Cement a Review* (Geopolymer Sci. Tech.). 2013.

[4] C. G. S. Severo, D. L. Costa, I. M. T. Bezerra, R. R. Menezes, and G. A. Neves, "“Características, particularidades e princípios científicos dos materiais ativados alcalinamente," *Rev. Eletrônica Mater. Process.*, vol. 8, no. 2, pp. 55–67, 2013.

[5] P. Timakul, W. Rattanaprasit, and P. Aungkavattana, "Improving compressive strength of fly ash-based geopolymer composites by basalt fibers addition," *Ceram. Int.*, vol. 42, no. 5, pp. 6288–6295, 2016, http://dx.doi.org/10.1016/j.ceramint.2016.01.014.

[6] M. Esaifan, M. Hourani, H. Khoury, H. Rahier, and J. Wastiels, "Synthesis of hydroxysodalite zeolite by alkali-activation of basalt powder rich in calc-plagioclase," *Adv. Powder Technol.*, vol. 28, no. 2, pp. 473–480, 2017, http://dx.doi.org/10.1016/j.apt.2016.11.002.

[7] A. Solouki, G. Viscomi, R. Lamperti, and P. Tataranni, "Quarry waste as precursors in geopolymers for civil engineering applications: A decade in review," *Materials*, vol. 13, no. 14, pp. 3146, 2020, http://dx.doi.org/10.3390/ma13143146.

[8] P. Tataranni, "Recycled waste powders for alkali-activated paving blocks for urban pavements: a full laboratory characterization," *Infrastructures*, vol. 4, no. 4, pp. 73, 2019., http://dx.doi.org/10.3390/infrastructures4040073.

[9] A. Koppe, E. N. Guindani, and M. Manci, "Avaliação do potencial de resíduo de rochas basálticas como matéria-prima para a produção de cimentos alternativos: processo de álcali-ativação," *Rev. Arquitetura IMED*, vol. 4, no. 2, pp. 24–32, 2015., http://dx.doi.org/10.18256/2318-1109/arqimed.v4n2p24-32.

[10] P. Tataranni and C. Sangiorgi, "Synthetic aggregates for the production of innovative low impact porous layers for urban pavements," *Infrastructures Infrastructures*, vol. 4, no. 3, pp. 48, 2019., http://dx.doi.org/10.3390/infrastructures4030048.

[11] H. Jamshaid and R. Mishra, "A green material from rock: basalt fiber: a review," *J. Textil. Inst.*, vol. 107, no. 7, pp. 923–937, 2016, http://dx.doi.org/10.1080/00405000.2015.1071940.

[12] Associação Brasileira de Normas Técnicas, *Agregados para Concreto – Especificação*, ABNT NBR 7211:2009, 2009.

[13] C. Drago, J. C. K. Verney, and F. M. Pereira, "Efeito da utilização de areia de britagem em concretos de cimento Portland," *Rem Rev. Esc. Minas*, vol. 62, no. 3, pp. 399–408, 2009, http://dx.doi.org/10.1590/S0370-44672009000300021.

[14] J. S. J. Van Deventer, J. L. Provis, P. Duxson, and D. G. Brice, "Chemical research and climate change as drivers in the commercial adoption of alkali activated materials," *Waste Biomass Valoriz.*, vol. 1, no. 1, pp. 145–155, 2010, http://dx.doi.org/10.1007/s12649-010-9015-9.

[15] J. L. Provis, R. J. Myers, C. E. White, V. Rose, and J. S. J. Van Deventer, "X-ray microtomography shows pore structure and tortuosity in alkali-activated binders," *Cement Concr. Res.*, vol. 42, no. 6, pp. 855–864, 2012, http://dx.doi.org/10.1016/j.cemconres.2012.03.004.

[16] M. A. B. Promentilla, T. Sugiyama, T. Hitomi, and N. Takeda, "Quantification of tortuosity in hardened cement pastes using synchrotron-based X-ray computed microtomography," *Cement Concr. Res.*, vol. 39, no. 6, pp. 548–557, 2009, http://dx.doi.org/10.1016/j.cemconres.2009.03.005.

[17] Associação Nacional das Entidades de Produtores de Agregados para Construção, "Areia de brita para construção: Evolução de processos e mudanças estruturais nos grandes centros urbanos favorecem utilização do produto para o mercado," *Rev. Areia Brita*, pp. 20–24, 2018.

[18] Brasil, *Resolução nº 307, de 5 de Julho de 2002*, 2002.

[19] E. Álvarez-Ayuso et al., "Environmental, physical and structural characterisation of geopolymer matrixes synthesised from coal (co-)combustion fly ashes," *J. Hazard. Mater.*, vol. 154, no. 1-3, pp. 175–183, 2008, http://dx.doi.org/10.1016/j.jhazmat.2007.10.008.

[20] D. C. Montgomery, G. C. Runger, and N. F. Hubele, *Estatística Aplicada à Engenharia*, 2a ed. Rio de Janeiro: LTC, 2004.

[21] L. C. Briese, S. Selle, C. Patzig, J. Deubener, and T. Höche, "Depth-profiling of nickel nanocrystal populations in a borosilicate glass: a combined TEM and XRM study," *Ultramicroscopy*, vol. 205, pp. 39–48, 2019, http://dx.doi.org/10.1016/j.ultramic.2019.06.004.

[22] O. L. Alves, I. F. Gimenez, and O. P. Ferreira, "Desenvolvimento de ecomateriais: materiais porosos para apluicação em Green Chemistry (Química Verde)," in *Química Verde en Latinoamérica*, P. Tundo and R. H. Rossi, Eds., Buenos Aires: IUPAC, 2004.

[23] Associação Brasileira de Normas Técnicas, *Cimento Portland – Determinação da Resistência à Compressão de Corpos de Prova Cilíndricos*, ABNT NBR 7215, 2019.

[24] M. Dobiszewska, A. K. Schindler, and W. Pichór, "Mechanical properties and interfacial transition zone microstructure of concrete with waste basalt powder addition," *Constr. Build. Mater.*, vol. 177, pp. 222–229, 2018, http://dx.doi.org/10.1016/j.conbuildmat.2018.05.133.

[25] U. Rattanasak and K. Kendall, "Pore structure of cement/pozzolan composites by X-ray microtomography," *Cement Concr. Res.*, vol. 35, no. 4, pp. 637–640, 2005, http://dx.doi.org/10.1016/j.cemconres.2004.04.022.

[26] C. Medina, M. Frías, M. I. Sánchez De Rojas, C. Thomas, and J. A. Polanco, "Gas permeability in concrete containing recycled ceramic sanitary ware aggregate," *Constr. Build. Mater.*, vol. 37, pp. 597–605, 2012, http://dx.doi.org/10.1016/j.conbuildmat.2012.08.023.

[27] W. Franus, A. Halicka, K. Lamorski, and G. Jozefaciuk, "Microstructural differences in response of thermoresistant (ceramic) and standard (granite) concretes on heating. studies using SEM and nonstandard approaches to microtomography and mercury intrusion porosimetry data," *Materials*, vol. 11, no. 7, pp. 1126, 2018, http://dx.doi.org/10.3390/ma11071126.

[28] F. Collins and J. G. Sanjayan, "Effect of pore size distribution on drying shrinkage of alkali-activated slag concrete," *Cement Concr. Res.*, vol. 30, no. 9, pp. 1401–1406, 2000, http://dx.doi.org/10.1016/S0008-8846(00)00327-6.

[29] W. M. Kriven, J. L. Bell, and M. Gordon, "Microstructure and nanoporosity of as-set geopolymers," in *Mechanical Properties and Performance of Engineering Ceramics II*, R. Tandon, A. Wereszczak, and E. Lara-Curzio, Eds., Hoboken: Wiley, 2008.

Author contributions: RG and ERB: conceptualization, methodology, supervision, writing; LLS and MAF: conceptualization, data curation, formal analysis and review of article writing.

Editors: Edna Possan, Guilherme Aris Parsekian.

IBRACON Structures and Materials Journal
Revista IBRACON de Estruturas e Materiais
ISSN 1983-4195 ismj.org

ORIGINAL ARTICLE

Nonlinear analysis method of concrete structures under cyclic loading based on the generalized secant modulus

Método para análise não linear de estruturas de concreto submetidas a carregamentos cíclicos baseado no módulo secante generalizado

Lívia Ramos Santos Pereira[a]
Samuel Silva Penna[a]

[a]Universidade Federal de Minas Gerais – UFMG, Departamento de Engenharia de Estruturas, Belo Horizonte, MG, Brasil

Received 01 July 2021
Accepted 03 December 2021

Abstract: A smeared crack model to represent cyclic concrete behavior is presented in this work. The model is based on analytical and experimental studies from the literature and proposes a numerical approach using a new concept, the generalized secant modulus. The monotonic formulation is described, followed by the changes to include the cyclic response, and the stress-strain laws to reproduce the hysteresis. Simulations adopting the proposed model were compared with experimental tests of cyclic tension and compression available in the literature, resulting in consistent load cycles. Three-point bending was simulated to display the structural response under non-elementary load. Finally, a reinforced concrete beam was studied to evaluate the model performance under usual loadings. The results show the model capacity to reproduce cyclic analyses and its potential to be extended to general loadings.

Keywords: concrete, cyclic load, constitutive model, generalized secant modulus, stress-strain law.

Resumo: Um modelo de fissuração distribuída para representar o comportamento cíclico do concreto é apresentado neste trabalho. O modelo é baseado em estudos analíticos e experimentais presentes na literatura e propõe uma abordagem numérica utilizando um conceito novo, o módulo secante generalizado. A formulação monotônica é descrita, seguida pelas alterações para inclusão da resposta cíclica e pelas leis tensão-deformação para reproduzir a histerese. Simulações adotando o modelo proposto foram comparadas com ensaios experimentais de tração e compressão cíclicas disponíveis na literatura, resultando em uma representação consistente dos ciclos de carga. Uma flexão em três pontos foi simulada para exibir a resposta estrutural sob cargas não elementares. Por fim, uma viga de concreto armado foi estudada para avaliar o desempenho do modelo sob carregamentos usuais. Os resultados mostram a capacidade do modelo em reproduzir análises cíclicas e seu potencial de extensão a casos gerais de carregamento.

Palavras-chave: concreto, carga cíclica, modelo constitutivo, módulo secante generalizado, lei tensão-deformação.

How to cite: L. R. S. Pereira and S. S. Penna, "Nonlinear analysis method of concrete structures under cyclic loading based on the generalized secant modulus," *Rev. IBRACON Estrut. Mater.*, vol. 15, no. 4, e15406, 2022, https://doi.org/10.1590/S1983-41952022000400006

1 INTRODUCTION

The complete description of a concrete structure subjected to mechanical loadings demands constitutive models capable of representing loading, unloading, and reloading regimes. Even under monotonic loading, the structural equilibrium can result in a stress redistribution related, e.g., to microcrack nucleation [1]. In other situations, the external load solicitation is cyclic [2]. Thus, cyclic constitutive models are required to represent the structural behavior.

Corresponding author: Lívia Ramos Santos Pereira. E-mail: lrsp@ufmg.br
Financial support: CNPq, in Portuguese *Conselho Nacional de Desenvolvimento Científico e Tecnológico*. Grant: nº 307985/2020-2.
Conflict of interest: Nothing to declare.
Data Availability: The data that support the findings of this study are available from the corresponding author, LRSP, upon reasonable request.
This is an Open Access article distributed under the terms of the Creative Commons Attribution License, which permits unrestricted use, distribution, and reproduction in any medium, provided the original work is properly cited.

The literature presents a variety of constitutive models for quasi-brittle materials, as concrete, standing out the smeared crack models [3]-[6] and the damage models [7]-[9]. Nevertheless, most of them are restricted to monotonic behavior. A complete constitutive model must also cover the unloading/reloading regimes. Sinha et al. [10] and Karsan and Jirsa [11] were the pioneers in cyclic models, whose works motivated further studies [1], [12],[13].

Sima and Molins [14] proposed a constitutive model for concrete subjected to cyclic loadings in compression and tensile. A smeared crack approach is adopted to describe the strength and stiffness degradation. Because of the different properties of concrete under tensile and compression, two independent damage parameters were introduced to this model. Another improvement in the loop's representation is related to the dependency between the cyclic variables and the damage level in the envelope curve. Later, Breccolotti et al. [15] extended such a model, including special conditions to represent incomplete unload and reload paths.

Another numerical strategy that considers the distinct behavior of concrete under tensile and compression was developed by Feng et al. [16]. The authors analyzed the cyclic behavior in precast concrete structures, using a damage mechanics-based model to describe hysteresis in the effective stress space. Then, the effective stress is divided into tensile and compression parts, and the Helmholtz free energy is applied. The plastic strain evolution is based on an empirical model, while the energy release rates limit the damage evolution.

Alva et al. [17] also proposed a cyclic model based on damage. This research presents a numerical strategy formulated from the Lumped Damage Mechanics. Such an approach concentrates the dissipation of energy in hinges at the ends of the structural members. For cyclic action, an additional damage parameter is demanded, determined by experimental tests. The study by Chen et al. [18], on the other hand, is restricted to hysteresis loops in tensile tests, and a statistical damage model is the used method to represent the cyclic loading.

Besides the damage models, other numerical strategies are available in the literature. Moharrami and Koutromanos [19] developed an elastoplastic formulation to reproduce cyclic loading. A crack criterion is adopted to verify the degradation, while a return mapping algorithm calculates the stress update. For Mourlas et al. [20], the decomposition of the stress-strain relationship into hydrostatic and deviatoric components identifies the load loops. Li and Ren [21] proposed a modified version of the Chinese Standard Model: *Code for design concrete structures,* replacing the unloading/reloading single line path with two different tracks. The unloading path was reformulated to fit studies that show it has a curve shape.

Although the diversity of models to reproduce concrete cyclic behavior, most of them are restricted to fixed cyclic shapes, limiting their representation capacity. The current paper presents a formulation based on the approach of Lee et al. [22] to overcome this drawback and become the cyclic analysis more practical and general. The study by Lee et al. [22] is highlighted because of its simplicity and ease of application in the computational context. The authors developed an analytical method to obtain a material elastic modulus used for mapping the load loops. This method is based on the focal point concept, a pole that controls the unloading/reloading regimes, dividing the total strain into elastic and permanent parts.

In this paper, the methodology by Lee et al. [22] is incorporated into a smeared crack model, providing a variety of load cycles shapes. A mathematical formulation permitted the coupling among the elastic degradation model, the stress-strain total relation, and the generalized secant modulus to represent degradation and plastification. The stress-strain laws are an essential part of the proposed method. However, most well-known laws [23]-[26] are restricted to the monotonic curve. Unloading/reloading stress-strain relations were added into the constitutive model to cover this gap. It is presented four cyclic strategies: the secant, the elastic, the linear path based on the focal point [22], [27], and the nonlinear hypothesis by Popovics-Saenz [28]-[31]. Numerical simulations of structures under cyclic loads in a plane stress state have been simulated via the Finite Element Method (FEM) to validate this model.

2 ELASTIC DEGRADATION MODEL APPLIED TO CYCLIC ANALYSIS

The nonlinear cyclic analysis is a quasi-static analysis with load increase/decrease. Under a hysteretic state, the material has a nonlinear behavior, and load loops are observed in structural response. In concrete structures, the nonlinearity comes from material degradation. A common choice to represent such a process is the smeared crack models. In this paper, the model proposed by Penna [32] has been extended to include cyclic simulations.

A load script is required to reproduce hysteresis by operating the loading sign. The standard Newton-Raphson method controls the loading evolution, and the incremental load depends on a control method. The direct displacement method [33] was adopted. This strategery favors the cycle monitoring, directly changing the sign of the degree of freedom controlled.

Although the current work aims to reproduce cyclic loads, the fatigue process is not addressed. Fatigue is related to repetitive loads and a significant number of cycles, causing structural collapse even under stresses lower than the material strength. The present paper studies the cyclic reproduction in the softening branch (post-peak) of the equilibrium path.

2.1 Smeared crack model

Since the 1960s, constitutive models have been developed to describe concrete cracking [3], [34]. The smeared crack models consider phenomenological hypotheses to obtain concrete degradation. Initially regarded as linear, elastic, homogeneous, and isotropic, the material medium can become nonlinear, inelastic, and orthotropic under mechanical loads. The homogeneity, on the other hand, is preserved. In these models, the elastic material properties are modified considering the orthotropic directions to reproduce the deterioration. These changes depend on the material stress/strain state [35], [36]. Consequently, such models are also known as elastic degradation models [37]-[39].

A wide variety of these models could be found in Penna [32], including the monotonic smeared crack model. Such model is based on total strains, and a secant (represented by the superscript s) constitutive relation computes the stresses. The principal strain directions are the local crack system (referred by ℓ), i.e., the evaluation of the material properties considers the directions normal and tangential to the crack plane to compose the constitutive tensor. Such a tensor can assume different forms [40], including the plane stress state matrix of Equation 1.

$$[{}^{s}_{\ell}\mathrm{D}] = \begin{bmatrix} {}^{s}_{\ell}\mathrm{D}_{11} & {}^{s}_{\ell}\mathrm{D}_{12} & {}^{s}_{\ell}\mathrm{D}_{13} \\ {}^{s}_{\ell}\mathrm{D}_{21} & {}^{s}_{\ell}\mathrm{D}_{22} & {}^{s}_{\ell}\mathrm{D}_{23} \\ {}^{s}_{\ell}\mathrm{D}_{31} & {}^{s}_{\ell}\mathrm{D}_{32} & {}^{s}_{\ell}\mathrm{D}_{33} \end{bmatrix} = \frac{1}{1-\frac{\mathrm{E_n E_t}}{\mathrm{E_0^2}}\upsilon^2} \begin{bmatrix} \mathrm{E_n} & \frac{\upsilon \mathrm{E_n E_t}}{\mathrm{E_0}} & 0 \\ \frac{\upsilon \mathrm{E_n E_t}}{\mathrm{E_0}} & \mathrm{E_t} & 0 \\ 0 & 0 & \left(1-\frac{\mathrm{E_n E_t}}{\mathrm{E_0^2}}\upsilon^2\right)\mathrm{G_{nt}} \end{bmatrix} \quad (1)$$

where $\mathrm{E_0}$ is the Young modulus, υ is the Poisson coefficient, and n and t are the material orthotropic directions: n is the normal direction, and t is the tangential direction to the crack plane. $\mathrm{G_{nt}}$ is the shear modulus, calculated by Equation 2.

$$\mathrm{G_{nt}} = \frac{\mathrm{E_0 E_n E_t}}{\mathrm{E_0 E_n} + \mathrm{E_0 E_t} + 2\upsilon \mathrm{E_n E_t}} > \beta_r \mathrm{G_0} \quad (2)$$

where β_r is the shear retention factor and $\mathrm{G_0}$ is the shear modulus of the undamaged material.

Then, the secant moduli are calculated in function of the principal strains. At this point, stress-strain laws are required to obtain the elastic modulus degradation. Particular relations may be necessary to represent the concrete behavior under tension and compressive loads.

The total relation for the stress state calculation is symbolically written by Equation 3.

$$\{\sigma_\ell\} = [{}^{s}_{\ell}\mathrm{D}].\{\varepsilon_\ell\}. \quad (3)$$

Or, in the matrix form, by Equation 4.

$$\begin{Bmatrix} \sigma_n \\ \sigma_t \\ \tau_{nt} \end{Bmatrix} = \frac{1}{1-\frac{\mathrm{E_n E_t}}{\mathrm{E_0^2}}\upsilon^2} \begin{bmatrix} \mathrm{E_n} & \frac{\upsilon \mathrm{E_n E_t}}{\mathrm{E_0}} & 0 \\ \frac{\upsilon \mathrm{E_n E_t}}{\mathrm{E_0}} & \mathrm{E_t} & 0 \\ 0 & 0 & \left(1-\frac{\mathrm{E_n E_t}}{\mathrm{E_0^2}}\upsilon^2\right)\mathrm{G_{nt}} \end{bmatrix} \begin{Bmatrix} \varepsilon_n \\ \varepsilon_t \\ \gamma_{nt} \end{Bmatrix}, \quad (4)$$

where σ_n, σ_t and τ_{nt} are the stress components, while ε_n, ε_t and γ_{nt} are the strain components in the local crack system.

In an iterative-incremental solution based on the standard Newton-Raphson method, the tangential constitutive relation is also required, derived from the total relation, as expressed by Equation 5.

$$[{}^{t}_{\ell}\mathrm{D}] = \frac{\partial\{\sigma_\ell\}}{\partial\{\varepsilon_\ell\}} = \left[{}^{s}_{\ell}[\mathrm{D}] + \frac{\partial[{}^{s}_{\ell}\mathrm{D}]}{\partial\{\varepsilon_\ell\}}\{\varepsilon_\ell\}\right], (5)$$

where $\frac{\partial[{}^{s}_{\ell}\mathrm{D}]}{\partial\{\varepsilon_\ell\}}\{\varepsilon_\ell\}$ is calculated with Equation 6.

$$\frac{\partial[{}^{s}_{\ell}\mathrm{D}]}{\partial\{\varepsilon_\ell\}}\{\varepsilon_\ell\} = \begin{bmatrix} \frac{\partial{}^{s}_{l}\mathrm{D}_{11}}{\partial\varepsilon_n}\varepsilon_n + \frac{\partial\mathrm{D}_{12}}{\partial\varepsilon_n}\varepsilon_t & \frac{\partial{}^{s}_{l}\mathrm{D}_{11}}{\partial\varepsilon_t}\varepsilon_n + \frac{\partial\mathrm{D}_{12}}{\partial\varepsilon_t}\varepsilon_t & 0 \\ \frac{\partial{}^{s}_{l}\mathrm{D}_{21}}{\partial\varepsilon_n}\varepsilon_n + \frac{\partial\mathrm{D}_{22}}{\partial\varepsilon_n}\varepsilon_t & \frac{\partial{}^{s}_{l}\mathrm{D}_{21}}{\partial\varepsilon_t}\varepsilon_n + \frac{\partial\mathrm{D}_{22}}{\partial\varepsilon_t}\varepsilon_t & 0 \\ 0 & 0 & 0 \end{bmatrix}. (6)$$

The model was presented in the local system. The formulation in global systems is given by Equation 7 and Equation 8.

$$\{\sigma_\ell\} = [T_\sigma]\,\{\sigma_g\}\ (7), \{\varepsilon_\ell\} = [T_\varepsilon]\{\varepsilon_g\}. (8)$$

Where $\{\sigma_g\}$ is the global stress vector, $\{\varepsilon_g\}$ is the global strain vector, $[T_\sigma]$ and $[T_\varepsilon]$ are the stress and the strain transformation matrices, respectively.

Thus, by replacing Equation 7 and Equation 8 in Equation 3, the Equation 9 is determined.

$$[T_\sigma]\{\sigma_g\} = [{}^{s}_{\ell}D][T_\varepsilon]\{\varepsilon_g\}. (9)$$

Isolating $\{\sigma_g\}$ in Equation 9, the global stress vector is expressed as Equation 10.

$$\{\sigma_g\} = [T_\sigma]^{-1}[{}^{s}_{\ell}D][T_\varepsilon]\{\varepsilon_g\}. (10)$$

Since the global matrix is given by Equation 11

$$[{}^{s}_{g}D] = [T_\sigma]^{-1}[{}^{s}_{\ell}D][T_\varepsilon], (11)$$

the total relation in the global system is written by Equation 12.

$$\{\sigma_g\} = [{}^{s}_{g}D]\{\varepsilon_g\}\ (12)$$

The global tangent operator comes from the derivative of total relation in the global system to the strain vector, resulting in Equation 13.

$$[{}^{t}_{g}D] = \frac{\partial\{\sigma_g\}}{\partial\{\varepsilon_g\}} = [{}^{s}_{g}D] + [T_\varepsilon]^T\,\frac{\partial[{}^{s}_{\ell}D]}{\partial\{\varepsilon_\ell\}}\{\varepsilon_\ell\}[T_\varepsilon] + \frac{\partial[T_\varepsilon]^T}{\partial\theta}\{\sigma_\ell\}\left(\frac{\partial\theta}{\partial\{\varepsilon_g\}}\right)^T, (13)$$

where θ is the angle direction of the local crack system.

If the local system is fixed during the crack nucleation, the transformation matrix does not present variation. Consequently, the global tangent matrix can be defined as Equation 14.

$$\left[{}_{g}^{t}D\right] = \frac{\partial\{\sigma_{g}\}}{\partial\{\varepsilon_{g}\}} = \left[{}_{g}^{s}D\right] + [T_{\varepsilon}]^{T}\,\frac{\partial[{}_{\ell}^{s}D]}{\partial\{\varepsilon_{\ell}\}}\{\varepsilon_{\ell}\}[T_{\varepsilon}].\,(14)$$

The secant modulus monitoring can establish the loading regime. Although, a more efficient control method based on loading functions is adopted. The loading functions are expressed in terms of strain components (ε_n, ε_t) by Equation 15 and Equation 16.

$$f_n = \varepsilon_n - \kappa_n,\,(15)\; f_t = \varepsilon_t - \kappa_t.\,(16)$$

Where f_n and f_t are, respectively, the loading function in the normal and tangential directions to the crack plane; ε_n and ε_t are the strain components; κ_n and κ_t are historical parameters, i.e., the maximum values of ε_n and ε_t during the analysis. The initial values of the historical parameters (κ_{0n}, κ_{0t}) represents the strain in the elastic limit. When κ_{0n} or κ_{0t} are exceeded, the degradation starts, and the material behavior turns inelastic in this direction.

Regarding the loading regime, the loading function variation ($\dot{f}$) and the historical variable evolution ($\dot{\kappa}$) are calculated by Equation 17 and Equation 18, respectively, in a pseudo-time of the iterative-incremental process.

$$\dot{f} = f_{(t)} - f_{(t-1)},\,(17)\; \dot{\kappa} = \kappa_{(t)} - \kappa_{(t-1)}.\,(18)$$

Where (t) and $(t-1)$ represent the current and the previous moments, respectively.

At last, the Kuhn-Tucker conditions are applied to identify the loading regime: elastic loading ($f < 0$; $\dot{f} > 0$; $\kappa = \kappa_0$; $\dot{\kappa} = 0$); inelastic loading ($f = 0$; $\dot{f} = 0$; $\kappa > \kappa_0$; $\dot{\kappa} > 0$); unloading $\left(f < 0;\ \dot{f} < 0;\ \kappa > \kappa_0;\ \dot{\kappa} = 0\right)$; and reloading ($f < 0$; $\dot{f} > 0$; $\kappa > \kappa_0$; $\dot{\kappa} = 0$).

Since the regimes are known, the secant moduli (E_n, E_t) can be calculated by stress-strain laws. Such moduli reproduce the material degradation and are part of the constitutive matrix that provides the stress. In cyclic analyses, the secant moduli need to be reformulated for the unloading/reloading. Nevertheless, the historical variables remain the same during hysteresis.

A change in the constitutive matrix (Equation 1) has been proposed to perform the cycles. The generalized secant moduli E_{GSn}, E_{GSt} replaces the traditional secant moduli E_n, E_t in unloading/reloading stages. The stress-strain laws that provide the secant moduli must also be redefined to include cyclic paths and the E_{GS} calculation. Figure 1 summarizes the process.

2.2 Stress-strain laws for cyclic loading

The constitutive models are mechanical-mathematics representations that describe the behavior of a material media. The degradation is computed by the secant modulus variation for the proposed model, using stress-strain laws defined from approximations of experiments. Such laws can assume different formats: linear, polynomial, exponential, among others.

Besides the traditional approximations, concrete stress-strain laws for tension and compression loadings are highlighted. Some of them were proposed by Carreira and Chu [23, 24] (Equation 19), Boone et al. [25], and Bone and Ingraffea [26] (Equation 20).

$$\sigma = f_i\,\frac{k(\varepsilon/\varepsilon_i)}{k - 1 + (\varepsilon/\varepsilon_i)^k},\,where\; k = \frac{1}{1 - (f_i/\varepsilon_i.\,E_0)}\; and\; i = t, c.\,(19)$$

σ is the stress, f_i is the strength limit, ε_i is the strain related with the elastic limit, ε is the current strain, and $i = t$ represents tension, while $i = c$ represents compression.

$$\sigma = f_t e^{-k(\varepsilon\,-\,\varepsilon_t)},\,with\!: k = h\, f_t/G_f\,.\,(20)$$

Where σ is the stress, f_t is the tensile strength, ε is the current strain, ε_t is the strain in the elastic tension limit, h is the characteristic length, and G_f is the fracture energy.

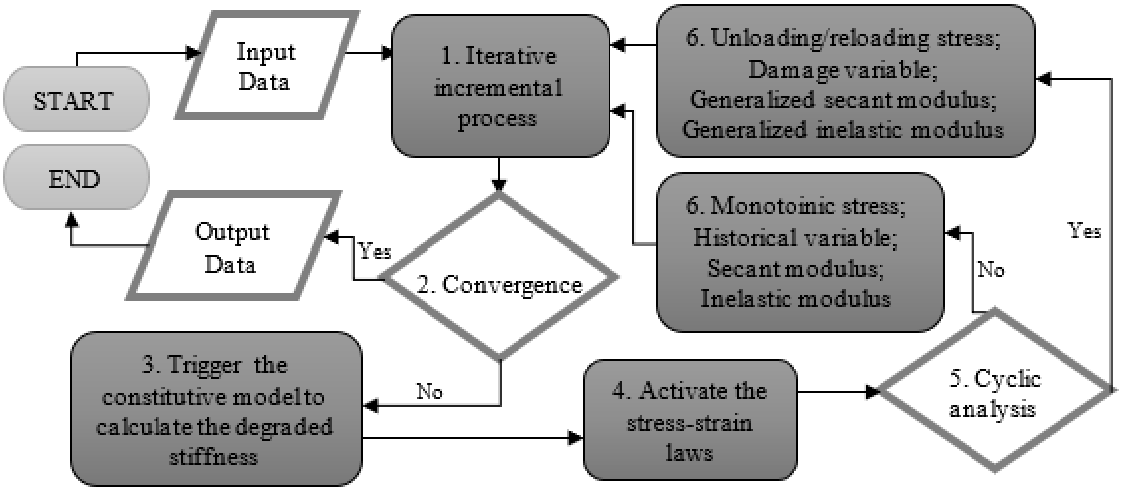

Figure 1. Cyclic analysis process.

The stress-strain relations, although are restricted to monotonic loadings. In this work, four hypotheses have been incorporated in the original laws to reproduce the load cycles: the secant cycle, based on the traditional secant modulus; the linear cycle, using the undamaged elastic modulus; the linear cycle based on focal point concept; and an extended version presented by Bono [29] of the law initially proposed by Popopovics-Saenz. All cyclic strategies adopted the generalized secant modulus proposal detailed as follows.

2.2.1 Secant unloading/reloading

The secant hypothesis is the most common representation of concrete behavior because of its simplicity and precision in reproducing monotonic loadings. Another relevant feature is the maximum strain and the current material degradation monitoring. The degraded modulus can be calculated as the straight slope that starts in origin and goes until the unloading point. Figure 2 illustrates the secant hypothesis. The point with coordinates ε_r, σ_r is a generic point where the reloading begins, that is the origin of the system σ-ε for a complete cycle.

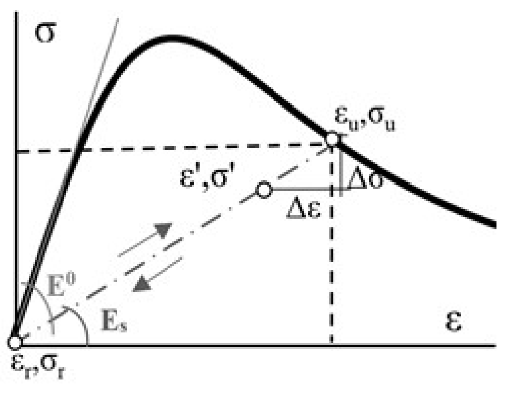

Figure 2. Secant unloading/reloading.

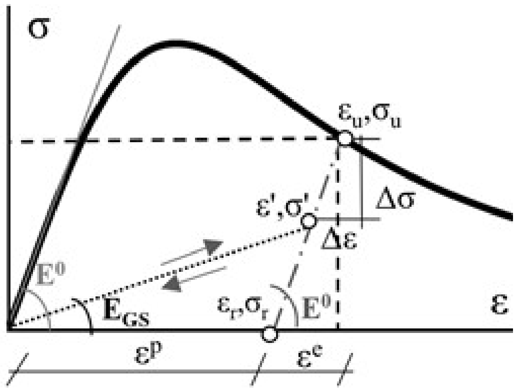

Figure 3. Linear elastic unloading/reloading.

The secant modulus Es is given by the stress-strain law as Equation 21.

$$E_s = \sigma(\varepsilon_u)/\varepsilon_u\,.\,(21)$$

Where the unloading strain (ε_u) is the maximum strain the material has ever experienced, the historical parameter. Despite the simplicity, the secant strategy loses representativity during cycles with an advanced strain stage since the permanent strains are not considered.

2.2.2 Linear elastic unloading/reloading

The linear elastic approach is based on the undamaged elastic modulus (E_0), as shown in Figure 3. The cycle is simplified by a straight line whose slope is E_0, which goes from the unloading point to the strain axis. The E_{GS} is required during the unloading/reloading regimes. Such modulus is represented by a straight line that starts in origin and intersects the cyclic path. The E_{GS} can be expressed as Equation 22.

$$E_{GS} = \sigma'/\varepsilon',\ (22)$$

where ε' is the current strain in the cycle, and σ' is the stress associated with ε' (Figure 3). The current stress σ' (Equation 23) is the unloading stress subtract from a stress variation Δσ and must be written as a function of the known parameters E_0, σ_u, ε_u, ε'.

$$\sigma' = \sigma_u - \Delta\sigma.\,(23)$$

The unloading strain (ε_u) can be divided into elastic and permanent parcels, as indicated by Equation 24.

$$\varepsilon_u = \varepsilon^e + \varepsilon^p.\ (24)$$

As the cyclic path follows the undamaged elastic modulus, the stress variation is calculated with Equation 25.

$$\Delta\sigma = E^0(\varepsilon_u - \varepsilon').\,(25)$$

Replacing $\Delta\sigma$ in Equation 23, the stress at any point of the cycle is given by Equation 26.

$$\sigma' = \sigma_u - E^0\varepsilon_u + E^0\varepsilon'.\,(26)$$

The linear elastic approach represents permanent strains, neglecting stiffness degradation. The E_{SG} is used in the cycles, but the degradation remains fixed as the historical variable.

2.2.3 Linear unloading/reloading based on the focal point

In experiments, Lee et al. [22] and Lee and Willam [27] observed that the material unloading is directed to a pole. As presented in Figure 4, the cyclic path is a straight line defined by the unloading point (ε_u, σ_u) and the focal point (ε_f, σ_f).

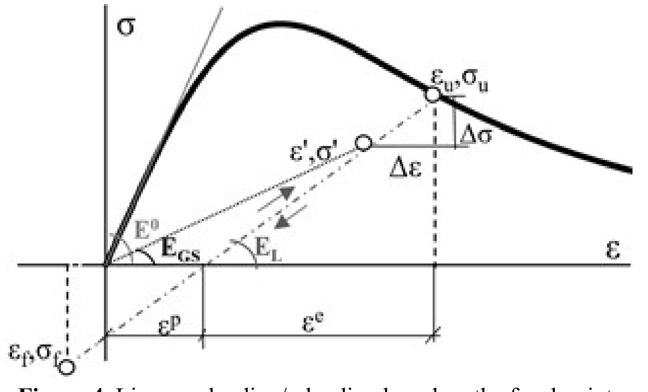

Figure 4. Linear unloading/reloading based on the focal point.

In the proposed method, the first step is the linear modulus (E_L) calculus. This modulus represents the unloading/reloading straight slope given by Equation 27.

$$E_L = \frac{\Delta\sigma}{\Delta\varepsilon} = \frac{(\sigma_u - \sigma_f)}{(\varepsilon_u - \varepsilon_f)} = \frac{(\sigma_u - \sigma')}{(\varepsilon_u - \varepsilon')}. (27)$$

Then, Equation 27 is rewritten as Equation 28 to provide σ'

$$\sigma' = \sigma_u - \frac{(\sigma_u - \sigma_f)}{(\varepsilon_u - \varepsilon_f)}(\varepsilon_u - \varepsilon'). (28)$$

At last, the generalized secant modulus is obtained as Equation 29.

$$E_{GS} = \frac{1}{\varepsilon'}\left[\sigma_u - \frac{(\sigma_u - \sigma_f)}{(\varepsilon_u - \varepsilon_f)}(\varepsilon_u - \varepsilon')\right]. (29)$$

The linear path based on a focal point improves cyclic material behavior representation since it can reproduce both stiffness degradation and permanent strain.

2.2.4 Nonlinear unloading/reloading

The previous focal point law has been extended to distinct unloading/reloading paths. Bono[29] adapted the original monotonic formulation of Popovics-Saez, introducing modifications in the origin and peak coordinates to make the cyclic analysis feasible. The Popovics-Saenz law proposed to describe the concrete monotonic compression behavior is calculated with Equation 30.

$$\sigma = f_i \frac{K(\varepsilon/\varepsilon_i)}{1 + A(\varepsilon/\varepsilon_i) + B(\varepsilon/\varepsilon_i)^2 + C(\varepsilon/\varepsilon_i)^3 + D(\varepsilon/\varepsilon_i)^R}, \text{with } i = c, t. (30)$$

Where $K = E_0(\varepsilon_i / f_i)$, $R = K / (K - 1)$; f_i represents concrete strength, ε is the current strain, and ε_i is the strain related to f_i. Physically, R is the reason between the elastic stress related to ε_i and the difference of this stress and f_i. A, B, C, D are variables dependent on the branch curve and the adjustment parameters β_{ref} and k_{ref}.

Kwon and Spacone [41] defined the focal point for compressive loading as the tensile strength. Under tension loading, an adequate monotonic curve should be adopted. The unloading/reloading paths, although, can be used without restrictions. In this case, the focal coordinate is the compressive strength. The E_{GS} is calculated as shown in Equation 29.

2.3 Cyclic monitoring

The iterative incremental method requires a technique to control the load cycles imposed on the numerical model. Therefore, two monitoring methods have been developed to inform the start and end of the loops: the step count method and the load limit method.

The step count method (Figure 5) needs the step numbers where the unloading starts and ends. Despite its efficiency, the monotonic path must be previously known, and the load script depends on the increment size. On the contrary, the load limit method (Figure 6) defines the cycles from the load values at the beginning of unloading and reloading. Tolerance is required since the equilibrium path points may not coincide with the specified limits. The load limit method is practical if the cycles loci are known from experimental data.

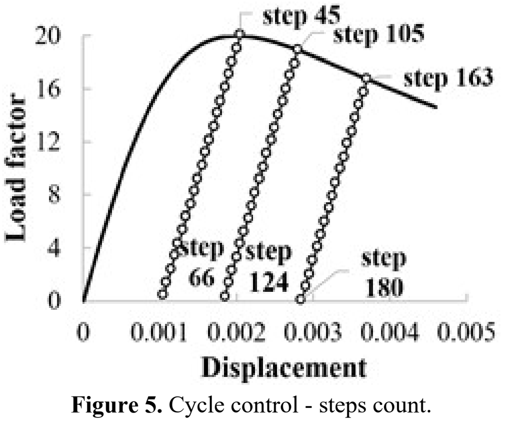

Figure 5. Cycle control - steps count.

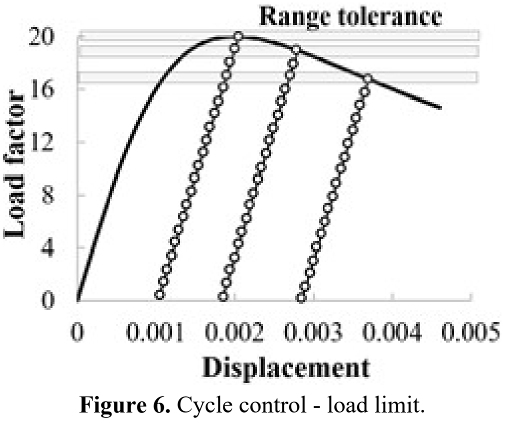

Figure 6. Cycle control - load limit.

Both monitoring methods operate at the displacement increment. To perform the unloading, once the critical point is identified into the Newton-Raphson algorithm, such increment is multiplied by -1.0. The reloading occurs with a second sign inversion. At this moment, the loading is resumed, driving back to the monotonic curve. For material points under the elastic regime, the unloading/reloading path agrees with the monotonic curve. This strategy is applied to the direct displacement control method, and there is no cycle number limit. The algorithm presented in Figure 7 summarizes the cyclic monitoring procedure.

Input: **P**, flag	**P**: reference load vector; flag: informs where the unload/reload starts
Output: λ_i, $\mathbf{d}_i$	λ_i: load factor; $\mathbf{d}_i$: displacement vector
while i $\leq i_{max}$ **do**	Step loop
while j $\leq j_{max}$ **do**	Iteration loop
$\mathbf{K}_{i-1}^{j}$	Stiffness matrix
$\delta\mathbf{d}_j^P, \delta\mathbf{d}_j^Q$	Displacement increments of reference ($\delta\mathbf{d}_j^P$) and residual forces ($\delta\mathbf{d}_j^Q$)
$\delta\lambda_j^i$	Load factor increment
$\delta\mathbf{d}_j^i$	Displacement vector increment
$\lambda_i, \mathbf{d}_i$	Variables update
if i == flag || (λ_{i-1} − flag) < tolerance **then**	Cyclic monitoring
$\lambda_j^i \leftarrow -1.0 \times \lambda_j^i$	Signal inversion of the load factor
end if	
$\mathbf{F}_i$	Internal forces vector
$\mathbf{Q}_i$	Residual forces vector
if Convergence is false **then**	Convergence verification
$j \leftarrow j + 1$	New iteration
end if	
end while	
$i \leftarrow i + 1$	New step
end while	

Figure 7. Standard Newton-Raphson algorithm, including the cyclic monitoring.

3 NUMERICAL SIMULATIONS

Numerical analyses have been performed in the INSANE (INteractive Structural ANalysis Environment), an open-source code developed at the Department of Structural Engineering of the Federal University of Minas Gerais, to evaluate the response of the proposed model. The first two examples consist of direct tension and direct compression, respectively. The proposed method has been validated by comparing the obtained results with experimental curves from the literature. The third example is a three-point bending test of a plain concrete beam. Finally, a reinforced concrete (RC) beam is submitted to a cyclic distributed load.

3.1 Direct tension

Golaparatnam and Sha [42] performed a series of experiments in plain concrete samples under cyclic tension with prismatic geometry (76 x 19 x 305 mm). The concrete properties are tensile strength f_t = 3.53 MPa, tensile strain limit in the elastic regime ε_t = 1.18 x 10^{-4}, and fracture energy G_f = 0.0564 N/mm.

Initially, a refinement test was performed in a monotonic analysis to define the mesh sensitivity. In the simulation, five meshes were analyzed, with 1, 4, 16, 60, and 320 elements. Since no evidence of localization effects was verified, the mesh with 60 four-node quadrilateral finite elements was adopted, considering an intermediate level of refinement.

The loading process assumed a reference load q = 19 N/mm, displacement increment of 5.0 x 10^{-7} m, and tolerance for the convergence in displacement of 1.0 x 10^{-4}. The cycles were introduced by the load limit monitoring method. Figure 8 illustrates the geometry configuration, the boundary conditions, the mesh, and the controlled degree of freedom.

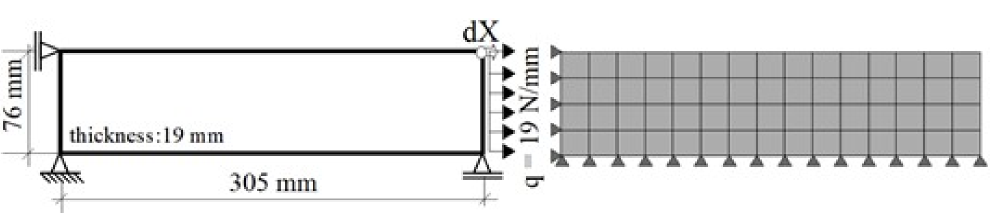

Figure 8. Direct tension simulation - geometry and mesh.

The material law by Boone et al. [25] and Boone and Ingraffea [26], and the Carreira and Chu [23], [24] were adopted to tension and compression, respectively. Besides the experimental parameters [42], other material properties were considered: Poisson ratio of 0.18 [43]; compressive strength of 40.4 MPa estimate from the relation [44], indicated in Equation 31.

$$\mathrm{f}_t = 0.3\ (f_c)^{2/3};\ (31)$$

and the elastic limit of the compressive strain $\varepsilon_c = 0.002$, from the NBR 6118 [45].
The characteristic length (h) is a parameter associated with the fracture process zone. Such value is usually related to the maximum aggregate size [46]. In the absence of information, (h) can be obtained from the region dimension used to measure the experimental strains. Here, it was considered h = 166 mm. The shear retention factor was admitted as βr = 0,05, a traditional value for plain concrete [47]. The maximum secant moduli degradation was limited to 92%. This number came from the monotonic path fitting to the experimental curve. For the linear unloading/reloading approach, the focal point is the concrete compressive strength. For the nonlinear cyclic strategy, the focal point of the stretch direction (ε_{f1}, σ_{f1}) is also the compressive strength, while the compressed direction focus (ε_{f2}, σ_{f2}) is the tensile strength [41]. An extra simulation was performed for the nonlinear formulation considering the origin as the focus to both directions. Parametrization of the law by Popovic-Saez was done to fit Carreira and Chu [23], [24] monotonic curve, providing β_{ref} = 1.8 and k_{ref} = 0.85. Table 1 resumes the material parameters.

Table 1. Material parameters: direct tension.

Compressive [23], [24] and tension [25], [26] law				**Linear focus law [22], [27]**			
				ε_f	-0.002	σ_f	-40.4 MPa
f_c	40.4 MPa	f_t	3.53 MPa	**Popovics-Saenz law [28]-[31]**			
ε_c	0.002	E	29,915 MPa	β_{ref}	1.8	k_{ref}	0.85
ν	0.18	G_f	0.0564 N/mm	ε_{f1}	-0.002	σ_{f1}	-40.4 MPa
h	166 mm	β_r	0.05	ε_{f2}	0.000118	σ_{f2}	3.53 MPa

The numerical stress-strain relations are shown in Figure 9, contrasting with the experimental curve from Gopalaratnam e Shah [42].

Since the secant strategy is based on an elastic degradation model, all the cycles are directed to the origin, and its priority is stiffness deterioration reproduction. The agreement between the simulated cycle initiation and the unloading points from the experimental curve was used to achieve representative results. The permanent strain is represented in the elastic approach. Thus, the reloading points were prescribed to be as close as possible to the experimental residual strains. The stiffness degradation, however, is neglected.

The cyclic laws based on the focal point embrace both phenomena: stiffness degradation and permanent strain representation. The cyclic path remained linear for the simulation using the nonlinear law where the focus is concrete compressive strength, presenting a similar result to the elastic strategy. This fact is related to the distance between the unloading points and the focus. Although, this approach showed its potential to represent hysteresis with distinct unloading/reloading paths when the focal point was set in origin.

As observed in the comparison between experimental and numerical curves, the last cycles have presented a less accurate representation. This result is related to the high level of degradation [1], [12], [13]. Therefore, a possible solution includes a variable focal point, depending on the current material degradation.

The last analysis evaluated the potential of a variable focus. The focal point coordinates of each cycle coincide with the null stress and the plastic strain related to that loop in the experimental curve. Figure 9 shows that the focal point strongly affects the configuration of the cycles, permitting a better adjustment of the numerical response.

Despite the restrictions of the adopted stress-strain laws, described as a linear path in most cases, they have represented concrete cyclic behavior satisfactorily. The approaches based on the focal point are more efficient in reproducing experimental results since they couple stiffness degradation and residual strain. However, analyzing such phenomena individually and disregarding the configuration of the cycles, the elastic strategy has been the most adequate approach to describe permanent strain. The secant representation has shown numerical robustness using the actual secant modulus. Based on these issues, the cyclic law selection must be guided by the drawbacks and the advantages of each law.

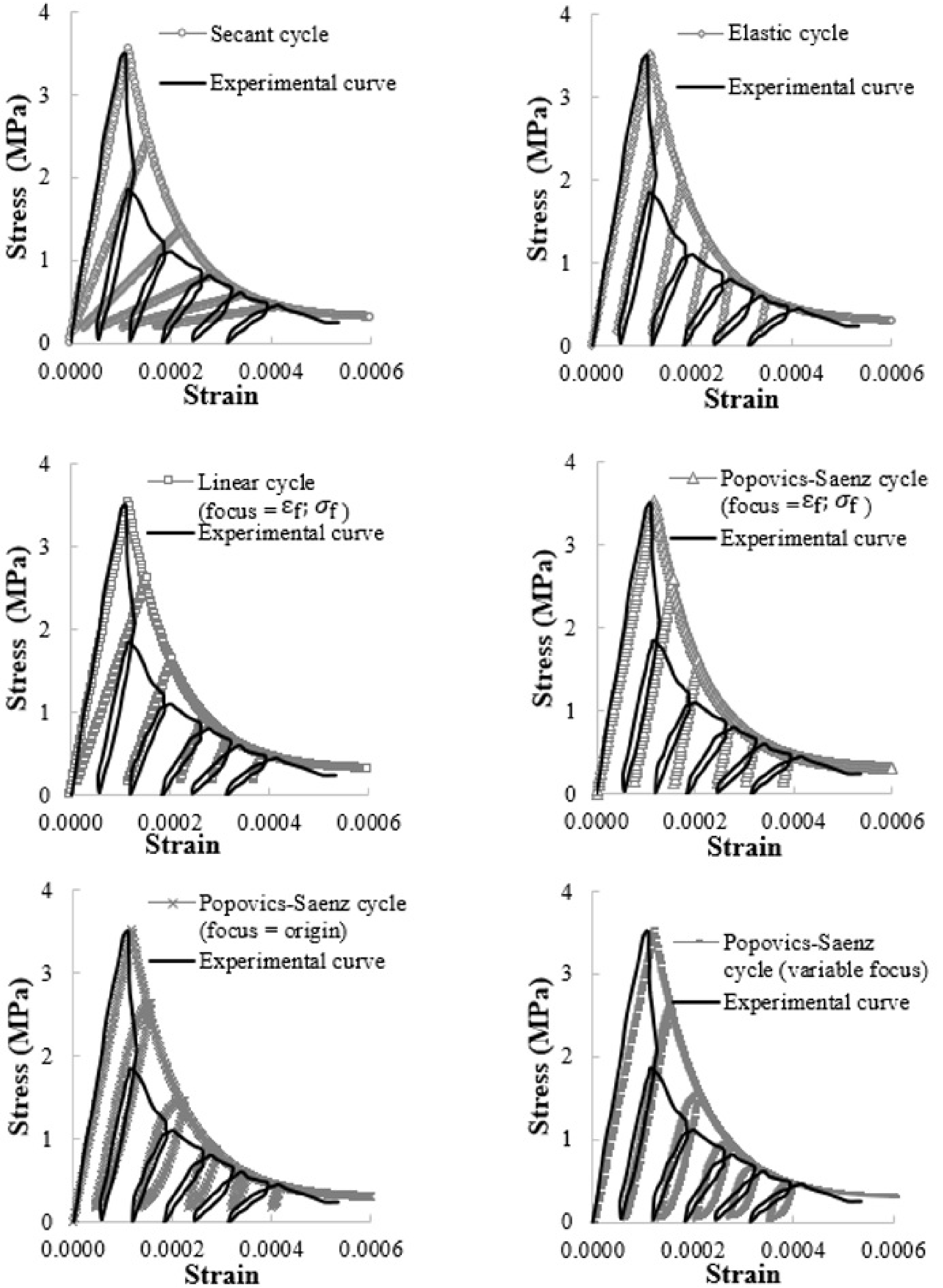

Figure 9. Direct tension simulations: different strategies to represent the load cycles.

3.2 Direct compression

Based on the experimental tests by Karsan and Jirsa [11], a cyclic compression was modeled. A refinement test was performed to define the mesh of 4 x 4 four-nodes quadrilateral (Figure 10). A load of q = 19 N/mm, a displacement increment of -5.0×10^{-7} m, and a tolerance convergence in load and displacement of 1.0×10^{-4} drove the loading process. The cycles were controlled by the load limit method.

The material parameters from the experimental test are: Poisson ratio $\nu = 0.18$; elastic modulus E = 31,700 MPa; fracture energy $G_f = 0.04$ N/mm; concrete compressive strength $f_c = 27.6$ MPa; and characteristic length h = 82.6 mm. The other parameters were estimated as: concrete tensile strength $f_t = 2.76$ MPa (Equation 31); strain in the compressive elastic limit $\varepsilon_c = 0.0016$ [45]; shear retention factor $\beta_r = 0{,}05$ [47].

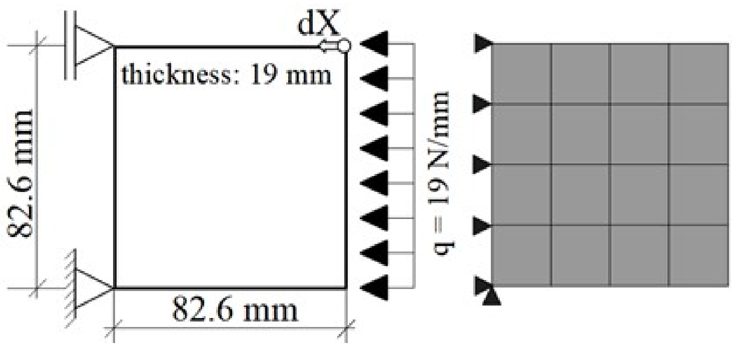

Figure 10. Direct compression simulation - geometry and mesh.

The concrete tensile strength parameter (f_t) is necessary to determine the focus of the linear law based on the focal point. Such focus was also adopted to the compressive direction for the law by Popovics-Saenz [28]-[31]. The concrete compressive strength, otherwise, was defined as the focal point for the tension direction. The parameters of the law proposed by Popovics-Saenz's were established to fit Carreira and Chu [23], [24] monotonic curve. The secant moduli maximum degradation was 90%. Table 2 summarizes all the parameters required by the stress-strain laws.

Table 2. Material parameters: direct compression.

Compressive [23], [24] and tension [25], [26] law				Linear focus law [22], [27]			
				ε_f	0,000087	σ_f	2.76 MPa
f_c	27.6 MPa	f_t	2.76 MPa	**Popovics-Saenz law [28]-[31]**			
ε_c	0.0016	E	31,700 MPa	β_{ref}	1.7	k_{ref}	0.85
ν	0.18	G_f	0.04 N/mm	ε_{f1}	0.000087	σ_{f1}	2.76 MPa
h	82.6 mm	β_r	0.05	ε_{f2}	-0.0016	σ_{f2}	-27.6 MPa

The responses (Figure 11) highlight the conclusions obtained in the compression simulations.

The secant law is restricted to degradation stiffness representation, while the elastic law can only reproduce residual strains. The results from the linear law based on the focal point show both phenomena, although the cycles remain simplified by a straight. Nevertheless, the cycles reproduced by the nonlinear law, considering the focus either in the concrete tensile strength or origin, showed the capacity to describe the experimental cyclic paths. Although, a discrepancy between the hysteresis loops from the test and the numerical simulations is noted. Such differences are related to the parametrization difficulty of the cyclic models. Since monotonic tests define the variables of the stress-strain laws, a relation among these parameters and the unloading/reloading regimes is unknown. The only variable that may change the cyclic configuration is the focal point.

In general, Popovics-Saenz [28]-[31] law with the focal point on the concrete tensile strength is a valid representation of the experimental curve. The proposed model could present a more precise reproduction of the cycles with an accurate definition of the focal point. Like the tension analysis, a numerical simulation was performed considering a variable focal point. Each cycle was directed to the intersection point between the empirical loop and the strain axis. The shapes of the load cycles fit the experimental curve better, although it is still necessary to determine a variable capable of controlling the hysteresis amplitude.

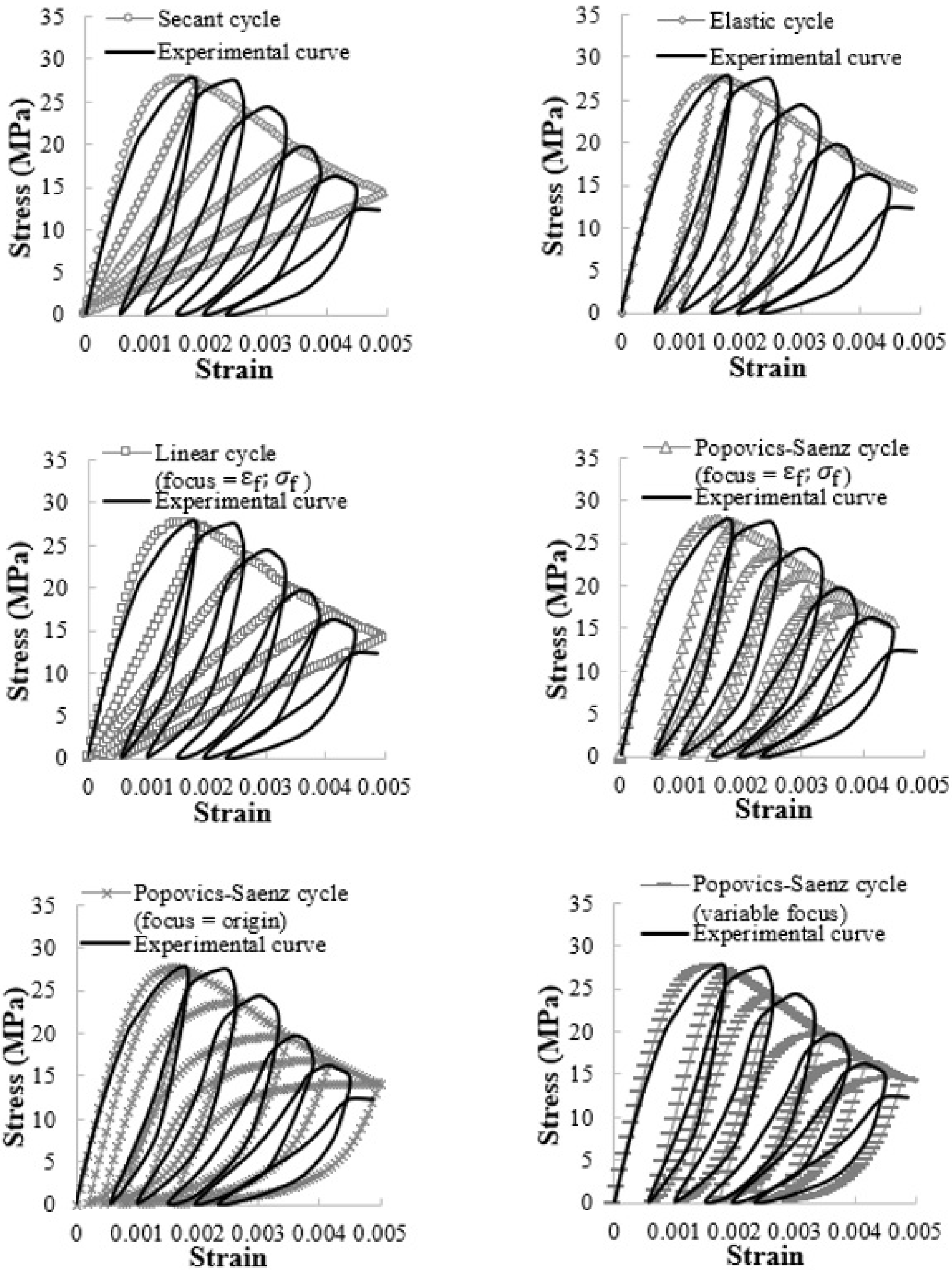

Figure 11. Direct compression simulations: different strategies to represent the load cycles.

3.3 Three-point bending test

This simulation modeled a three-point bending to evaluate the model response in more general load conditions. The geometry of the beam is illustrated in Figure 12, as in the reference work of Hordijk [48]. The node and the direction controlled are also highlighted. Because of the geometric symmetry, only half of the beam was modeled. The finite element model consists of 180 four-nodes quadrilateral elements in a plane stress state.

The loading process has assumed a unit load P, a displacement increment of -2.0 x 10^{-3} m, and a convergence in displacement of 1.0 x 10^{-4}. The monitoring method by load limit was selected. The plain concrete is characterized by the parameters in Table 3, as given by [48].

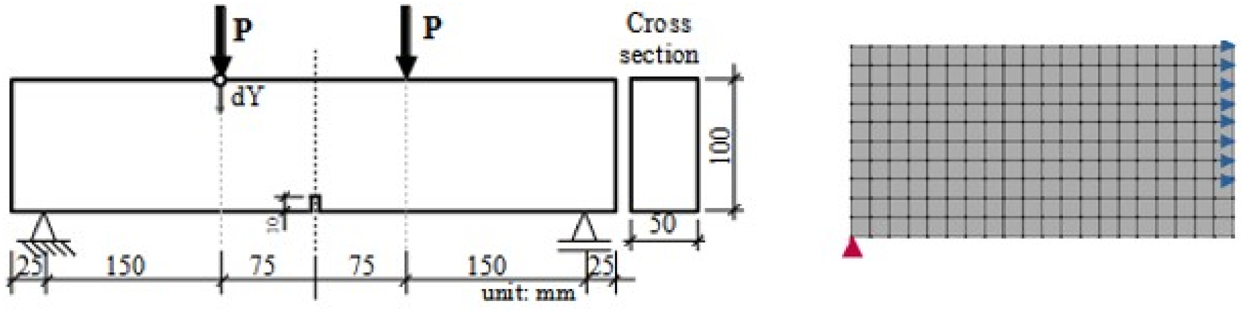

Figure 12. Three-point bending test: geometry and mesh.

The reference curve is the experimental test of Hordijk [48]. Variable focal points were adopted in the linear law based on the experimental reload points. The origin was the focus of the Popovics-Saenz law. The results are shown in Figure 13.

Table 3. Material parameters: three-point bending test.

Compressive [23], [24] and tension [25], [26] law				Popovics-Saenz law [28]-[31]			
f_c	59.5 MPa	f_t	3.75 MPa	β_{ref}	1.8	k_{ref}	0.85
ε_c	0.002	E	40485 MPa	ε_f	0.0	σ_f	0.0
ν	0.2	G_f	0.115 MN/m				
h	15 m	β_r	0.0001				

The secant strategy showed robustness in cyclic reproduction, while the other approaches exhibited instabilities. The cyclic elastic approach reproduced only the first cycle, and not even the step size reduction allowed it to conclude the simulation. The laws based on the focal point reached a more advanced strain state in the analysis, but they failed after the third cycle when numerical instabilities interrupted the simulation by not meeting the convergence.

These instabilities must be related to the E_{GS} in complex load states since the material points can present load sign inversion, even when an inversion is not observed in the structural behavior. A quadrant mapping of the stress-strain space is required to consider negative and positive quantities, improving the proposed model to embrace general load cases. The focal point is another subject that deserves attention in future works because of the dependency of the load loops on this variable. Nevertheless, the results show that all cycle hypotheses agree with the behavior observed in direct tension and direct compression from the literature.

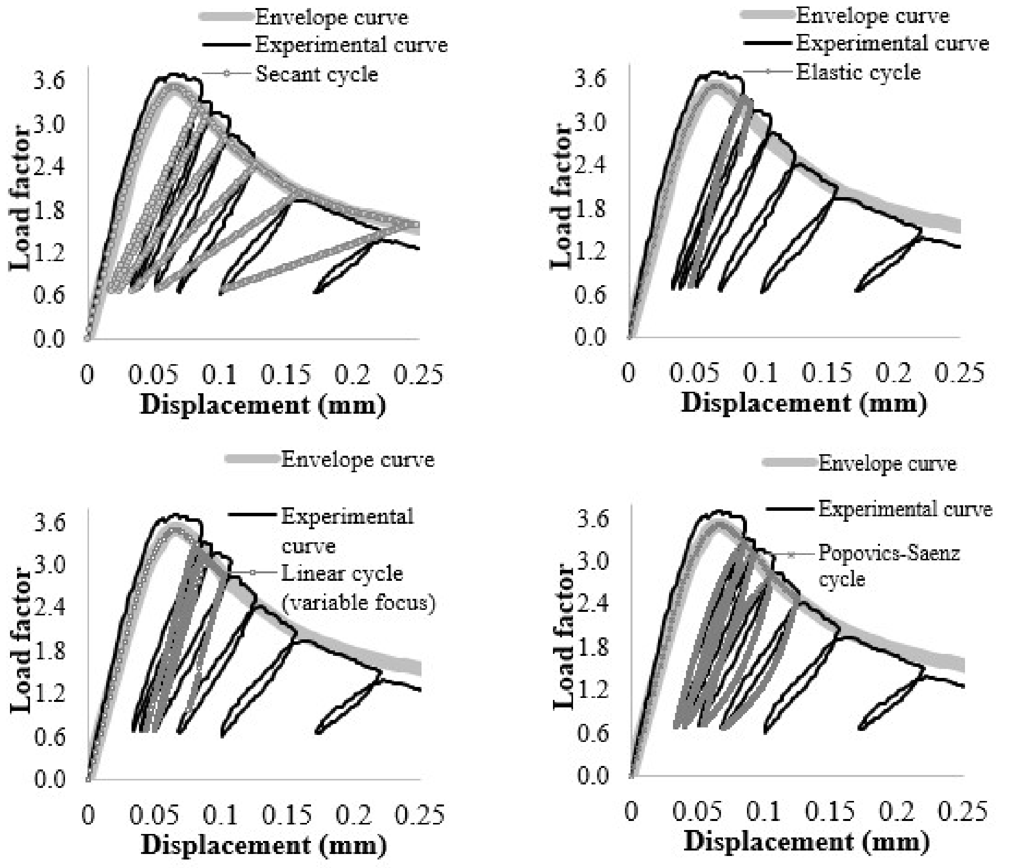

Figure 13. Three-point bending test: different strategies to represent the load cycles

3.4 Reinforced concrete beam subjected to uniform loading

A reinforced concrete (RC) beam subjected to a uniformly distributed load was modeled. Since RC is a material compound of concrete and steel, a combination of cyclic behaviors was adopted. The secant cycles were selected to represent the concrete elastic degradation, while the elastic cycles were adopted for steel to reproduce plastic strains during the yielding.

The structure dimensions were based on typical beams from projects (Figure 14). The mesh has 420 four-node quadrilateral concrete elements, and two-node bar elements represent the reinforcing steel. The material parameters are summarized in Table 4. The steel behavior was considered elastic-perfectly plastic with a perfect bond between steel and concrete.

The vertical displacement in the midspan of the beam was controlled with an increment of -1.0×10^{-4} m, convergence tolerance in displacement of 1.0×10^{-5}, and a distributed loading of q = 0.33 MN/m. The monitoring method by step count was selected, introducing three arbitrary cycles in the equilibrium path after the steel yielding to reproduce an intense unloading/reloading regime. The secant cycles were performed considering two different compressive laws for concrete: Carreira and Chu [23], [24], and Popovics-Saenz [28]-[31].

The structural response is shown in Figure 15, and the critical degradation stages are highlighted along the equilibrium path. As a reference, a curve is presented based on the reinforced concrete stages representing the elastic behavior of the materials, the concrete cracking phase, and the yield of the reinforcement. The microcrack nucleation (1) is observed when the graphic becomes nonlinear, and concrete starts to damage. Then, the microcracks grow (2) until a critical point in which the nonlinearities are significant. Thus, the microcracks coalescence culminate in macrocracks (3). In the last stage, the macrocracks propagate in concrete, and the steel reaches the plastification (4).

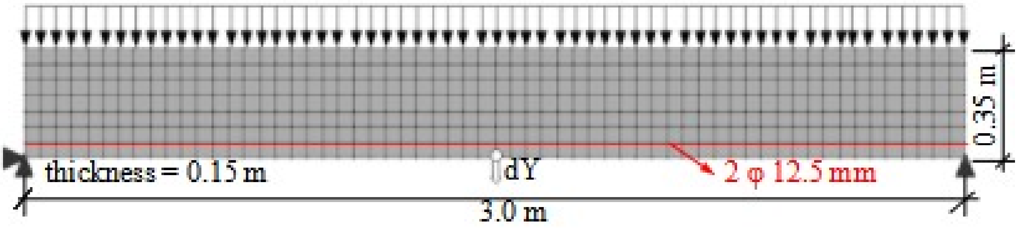

Figure 14. Reinforced concrete beam - geometry and mesh.

Table 4. Material parameters: concrete and steel.

Concrete: compressive [23], [24] and tension [25], [26] law								Steel: Von Mises criteria	
f_c	20.0 MPa	f_t	2.0 MPa	ν	0.2	G_f	3.0 x 10^{-5} MN/m	E	210,000 MPa
ε_c	0.002	ε_t	0.00008	β_{ref}	1.8	k_{ref}	0.85	ν	0.2
E	25,000 MPa	β_r	0.05	h	0.06 m	focus	origin	f_y	500 MPa

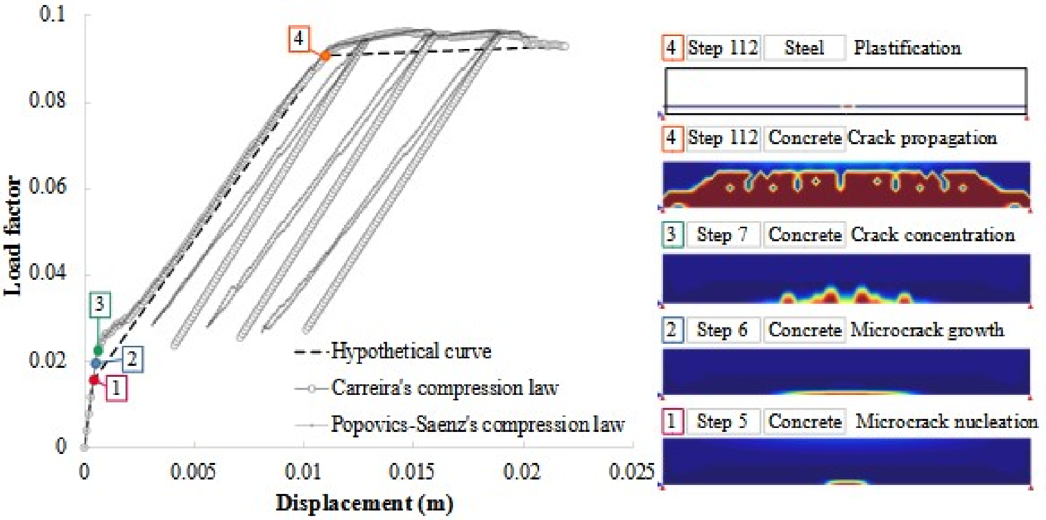

Figure 15. Reinforced concrete beam cyclic simulations.

The results from the simulation with the law by Carreira and Chu [23], [24] show an elastic cyclic behavior, while the simulation using the material description by Popovics-Saenz has a response between the elastic and the secant approaches. The selected concrete monotonic curve changed the cyclic configuration, but the steel conducted the unloading/reloading process in both analyses during the yielding stage.

4 CONCLUSIONS

A smeared crack model based on elastic degradation under cyclic loadings has been presented, aiming at a generalized secant modulus numerical approach. Four stress-strain laws with unloading/reloading descriptions have been adopted. The proposed method was validated by comparing numerical results of concrete under cyclic loading in compression and tension with experimental curves from the literature, resulting in good agreement. Three-point bending tests have been simulated for plain and reinforced concrete to evaluate the viability of applying this model to general cases. In this context, the main conclusions are:

i. The numerical analyses have shown that the developed method based on the generalized secant modulus fulfill the proposed aim, simulating load cycles with distinct characteristics;
ii. The examples validated by experimental curves prove the effectiveness of the strategies developed for concrete structures subjected to cyclic tension and cyclic compression;
iii. The implementation of the cyclic stress-strain laws has been successfully realized, and the variety of material laws allows versatility in the hysteresis representation;
iv. The approaches based on the focal point have the advantage of reproducing both stiffness degradation and residual strains;
v. The bending analysis has evaluated the present formulation application to simulate structures under conventional loads. Since numerical instabilities have been observed, an investigation must be carried to improve the proposed model to embrace general loads;
vi. The proposed methodology seems capable of simulating reinforced concrete structures, coupling the developed cyclic model for concrete with a plasticity model for steel.

ACKNOWLEDGEMENTS

The authors are grateful for the financial support of CNPq (in Portuguese "Conselho Nacional de Desenvolvimento Científico e Tecnológico") – Grant nº 307985/2020-2.

CITATIONS

[1] D. Z. Yankelevsky and H. W. Reinhardt, "Uniaxial behavior of concrete in cyclic tension," *J. Struct. Eng.*, vol. 115, no. 1, pp. 166–182, Jan. 1989, http://dx.doi.org/10.1061/(ASCE)0733-9445(1989)115:1(166).

[2] P. Zhang, Q. Ren, and D. Lei, "Hysteretic model for concrete under cyclic tension and cyclic tension-compression reversals," *Eng. Struct.*, vol. 163, pp. 388–395, May. 2018, http://dx.doi.org/10.1016/j.engstruct.2018.02.051.

[3] Y. R. Rashid, "Ultimate strength analysis of prestressed concrete pressure vessels," *Nucl. Eng. Des.*, vol. 7, no. 4, pp. 334–344, Apr. 1968, http://dx.doi.org/10.1016/0029-5493(68)90066-6.

[4] Z. P. Bažant, "Instability, ductility and size effect in strain-softening concrete," *ASCE J. Eng. Mech. Div.*, vol. 102, no. 2, pp. 331–344, Apr. 1976, http://dx.doi.org/10.1061/JMCEA3.0002111.

[5] J. G. Rots, P. Nauta, G. M. Kusters, and J. Blaauewendrra, "Smeared crack approach and fracture localization in concrete," *Heron*, vol. 30, no. 1, pp. 1–48, Jan. 1985.

[6] J. G. Rots and R. Borst, "Analysis of mixed-mode fracture in concrete," *J. Eng. Mech.*, vol. 113, no. 11, pp. 1739–1758, Nov 1987., http://dx.doi.org/10.1061/(ASCE)0733-9399(1987)113:11(1739).

[7] J. Mazars and G. Pijaudier-Cabot, "Continuum damage theory – application to concrete," *J. Eng. Mech.*, vol. 115, no. 2, pp. 345–365, Feb. 1989, http://dx.doi.org/10.1061/(ASCE)0733-9399(1989)115:2(345).

[8] J. Lemaitre, *A course on damage mechanics*, 1st ed. New York, US: Springer, 1992.

[9] J. H. P. Vree, W. A. M. Brekelmans, M. A. J. Van Gils, "Comparison of nonlocal approaches in continuum damage mechanics," *Comput. Struc.*, vol. 55, no. 4, pp. 581–588, May. 1995, http://dx.doi.org/10.1016/0045-7949(94)00501-S.

[10] B. P. Sinha, K. H. Gerstle, and L. G. Tulin, "Stress-strain relations for concrete under cyclic loading," *ACI Struct. J.*, vol. 61, no. 2, pp. 195–212, Feb. 1964, http://dx.doi.org/10.14359/7775.

[11] I. D. Karsan and S. O. Jirsa, "Behavior of concrete under compressive loadings," *J. Struct. Div.*, vol. 95, no. 12, pp. 2543–2563, Dec. 1969, http://dx.doi.org/10.1061/JSDEAG.0002424.

[12] D. Z. Yankelevsky and H. W. Reinhardt, "Model for cyclic compressive behavior of concrete," *J. Struct. Eng.*, vol. 113, no. 2, pp. 228–240, Feb. 1987, http://dx.doi.org/10.1061/(ASCE)0733-9445(1987)113:2(228).

[13] D. Z. Yankelevsky and H. W. Reinhardt "Focal point model for uniaxial cyclic behavior of concrete," in *IABSE Colloquium (Delft)*, 1987, pp. 99–106. http://doi.org/10.5169/seals-41920.

[14] J. F. Sima, P. Roca, and C. Molins, "Cyclic constitutive model of concrete," *Eng. Struct. J.*, vol. 30, no. 3, pp. 695–706, Mar. 2008, http://dx.doi.org/10.1016/j.engstruct.2007.05.005.

[15] M. Breccolotti, M. Bonfible, A. D'Alessandro, and A. Materazzi, "Constitutive modeling of plain concrete subjected to cyclic uniaxial compressive loading," *Constr. Build. Mater.*, vol. 94, pp. 172–180, Jul. 2015, http://dx.doi.org/10.1016/j.conbuildmat.2015.06.067.

[16] D.-C. Feng, Z. Wang, X.-Y. Cao, and G. Wu, "Damage mechanics-based modeling approaches for cyclic analysis of precast concrete structures," *Int. J. Damage Mech.*, vol. 29, no. 6, pp. 965–987, Jan. 2020, http://dx.doi.org/10.1177/1056789519900783.

[17] G. M. S. Alva, R. M. F. Canha, J. Oliveira Fo., and A. L. H. C. El Debs, "Numerical model for analysis of reinforced concrete beams under repeated cyclic loads," *Sci. Eng. J.*, vol. 22, no. 2, pp. 105–114, Dec. 2013, http://dx.doi.org/10.14393/19834071.2013.23805.

[18] X. Chen, L. Xu, and J. Bu, "Experimental study and constitutive model on complete stress-strain relation of plain concrete in uniaxial cyclic tension," *KSCE J. Civ. Eng.*, vol. 21, no. 5, pp. 1829–1835, Sep. 2017, http://dx.doi.org/10.1007/s12205-016-0802-0.

[19] M. Moharrami and I. Koutromanos, "Triaxial constitutive model for concrete under cyclic loading," *J. Struct. Eng.,* vol. 142, no. 7, pp. 1–15, Feb. 2016, https://doi.org/10.1061/(ASCE)ST.1943-541X.0001491.

[20] C. Mourlas, M. Papadrakakis, and G. Markou, "A computationally efficient model for the cyclic behavior of reinforced concrete structural members," *Eng. Struct.*, vol. 141, pp. 97–125, Mar. 2017, http://dx.doi.org/10.1016/j.engstruct.2017.03.012.

[21] Z. Li and Q. Ren "Development of a practical uniaxial cyclic constitutive model for concrete," in *IOP Conf. Ser.: Earth Environ. Sci.,* vol. 295, pp. 1–10, Jul. 2019, https://doi.org/10.1088/1755-1315/295/4/042057.

[22] Y. H. Lee, K. Willam, and H. D. Kang "Experimental observations of concrete behavior under uniaxial compression," in *Proceedings FRAMCOS-2,* 1995, pp. 397–414.

[23] D. J. Carreira and K.-H. Chu, "Stress-strain relationship for plain concrete in compression," *J. Am. Concr. Inst.*, vol. 82, no. 6, pp. 797–804, Nov. 1985, http://dx.doi.org/10.14359/10390.

[24] D. J. Carreira and K.-H. Chu, "Stress-strain relationship for reinforced concrete in tension," *J. Am. Concr. Inst.*, vol. 83, no. 1, pp. 21–28, Jan. 1986, http://dx.doi.org/10.14359/1756.

[25] T. Boone, P. A. Wawrzynek, and A. R. Ingraffea, "Simulation of the fracture process in rock with application to hydrofracturing," *Int. J. Rock Mech. Min. Sci.*, vol. 23, no. 3, pp. 255–265, 1986, http://dx.doi.org/10.1016/0148-9062(86)90971-X.

[26] T. Boone and A. R. Ingraffea "Simulation of the fracture process at rock interfaces," in *4th Int. Conf. on Numerical Methods in Fracture Mec.*, 1987, pp. 519–531.

[27] Y. H. Lee and K. Willam, "Mechanical properties of concrete in uniaxial compression," *ACI Mater. J.*, vol. 94, no. 6, pp. 457–471, Nov 1997, http://dx.doi.org/10.14359/329.

[28] J. J. C. Popovics, "A numerical approach to the complete stress-strain curve of concrete," *Cement Concr. Res.*, vol. 3, no. 5, pp. 583–599, Sep 1973, http://dx.doi.org/10.1016/0008-8846(73)90096-3.

[29] G. F. F. Bono "Modelos constitutivos para análise tridimensional de estruturas de concreto armado através do método dos elementos finitos," Ph.D. dissertation, Dept. Civ. Eng., UFRGS, Porto Alegre, RS, 2008. [Online]. Available: https://lume.ufrgs.br.

[30] H. O. Korsal, T. Turgay, C. Karakoç, and S. Ayçenk, "Modeling aspects concerning the axial behavior of RC columns," *WIT Trans. Eng. Sci.*, vol. 72, pp. 175–183, 2011, http://dx.doi.org/10.2495/MC110161.

[31] B. Y. Bahn "Behavior of concrete and slender reinforced concrete columns under cyclic axial compression with bidirectional eccentricities," Ph.D. dissertation, Dept. Civ. Env. Eng., NJIT, Newwark, NJ, 1994. [Online]. Available: https://digitalcommons.njit.edu.

[32] S. S. Penna "Formulação multipontecial para modelos de degradação elástica – Unificação teórica, proposta de novo modelo, implementação computacional e modelagem de estruturas de concreto," Ph.D. dissertation, Dept. Struct. Eng., UFMG, Belo Horizonte, MG, 2011. [Online]. Available: http://www.pos.dees.ufmg.br.

[33] J.-L. Batoz and G. Dhat, "Incremental displacement algorithms for nonlinear problems," *Int. J. Numer. Methods Eng.*, vol. 14, pp. 1262–1267, 1979, http://dx.doi.org/10.1002/nme.1620140811.

[34] D. Ngo and A. C. Scordelis, "Finite element analysis of reinforced concrete beams," *J. Am. Concr. Inst.*, vol. 64, no. 3, pp. 152–163, Mar. 1967, http://dx.doi.org/10.14359/7551.

[35] R. de Borst and M. A. Gutiérrez, "A unified framework for concrete damage and fracture models including size effects," *Int. J. Fract.*, vol. 95, pp. 261–277, Jan. 1999, http://dx.doi.org/10.1023/A:1018664705895.

[36] R. de Borst, "Fracture in quasi-brittle materials: a review of continuum damage-based approaches," *Eng. Fract. Mech.*, vol. 69, no. 2, pp. 95–112, Jan. 2002, http://dx.doi.org/10.1016/S0013-7944(01)00082-0.

[37] I. Carol, E. Rizzi, and K. Willam, "A unified theory of elastic degradation and damage based on a loading surface," *Int. J. Solids Struct.*, vol. 31, no. 20, pp. 2835–2865, Oct. 1994, http://dx.doi.org/10.1016/0020-7683(94)90072-8.

[38] I. Carol, E. Rizzi, and K. Willam, "On the formulation of anisotropic elastic degradation. I. Theory based on a pseudo-logarithmic damage tensor rate," *Int. J. Solids Struct.*, vol. 38, no. 4, pp. 491–518, Jan. 2001, http://dx.doi.org/10.1016/S0020-7683(00)00030-5.

[39] I. Carol, E. Rizzi, and K. Willam, "On the formulation of anisotropic elastic degradation. II. Generalized pseudo-Rankine model for tensile damage," *Int. J. Solids Struct.*, vol. 38, no. 4, pp. 519–546, Jan. 2001, http://dx.doi.org/10.1016/S0020-7683(00)00031-7.

[40] L. R. S. Pereira, "Formulação de modelos de dano tensorial para análise fisicamente não linear de estruturas de concreto submetidas a carregamentos monotônicos e cíclicos," M. S. thesis, Dept. Struct. Eng., UFMG, Belo Horizonte, MG, 2020. [Online]. Available: http://www.pos.dees.ufmg.br.

[41] M. Kwon and E. Spacone, "Three-dimensional finite element analyses of reinforced concrete columns," *Comput. Struc.*, vol. 80, no. 2, pp. 199–2021, 2002, http://dx.doi.org/10.1016/S0045-7949(01)00155-9.

[42] V. Gopalaratnam and S. Shah, "Softening response of plain concrete in direct tension," *ACI J. Proc.*, vol. 82, no. 3, pp. 310–323, May. 1985, http://dx.doi.org/10.14359/10338.

[43] J. K. Wight and J. G. MacGregor, *Reinforced Concrete – Mechanics and Design*, 6th ed. New Jersey, US: Pearson, 2012.

[44] Federation International Du Beton, *FIB Model Code for Concrete Structures*, 2010.

[45] Associação Brasileira de Normas Técnicas, *Projeto de Estruturas De Concreto – Procedimento, NBR 6118*, 2014.

[46] Z. P. Bažant and G. Pijaudier-Cabot, "Measurement of characteristic length of nonlocal continuum," *J. Eng. Mech.*, vol. 115, no. 4, pp. 755–767, 1989, http://dx.doi.org/10.1061/(ASCE)0733-9399(1989)115:4(755).

[47] D. L. Araújo, L. C. Carmo, F. G. T. Nunes, and R. D. Toledo Fo., "Computational modeling of steel fiber reinforced concrete beams subjected to shear," *Rev. IBRACON Estrut. Mater.*, vol. 3, no. 1, pp. 68–94, 2010, http://dx.doi.org/10.1590/S1983-41952010000100005.

[48] D. A. Hordijk "Local approach to fatigue of concrete," Ph.D. dissertation, TU Delft, Delft, ZH, 1991. [Online]. Available: https://repository.tudelft.nl.

Author contributions: LRSP, SSP: computer programming, conceptualization, methodology, writing, formal analysis.

Editors: Osvaldo Manzoli, Guilherme Aris Parsekian.

IBRACON Structures and Materials Journal
Revista IBRACON de Estruturas e Materiais
ISSN 1983-4195 ismj.org

ORIGINAL ARTICLE

Nonlinear analysis of reinforced concrete structures using thin flat shell elements

Análise não linear de estruturas de concreto armado usando elementos finitos de cascas finas e planas

Jordlly Reydson de Barros Silva[a,b]
Bernardo Horowitz[b]

[a]Universidade Federal Rural de Pernambuco – UFRPE, Unidade Acadêmica do Cabo de Santo Agostinho – UACSA, Cabo de Santo Agostinho, PE, Brasil
[b]Universidade Federal de Pernambuco – UFPE, Departamento de Engenharia Civil, Programa de Pós-graduação em Engenharia Civil, Recife, PE, Brasil

Received 04 October 2021
Accepted 02 January2022

Abstract: This paper presents the development of a nonlinear finite element analysis program for reinforced concrete structures, subject to monotonic loading, using thin flat shell finite elements. The element thickness is discretized in concrete and steel layers. It is adopted the Newton-Raphson method, considering a secant stiffness approach for the Material Nonlinear Analysis, based on the Modified Compression Field Model (MCFT), unlike the usual tangent stiffness approach. The original formulation was expanded to also consider the Geometric Nonlinear Analysis, through a Total Lagrangian Formulation. The program was validated through comparison with experimental results, for different structures. It was observed good agreement, besides adequate computational cost.

Keywords: reinforced concrete, finite elements, nonlinear analysis, shells, plates.

Resumo: O presente artigo apresenta o desenvolvimento de uma ferramenta para a análise não-linear de estruturas de concreto armado, sujeitas a carregamentos monotônicos, utilizando o elemento finito de cascas finas e planas, o qual, é discretizado, ao longo da sua espessura, em lamelas de concreto e camadas de aço. É utilizado o método de Newton-Raphson, adotando, na consideração da não-linearidade física, a rigidez secante do material, baseada no modelo do campo de compressão modificado, no lugar da abordagem via rigidez tangente. A formulação original do elemento foi expandida para considerar também a não-linearidade geométrica, através de uma formulação Lagrangiana total. A validação da ferramenta é via comparação com resultados experimentais da literatura, para diversas estruturas, onde pode ser observada boa aderência além de adequado custo computacional.

Palavras-chave: concreto armado, elementos finitos, análise não-linear, cascas, placas.

How to cite: J. R. B. Silva and B. Horowitz, "Nonlinear analysis of reinforced concrete structures using thin flat shell elements," *Rev. IBRACON Estrut. Mater.*, vol. 15, no. 4, e15407, 2022, https://doi.org/10.1590/S1983-41952022000400007

1 INTRODUCTION

In reinforced concrete structures design, the civil engineer analyzes the real situation based on simplifying hypotheses, so that the structural models used in the analysis are sufficiently accurate and safe, but still having adequate simplicity, for use on project office.

Besides that, the development of construction technology has allowed the achievement of complex structures, with large spans and highly slender elements. In these cases, some of usual simplifying hypotheses may no longer represent

Corresponding author: Jordlly Reydson de Barros Silva. E-mail: jordlly.silva@ufrpe.br
Financial support: None.
Conflict of interest: Nothing to declare.
Data Availability: The data that support the findings of this study are available from the corresponding author, J. R. B. Silva, upon reasonable request.
This is an Open Access article distributed under the terms of the Creative Commons Attribution License, which permits unrestricted use, distribution, and reproduction in any medium, provided the original work is properly cited.

the actual structural behavior, due to the increase of relevant nonlinear effects associated with the material response, such as concrete cracking (material nonlinearity) or large displacements (geometric nonlinearity).

Fortunately, the modern computer has allowed the use of sophisticated structural models, once considered unfeasible for practical applications, to gain space in the market, including nonlinear finite element analysis (NL-FEA). It leads the technical community to a constant review of the structural models used, always seeking to associate a safe design with the productivity resulting from the most efficient technologies available.

Several structural practical applications can be analyzed through shell models, such as: shear walls, shell roofs, water tanks or other storage structures. The analysis complexity and the computer development has been stimulating the search for numerical tools to solve this problem (shell finite elements). The challenge becomes greater when the structure material is reinforced concrete (RC), where the material behavior plays a crucial role in the construction response. Consequently, the material constitutive models are a determining point for a satisfactory analysis. Among the most common approaches for shell element formulation, one can mention degenerate shell elements, which are based on three-dimensional equilibrium equations, and shell elements developed by the superposition of membrane and plate elements.

Following the first option, Luu et al. [1] proposed the CSMM-based shell element for reinforced concrete structures, for material nonlinear analysis (MNA). It uses the smeared crack theory Cyclic Softened Membrane Model (CSMM), created at the University of Houston. This 8-node degenerate shell element has 40 degrees of freedom (DOF): 3 translations and 2 rotations per node, where each nodal rotation follows a specific nodal coordinate system. Its nonlinear analysis procedure uses a Newton-Raphson approach (tangent stiffness).

Another notorious tool that also makes use of degenerate shell elements is VecTor4. This software considers both MNA and Geometric Nonlinear Analysis (GNA), through a Total Lagrangian Formulation (TLF). It was developed at the University of Toronto and its material model is based on the Modified Compression Field Theory (MCFT) [2], [3]. The VecTor4 quadrilateral 9-node shell element has 42 DOF: 3 translation (all nodes) and two rotations (only at the edge nodes). Again, the nodal rotations follow specific nodal coordinate systems, defined in each node. It is an element that combines in its formulation Langrangian and Serendipity shape functions, being therefore also called heterosis [4]. Its nonlinear analysis procedure differs from Luu et al. [1] and uses a direct secant stiffness approach.

Following the other mentioned option in shell element development (superposing membrane and plate elements), Barrales [5] proposed a simple and efficient quadrilateral thin fat layered shell element (QTFLS), for MNA. This 4-node element has 6 DOF per node (3 translations and 3 rotations). Its nonlinear analysis procedure also uses a Newton-Raphson approach (tangent stiffness). An interesting point about this formulation is that, unlike degenerate shell elements, this element explicitly has the nodal in-plane rotation DOF (drilling). Therefore, it is not necessary to use nodal coordinate systems to assemble the elements rotation DOF. According to Silva and Horowitz [6], when modeling U-Shaped RC shear walls using degenerate elements, such as VecTor4, special attention is required in the rotations DOF compatibility, in the L-connection elements (through nodal coordinate systems). The Barrales [5] element requires only local and global coordinate systems, an attractive feature. As usual in RC Shell structures NL-FEA, all discussed elements have its thickness discretized in concrete and steel layers, to properly consider the internal stresses variation along the thickness.

This paper expands the Barrales [5] QTFLS shell element formulation to consider both MNA and GNA, using a TLF [7]. The formulation is implemented in a NL-FEA program for RC structures, subject to monotonic loads. The element thickness is also discretized in concrete and steel layers. It is adopted the Newton-Raphson method, but considering a secant stiffness approach, using the basis of the Modified Compression Field Model (MCFT), unlike the original tangent stiffness approach. The program was validated through comparison with experimental and numerical results [1], [4], for different structures. It was observed good agreement, besides adequate computational cost.

2 NONLINEAR FINITE ELEMENT PROCEDURE

This section presents the material and geometric nonlinear finite element procedure used for analysis of reinforced concrete structures.

2.1 Incremental-iterative procedure

In nonlinear analysis, the set of equilibrium equations can be obtained through the principle of virtual works (PVW). Based on these equations, and discretizing the structure in finite elements, usually, the problem can be solved iteratively, using the Newton-Raphson method, Equation 1:

$$\{d\}_{n+1} = \{d\}_n + [K_G]_n^{-1}(\{F_{ext}\} - \{F_{int}\}) \quad (1)$$

where the subscript n indicates the iteration number where the parameter must be evaluated, $\{d\}$ is the global nodal displacements vector, $\{F_{ext}\}$ is the external forces vector, and $[K_G]$ and $\{F_{int}\}$ are, respectively, the tangent stiffness matrix and the internal forces vector that can be obtained through the corresponding elements contributions, $[k_e]$ and $\{f_e\}$. The iterative process continues until a stopping criterion is met, such as: the iteration number exceeds the maximum value or, for a given tolerance tol, the relative norm of the difference between the vectors $\{d\}_{n+1}$ and $\{d\}_n$, convergence criterion parameter $error$, is small enough, namely Equation 2.

$$error = \frac{|\{d\}_{n+1} - \{d\}_n|}{|\{d\}_{n+1}|} < tol \quad (2)$$

According to De Borst et al. [8], it is important to apply the external forces incrementally, otherwise, due to the material nonlinear behavior or numerical characteristics of the solution procedure, in very large load steps, it is possible to arise serious convergence problems or inappropriate results. Thus, the solution procedure adopted in this paper is called incremental-iterative, using a load control approach, where Equation 1 is applied iteratively in each incremental load step.

Also, according to De Borst et al. [8], since the solution procedure tends to reach an equilibrium configuration, in most cases, which stiffness matrix was adopted in the iterative process is less relevant. Based on this and knowing the numerical stability, which is often observed in secant stiffness analysis, even though the convergence rate may be lower compared to tangent stiffness analysis [9], in this paper, it was used a secant stiffness approach, unlike Barrales [5] who adopted a tangent stiffness approach.

2.2 Quadrilateral thin flat layered shell element - QTFLS

In this paper, the Quadrilateral Thin Flat Layered Shell Element - QTFLS, proposed by Barrales [5] and Rojas et al. [10], was adopted. It is a combination of the Quadrilateral Layered Membrane Element with Drilling Degrees of Freedom (DOF) - QLMD [11], and the Discrete Kirchhoff Quadrilateral Element - DKQ [12], where the Kirchhoff's assumptions for thin plates are considered. Figure 1 represents this 4-nodes finite element, the discretization of the element thickness in layers and its 6 degrees of freedom per node: 2 in-plane translations, 1 in-plane rotation (drilling), 2 out-of-plane rotations and 1 translation perpendicular to the element plane.

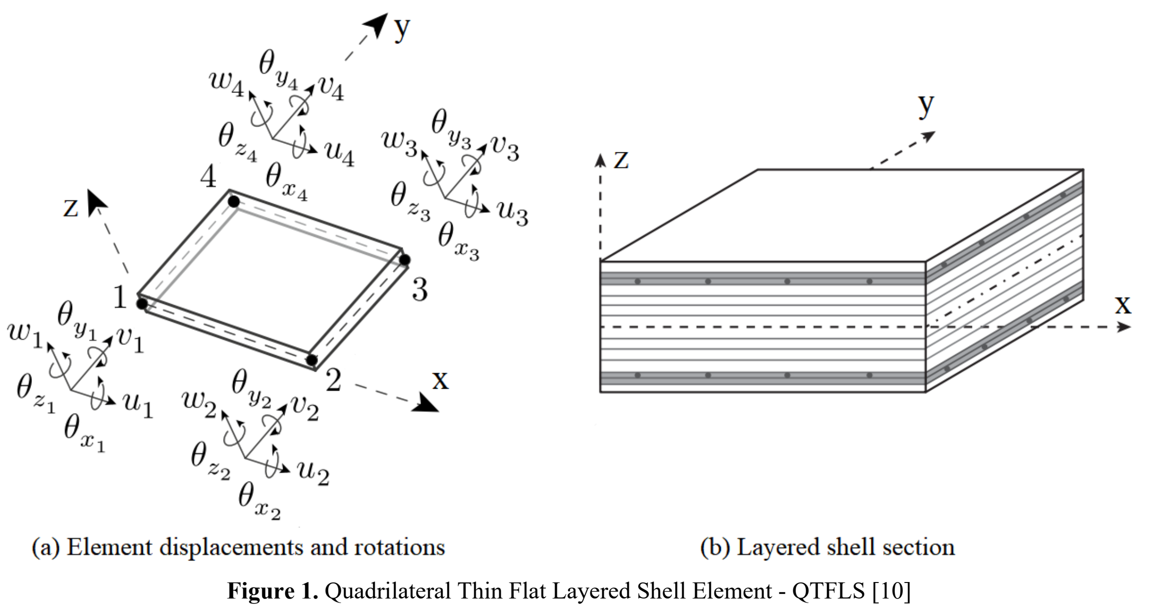

Figure 1. Quadrilateral Thin Flat Layered Shell Element - QTFLS [10]

In the QTFLS element, both the displacement and deformation fields are established through the superposition of membrane and plate behaviors. According to Barrales [5], this approach has the advantage of allowing different shape functions for each behavior.

As usual in finite element analysis, the strain vector $\{\varepsilon\}$ can be related to the element displacement vector $\{\mathrm{d_e}\}$ through the kinematic matrix $[\mathrm{B}']$. Equation 2 expands this relationship by superposing the linear membrane component $\{\varepsilon_\mathrm{m}\}$, the linear plate component $\{\varepsilon_\mathrm{b}^0\}$ and the nonlinear plate component $\{\varepsilon_\mathrm{b}^\mathrm{L}\}$:

$$\{\varepsilon\} = [B']\{d_e\} = \{\varepsilon_m\} + \{\varepsilon_b^0\} + \{\varepsilon_b^L\} = [B_m]\{d_e^m\} + z_L[B_b^0]\{d_e^b\} + \frac{1}{2}[B_b^L]\{d_e^b\} \tag{2}$$

where $[B_m]$ and $[B_b^0]$ are the kinematic matrices that represent the linear relationship between the membrane $\{d_e^m\}$ and plate $\{d_e^b\}$ element displacements and the corresponding strain component $\{\varepsilon_m\}$ and $\{\varepsilon_b^0\}$. On the other hand, the matrix $[B_b^L]$ is related to the consideration of the geometric nonlinearity of the problem, through the nonlinear plate strain component $\{\varepsilon_b^L\}$, discussed in section 2.5. The z_L parameter refers to the layer z local coordinate. The formulation of the matrices $[B_m]$, $[B_b^0]$ and $[B_b^L]$ are well-known in the technical community and its detailed development can be easily found in appropriate bibliographies [5], [10]–[13]. However, to contribute to the paper completeness, these parameters will be briefly discussed in the following subsections.

2.3 Quadrilateral Layered Membrane Element with Drilling DOF – QLMD

The QLMD membrane element uses a combination of linear shape functions, Equation 3, and cubic Hermite functions, Equation 4. This 4-node element has 3 degree of freedom per node (2 in-plane translations and 1 in-plane rotation, drilling).

$$M_1(\eta) = \frac{1}{2}(1-\eta) \qquad M_2(\eta) = \frac{1}{2}(1+\eta) \tag{3}$$

$$N_1(\eta) = \frac{1}{2} - \frac{3}{4}\eta + \frac{1}{4}\eta^3 \qquad N_2(\eta) = +\frac{1}{4} - \frac{1}{4}\eta - \frac{1}{4}\eta^2 + \frac{1}{4}\eta^3 \tag{4a}$$

$$N_3(\eta) = \frac{1}{2} + \frac{3}{4}\eta - \frac{1}{4}\eta^3 \qquad N_4(\eta) = -\frac{1}{4} - \frac{1}{4}\eta + \frac{1}{4}\eta^2 + \frac{1}{4}\eta^3 \tag{4b}$$

The membrane displacement field in natural coordinates (ξ, η) is given by the following interpolation:

$$\begin{Bmatrix} u_m \\ v_m \end{Bmatrix} = [MN]_{(2\times16)}[Tr]_{(16\times12)}\{d_e^m\}_{(12\times1)} \tag{5a}$$

$$[MN] = \begin{bmatrix} M_1(\xi)N_1(\eta) & 0 \\ 0 & M_1(\eta)N_1(\xi) \\ -M_1(\xi)N_2(\eta) & 0 \\ 0 & M_1(\eta)N_2(\xi) \\ M_2(\xi)N_1(\eta) & 0 \\ 0 & M_1(\eta)N_3(\xi) \\ -M_2(\xi)N_2(\eta) & 0 \\ 0 & M_1(\eta)N_4(\xi) \\ M_2(\xi)N_3(\eta) & 0 \\ 0 & M_2(\eta)N_3(\xi) \\ -M_2(\xi)N_4(\eta) & 0 \\ 0 & M_2(\eta)N_4(\xi) \\ M_1(\xi)N_3(\eta) & 0 \\ 0 & M_2(\eta)N_1(\xi) \\ -M_1(\xi)N_4(\eta) & 0 \\ 0 & M_2(\eta)N_2(\xi) \end{bmatrix}^T \tag{5b}$$

$$[Tr]=\frac{1}{2}\begin{bmatrix}2&0&0&0&0&0&0&0&0&0&0&0\\0&2&0&0&0&0&0&0&0&0&0&0\\0&0&y_4-y_1&0&0&0&0&0&0&0&0&0\\0&0&x_2-x_1&0&0&0&0&0&0&0&0&0\\0&0&0&2&0&0&0&0&0&0&0&0\\0&0&0&0&2&0&0&0&0&0&0&0\\0&0&0&0&0&y_3-y_2&0&0&0&0&0&0\\0&0&0&0&0&x_2-x_1&0&0&0&0&0&0\\0&0&0&0&0&0&2&0&0&0&0&0\\0&0&0&0&0&0&0&2&0&0&0&0\\0&0&0&0&0&0&0&0&y_3-y_2&0&0&0\\0&0&0&0&0&0&0&0&x_3-x_4&0&0&0\\0&0&0&0&0&0&0&0&0&2&0&0\\0&0&0&0&0&0&0&0&0&0&2&0\\0&0&0&0&0&0&0&0&0&0&0&y_4-y_1\\0&0&0&0&0&0&0&0&0&0&0&x_3-x_4\end{bmatrix} \tag{5c}$$

$$\{d_e^m\}=\{u_1 \quad v_1 \quad \theta_{z1} \quad u_2 \quad v_2 \quad \theta_{z2} \quad u_3 \quad v_3 \quad \theta_{z3} \quad u_4 \quad v_4 \quad \theta_{z4}\}^T \tag{5d}$$

where [MN] is a matrix defined by the shape functions in Equations 3 and 4 and [Tr] is a transformation matrix to ensure the compatibility between the rotation DOF, where x_1 to x_4 and y_1 to y_4 are the element nodes local coordinates. Thereby, the kinematic matrix $[B_m]$ can be obtained according to Equation 6, where $[\mathrm{J}]^{-1}$ represents the inverse of the Jacobian matrix $[\mathrm{J}]_{(2\times2)}$, which relates, through bilinear shape functions, the natural (ξ,η) and local (x,y) coordinate systems. The corresponding formulation can be found in finite elements introductory textbooks [14].

$$\{\varepsilon_m\}=\begin{Bmatrix}\frac{\partial u_m}{\partial x}\\ \frac{\partial v_m}{\partial y}\\ \frac{\partial u_m}{\partial y}+\frac{\partial v_m}{\partial x}\end{Bmatrix}=[B_m]\{d_{em}\}=\begin{bmatrix}1&0&0&0\\0&0&0&1\\0&1&1&0\end{bmatrix}\begin{bmatrix}[J]^{-1}&[0]\\ [0]&[J]^{-1}\end{bmatrix}\begin{bmatrix}\frac{\partial MN_{1,i}}{\partial \xi}\\ \frac{\partial MN_{1,i}}{\partial \eta}\\ \frac{\partial MN_{2,i}}{\partial \xi}\\ \frac{\partial MN_{2,i}}{\partial \eta}\end{bmatrix}[Tr]\{d_e^m\} \tag{6}$$

2.4 Discrete Kirchhoff Quadrilateral Element - DKQ

According to Barrales [5], in the DKQ plate element, proposed by Batoz and Tahar [12], initially, the deflection and rotation fields are established independently, and later, they are related by applying the Kirchhoff's assumptions in a discrete manner on the element edges. For this purpose, it is adopted 8-node serendipity isoparametric element shape functions for the rotation fields, Equation 7, and cubic function for the deflections along the edges.

$$\psi_i(\xi,\eta)=-\frac{1}{4}(1+\xi_i\xi)(1+\eta_i\eta)(1-\xi_i\xi-\eta_i\eta)\ for\ i=1,2,3\ and\ 4 \tag{7a}$$

$$\psi_k(\xi,\eta)=\frac{1}{2}(1-\xi^2)(1+\eta_k\eta)\ for\ i=5\ and\ 6 \tag{7b}$$

$$\psi_k(\xi,\eta)=\frac{1}{2}(1+\xi_k\xi)(1-\eta^2)\ for\ i=7\ and\ 8 \tag{7c}$$

Although this shape functions are related to an 8-node element, in the DKQ element development, using: coordinate transformations, applying Kirchhoff's assumptions in a discrete manner on the element nodes, especially in nodes 5 to 8, and other simplifications, it is possible to reduce the element node number to 4, even using the Equation 7 shape functions. Consequently, the DKQ is a 4-node element that has 3 degree of freedom per node (2 out-of-plane rotations and 1 translation perpendicular to the element plane).

According to Rojas et al. [10], the middle surface normal rotation field of the plate element, in natural coordinates (ξ, η), is given by the following interpolation:

$$\begin{Bmatrix} \beta_x \\ \beta_y \end{Bmatrix} = [\Psi]_{(2\times12)}\{d_e^b\}_{(12\times1)} \tag{8a}$$

$$[\Psi] = \begin{bmatrix} 3/2[\psi_5(\xi,\eta)a_5 - \psi_8(\xi,\eta)a_8] & 3/2[\psi_5(\xi,\eta)d_5 - \psi_8(\xi,\eta)d_8] \\ \psi_5(\xi,\eta)b_5 + \psi_8(\xi,\eta)b_8 & -\psi_1(\xi,\eta) + \psi_5(\xi,\eta)e_5 + \psi_8(\xi,\eta)e_8 \\ \psi_1(\xi,\eta) - \psi_5(\xi,\eta)c_5 - \psi_8(\xi,\eta)c_8 & -\psi_5(\xi,\eta)b_5 - \psi_8(\xi,\eta)b_8 \\ 3/2[\psi_6(\xi,\eta)a_6 - \psi_5(\xi,\eta)a_5] & 3/2[\psi_6(\xi,\eta)d_6 - \psi_5(\xi,\eta)d_5] \\ \psi_6(\xi,\eta)b_6 + \psi_5(\xi,\eta)b_5 & -\psi_2(\xi,\eta) + \psi_6(\xi,\eta)e_6 + \psi_5(\xi,\eta)e_5 \\ \psi_2(\xi,\eta) - \psi_6(\xi,\eta)c_6 - \psi_5(\xi,\eta)c_5 & -\psi_6(\xi,\eta)b_6 - \psi_5(\xi,\eta)b_5 \\ 3/2[\psi_7(\xi,\eta)a_7 - \psi_6(\xi,\eta)a_6] & 3/2[\psi_7(\xi,\eta)d_7 - \psi_6(\xi,\eta)d_6] \\ \psi_7(\xi,\eta)b_7 + \psi_6(\xi,\eta)b_6 & -\psi_3(\xi,\eta) + \psi_7(\xi,\eta)e_7 + \psi_6(\xi,\eta)e_6 \\ \psi_3(\xi,\eta) - \psi_7(\xi,\eta)c_7 - \psi_6(\xi,\eta)c_6 & -\psi_7(\xi,\eta)b_7 - \psi_6(\xi,\eta)b_6 \\ 3/2[\psi_8(\xi,\eta)a_8 - \psi_7(\xi,\eta)a_7] & 3/2[\psi_8(\xi,\eta)d_8 - \psi_7(\xi,\eta)d_7] \\ \psi_8(\xi,\eta)b_8 + \psi_7(\xi,\eta)b_7 & -\psi_4(\xi,\eta) + \psi_8(\xi,\eta)e_8 + \psi_7(\xi,\eta)e_7 \\ \psi_4(\xi,\eta) - \psi_8(\xi,\eta)c_8 - \psi_7(\xi,\eta)c_7 & -\psi_8(\xi,\eta)b_8 - \psi_7(\xi,\eta)b_7 \end{bmatrix}^T \tag{8b}$$

$$\{d_e^b\} = \{w_1 \quad \theta_{x1} \quad \theta_{y1} \quad w_2 \quad \theta_{x2} \quad \theta_{y2} \quad w_3 \quad \theta_{x3} \quad \theta_{y3} \quad w_4 \quad \theta_{x4} \quad \theta_{y4}\}^T \tag{8c}$$

Table 1. Geometric coefficients.

Coefficient	**Equation***
a_k	$-\dfrac{(x_i - x_j)}{(x_i - x_j)^2 + (y_i - y_j)^2}$
b_k	$\dfrac{3(x_i - x_j)(y_i - y_j)}{4(x_i - x_j)^2 + 4(y_i - y_j)^2}$
c_k	$\dfrac{(x_i - x_j)^2/4 - (y_i - y_j)^2/2}{(x_i - x_j)^2 + (y_i - y_j)^2}$
d_k	$-\dfrac{(y_i - y_j)}{(x_i - x_j)^2 + (y_i - y_j)^2}$
e_k	$\dfrac{-(x_i - x_j)^2/2 + (y_i - y_j)^2/4}{(x_i - x_j)^2 + (y_i - y_j)^2}$

*The indexes (k, i, j) can be related as (5,1,2), (6,2,3), (7,3,4) and (8,4,1).

where $[\Psi]$ is a matrix developed based on the discrete application of Kirchhoff's assumptions, and the geometric coefficients a_k, b_k, c_k, d_k and e_k are functions of the element nodes local coordinates, Table 1. Thereby, the kinematic matrix $[B_b^0]$ can be obtained according to Equation 9:

$$\{\varepsilon_b^0\} = z_L \begin{Bmatrix} \dfrac{\partial \beta_x}{\partial x} \\ \dfrac{\partial \beta_y}{\partial y} \\ \dfrac{\partial \beta_x}{\partial y} + \dfrac{\partial \beta_y}{\partial x} \end{Bmatrix} = z_L [B_b^0]\{d_{eb}\} = z_L \begin{bmatrix} 1 & 0 & 0 & 0 \\ 0 & 0 & 0 & 1 \\ 0 & 1 & 1 & 0 \end{bmatrix} \begin{bmatrix} [J]^{-1} & [0] \\ [0] & [J]^{-1} \end{bmatrix} \begin{bmatrix} \dfrac{\partial \Psi_{1,i}}{\partial \xi} \\ \dfrac{\partial \Psi_{1,i}}{\partial \eta} \\ \dfrac{\partial \Psi_{2,i}}{\partial \xi} \\ \dfrac{\partial \Psi_{2,i}}{\partial \eta} \end{bmatrix} \{d_e^b\} \tag{9}$$

2.5 Geometric Nonlinearity

In the present paper, the geometric nonlinearity is considered through a Total Lagrangian Formulation (TLF), where the problem is analyzed in terms of the structure undeformed configuration. The Von Karman's hypotheses for large deflections of plates are considered, as presented by Figueiras [7]:

- The shell thickness t is small compared to the other dimensions;
- The shell transverse deflection w is of the same order of magnitude as the thickness;
- The slopes are small, $|\partial w/\partial x| \ll 1$ and $|\partial w/\partial y| \ll 1$;
- The tangential displacements u and v are small enough to allow the nonlinear terms associated with these fields be disregarded;
- All the strain vector components are small.

Based on these hypotheses, the nonlinear plate strain component can be written as:

$$\{\varepsilon_b^L\} = \begin{Bmatrix} \frac{1}{2}\left(\dfrac{\partial w}{\partial x}\right)^2 \\ \frac{1}{2}\left(\dfrac{\partial w}{\partial y}\right)^2 \\ \dfrac{\partial w}{\partial x}\dfrac{\partial w}{\partial y} \end{Bmatrix} = \frac{1}{2} \begin{bmatrix} \dfrac{\partial w}{\partial x} & 0 \\ 0 & \dfrac{\partial w}{\partial y} \\ \dfrac{\partial w}{\partial y} & \dfrac{\partial w}{\partial x} \end{bmatrix} \begin{Bmatrix} \dfrac{\partial w}{\partial x} \\ \dfrac{\partial w}{\partial y} \end{Bmatrix} = \frac{1}{2}[A]\{\theta\} \tag{10}$$

where the vector $\{\theta\}$ with the derivatives of shell transverse deflection w can be evaluated based on the element plate displacements $\{d_e^m\}$ and considering a bilinear interpolation in this field, as used in the Jacobian matrix $[J]$, Batoz and Tahar [12] and Rojas *et al.* [10], Equation 11:

$$\{\theta\} = \begin{Bmatrix} \dfrac{\partial w}{\partial x} \\ \dfrac{\partial w}{\partial y} \end{Bmatrix} = [J]^{-1} \begin{Bmatrix} \dfrac{\partial w}{\partial \xi} \\ \dfrac{\partial w}{\partial \eta} \end{Bmatrix} = [G]_{(2\times 12)}\{d_e^b\}_{(12\times 1)} \tag{11}$$

Based on the vector $\{\theta\}$ components, it is possible to assemble the matrix $[A]$. Thereby, it is possible to note that these two elements depend on the nodal displacements $\{d_e^b\}$, and the multiplication between them results in a nonlinear relationship between $\{\varepsilon_b^L\}$ and $\{d_e^b\}$. Calculating the variation of $\{\varepsilon_b^L\}$ with respect to $\{d_e^m\}$ we obtain the matrix $[B_b^L]$:

$$\partial\{\varepsilon_b^L\} = \frac{1}{2}\partial([A])\{\theta\} + \frac{1}{2}[A]\partial(\{\theta\}) = [A]\partial(\{\theta\}) = [A][G]\partial\{d_e^b\} = [B_b^L]\partial\{d_e^b\} \tag{12}$$

Unlike the matrices $[B_m]$, $[B_b^0]$ and $[G]$ which remain constants through the analysis, the matrix $[B_b^L]$ depends on the nodal displacements $\{d_e^b\}$ and needs to be updated in each iteration.

The incremental kinematic matrix $[B]$, which differs from the kinematic matrix $[B']$ due to the problem linearization process, can be written as:

$$[B]_{(3\times 24)} = \left[[B_m]_{(3\times 12)} \quad z_L[B_b^0]_{(3\times 12)} + [B_b^L]_{(3\times 12)} \right] \tag{13}$$

2.6 Element stiffness matrix

Through the Total Lagrangian Formulation, the element stiffness matrix $[k_e]$ is defined by two components $[k_e^L]$ and $[k_e^\sigma]$ which consider, respectively, the large displacements and the stresses acting on the structure:

$$[k_e] = [k_e^L] + [k_e^\sigma] = \int_{V_e}[B]^T[D][B]dV_e + \int_{V_e}[G]^T[M][G]dV_e \tag{14}$$

where $[D]$ is the material tangent stiffness matrix, being adopted in its place, in this paper, the material secant stiffness matrix, and $[M]$ is a matrix defined according to the acting stresses.

The element volume V_e integrals are evaluated numerically. In the element plane, it is adopted the Gauss quadrature [14]. As the shell thickness is discretized in n_c concrete layers and n_s steel layers, in the integral along the thickness, it is used a mixed approach between the presented by Zhang et al. [15], [16], Barrales [5] and Vasilescu [13], which considers the sum of each layer individual contribution.

Thereby, using Equations 13 and 14, the matrix $[k_e^L]$ is evaluated as:

$$[k_e^L] = \sum_{k=1}^{n_g} p_k|[J]_k|\left(\sum_{i=1}^{n_c}\begin{bmatrix}[k_{c.mm}^L]_{k,i} & [k_{c.mb}^L]_{k,i}\\ [k_{cbm}^L]_{k,i} & [k_{c.bb}^L]_{k,i}\end{bmatrix} + \sum_{j=1}^{n_s}\begin{bmatrix}[k_{s.mm}^L]_{k,j} & [k_{s.mb}^L]_{k,j}\\ [k_{s.bm}^L]_{k,j} & [k_{s.bb}^L]_{k,j}\end{bmatrix}\right) \tag{15}$$

The parameters p_k and $|[J]_k|$ represent, respectively, the integration weights of the n_g Gauss points, and the determinant of the corresponding Jacobian matrix $[J]_k$.
The concrete layers contributions to the $[k_e^L]$ matrix, evaluated for each k Gauss point and each i concrete layer, are given by:

$$[k_{c.mm}^L]_{k,i} = z_{c1_i}[B_m^0]_i^T[D_c]_{k,i}[B_m^0]_i \tag{16a}$$

$$[k_{c.mb}^L]_{k,i} = z_{c2_i}[B_m^0]_i^T[D_c]_{k,i}[B_b^0]_i + z_{c1_i}[B_m^0]_i^T[D_c]_{k,i}[B_b^L]_i \tag{16b}$$

$$[k_{c.bm}^L]_{k,i} = z_{c2_i}[B_b^0]_i^T[D_c]_{k,i}[B_m^0]_i + z_{c1_i}[B_m^L]_i^T[D_c]_{k,i}[B_m^0]_i \tag{16c}$$

$$[k_{c.bb}^L]_{k,i} = z_{c3_i}[B_b^0]_i^T[D_c]_{k,i}[B_b^0]_i + z_{c2_i}[B_b^0]_i^T[D_c]_{k,i}[B_b^L]_i + z_{c2_i}[B_b^L]_i^T[D_c]_{k,i}[B_b^0]_i + z_{c1_i}[B_b^L]_i^T[D_c]_{k,i}[B_b^L]_i \tag{16d}$$

The parameter $[D_c]_{k,i}$ is the material secant stiffness matrix, evaluated at the i concrete layer in the k Gauss points, discussed in section 3. The terms z_{c1_i}, z_{c2_i} and z_{c3_i} arise from the numerical integration of the layer coordinate parameter z_L in the matrices $[B_b^0]$, component of $[B]$ matrix, and are calculated in a discrete way, for each concrete layer, as shown in Equation 17, where $z_{c_i}^{top}$ and $z_{c_i}^{bot}$ represent, respectively, the analyzed layer top and bottom coordinates.

$$z_{c1_i} = \left[z_{c_i}^{top} - z_{c_i}^{bot}\right] \tag{17a}$$

$$z_{c2_i} = \frac{1}{2}\left[\left(z_{c_i}^{top}\right)^2 - \left(z_{c_i}^{bot}\right)^2\right] \tag{17b}$$

$$z_{c3_i} = \frac{1}{3}\left[\left(z_{c_i}^{top}\right)^3 - \left(z_{c_i}^{bot}\right)^3\right] \tag{17c}$$

The steel layers contributions to the $[k_e^L]$ matrix, evaluated for each k Gauss point and each j steel layer, are given by:

$$[k_{s.mm}^L]_{k,j} = \rho_{s_j} t_{s_j} [B_m^0]_j^T [D_s]_{k,j} [B_m^0]_j \tag{18a}$$

$$[k_{s.mb}^L]_{k,j} = \rho_{s_j} t_{s_j} z_{s_j} [B_m^0]_j^T [D_s]_{k,j} [B_b^0]_j + \rho_{s_j} t_{s_j} [B_m^0]_j^T [D_s]_{k,j} [B_b^L]_j \tag{18b}$$

$$[k_{s.bm}^L]_{k,j} = \rho_{s_j} t_{s_j} z_{s_j} [B_b^0]_j^T [D_s]_{k,j} [B_m^0]_j + \rho_{s_j} t_{s_j} [B_m^L]_j^T [D_s]_{k,j} [B_m^0]_j \tag{18c}$$

$$\begin{aligned}[k_{s.bb}^L]_{k,j} = {}& \rho_{s_j} t_{s_j} z_{s_j}^2 [B_b^0]_j^T [D_s]_{k,j} [B_b^0]_j + \rho_{s_j} t_{s_j} z_{s_j} [B_b^0]_j^T [D_s]_{k,j} [B_b^L]_j + \\ & \rho_{s_j} t_{s_j} z_{s_j} [B_b^L]_j^T [D_s]_{k,j} [B_b^0]_j + \rho_{s_j} t_{s_j} [B_b^L]_j^T [D_s]_{k,j} [B_b^L]_j\end{aligned} \tag{18d}$$

The parameter $[D_s]_{k,i}$ is the material secant stiffness matrix, evaluated at the j steel layer in the k Gauss points, also discussed in section 3. The variable z_s refers to the position of the j steel layer axis. On the other hand, t_{s_j} and ρ_{s_j} are the corresponding layer thickness and reinforcement ratio.
Similarly, the matrix $[k_e^\sigma]$ can be defined numerically as:

$$[k_e^\sigma] = \int_V [G]^T [M][G] dV = \begin{bmatrix} [0]_{(12\times12)} & [0]_{(12\times12)} \\ [0]_{(12\times12)} & \sum_{k=1}^{n_g} p_k |[J]_k| \left(\sum_{i=1}^{n_c} [k_c^\sigma]_{k,i} + \sum_{j=1}^{n_s} [k_s^\sigma]_{k,j} \right) \end{bmatrix} \tag{19a}$$

$$[k_c^\sigma]_{k,i} = [G]_i^T [M_c]_{k,i} [G]_i = z_{c1_i} [G]_i^T \begin{bmatrix} \sigma_{xx_i}^c & \tau_{xy_i}^c \\ \tau_{xy_i}^c & \sigma_{yy_i}^c \end{bmatrix} [G]_i \tag{19b}$$

$$[k_s^\sigma]_{k,j} = [G]_j^T [M_s]_{k,j} [G]_j = \rho_{s_j} t_{s_j} [G]_j^T \begin{bmatrix} \sigma_{xx_j}^s & \tau_{xy_j}^s \\ \tau_{xy_j}^s & \sigma_{yy_j}^s \end{bmatrix} [G]_j \tag{19c}$$

where σ_{xx}, σ_{yy} and τ_{xy} represent the stresses acting on the concrete and steel layers. Note that the matrix $[k_e^\sigma]$ contributes to $[k_e]$ only in the region associated with the plate degrees of freedom, a consequence of considering nonlinear deformations only in the nonlinear plate strain component $\{\varepsilon_b^L\}$.

2.7 Internal forces vector

The internal forces vector $\{F_{int}\}$ unlike the external forces vector $\{F_{ext}\}$ is not constant. It depends on the structure nodal displacement vector $\{d\}$ and must be updated at each iteration. The corresponding element contribution $\{f_e\}$ can be defined by Equation 20a and calculated numerically by Equation 20b.

$$\{f_e\} = \int_{V_e} [B]^T \{\sigma\} dV_e = \int_{V_e} [B]^T \begin{Bmatrix} \sigma_{xx} \\ \sigma_{yy} \\ \tau_{xy} \end{Bmatrix} dV_e \tag{20a}$$

$$\{f_e\} = \sum_{k=1}^{n_g} p_k |[J]_k| \left(\sum_{i=1}^{n_c} [B_c]_{k,i}^T \begin{Bmatrix} \sigma_{xx_i}^c \\ \sigma_{yy_i}^c \\ \tau_{xy_i}^c \end{Bmatrix} + \sum_{j=1}^{n_s} [B_s]_{k,j}^T \begin{Bmatrix} \sigma_{xx_j}^s \\ \sigma_{yy_j}^s \\ \tau_{xy_j}^s \end{Bmatrix} \right) \tag{20b}$$

where the matrices $[B_c]_{k,i}$ and $[B_s]_{k,j}$ can be calculated as:

$$[B_c]_{k,i} = \begin{bmatrix} z_{c1_i} [B_m]_k & z_{c2_i} [B_b^0]_k + z_{c1_i} [B_b^L]_k \end{bmatrix} \tag{21a}$$

$$[B_s]_{k,j} = \left[\rho_{s_j} t_{s_j} [B_m]_k \quad \rho_{s_j} t_{s_j} z_{s_j} [B_b^0]_k + \rho_{s_j} t_{s_j} [B_b^L]_k\right] \tag{21b}$$

2.8 Program implementation

The program was developed using a simple imperative concept with repetition statements, to perform the necessary calculations on all elements and Gaussian points, as well as for each load step. It is possible to apply the presented formulation using other strategies, such as the Object-Oriented Programming (OOP) to ensure greater code reusability.

Figure 2 details the implemented program. As this figure illustrates, in the first load step first iteration, the concrete constitutive matrix can be initialized based on a linear-elastic model, Equation. (4.22), where υ_0 is the initial Poisson ratio and E_c is the Modulus of elasticity of concrete.

$$[D_{linear}] = \frac{E_c}{1-\upsilon_0^2} \begin{bmatrix} 1 & \upsilon_0 & 0 \\ \upsilon_0 & 1 & 0 \\ 0 & 0 & \frac{1-\upsilon_0}{2} \end{bmatrix} \tag{22}$$

3 MATERIAL CONSTITUTIVE MODELS

This section presents, in a concise way, the material constitutive models implemented in the developed computational program, since they are known formulations and widely discussed in the technical literature [2] [3], [17]. In addition, this section also details the formulation of the concrete $[D_c]$ and steel $[D_s]$ layers secant stiffness matrices, according to Vecchio [3]. In this study, the cracked concrete, despite its evident discrete nature, is modeled as a homogeneous orthotropic material, through the concept of mean stress and strain evaluated in regions containing several cracks, following the basis of the Modified Compression Field Theory (MCFT) [2].

3.1 Concrete in compression

Concrete in compression is modeled using a combination between the well-known Hognestad parabola, Equation 23, for both pre-peak and post-peak behavior, and the Vecchio 1992-A model (e1/e2- Form) [17], which through the softening coefficient β_d, models the material strength loss due to transversal tension, Equation 24.

$$\sigma_{cc} = \begin{cases} -f_p\left[2\left(\frac{\varepsilon_{cc}}{\varepsilon_p}\right) - \left(\frac{\varepsilon_{cc}}{\varepsilon_p}\right)^2\right], if\ |\varepsilon_{cc}| < 2|\varepsilon_p| \\ 0, if\ |\varepsilon_{cc}| < 2|\varepsilon_p| \end{cases} \tag{23}$$

$$f_p = \beta_d f_c \tag{24a}$$

$$\varepsilon_p = \beta_d \varepsilon_0 \tag{24b}$$

$$\beta_d = \frac{1}{1+C_s C_d} \leq 1 \tag{24c}$$

$$C_d = \begin{cases} 0, if\ \min\left(-\varepsilon_{c1}/\varepsilon_{c2}, 400\right) \geq 0.28 \\ 0.35[\min\left(-\varepsilon_{c1}/\varepsilon_{c2}, 400\right) - 0.28]^{0.80}, if\ \min\left(-\varepsilon_{c1}/\varepsilon_{c2}, 400\right) \geq 0.28 \end{cases} \tag{24d}$$

where σ_{cc} and ε_{cc} are, respectively, the average compressive stress and strain. The variable f_c is the cylinder compressive strength (at 28 days), and ε_0 is the corresponding peak strain. The factor C_d represents the influence of the relationship between the principal tensile ε_{c1} and compression ε_{c2} strains in concrete. The factor C_s is equal to 0.55 when the slip deformations in the cracks are considered in the model (subsection 3.6), and 1.0 otherwise.

ALGORITHM 1: Nonlinear analysis procedure

Inputs: Finite element mesh, material properties, boundary conditions, and analysis criteria.

Initialize the nodal displacement vector: $\{d\} \leftarrow \{0\}$;
Initialize the internal forces and external forces vectors: $\{F_{int}\} \leftarrow \{0\}$ and $\{F_{ext}\} \leftarrow \{0\}$;
for *all e elements* **and** *all k Gauss points* **do**
    for *all i concrete layers* **do**
        Initialize the constitutive matrix: $[D_c]_{k,i} \leftarrow [D_{linear}]$, Eq. (**22**);
    end
    for *all j steel layers* **do**
        Initialize the constitutive matrix: $[D_s]_{k,j} \leftarrow [0]_{(3\times3)}$;
    end
end
repeat
    Increment the external forces vector $\{F_{ext}\}$;
    Initialize the convergence criterion parameter: $error \leftarrow 1$;
    while $error > tol$ **do**
        for *all e elements* **do**
            for *all k Gauss points* **do**
                Calculate the Jacobian matrix $[J]$;
                Calculate the matrix $[k_e^L]$ and $[k_e^\sigma]$ contributions, Eq. (**15**) to (**19**);
            end
        end
        Assemble the global stiffness matrix $[K_G]$;
        Calculate the new nodal displacements vector $\{d\}$, Eq. (**1**);
        for *all e elements* **do**
            for *all k Gauss points* **do**
                for *all i concrete layers* **do**
                    Recalculate the matrix $[D_c]_{k,i}$ and the vector $\{\sigma_c\}_{k,i}$, Figure 3;
                end
                for *all j steel layers* **do**
                    Recalculate the matrix $[D_s]_{k,j}$ and the vector $\{\sigma_s\}_{k,j}$, Figure 4;
                end
            end
        end
        Calculate the internal forces vector through the element contribution, Eq. (**20**);
        Calculate the convergence criterion parameter $error$, Eq. (**2**);
    end
    Save the solution;
until *the maximum load be reached*;

Figure 2. Nonlinear analysis procedure

3.2 Concrete in tension

The concrete tensile model is defined by two distinct behaviors: pre-cracking and post-cracking, Equation 25. According to Wong et al. [17], after cracking, the reinforced concrete leaves the linear-elastic behavior, and the concrete tensile stresses tend to zero, on the crack surface, while it can present considerable values, between cracks, due to steel interaction. The Modified Bentz 2003 tensile stiffening model can represent this behavior. Furthermore, according to Vecchio [3], the magnitude of the average principal tensile stress σ_{ct} must be limited by the remaining steel resistant capacity σ_{ct}^{max}.

$$\sigma_{ct} = \begin{cases} E_c\varepsilon_{ct}, if\ \varepsilon_{ct} < \varepsilon_{cr} \\ \frac{f_{cr}}{1+c_t\varepsilon_{ct}}, if\ \varepsilon_{ct} \geq \varepsilon_{cr} \end{cases} \leq \sigma_{ct}^{max} \tag{25a}$$

$$c_t = \frac{2.2}{4\frac{\rho_x}{\phi_x}|\cos(\theta-\alpha_x)| + 4\frac{\rho_y}{\phi_y}|\cos(\theta-\alpha_y)|} \tag{25b}$$

$$\sigma_{ct}^{max} = \rho_x(f_{scrx} - f_{sx})\cos(\theta - \alpha_x)^2 + \rho_y(f_{scry} - f_{sy})\cos(\theta - \alpha_y)^2 \tag{25c}$$

where ε_{ct} is the concrete average principal tensile strain. The parameters f_{cr} and ε_{cr} are, respectively, the crack stress and strain. The coefficient c_t refers to the influence of the reinforcement on the stiffening, and it is obtained based on: the steel ratios ρ_x and ρ_y; the reinforcement rebar nominal diameter ϕ_x and ϕ_y; and the angles θ, α_x and α_y that illustrate the principal system direction and the reinforcements orientation. The parameters f_{sx} and f_{sy} are the reinforcements average stresses, while f_{scrx} and f_{scry} represent these same parameters evaluated at the crack surface. The Modulus of elasticity of concrete E_c illustrates the ratio between f_{cr} and ε_{cr}, and can be estimated as $2f_c/|\varepsilon_0|$.

When the reinforcement properties are directly assigned to the finite element, like in reinforced concrete membranes analysis programs [18], for example, the application of equation Equation 25 is direct. However, in the present study, the thickness of the shell element is discretized in layers and the constitutive model must be applied separately in each one. In this case, it is necessary to define which reinforcement parameters should be considered in each concrete layer. Hrynyk [4] presented a solution to this problem, based on CEB-FIP [19], which consists in defining a rebar tensile stiffening influence area equal to 7.5 times the rebar diameter. Thus, the concrete layers located within the rebar influence area are considered stiffened by this reinforcement. However, it is important to note that this evaluation must be done for all concrete layer-steel layer combinations, where a concrete layer could be stiffened by more than one steel layer (or none). Therefore, it is possible to see that the adoption of this criterion in the tensile stiffening model, along the shell thickness, tends to obtain a more realistic structural response. In the concrete layer plane state analysis, the principal stresses σ_{c1} and σ_{c2} can be evaluated with either the tensile model, Equation 25, or the compression model, Equation 23, depending on the layer plane state: biaxial tension, biaxial compression or tension-compression state.

3.3 Steel in tension or compression

In this paper, two steel constitutive models were implemented, both for tension and compression: a simple perfect elastic-plastic curve, Equation 26, and a bilinear curve that considers the material hardening after it reaches the yield condition, Equation 27.

$$f_s = \begin{cases} \frac{f_y}{\varepsilon_{sy}}\varepsilon_s, if\ |\varepsilon_s| < \varepsilon_{sy} \\ f_y\,\mathbf{sign}(\varepsilon_s), if\ |\varepsilon_s| \geq \varepsilon_{sy} \end{cases} \tag{26}$$

$$f_s = \begin{cases} \frac{f_{sy}}{\varepsilon_{sy}}\varepsilon_s, if\ |\varepsilon_s| < \varepsilon_{sy} \\ \left[f_y + \frac{f_u - f_y}{\varepsilon_{su} - \varepsilon_{sy}}(\varepsilon_s - \varepsilon_{sy})\right]\mathbf{sign}(\varepsilon_s), if\ |\varepsilon_s| \geq \varepsilon_{sy} \end{cases} \tag{27}$$

where f_y and ε_{sy} are the yield stress and strain and f_s and ε_s are the reinforcement average stress and strain. The parameters f_u and ε_{su} are the corresponding steel ultimate stress and strain. The second model was implemented to allow the program to capture the post-yielding behavior, in the Polak shells problem, subsection 4.2.

3.4 Concrete confinement

Unlike the concrete softening effect, section 3.1, when this material is submitted to a biaxial (or triaxial) compression state, there is a confinement effect that tends to increase its resistant capacity. In the present study, this was modeled in a similar way to what was presented by Silva [18], based on the work of Vecchio [20], Kupfer et al. [21], Richart et al. [22] and Wong et al. [17], using the enhancement factors K_{c1} and K_{c2}:

$$K_{c1}(\sigma_{c2}) = 1 + 0.92\left(-\frac{\sigma_{c2}}{f_c}\right) - 0.76\left(-\frac{\sigma_{c2}}{f_c}\right)^2 + 4.1\frac{\rho_{sz}f_{sz}}{f_c} \tag{28a}$$

$$K_{c2}(\sigma_{c1}) = 1 + 0.92\left(-\frac{\sigma_{c1}}{f_c}\right) - 0.76\left(-\frac{\sigma_{c1}}{f_c}\right)^2 + 4.1\frac{\rho_{sz}f_{sz}}{f_c} \tag{28b}$$

where ρ_{sz} and f_{sz} are the reinforcement ratio and its stress in the out-of-plane direction. The stress f_{sz} can be evaluated by applying the concrete strain in the corresponding direction ε_{cz} in the steel constitutive model. In this paper, this strain is calculated in a simplified way regardless of whether the reinforcement yields or not as:

$$\varepsilon_{cz} = \frac{E_{cn}}{E_{cn}+\rho_{sz}E_{sz}}(-v_{12}\varepsilon_{c2} - v_{21}\varepsilon_{c1}) \tag{29}$$

where E_{cn} and E_{sz} are the concrete and steel modulus of elasticity in the out-of-plane direction, where E_{cn} is considered equal to $|2f_c/\varepsilon_0|$. The parameter v_{12} represents the Poisson ratio that relates the strain in the 1-direction due to the stress in 2-direction [20]. The parameter v_{21} is defined similarly. The model adopted for calculating the Poisson coefficients v_{12} and v_{21} is detailed in the following subsection. The factors K_{c1} and K_{c2} are used to determine the peak stress and strain in the principal system (1-2):

$$f_{p1} = K_{c1}f_c \tag{30a}$$

$$f_{p2} = K_{c2}f_c \tag{30b}$$

$$\varepsilon_{p1} = (3K_{c1} - 2)\varepsilon_0 \tag{31a}$$

$$\varepsilon_{p2} = (3K_{c2} - 2)\varepsilon_0 \tag{31b}$$

The peak stresses and strains can be used to calculate the concrete average principal compressive stresses. Analyzing the set of equations described in this subsection, it is possible to see the evaluation of the concrete behavior in biaxial compression as a nonlinear system of equations with two equations and two variables:

$$f(\sigma_{c1}, \sigma_{c2}) = \begin{Bmatrix} \sigma_{c1} - \sigma_{cc}(f_{p1}, \varepsilon_{p1}, \varepsilon_{c1}) \\ \sigma_{c2} - \sigma_{cc}(f_{p2}, \varepsilon_{p2}, \varepsilon_{c2}) \end{Bmatrix} = \begin{Bmatrix} 0 \\ 0 \end{Bmatrix} \tag{32}$$

This solution strategy was implemented in the developed program, where optimization functions from *SciPy* [23] scientific computational library were applied. It was observed good results, in addition to an adequate convergence, even applying a simple initial estimate for the solution (coordinate system origin).

3.5 Poisson ratio and lateral strains

According to Vecchio [20], lateral strains related to the Poisson ratio can be relevant for the reinforced concrete structures behavior, especially near failure. The Equation 33 represents the Poisson ratio model adopted in this paper. This model, in addition to considering the initial Poisson ratio v_0 increase, also disregards this parameter when the concrete presents, in the transverse direction, a principal tensile strain greater than the cracking strain ε_{cr}.

$$v_{12} = \begin{cases} 0, if\ \varepsilon_{c2} \geq 0\ and\ \varepsilon_{c2} \geq \varepsilon_{cr} \\ v_0, if\ \varepsilon_{c2} \geq 0\ and\ \varepsilon_{c2} < \varepsilon_{cr} \\ v_0, if\ \varepsilon_{c2} < 0\ and\ |\varepsilon_{c2}| < |\varepsilon_0|/2 \\ v_0\left[1 + 1.5\left(\frac{2\varepsilon_{c2}}{\varepsilon_0} - 1\right)^2\right] \ngtr 0.5, if\ \varepsilon_{c2} < 0\ and\ |\varepsilon_{c2}| \geq |\varepsilon_0|/2 \end{cases} \tag{33}$$

The concrete principal lateral strain in 1-direction ε_{c01} is given by Equation 34. It is important to note that the corresponding strain in 2-direction ε_{c02} and its Poisson ratio v_{21} can be obtained through Equations 33 and (34) switching the indexes.

$$\varepsilon_{c01} = -v_{21}\varepsilon_{c2} \tag{34}$$

The concrete principal lateral strain vector $\{\varepsilon_{c0}^{1-2}\}$ can be transformed to the corresponding cartesian system vector $\{\varepsilon_{c0}\}$, Equation 35, using the rotation matrix $[T]$, Equation 36.

$$\{\varepsilon_{c0}\} = [T(-\theta)]\{\varepsilon_{c0}^{1-2}\} = [T(-\theta)]\{\varepsilon_{c01} \quad \varepsilon_{c02} \quad 0\}^T \tag{35}$$

$$[T(\theta)] = \begin{bmatrix} \cos(\theta)^2 & \sin(\theta)^2 & \cos(\theta)\sin(\theta) \\ \sin(\theta)^2 & \cos(\theta)^2 & -\cos(\theta)\sin(\theta) \\ -2\cos(\theta)\sin(\theta) & 2\cos(\theta)\sin(\theta) & \cos(\theta)^2 - \sin(\theta)^2 \end{bmatrix} \tag{36}$$

3.6 Slip strain model

The Disturbed Stress Field Model (DSFM) is an extension of the well-known Modified Compression Field Theory (MCFT) [2], which admits disagreements between the stress and strain principal systems, through the consideration of crack slip strains. The DSFM was proposed by Vecchio [3] to solve some MCFT drawbacks in calculate the strength and stiffness of high or low reinforcement ratio elements.

The crack surface shear stress v_c can be evaluated applying equilibrium in the reinforced concrete element:

$$v_c = \rho_x(f_{scrx} - f_{sx})\cos(\theta - \alpha_x)\sin(\theta - \alpha_x) + \rho_y(f_{scry} - f_{sy})\cos(\theta - \alpha_y)\sin(\theta - \alpha_y) \tag{37}$$

According to Vecchio [3] due to this shear stress there is a rigid body local slip along the crack (slip displacement δ_s) which causes slip strains $\{\varepsilon^s\}$. These strains must be considered in the model additionally to the principal strains related to the material constitutive response. According to Vecchio [3], the displacement δ_s can be calculated as:

$$\delta_s = \frac{v_c}{1.8w_{cr}^{-0.8} + (0.234w_{cr}^{-0.707} - 0.20)f_{cc}} \tag{38}$$

where w_{cr} represents the average crack width, which can be estimated from the average crack spacing s_{cr}, Equation 39, based on the nominal crack spacings in *x* and *y* ($s_x = s_y = 50mm$).

$$w_{cr} = \varepsilon_{c1}s_{cr} = \varepsilon_{c1}\frac{1}{\sin(\theta)/s_x + \cos(\theta)/s_y} \tag{39}$$

When the average crack width is greater than or equal to 5 mm, the concrete principal compressive stress σ_{c2} is considered equal to zero. The parameter f_{cc} is cubic compressive strength, adopted as: $f_{cc} = f_c/0.85$. The crack slip shear strain γ_s is evaluated as the ratio between δ_s and s_{cr}.
Based on Mohr's circle coordinate transformations, the slip strain vector in the Cartesian system $\{\varepsilon^s\}$ can be written as:

$$\{\varepsilon^s\} = \gamma_s \begin{Bmatrix} -0.5\sin(2\theta) \\ 0.5\sin(2\theta) \\ \cos(2\theta) \end{Bmatrix} \tag{40}$$

The formulation described above represents an overview of the slip strain vector $\{\varepsilon^s\}$ calculation procedure. However, it is important to present some additional details about the shear stresses along the crack surfaces v_c. Although this parameter can be obtained by Equation 37, according to Silva [18], it should be limited to the maximum shear stress that can be resisted on the crack by aggregate interlock, Equation 41.

$$v_c \leq v_c^{max} = \frac{0.18\sqrt{f_c}}{0.31+24w_{cr}/(a_g+26)} \tag{41}$$

where a_g is the aggregate size (adopted as 25mm). Furthermore, according to Equation 37, to evaluate the shear stress v_c it is previously necessary to calculate the reinforcement stresses in the crack surface f_{scrx} and f_{scry}. Although these parameters can be easily obtained using the steel constitutive models, section 3.3, the evaluation of the corresponding steel strains, in the crack surface, ε_{scrx} and ε_{scry}, necessary to obtain these stresses, is not immediate. Through the reinforced concrete element equilibrium in the crack surface, there is a steel stress (and strain) increment, due to the concrete tensile stress absence. Thus, Vecchio [3] proposes that the steel strains, in the cracks ε_{scrx} and ε_{scry}, should be determined through the sum of the corresponding average strain ε_{sx} and ε_{sy} and the local incremental strain contribution in 1-direction, $\Delta\varepsilon_{1cr}$:

$$\varepsilon_{scrx} = \varepsilon_{sx} + \Delta\varepsilon_{1cr}\cos{(\theta - \alpha_x)^2} \tag{42a}$$

$$\varepsilon_{scry} = \varepsilon_{sy} + \Delta\varepsilon_{1cr}\cos{(\theta - \alpha_y)^2} \tag{42b}$$

Thus, considering the concrete in tension and steel constitutive models presented and the formulation described above, it is possible to formulate a nonlinear equation whose solution is the incremental strain $\Delta\varepsilon_{1cr}$, Equation 43. Again, it was used *SciPy* [23] scientific computing library optimization functions.

$$f(\Delta\varepsilon_{1cr}) = \sigma_{c1} - \rho_x(f_{scrx} - f_{sx})\cos(\theta - \alpha_x)^2 - \rho_y\left(f_{scry} - f_{sy}\right)\cos\left(\theta - \alpha_y\right)^2 = 0 \tag{43}$$

Finally, it is important to note that the slip theory is only applied to cracked concrete. Thus, it must be verified whether the concrete principal tensile strain ε_{c1} is greater than the crack strain ε_{cr}. Otherwise, the slip strain vector $\{\varepsilon^s\}$ can be computed as a null vector.

3.7 Material secant stiffness matrices

In the previous subsections, it was presented the lateral strain vector $\{\varepsilon_{c0}\}$ and the slip strain vector $\{\varepsilon^s\}$ calculation procedure. In order to ensure the concrete secant stiffness matrix symmetry and the associated benefits, according to Vecchio [3] and Silva [18], the concrete total strain vector $\{\varepsilon\}$ is defined by three distinct components: $\{\varepsilon_c\}$, $\{\varepsilon_{c0}\}$ and $\{\varepsilon^s\}$, where, $\{\varepsilon_c\}$ represents the elastic strains due to stress, which can be evaluated, as:

$$\{\varepsilon_c\} = \{\varepsilon\} - \{\varepsilon_{c0}\} - \{\varepsilon^s\} = \{\varepsilon_{cx} \quad \varepsilon_{cy} \quad \gamma_{cxy}\}^T \tag{44}$$

Once the vector $\{\varepsilon_c\}$ are obtained, it is possible to estimate the inclination of the principal strains θ, Equation 45, and the concrete principal strains:

$$\theta = 0.5tan^{-1}\left(\frac{\gamma_{cxy}}{\varepsilon_{cx}-\varepsilon_{cy}}\right) \tag{45}$$

$$\varepsilon_{c1}, \varepsilon_{c2} = \frac{\varepsilon_{cx}+\varepsilon_{cy}}{2} \pm \frac{1}{2}\sqrt{(\varepsilon_{cx} - \varepsilon_{cy})^2 + \gamma_{cxy}{}^2} \tag{46}$$

Through Equations 44 and (46) and the models presented in the previous subsections, it is possible to see the nonlinear relationship between the vectors $\{\varepsilon_c\}$, $\{\varepsilon_{c0}\}$ and $\{\varepsilon^s\}$. In the present paper, this problem was solved iteratively, as illustrated in Figure 3. In the cracked reinforced concrete element, the concrete stress vector $\{\sigma_c\}$ can be related to the corresponding strain vector $\{\varepsilon_c\}$ as:

$$\{\sigma_c\} = [D_c]\{\varepsilon_c\} \tag{47}$$

where the concrete layer secant stiffness matrix $[D_c]$ in the Cartesian system is obtained by a coordinate transformation of the corresponding matrix in the principal system $[D_c^{1-2}]$, which is defined based on the concrete secant moduli $\bar{E}_{c1}$ and $\bar{E}_{c2}$, Equations 48 and 49.

$$[D_c] = [T(\theta)]^T[D_c^{1-2}][T(\theta)] = [T(\theta)]^T \begin{bmatrix} \bar{E}_{c1} & 0 & 0 \\ 0 & \bar{E}_{c2} & 0 \\ 0 & 0 & \frac{\bar{E}_{c1}\bar{E}_{c2}}{\bar{E}_{c1}+\bar{E}_{c2}} \end{bmatrix} [T(\theta)] \tag{48}$$

$$\bar{E}_{c1} = \sigma_{c1}/\varepsilon_{c1} \; \bar{E}_{c2} = \sigma_{c2}/\varepsilon_{c2} \tag{49}$$

ALGORITHM 2: Concrete layer secant constitutive model

if *load step = 1* and *iteration = 1*:
    Initialize the vectors $\{\varepsilon_{c0}\} \leftarrow \{0\}$ and $\{\varepsilon^s\} \leftarrow \{0\}$;
else:
    Consider the vectors $\{\varepsilon_{c0}\}$ and $\{\varepsilon^s\}$ calculated in the last iteration;
end
Calculate the concrete strain vector $\{\varepsilon_c\}$, Eq. (**44**);
Calculate the concrete principal strains ε_{c1} and ε_{c2}, Eq. (**46**);
Calculate the inclination of the principal strains θ, Eq. (**45**);
Calculate the equivalent reinforcement properties in the concrete layer, subsection **3.2**;
Calculate the equivalent reinforcement stress in the concrete layer, Eq. (**26**) or (**27**);
Calculate the lateral strains (Poisson coefficient) ε_{c01} and ε_{c02}, Eq. (**34**);
Calculate the lateral strains vector $\{\varepsilon_{c0}\}$, Eq. (**35**);
if $\varepsilon_{c1} < 0$ and $\varepsilon_{c2} < 0$ (biaxial compression):
    Calculate the principal stresses σ_{c1} and σ_{c2} solving Eq. (**32**);
else:
    if $\varepsilon_{c1} < 0$:
        Calculate σ_{c1} (compression model) Eq. (**23**) and (**24**);
    else:
        Calculate σ_{c1} (tension model), Eq. (**25**);
    end
    if $\varepsilon_{c2} < 0$:
        Calculate σ_{c2} (compression model) Eq. (**23**) and (**24**);
    else:
        Calculate σ_{c2} (tension model), Eq. (**25**);
    end
end
if $\varepsilon_{c1} > \varepsilon_{cr}$ (concrete cracked):
    Calculate the average crack spacing w_{cr}, Eq. (**39**);
    if $\varepsilon_{c2} < 0$ and $w_{cr} > 5mm$ **then** $\sigma_{c2} \leftarrow 0$ [3];
    Calculate the local increment strain $\Delta\varepsilon_{1cr}$ solving Eq. (**43**);
    Calculate the reinforcement local strains ε_{scrx} and ε_{scry}, Eq. (**42**);
    Calculate the reinforcement local stresses f_{scrx} and f_{scry}, Eq. (**26**) or (**27**);
    Calculate the shear stress along the crack surface v_c, Eq. (**37**) and (**41**);
    Calculate the slip along the crack surface δ_s, Eq. (**38**);
    Calculate the average shear slip strain γ_s;
    Calculate the slip strain vector $\{\varepsilon^s\}$, Eq. (**40**);
else:
    Set the slip strain vector to zero $\{\varepsilon^s\} \leftarrow \{0\}$;
end
Calculate the concrete layer secant moduli $\bar{E}_{c1}$ and $\bar{E}_{c2}$, Eq. (**49**);
Calculate the concrete layer secant stiffness matrix $[D_c]$, Eq. (**48**);
Calculate the concrete layer stress vector $\{\sigma_c\}$, Eq. (**47**);

Figure 3. Concrete layer secant constitutive model

ALGORITHM 3: Reinforcement layer secant constitutive model
1 Calculate the reinforcement layer stresses f_{sx} and f_{sy}, Eq. (**26**) or (**27**);
2 Calculate the reinforcement layer secant stiffness matrix $[D_s]$, Eq. (**50**);
3 Calculate the reinforcement layer stress vector $\{\sigma_s\}$, Eq. (**51**);

Figure 4. Reinforcement layer secant constitutive model

Like Equation 48, the steel secant stiffness matrix $[D_s]$ (in x or y-direction) can be calculated as shown in Equation 50.

$$[D_s] = [T(\alpha_s)]^T[D_s'][T(\alpha_s)] = [T(\alpha_s)]^T \begin{bmatrix} f_s/\varepsilon_s & 0 & 0 \\ 0 & 0 & 0 \\ 0 & 0 & 0 \end{bmatrix} [T(\alpha_s)] \tag{50}$$

where the angle α_{sj} represents the reinforcement direction. Finally, the reinforcement layer stress vector $\{\sigma_s\}$ is calculated by:

$$\{\sigma_s\} = [T(\alpha_s)]\{\sigma_s'\} = [T(\alpha_s)]\{f_s \quad 0 \quad 0\}^T \tag{51}$$

Figures 3 and 4 detail the constitutive models' implementation in the developed computer program, to obtain the secant stiffness matrices $[D_c]$ and $[D_s]$, and the stress vectors $\{\sigma_c\}$ and $\{\sigma_s\}$, on each layer.

4 PROGRAM VALIDATION AND DISCUSSIONS

This section presents the developed computer program validation through comparison with experimental and some numerical results [1], [4], available in the technical literature, for different structures. The load-displacement curves presented were created by the program, while the nodal displacements diagrams and the average internal forces diagrams, in the Gauss points, were obtained using the software *Paraview* [24], a *Python* module called *PyEVTK* [25] and additional codes written by the author, in the same language. Other useful structure diagrams for practical applications, like principal stresses, reinforcement stresses and crack pattern, are features that have not been implemented yet in the presented code. However, it can be done using the same approach mentioned above. In fact, any node or element property, in each load step, can be represented this way, in the program post-processor.

4.1 Cervenka deep beam

Initially, to evaluate the program performance in material nonlinear membrane problems, the deep beam W2 tested by Cervenka [26], Figure 5, was analyzed. All the plate degrees of freedom have been fixed. It was adopted 3 steel layers (2 horizontal and 1 vertical) to model the reinforcement, where its positions were defined according to the experiment. It was considered the steel perfect elasto-plastic model. The external load was applied using an initial load of 40 kN, in addition to 85 increments equal to 0.88 kN. The stopping criteria tolerance tol, associated with the increment displacement criterion described in subsection 2.1, was equal to 1%, . Figure 5 illustrates the results obtained, using the problem symmetry. Figure 4 also shows a comparison between the obtained load-displacement curve (y-displacement at the deep beam bottom midpoint), the experiment and a literature numerical response [27]. It was observed an adequate structural behavior and a good accuracy to the experimental data. The processing time was about 6 minutes, using a processor: Intel Core i7-5500U CPU @ 2.40GHz.

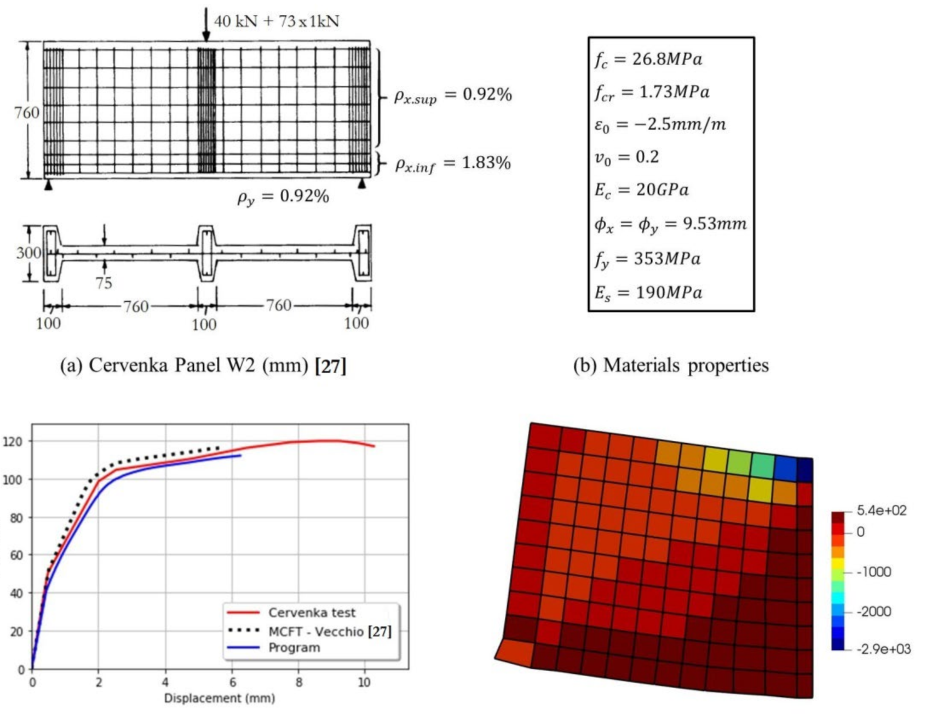

(a) Cervenka Panel W2 (mm) **[27]** (b) Materials properties

(c) Load-deflection curve (d) Horizontal axial force (kN/m)

Figure 5. Cervenka deep beam

4.2 Polak shells

To evaluate the program performance in material nonlinear plate and shell problems, three reinforced concrete shells (SM1, SM2 and SM3) tested by Polak and Vecchio [28] were analyzed. The specimens' characteristics, in addition to the results obtained, in comparison with literature numerical solutions [1], [4], are illustrated in Figure 6. It was adopted 4 steel layers (2 horizontal and 2 vertical), in addition to an out-of-plane reinforcement, to model the structures rebars, where its positions were defined according to the experiment. In all three cases, the load increments number was about 90. The stopping criteria tolerance tol was equal to 1%, subsection 2.1. The finite element mesh used contains 8x8 elements, and its thickness were discretized into 10 concrete layers. In the problem analysis, the program was not able to find a post-yielding equilibrated response, in less than 100 iterations (default maximum iterations number). However, during the study, it was observed that, considering the bilinear steel constitutive model, Equation 27, and disregarding the confinement (subsection 3.4) and slip strain models (subsection 3.6), consequently a simpler set of constitutive models, the tool found an equilibrated configuration, between 20 and 50 iterations. After these considerations, again, a good agreement was observed between the developed program and the experimental results. The total processing time was 15 minutes, where most of this time refer to the post-yielding behavior.

4.3 Geometric nonlinear plates analysis

Three rectangular linear-elastic plates, subjected to a uniform load q, presented by Figueiras [7], were analyzed to verify the geometric nonlinear model implemented. The plates span l were equal to 6m and its thickness h was assumed as 0.15m. The material elastic modulus E and Poisson ratio were adopted, respectively, as $30kN/m^2$ and 0.316. The difference between the three structures was the boundary conditions applied to the edges: clamped, simply supported (horizontally fixed) and simply supported (horizontally free). The finite element mesh used contains 6x6 elements, and its thickness were discretized into 10 concrete layers. In all three cases, the number of load increments was equal to 100. The stopping criteria tolerance tol was equal to 10^{-5}. Figure 7 shows the load parameter ($q.l^4/E.h^4$) versus central displacement parameter (w/h) curves obtained in this study, where it is possible to observe good accuracy when compared with literature analytical [29] and numerically [7] solutions. The processing time was about 12 minutes.

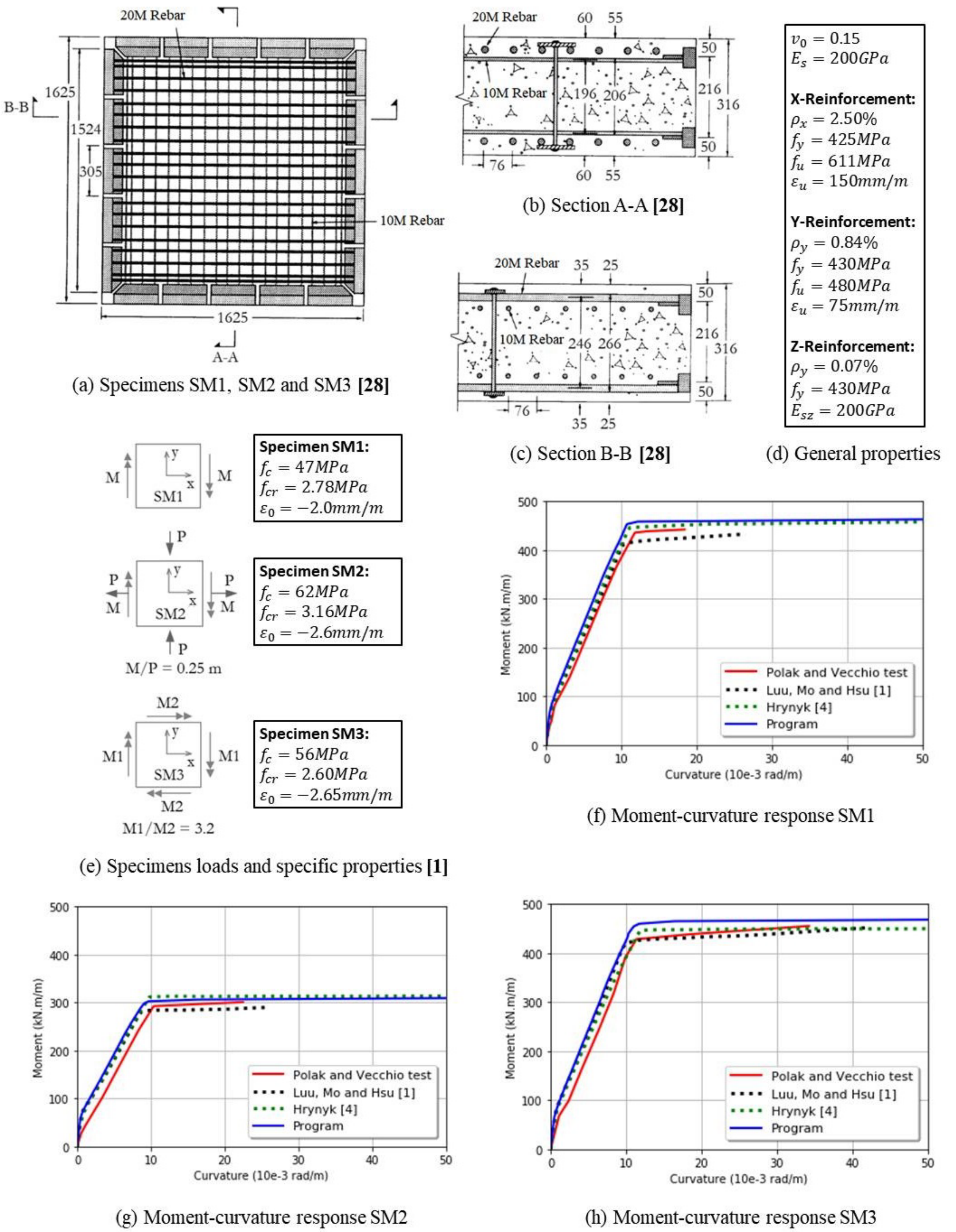

Figure 6. Polak shells

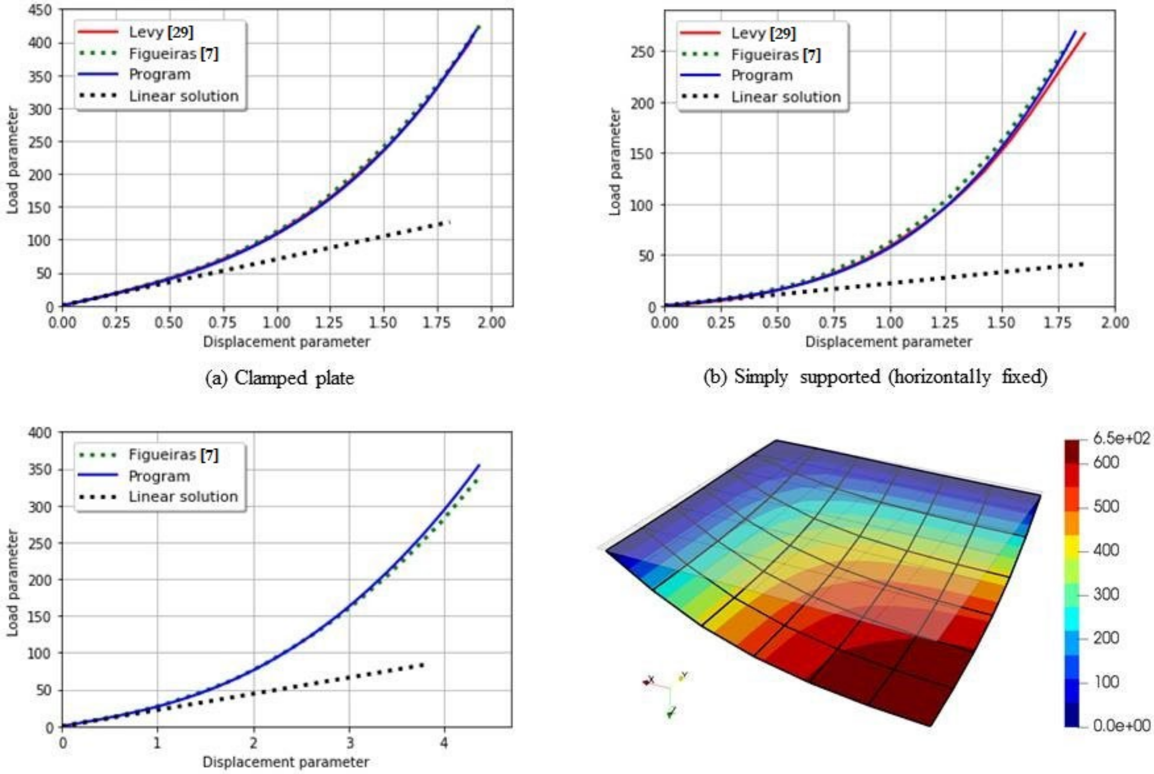

(a) Clamped plate (b) Simply supported (horizontally fixed)

(c) Simply supported (horizontally free) (d) Simply supported (horizontally free) – z-displacement

Figure 7. Geometrically nonlinear plate analysis

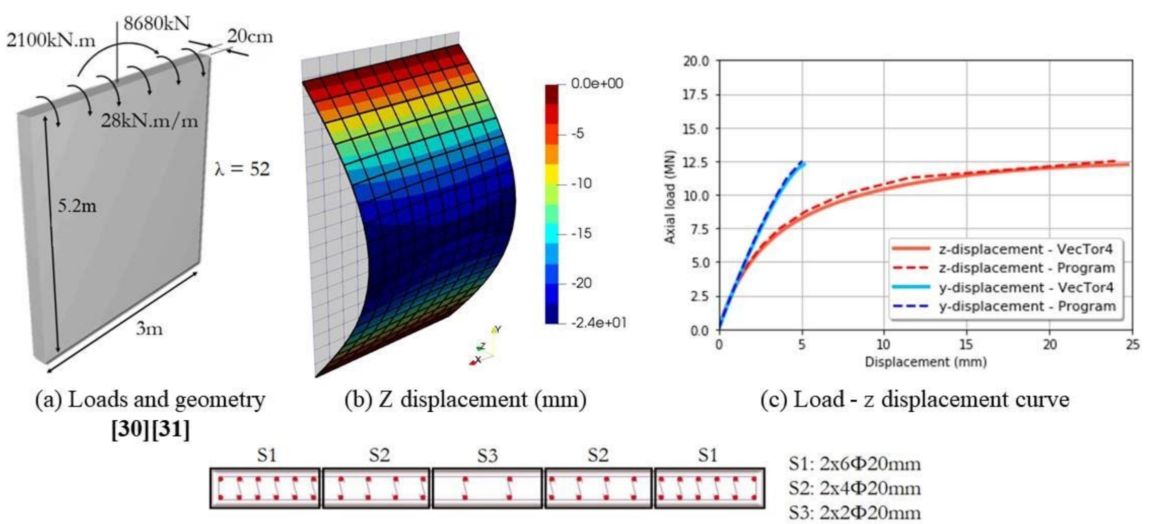

(a) Loads and geometry **[30][31]** (b) Z displacement (mm) (c) Load - z displacement curve

(d) Longitudinal reinforcement **[30][31]**

Figure 8. Slender shear wall

4.4 Slender shear wall

The last problem analyzed was a slender shear wall. The structure geometry was adapted from the literature [6], [30], [31] to reach a wall slenderness ratio equal to 90. It was considered both the material and the geometric nonlinearities The problem characteristics are illustrated in Figure 8. The thickness was discretized into 10 concrete layers. The shear wall is simply supported. The external loads were applied in 10 increments and stopping criteria tolerance tol was equal to 1%. The results obtained in the developed program were compared with VecTor 4 structural analysis software in Figure 8c. The two tools obtained similar results. However, it is important to emphasize that a proper validation must be performed using experimental results. VecTor 4 was adopted as a reference given the lack slender shear walls test results, like Figure 7a. The total processing time was close to 10 minutes.

5 CONCLUSIONS

This paper presents the development of a nonlinear finite element analysis program for reinforced concrete structures, subject to monotonic loading, using thin flat shell finite elements QTFLS [5]. The material nonlinear analysis considered a secant stiffness approach, based on the Modified Compression Field Theory (MCFT) [2]. The element original formulation was expanded to also consider the problem geometric, through a Total Lagrangian Formulation [7]. Based on this study, the following was observed:

- Reinforced concrete structures nonlinear analysis, based on the Newton-Raphson method, using the materials secant stiffness matrices and a Total Lagrangian Formulation can be considered an attractive approach, according to the results accuracy and the computational cost;
- However, the fact that part of the formulation needed to be adjusted to the program be able to find a post-yielding equilibrated response, in some problems (subsections 4.2), shows the difficulty present in the development of a tool with wide range of potential applications, as also exposed by Figueira [7].
- The slender shear wall validation, subsection 4.4, indicates the necessity to conduct experimental programs for this type of structure, in order not only to obtain a better understanding of the construction behavior, but also to produce test data to enable the development of more accuracy computational tools.

REFERENCES

[1] C. Luu, Y. Mo, and T. T. Hsu, "Development of csmm-based shell element for reinforced concrete structures," *Eng. Struct.*, vol. 132, pp. 778–790, 2017.

[2] F. J. Vecchio and M. P. Collins, "The modified compression field theory for reinforced concrete elements subjected to shear," *ACI Struct. J.*, vol. 83, no. 6, pp. 925–933, 1986.

[3] F. J. Vecchio, "Disturbed stress field model for reinforced concrete: formulation," *J. Struct. Eng.*, vol. 126, no. 9, pp. 1070–1077, 2000.

[4] T. D. Hrynyk, "Behaviour and modelling of reinforced concrete slabs and shells under static and dynamic loads," Ph.D. dissertation, Dept. Civ. Eng., Univ. Toronto, Toronto, Canada, 2013.

[5] F. R. Barrales, "Development of a nonlinear quadrilateral layered membrane element with drilling degrees of freedom and a nonlinear quadrilateral thin flat layered shell element for the modeling of reinforced concrete walls," Ph.D. dissertation, Fac. USC Grad. Sch., Univ. Southern California, EUA, 2012.

[6] J. R. B. Silva and B. Horowitz, "Nonlinear finite element analysis of reinforced concrete shear walls," *Rev. IBRACON Estrut. Mater.*, vol. 13, no. 6, pp. e13603, 2020.

[7] J. A. Figueiras, "Ultimate load analysis of anisotropic and reinforced concrete plates and shells," Ph.D. dissertation, Dept. Civ. Eng., Univ. Coll. Swansea, Swansea, 1983.

[8] R. De Borst et al., *Non-Linear Finite Element Analysis of Solids and Structures*, 2nd ed. Chichester: Wiley, 2012.

[9] H. R. V. Goudarzi, "Nonlinear dynamic analysis of reinforced concrete frames under extreme loadings", Ph.D dissertation, Sch. Civ. Environ. Eng., The Univ. New South Wales, Sydney, Australia, 2009.

[10] F. Rojas, J. Anderson, and L. Massone, "A nonlinear quadrilateral thin fat layered shell element for the modeling of reinforced concrete wall structures," *Bull. Earthquake Eng.*, vol. 17, no. 12, pp. 6491–6513, 2019.

[11] F. Rojas, J. Anderson, and L. Massone, "A nonlinear quadrilateral layered membrane element with drilling degrees of freedom for the modeling of reinforced concrete walls," *Eng. Struct.*, vol. 124, pp. 521–538, 2016.

[12] J. L. Batoz and M. B. Tahar, "Evaluation of a new quadrilateral thin plate bending element," *Int. J. Numer. Methods Eng.*, vol. 18, pp. 1655–1677, 1982.

[13] A. Vasilescu, "Analysis of geometrically nonlinear and softening response of thin structures by a new facet shell element," M.S. thesis, Dept. Civ. Environ. Eng., Carleton Univ., Ottawa, Ontario, 2000.

[14] L. E. Vaz, *Método dos Elementos Finitos em Análise de Estruturas*. Rio de Janeiro: Elsevier, 2011.

[15] Y. X. Zhang, M. A. Bradford, and R. I. Gilbert, "A layered cylindrical quadrilateral shell element for nonlinear analysis of RC plate structures," *Adv. Eng. Softw.*, vol. 38, pp. 488–500, 2007.

[16] Y. X. Zhang, M. A. Bradford, and R. I. Gilbert, "A layered shear-flexural plate/shell element using Timoshenko beam functions for nonlinear analysis of reinforced concrete plates," *Finite Elem. Anal. Des.*, vol. 43, pp. 888–900, 2007.

[17] P. S. Wong, H. Trommels, and F. J. Vecchio, *VecTor2 and FormWorks User's Manual. Technical Report*, 2nd ed. Toronto: Dept. Civ. Eng., Univ. Toronto, 2012.

[18] L. M. T. Silva, "Análise não-linear de estruturas de concreto armado submetido ao estado plano de tensões," M.S. thesis, Dept. Civ. Environ. Eng., Fed. Univ. Pernambuco, Recife, 2019.

[19] Comité EURO-International du Béton, *Model Code for Concrete Structures – Design Code*, 1990.

[20] F. J. Vecchio, "Finite element modeling of concrete expansion and confinement," *J. Struct. Eng.*, vol. 126, no. 9, pp. 1070–1077, 1992.

[21] H. Kupfer, H. K. Hilsdorf, and H. Rusch, "Behavior of concrete under biaxial stresses," *J. Proc.*, vol. 66, no. 8, pp. 656–666, 1969.

[22] F. Richart, A. Brandtzeag, and R. Brown, *A Study of the Failure of Concrete Under Combined Compressive Stresses* (Bulletin 185). Univ. Illinois Eng. Exp. Stn., p. 104, 1928.

[23] SciPy. "Python-based ecosystem of open-source software for mathematics, science, and engineering." scipy.org (accessed Sept. 23, 2021).

[24] J. Ahrens, B. Geveci, and C. Law, "ParaView: an end-user tool for large data visualization," in *Visualization Handbook*, C. D. Hansen and C. R. Johnson, Eds., Amsterdam: Elsevier, 2005.

[25] P. Herrera. "Evtk - Export Vtk." https:// pypi.org/ project/ pyevtk/ (accessed Feb. 26, 2021).

[26] V. Cervenka, "Inelastic finite element analysis of reinforced concrete panels," Ph.D. dissertation, Univ. Colorado, Colorado, EUA, 1970.

[27] F. J. Vecchio, "Reinforced concrete membrane element formulations," *J. Struct. Eng.*, vol. 116, no. 3, pp. 730–750, 1990.

[28] M. A. Polak and F. J. Vecchio, "Reinforced concrete shell elements subjected to bending and membrane loads," *ACI Struct. J.*, vol. 91, no. 3, pp. 261–268, 1994.

[29] S. Levy, *Square Plate with Clamped Edges Under Normal Pressure Producing Large Deflections* (DACA, Tech. Note 847). 1942.

[30] R. L. S. França and A. E. Kimura, "Resultados de recentes pesquisas para o dimensionamento das armaduras longitudinal e transversal em pilares-parede," in *9° Enc. Nac. Eng. Con. Estrut.*, 2006.

[31] A. E. Kimura, *Cálculo de Pilares de Concreto Armado – Introdução, Visão Geral & Exemplos*. São Paulo: Assoc. Bras. Eng. Con. Estrut., 2016.

Author contributions: JRBS: conceptualization, methodology, numerical analysis, writing. BH: conceptualization, methodology, writing, supervision.

Editors: Osvaldo Manzoli, Guilherme Aris Parsekian.

IBRACON Structures and Materials Journal
Revista IBRACON de Estruturas e Materiais
ISSN 1983-4195 ismj.org

ORIGINAL ARTICLE

Numerical analysis of piled rafts with short bored piles

Análise numérica de radier estaqueado com estaca escavada curta

Eduardo Augusto dos Santos Oliveira[a]
Marcos Oliveira Justino[a]
Jean Rodrigo Garcia[a]

[a] Universidade Federal de Uberlândia - UFU, Faculdade de Engenharia Civil, Uberlândia, MG, Brasil

Received: 14 January 2021
Accepted: 12 January 2022

Abstract: Numerical analysis of the behavior of piled rafts seated on uniform soil with low bearing capacity has been important to support the project design. The calibration of the numerical model with instrumented load test allows usage of the results, in given conditions, in the foundation design of small and medium-sized buildings built on soils with the same mechanical properties analyzed in this paper. In this context, this paper evaluates numerical models, which allow to consider the influence of short bored piles connected to the raft. The models are also assessed using piled rafts concepts. From the results obtained, the load supported by the total shaft resistance is significant for the case of bored piles, and this load is from 14% to 30% higher in the case more flexible or thinner raft. Inserting piles in the rafts reduces settlement and increases overall stiffness. Such effects are amplified in piles with higher slenderness ratios (L/d).

Keywords: piled raft, numerical modeling, bored piles, load sharing, settlement reduction.

Resumo: A análise numérica do comportamento de radiers estaqueados assentes em solo uniforme e de baixa capacidade de suporte tem se mostrado importante para subsidiar a concepção do projeto. A calibração do modelo numérico com uma prova de carga instrumentada permite que os resultados possam ser aplicados, dentro das condições estabelecidas, ao projeto de fundações para edificações de pequeno e médio porte assentes em solos com as mesmas propriedades mecânicas analisadas neste artigo. Nesse sentido, o artigo avalia modelos numéricos, que permitam estudar a influência de estaca curta executada por escavação acoplada ao radier. Os modelos também são avaliados a partir dos conceitos de radier estaqueado. A partir dos resultados obtidos, verifica-se que a carga suportada pela resistência lateral, significativa para o caso de estacas escavadas, é de 14% a 30% maior para radiers mais flexíveis ou com menores espessuras. A introdução de estacas nos radiers promove a redução de recalques e o aumento da rigidez do sistema, tendo seus efeitos ampliados para estacas com esbeltezes (L/d) mais elevadas.

Palavras-chave: radier estaqueado, modelagem numérica, estacas escavadas, distribuição de carga, redução de recalques.

How to cite: E. A. S. Oliveira, M. O. Justino, and J. R. Garcia, "Numerical analysis of piled rafts with short bored piles" *Rev. IBRACON Estrut. Mater.*, vol. 15, no. 4, e15408, 2021, https://doi.org/10.1590/S1983-41952022000400008

1 INTRODUCTION

Understanding the behavior of a piled raft foundation leads to the need of analyzing not just the foundation system in each separate element, the piles and the raft, but also the interactions among them over time.

In typical foundation projects, such as pile groups, the cap resistance is neglected in the design, even when the cap is in contact with the soil. Investigations and analytical methods have been developed to consider the soil-structure interaction, enabling to assess the contribution of the raft on the bearing capacity of the system. Sophisticated

Corresponding author: Jean Rodrigo Garcia. E-mail: jean.garcia@ufu.br
Financial support: This work was supported through a FAPEMIG grant funded by the State of Minas Gerais and Coordination for the Improvement of Higher Education Personnel (Coordenação de Aperfeiçoamento de Pessoal de Nível Superior - CAPES) financing code 001.
Conflict of interest: Nothing to declare.
Data Availability: The data that support the findings of this study are available from the corresponding author, JRG, upon reasonable request.

This is an Open Access article distributed under the terms of the Creative Commons Attribution License, which permits unrestricted use, distribution, and reproduction in any medium, provided the original work is properly cited.

methodologies and the search for refined results have become main points in the field of foundations, due to the decrease of computational costs. In practice, the creation of numerical models that can guide the engineer to an efficient foundation design is a key factor to achieve efficacy of a project.

Among other advantages, numerical modeling enables fast parametric analyses, saving tests and experimentations, even though it does not replace them. Correlations factors can be deduced from the model results, and then combined and calibrated with experimental results.

The foundations considered in this work consist of rafts of varying thicknesses and short bored piles of varying lengths. The concepts and characteristics of each one of these elements are discussed, as well as how they affect the behavior of the piled rafts studied. In addition, features and results are presented in terms of the behavior of the system and their elements separately.

The present work is limited to considering the following hypotheses:

- the soils have constant mechanical characteristics along its depth, since short piles are used;
- the load is applied of loading distributed over the entire raft area; loading takes place at time intervals that do not allow soil consolidation;
- pore pressure and saturation are not considered;
- effects due to suction are implicit in the calibration and validation of the model with experimental results.

The numerical analysis considered elastoplastic constitutive model materials, based on the elastic perfectly plastic behavior with of Mohr-Coulomb failure criterion.

From the analysis of sixteen cases of piled rafts, it was possible to quantify the load distribution between the raft and the pile, as well as to estimate the influence of the piles on reducing settlements, on the variation of the shaft resistance according to the pile depth, on the axial load transfer, on the pile lateral and toe strength portions and on the overall stiffness.

1.1 Previous works

The number of studies on the behavior of piled foundations has increased significantly since the 1950's, strengthening and consolidating the understanding of these systems. Several works have studied the influence of foundation geometry [1]–[4], the contribution of raft-soil contact and load distribution among the elements and their variables [5] and the use of numerical models for analysis of piled rafts [6].

Many authors report several advantages in considering the raft-soil contact, such as reduction and uniformity of settlements (differential and total) and the increase in load capacity [6]–[8]. According to Butterfield and Banerjee [5], the load supported by the raft can range from 20% to 60%, assuming larger values for higher spacing between piles. Experiments reported in Garcia and Albuquerque [4] and numerical studies reported in Garcia [9] considering porous residual soil and piles spacing (s) equal to five times their diameter, shows a contribution of 21% and 36% of the raft-soil contact, respectively. Kuwabara [10], reports study using boundary elements method in cases of piles spacing smaller than ten times their diameter normal spacing and compared pile groups and piled rafts and founding a distribution of 20% to 40% of the total load to the raft.

The parameters involving foundation geometry, number of piles, and materials properties influence the behavior of the foundation [2]. According to Ottaviani [6] and Kuwabara [10], the effect of raft-soil contact influences the load distribution and transfer to the soil, and are affected by in terms of the position of the pile in the raft. Brown and Wiesner [7] highlighted the importance of parameters such as pile slenderness, L/d, relative pile spacing, s/d, relative stiffness between raft and soil, and relative stiffness between pile and soil for a preliminary assessment of the piled foundation design.

Saeedi Azizkandi et al. [11] investigated the load sharing mechanisms in piled rafts using numerical analyses with and without connection of the piles to the raft. The authors reported that the increase in the pile length reflected an increase in the portion of shared load, particularly in rafts with connected piles.

An important aspect in the analysis of piled foundations is related to the raft and how it is designed to be either rigid or flexible. Clancy and Randolph [12] concluded that the behavior of the foundation changed with the increase in raft flexibility when the foundation models have few piles (less than 4 piles). Analyzing the measurements taken at the foundation of the Messeturm building in Frankfurt, Randolph [8] observed that the failure of the piled raft foundation occurred mostly by punching the raft, since the piles prevent the raft from moving with the soil, submitting it to the Ultimate Limit State of the foundation. However, pile rafts must be classified according to their dimensions in order to define the appropriate analysis. Russo and Viggiani [13] categorize piled rafts in two groups, calling "small" rafts those in which rafts do not have sufficient bearing capacity and the piling alone will ensure adequate safety factor, and "large" rafts, which have enough bearing capacity, ensuring a certain share of and requiring the introduction of piles as settlement reducers.

Katzenbach and Choudhury [14] recommended evaluating piled rafts at Ultimate Limit State (ULS) and at Service Limit State (SLS), by means modeling that can consider the effects of the interaction among the elements of the foundation. For each limit state, an external check, considering the behavior of the whole foundation, and an internal check, evaluating the elements separately, should be performed and the most unfavorable results used for design. In this context, the use of numerical tools for the analysis of the complexity involved in piled raft foundation is important, as well as its benefits to obtain the appropriate design and to avoiding overdesigning when considering simplified methods. Poulos [15] highlights the importance of considering the effects of interactions among the raft, pile and soil by using structural numerical models in order to avoid under designing the foundation with simplified methods.

Mandolini, Russo and Viggiani [16] and Randolph [8], report evaluating 125 pile load tests with different installation processes. They conclude that the type of installation affects more the load capacity of piles than their axial stiffnesses determined by estimation of the tangent to the curve containing the first three loading points.

The evaluation of the behavior of the elements that form piled rafts is related not only to load capacity and settlement, but also to how the shaft resistance and the toe resistance are mobilized.

Studies performed by Lee et al. [17] on the interaction among elements of piled raft in sands described the load distribution in the pile as a function of the overall displacement, and the established coefficients considering the initial rapid increase of the load on the pile with small displacements that do not considerably increase with larger displacements. These coefficients were later incorporated into the model proposed by Clancy and Randolph [18].

1.2 Some concepts on piled rafts

Katzenbach and Choudhury [14] and Abdel-Azim et al. [19] consider two parameters to distinguish the behavior of piled raft foundations with respect to the pile group and to isolated rafts. In the case of the piled rafts, the coefficient α_{pr} is a correlation related to the characteristic values and is presented as function of a given settlement, s, according to Equations 1 and 2:

$$\alpha_{pr} = \frac{\sum_{j=1}^{m} R_{pile,k,j}(s)}{R_{tot,k}(s)} \tag{1}$$

$$\alpha_s = \frac{s_{pr}}{s_r} \tag{2}$$

Where:

α_{pr} = piled raft coefficient;

α_s = settlement reduction coefficient;

$\sum_{j=1}^{m} R_{pile,k,j}(s)$ = sum of the characteristic pile resistances for a given settlement;

$R_{tot,k}(s)$ = characteristic value of the total resistance for a given settlement;

s_{pr} = settlement of piled raft foundation;

s_r = settlement of a spread foundation.

The α_{pr} values vary between 0 for raft alone and 1 for pile group without raft contribution, as well as the α_s value vary within the range from 0 (piled raft) to 1 (raft alone), as verified by Katzenbach and Choudhury [14], verified the interdependence between the foundation behavior as a function of stress level and settlement (Figure 1).

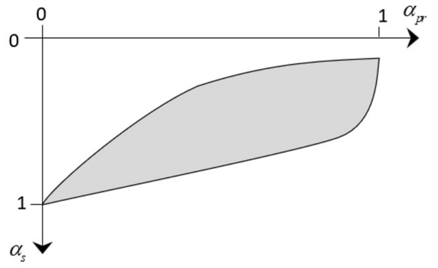

Figure 1. Correlation between settlement reduction coefficient, α_s, and load sharing coefficient α_{pr} of piled raft.

1.3 Effect of rafts on skin friction and axial force

Abdel-Azim et al. [19] analyzed numerically the piled foundations proposed by Katzenbach et al. [20] evaluating the distribution of skin friction along the 30-meter-long pile assessed for settlements, s, equal to 0.5%, 1% and 10% of "d". According to these authors, the best position to obtain the skin friction readings along the shaft interface is at a radial offset of 0.1d from the outer face of the shaft (Figure 2). It is observed that, for the first loading stages, the friction is mobilized to the toe, which has its skin friction exhausted from the sixth loading stage (60% of total load), and then leads to a greater resistance mobilization in a region close to the raft, as previously verified by Fioravante et al. [21].

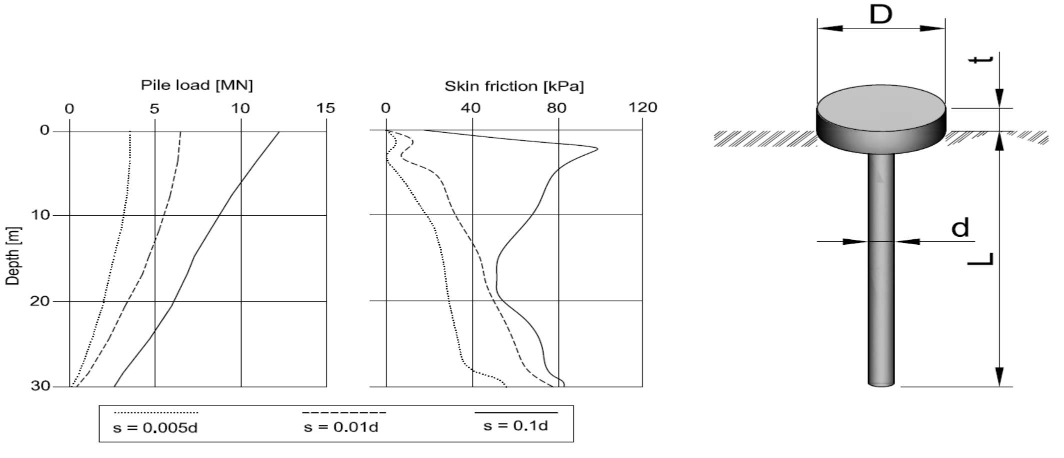

Figure 2. Influence of the pile-raft interaction on axial load transfer and skin friction with depth based on the Frankfurt Clay model (Katzenbach et al. [20]).

1.4 Bored piles

De Cock [22] describes a series of studies carried out by Caputo [23] and reinforced the influence of the pile installation method on soil confinement, and mentioning for example the tendency of the base of bored piles to move in the opposite direction of the excavation, which does not occur with driven piles.

Some studies show that shaft resistance of piles develops before toe resistance because it requires small displacements for mobilization [24], [25]. Through field tests, Garcia [9] observed that shaft resistance mobilization occurs mainly within a range of relative displacement to the pile diameter s/d between 1% and 5%.

Zhang et al. [26] outline three soil situations at the pile toe to explain the mechanism of toe resistance mobilization when there is relative displacement between the pile and the soil. In the first situation (Figure 3a), the soil layer shows a relatively normal resistance. In the second situation (Figure 3b), soil resistance is low, which may be caused by accumulated sediments at the pile base; in the third situation (Figure 3c) the soil under the toe has high resistance. The authors discuss the interaction between the lateral and toe resistance in the three situations with the use of the Mohr-Coulomb's failure criterion.

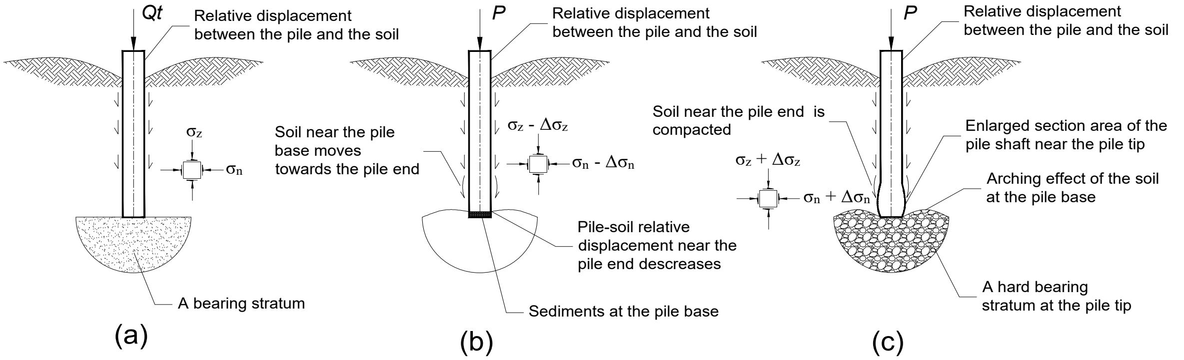

Figure 3. Stress state of soil element near pile end with different soil strengths at pile base (after Zhang et al. [26]).

The piles studied in this article relate to the situation described in Figure 3b, of low resistance soil at the base of the pile, aiming to better represent the behavior of foundations composed by short bored piles, also behaving as friction piles.

2 VALIDATION WITH EXPERIMENTAL STUDY

The material properties were obtained through calibration with experimental results obtained by Garcia [9] in piled cap composed of a short and small diameter bored pile, subjected to axial compression in residual soil. The block geometry (0.60 m x 0.60 m) was adjusted to an equivalent circular geometry, keeping the contact area with the soil to apply axisymmetric numerical modeling with Finite Elements (FEM-2D) by means of the Rocscience RS2 software. The pile used in the model has dimensions of 0.25-m diameter and 5-m length. The numerical model for validation considered non-contact between the side faces of the cap and the soil and included the modeling technique discussed in this work. Hence, the insertion of a region of low resistance soil under the pile toe (Figure 4) to represent the installation method of the pile usually employed in typical foundations.

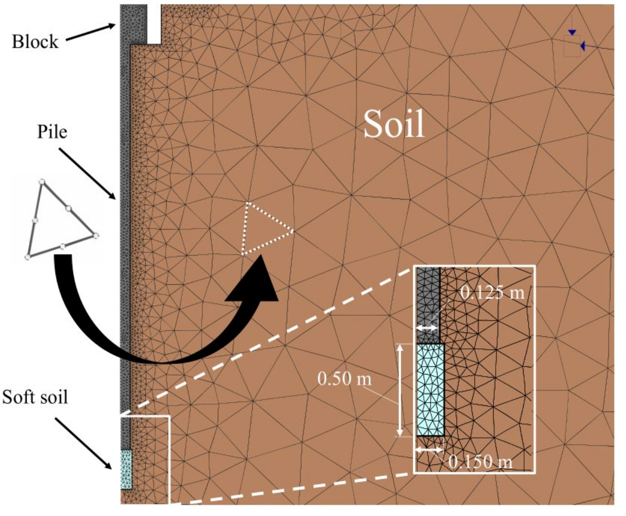

Figure 4. Numerical model for validation and detail of the soft material region inserted below the pile toe and graded mesh type and 6-noded triangle element.

The model was validated by comparing the load *vs.* settlement curve adjustment, both numerical and experimental, described by Garcia [9]. Although the numerical model has not taken into account the variation of soils and properties with the depth considered by Garcia [9], the results of the load-settlement curves (Figure 5) denote optimal adjustment up to the sixth stage of the applied load, in addition to the good agreement in the general behavior of the foundation under the aspect of load distribution, axial load transfer and skin friction. The material parameters obtained with the numerical calibration stage are shown in Table 1.

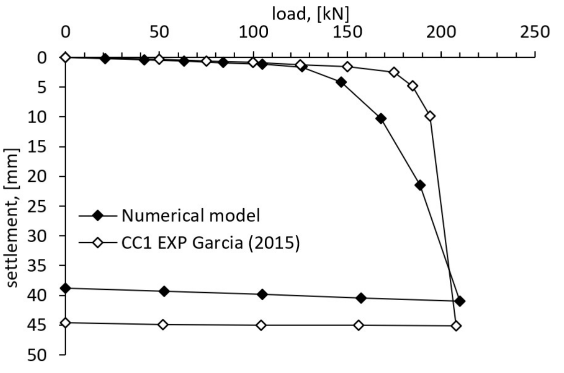

Figure 5. Load-settlement curves of the piled rafts by Garcia [9] versus numerical model.

The parameters were derived from compressive and tensile strengths for mass concrete based on the suggestion given by Ardiaca [27].

Table 1. Mechanical characteristics and materials deformability.

Material	E (MPa)	ν	K_0	γ (kN/m³)	Model	ϕ (°)	c (kPa)
Soil	30.0	0.33	0.8	15	Elastoplastic	21	22
Soft material	5e-2	0.40	0.8	15	Elastoplastic	3	0
Concrete	30,100	0.20	-	25	Elastic	50	300

Note: E is the Young's modulus; ν is the Poisson's ratio; K_0 is the coefficient of at-rest earth pressure; γ is the unit weight; ϕ is the soil friction angle; c is the cohesion.

3 PARAMETRIC ANALYSIS

The analyses were carried out based on a parametric study, varying the geometric characteristics, such as raft thickness and pile length (Table 2).

Table 2. Details of the piled raft geometries analyzed and their loads.

Case	D_r (m)	t (m)	L (m)	d (m)	L/d	t/d	Stress applied (kPa)	Load applied (kN)
1	1.25	0.1	3	0.25	12	0.4	264	324.0
2		0.2		0.25		0.8	284	348.5
3		0.3		0.25		1.2	300	368.2
4		0.4		0.25		1.6	310	380.4
5	1.25	0.1	4	0.25	16	0.4	293	359.6
6		0.2		0.25		0.8	310	380.4
7		0.3		0.25		1.2	328	402.5
8		0.4		0.25		1.6	336	412.3
9	1.25	0.1	5	0.25	20	0.4	320	392.7
10		0.2		0.25		0.8	340	417.2
11		0.3		0.25		1.2	352	432.0
12		0.4		0.25		1.6	370	454.1
13	1.25	0.1	6	0.25	24	0.4	350	429.5
14		0.2		0.25		0.8	371	455.3
15		0.3		0.25		1.2	380	466.3
16		0.4		0.25		1.6	390	478.6

Note: D_r is the raft diameter; t is the raft thickness; L is the pile length; d is the pile diameter; $A_{raft} = 1.227m^2$.

The geometry of the piled raft cases under consideration has fixed parameters such as raft and pile diameter, and variable parameters such as raft thickness and pile length (Figure 6).

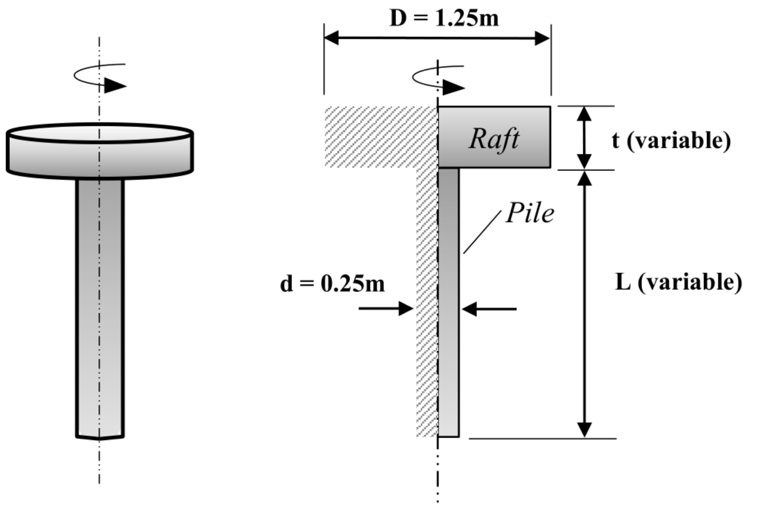

Figure 6. Geometry of the piled raft.

4 NUMERICAL ANALYSIS

The numerical analyses were performed with the aid of Rocscience RS2 software, which enables two-dimensional analyses on geotechnical structures and foundations by means of finite elements by considering, plane strain state or axisymmetric conditions.

The three-dimensional geometry of the foundation was converted into a plane model with axisymmetry around the axis of rotation (Figure 6). For the discretization of the soil mass and the piled raft, elements of the triangular type composed of 6 nodes were used (Figure 5). A graded mesh was adopted, discretized according to the number of dividing elements at the interfaces between the structure and the soil contour, having elements of size at a ratio of 1:70 between the interface around the contact of the structure with the ground and the interior of the soil mass. The number of elements in the models ranged from 4,000 to 6,000; such variation was due to the need for greater discretization inside the piled raft. Therefore, models with thicker rafts and longer piles resulted in a higher number of elements and nodes.

The type of loading chosen in the software was Body Force and Field Stress. It is divided into two stages: first a stress due to the self-weight of the elements is applied considering the horizontal response; then the loading is imposed, according to the stage.

The boundary dimensions were assumed to be about 1.6 times the length of the longest pile (L=6m). Moreover, the lateral boundaries of the model were restrained in the X-direction, and the lower boundary was restrained to move in X and Z-directions.

The dimensions of the low-strength soil element (soft material) were taken with a diameter of 1.2d and height equals to 2 times the diameter of the pile. The choice of extending the width of the region situated at the pile toe beyond the diameter was designed to overcome problems related to stress concentration in zones between different materials, as well as to improve the quality of the mesh in this region.

5 RESULTS AND DISCUSSION

From the methodology presented, an analytical structure was elaborated to briefly represent the steps that compose the present study (Figure 7).

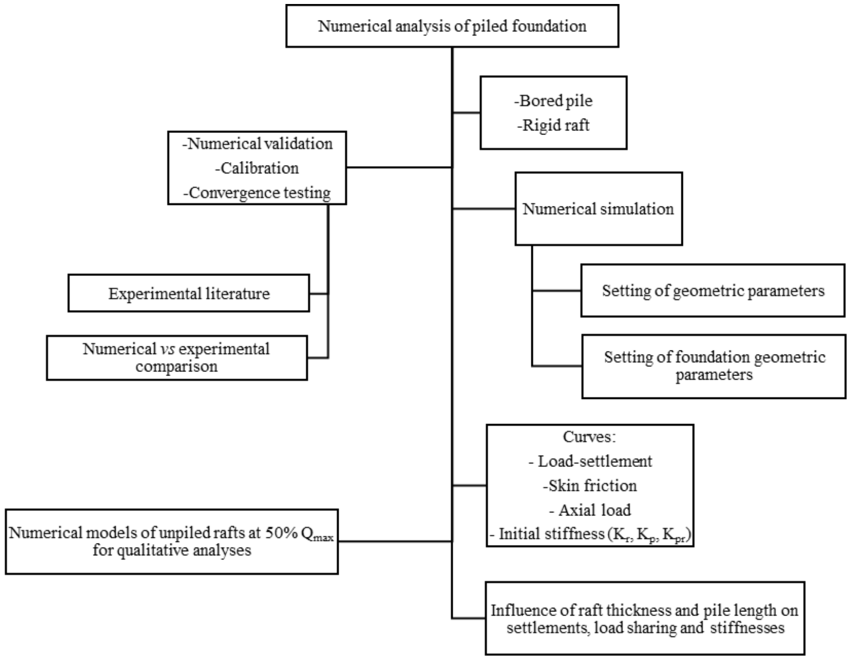

Figure 7. Scheme describing the steps of the present study.

5.1 Load settlement curves

The load versus displacement responses of each foundation under analysis were obtained from the application of a 10-stage series, with 10% increments up to the maximum load (Table 2). Unloading was performed in a 4-stage series, with 25% decreases of the maximum test load until total unloading (Figure 8 to Figure 23).

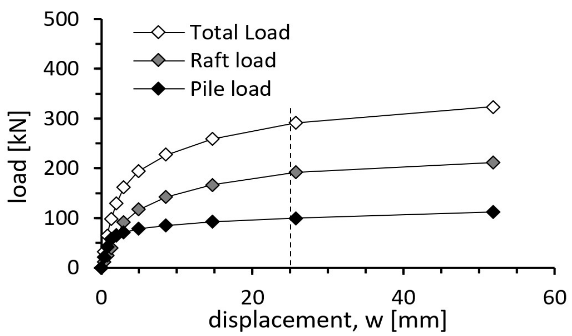

Figure 8. Load-settlement curve for case 1 - L=3m; t=0.1m

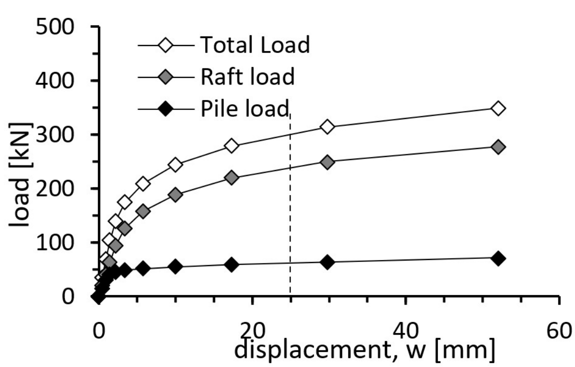

Figure 9. Load-settlement curves for case 2 - L=3m; t=0.2m

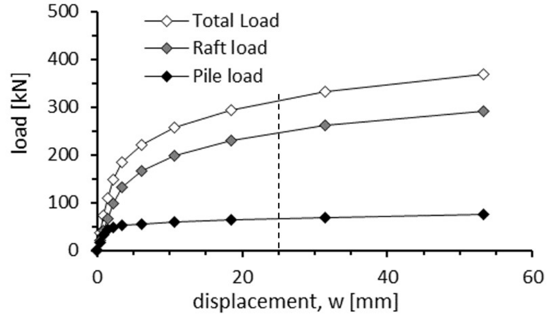

Figure 10. Load-settlement curves for case 3 - L=3m; t=0.3m

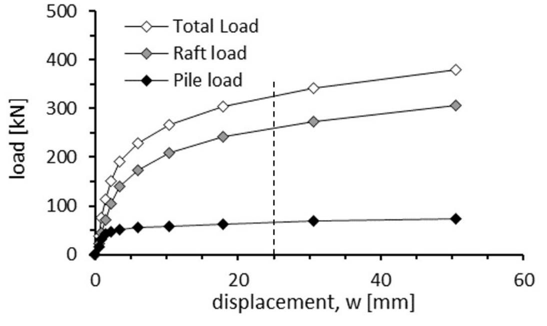

Figure 11. Load-settlement curves for case 4 - L=3m; t=0.4m

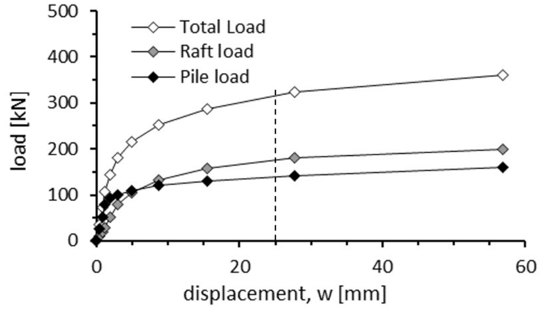

Figure 12. Load-settlement curves for case 8 - L=4m; t=0.1m

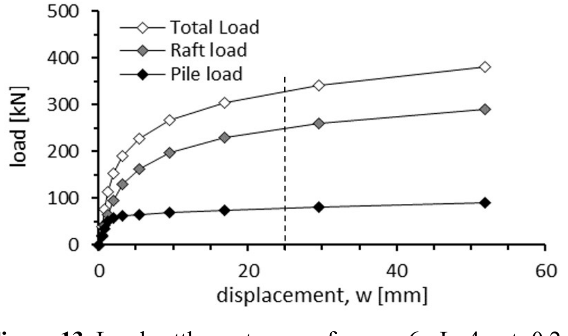

Figure 13. Load-settlement curves for case 6 - L=4m; t=0.2m

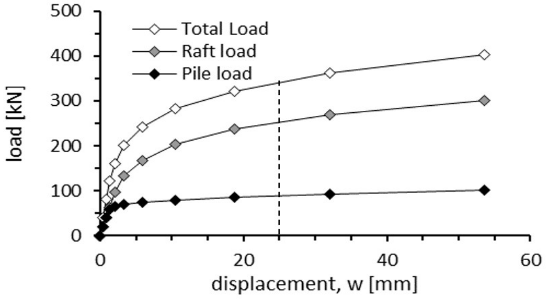

Figure 14. Load-settlement curves for case 7 - L=4m; t=0.3m

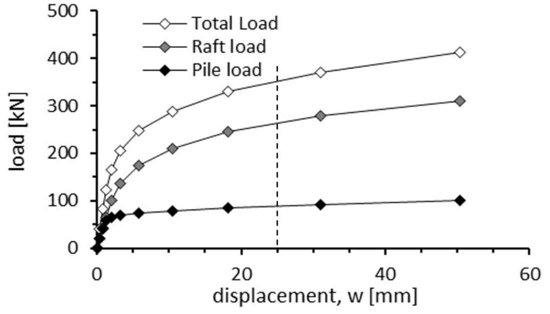

Figure 15. Load-settlement curves for case 8 - L=4m; t=0.4m

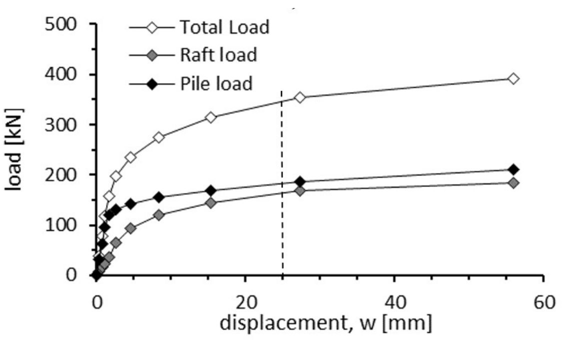

Figure 16. Load-settlement curve for case 9 - L=5m; t=0.1m

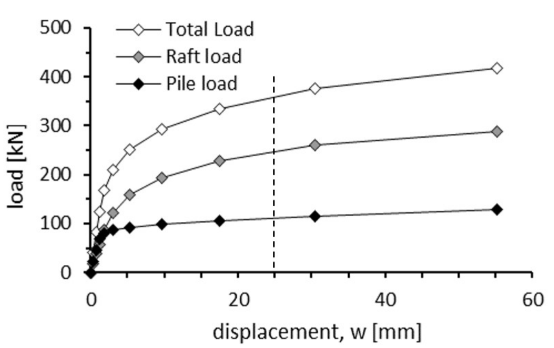

Figure 17. Load-settlement curves for case 10 - L=5m; t=0.2m

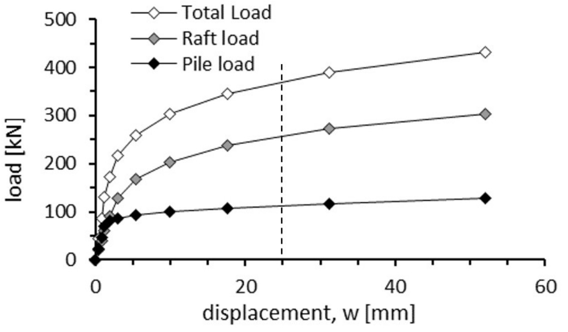

Figure 18. Load-settlement curves for case 11 - L=5m; t=0.3m

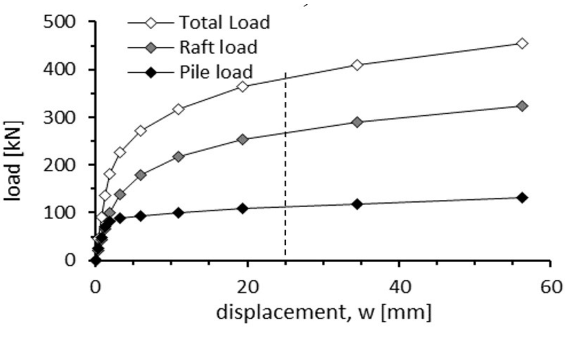

Figure 19. Load-settlement curves for case 12 - L=5m; t=0.4m

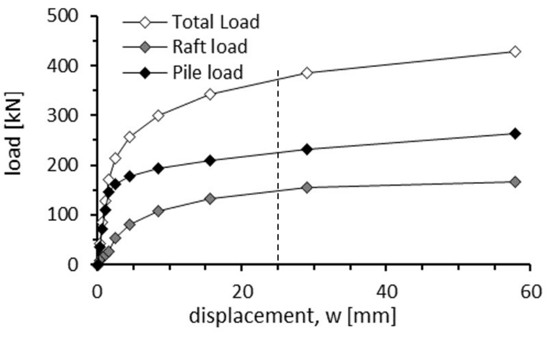

Figure 20. Load-settlement curves for case 13 - L=6m; t=0.1m

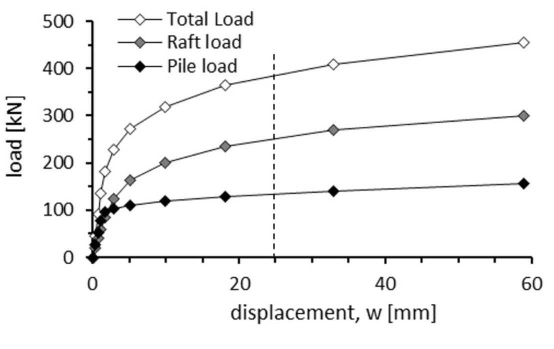

Figure 21. Load-settlement curves for case 14 - L=6m; t=0.2m

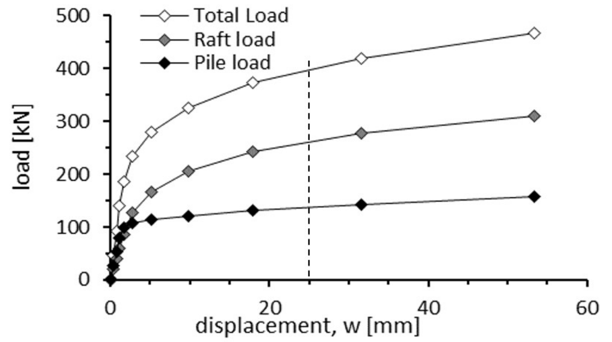

Figure 22. Load-settlement curves for case 15 - L=6m; t=0.3m

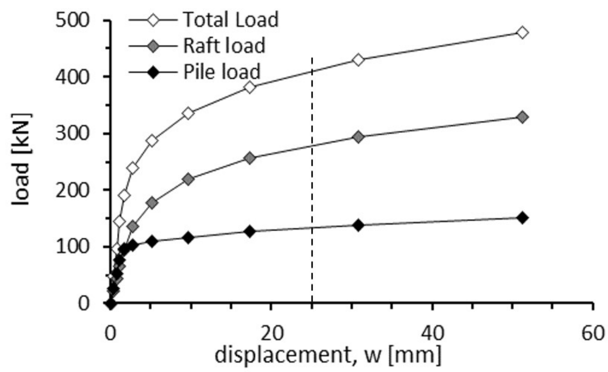

Figure 23. Load-settlement curves for case 16 - L=6m; t=0.4m

The maximum test loads were established for each piled raft to obtain approximately 50 mm of displacement, conventionalizing the geotechnical "failure" of the foundation by one of the limit states. As a failure criterion for ultimate resistance, according to the recommendations from the British Standard BS 8004:2015 [28], the displacement assumed was of 10% of the pile diameter or 25 mm.

The load settlement curves show a greater pile share in the load capacity of the foundation system for 0.10-m thick rafts. The contribution of the pile is reduced for rafts with thickness of 0.20 m or more. On the other hand, in all cases analyzed, the participation of the raft-soil contact is preponderant in comparison to the pile participation. Such evidence can be attributed to the high raft contribution area in the overall bearing capacity. The following curves are basically distinguished by the characteristics of the raft-soil stiffness, i.e., for rafts considered flexible (0.10 m in height) and rigid (> 0.20 m).

5.2 Influence of raft thickness on shaft resistance of piles

The effect of raft thickness on the portion of total load supported by total shaft resistance of piles (Figure 24). The 0.10-m thick rafts influenced positively the mobilization of skin friction, compared to models with 0.20 m, 0.30 m, 0.40 m thicknesses: differences between 14% and 30% can be seen. In addition, with increasing loads, rafts thicker than 0.10 m led to minor load sharing by the pile due to little toe resistance and to greater participation of the raft. During the loading test with piled rafts instrumented and described by Garcia [9], the values measured for total toe resistance were around 6% of the total load applied to the foundation, even at displacement levels of approximately 20% of the pile diameter. In all cases, the axial load reaching the pile toe was less than 2% of the total load, even for large relative displacements, close to 20% of the pile diameter (50 mm). The behavior of the piles compares to that of floating piles, which orient their resistance predominantly to the shaft. Such values imply that the model represents adequately a short bored pile of small diameter inserted in uniform soil.

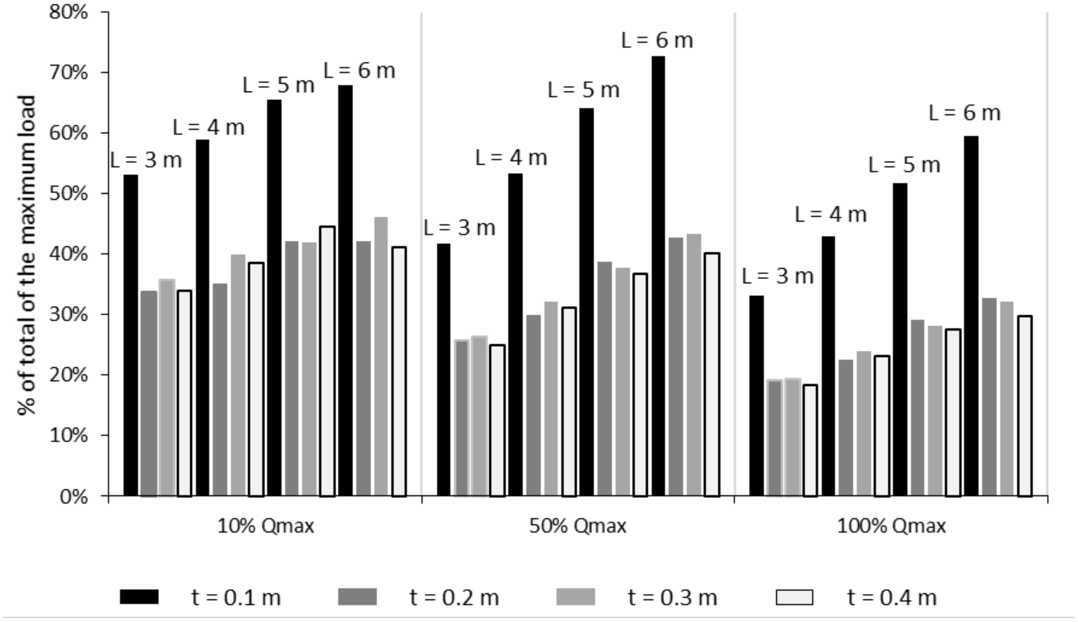

Figure 24. Portion of the maximum load taken by the total shaft resistance.

6 RESPONSE AND BEHAVIOR ANALYSES

The choice of geometric parameters to evaluate the interaction among the soil, raft and pile is based on previous works in the literature on piled foundations, among which, those of Poulos and Davis [2], Kuwabara [10] and Clancy and Randolph [18].

The behavior analyses regarding relative stiffness were established with respect to the pile slenderness ratio (L/d), and the ratio between raft thickness and pile diameter (t/d). Based on the parametric characteristics and properties of the mechanical behavior of foundations under analysis, this work seeks to correlate the favorable features to the appropriate design elaboration, supporting premises for a qualitative evaluation for conception and predesign of foundation elements of superstructures.

6.1 Initial Stiffnesses of Piled Rafts

For the 16 cases analyzed, the stiffness of piled rafts foundations ($K_{piled\ raft}$) and their elements (K_{pile} e K_{raft}) were calculated by means of the loading and displacement values obtained in the first stages (i.e., up to 50% of the maximum load of a given foundation (Q_{max}), and therefore, the structural elements exhibit a linear elastic behavior and they have a good potential to be used in practical applications.

The increase in raft thickness for a constant diameter (t/d) does not influence the increase in stiffness of the piled raft unit, which remains almost constant for the same pile slenderness ratio (Figure 25a). On the other hand, for a higher pile slenderness ratio, there is an increase in relative stiffness of the piled rafts under analysis, showing that the isolated stiffness of the pile (Figure 25b) is directly related to its slenderness ratio (L/d). The raft stiffness is small for flexible rafts (t/d = 0.4), but it remains almost constant for rafts considered as rigid (t/d $\geq$ 0.8) (Figure 25c). The models with 0.1-m thick rafts (t/d = 0.4) allow greater pile response, since the surface element has lower capacity to restrain displacements due to its lower stiffness.

When analyzing the influence of the use of longer piles connected to thicker rafts, it was found that piled raft stiffness is predominantly influenced by pile stiffness and its slenderness ratio (Figures 25 and 26). For rafts considered rigid (t/d $\geq$ 0.8), the raft response is practically uniform for different values of pile slenderness (L/d), while the contribution to pile stiffness and overall stiffness is linearly increasing. Distinct behavior is observed for rafts considered flexible (t/d= 0.4), in which raft stiffness (K_r) decreases linearly with increasing ratio L/d This is explained by the increasing pile stiffness (K_p), as seen in Figure 26b and Figure 26c.

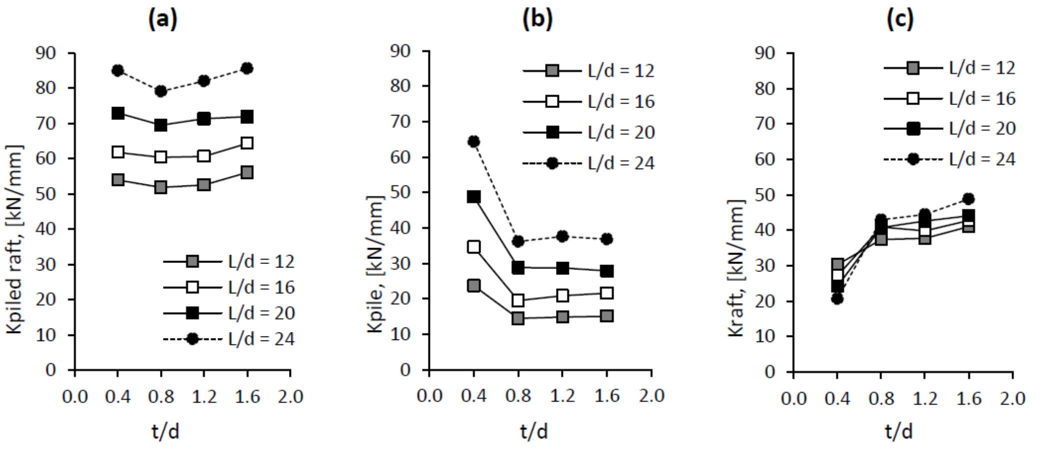

Figure 25. Effect of t/d ratio on piled raft, pile and raft responses

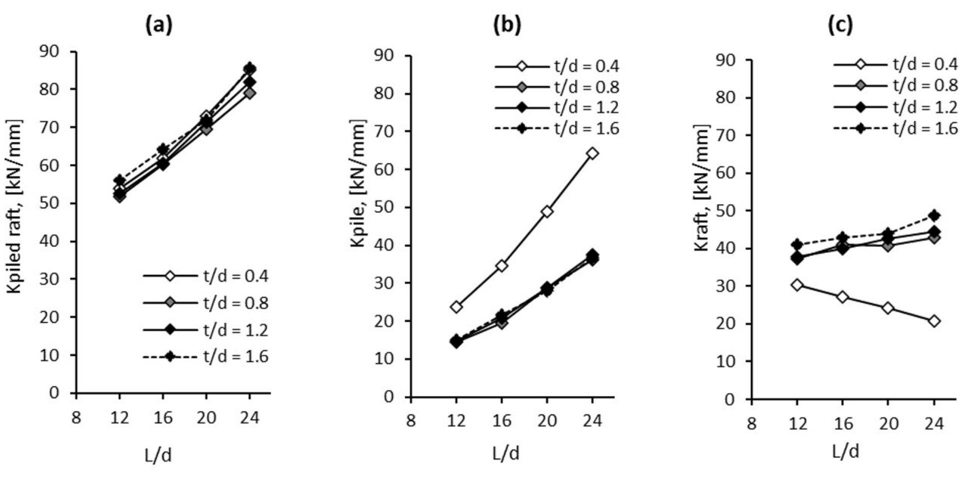

Figure 26. Effect of L/d ratio on piled raft, pile and raft responses.

6.2 Settlement Reduction and Load Sharing

A comparison of the effects of using piles combined with rafts shows that rafts of heights equal to 0.1 m are more sensitive to distribution of loads among the foundation elements, thus increasing the load portion supported by the piles.

Based on the analyses carried out and considering the reduced settlement in the piled foundation (Figure 27), it is verified that increasing raft thickness has little influence on the reduction of its total settlement (s_{pr}), when compared to those of unpiled rafts (s_r). The insertion of piles in the raft and the increase in pile length leads to a significant reduction of the total settlement of the piled raft, for all thicknesses analyzed.

The load sharing in the analyzed models increases with the increase of raft thickness, whose values varied from 28% to 45% (Table 3) for the cases of rigid rafts ($t \geq 0.2$ m). On other hand, based on the average of the coefficient α_s values, the total settlements presented 44% to 78% reduction when compared to isolated rafts, showing the efficiency of the pile insertion. In the cases analyzed in this work, the piles were positioned at the point of occurrence of the greatest displacement, i.e., the central region of the raft.

The results above agree with the propositions given in De Sanctis et al. [29] about what occurs in "small rafts" where the ratio is D/L <1. According to the classification of these authors, a "small" isolated raft does not have enough bearing capacity to support the total load, thus requiring the insertion of piles to ensure reduced settlement. It also improves the bearing capacity of the system. In this case, differential settlement is not essential for rafts considered as rigid since the raft in this situation has enough flexural stiffness.

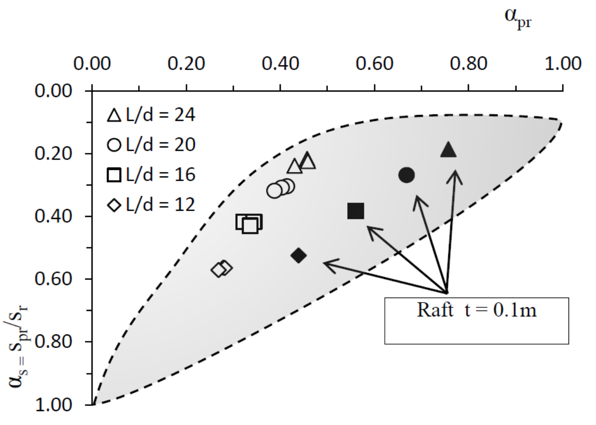

Figure 27. Evaluation of settlement reduction and load sharing for the piled rafts (at 50% of Q_{max}).

Table 3. Results from the evaluation of the piled raft units.

L/d	α_{pr} (t=0.1m)	$\overline{X}(\alpha_{pr})$ (t=0.2m;0.3m;0.4m)	Increasing % in the pile load $\Delta\alpha_{pr}$ (%)	Total settlement reduction
12	0.44	0.28	16%	44%
16	0.56	0.33	23%	59%
20	0.67	0.40	27%	70%
24	0.76	0.45	31%	78%

Note: d = 0.25m; α_{pr} =piled raft coefficient; $\overline{X}(\alpha_{pr})$ average of the values

7 CONCLUSIONS

The determination of parameters through numerical validation of experimental tests is an important tool to study the behavior of piled foundations, since it is possible to assess the interaction between the elements, by means of an appropriate modeling. A careful check is required during the modeling to verify if the conditions observed in the field can be implemented in the numerical model.

For a t/d ratio equal to or higher than 0.8 (t = 0.2 m), there is no increase in the overall initial response, although it is possible to reach a load sharing on the pile equal to 28% to 45% of the total applied load and a 44% to 78% reduction in piled raft settlements compared to those of unpiled rafts.

The pile length has a greater influence on the initial stiffness of the piled raft than the raft thickness. Models with 0.10 m raft thickness positively modified the axial response of the pile, and from the thickness of 0.20m, the models uniformed their behaviors, meaning more distant from the "flexible" raft condition pointed out by Clancy and Randolph [12].

The results of the present study showed good agreement with key points emphasized by El-Mossallamy, Lutz and Duerrwang [30] regarding the confinement caused by raft-soil contact that increases the stress in the region near the top of the pile, and also on the effects of interaction between the elements, for example the load sharing, that has been shown to be dependent on the level of loading.

The results here reported are valid for application under conditions similar to those conducted by this research, and therefore, it cannot be considered a generalized approach.

ACKNOWLEDGEMENTS

The authors would like to thank the Federal University of Uberlândia for the acquisition of the software license used in the analyses of this work and Professor Michael Andrade Maedo for his technical contribution. This work was supported by a FAPEMIG grant funded by the State of Minas Gerais and Coordination for the Improvement of Higher Education Personnel (Coordenação de Aperfeiçoamento de Pessoal de Nível Superior - CAPES) financing code 001.

REFERENCES

[1] T. Whitaker, "Experiments with model piles in groups," *Geotechnique*, vol. 7, no. 4, pp. 147–167, Dec 1957, http://dx.doi.org/10.1680/geot.1957.7.4.147.

[2] H. G. Poulos and E. H. Davis, *Pile Foundation Analysis and Design.* Rainbom-Bridge Book Co., 1980.

[3] J. E. Bezerra, R. P. Da Cunha, and M. M. Sales, “Optimization concepts for the design of piled raft foundation systems Optimisation concepts pour le projet de fondation en Radier sur piex,” in *Proc. 16th Int. Conf. Soil Mech. and Geotech. Eng.*, 2005, pp. 1947–1950, http://dx.doi.org/10.3233/978-1-61499-656-9-1947.

[4] J. R. Garcia and P. J. R. de Albuquerque, "Analysis of the contribution of the block-soil contact in piled foundations," *Lat. Am. J. Solids Struct.*, vol. 16, no. 6, pp. 1–22, 2019, http://dx.doi.org/10.1590/1679-78255565.

[5] R. Butterfield and P. K. Banerjee, "The problem of pile group–pile cap interaction," *Geotechnique*, vol. 21, no. 2, pp. 135–142, Jun 1971, http://dx.doi.org/10.1680/geot.1971.21.2.135.

[6] M. Ottaviani, "Three-dimensional finite element analysis of vertically loaded pile groups," *Geotechnique*, vol. 25, no. 2, pp. 159–174, 1975, http://dx.doi.org/10.1680/geot.1975.25.2.159.

[7] P. T. Brown and T. J. Wiesner, "The behaviour of uniformly loaded piled strip footings," *Soil Found.*, vol. 15, no. 4, pp. 13–21, Dec 1975, http://dx.doi.org/10.3208/sandf1972.15.4_13.

[8] M. F. Randolph, “Design methods for pile groups and piled rafts,” in *Int. Conf. Soil Mech. and Found. Eng.*, 1994, pp. 61–82.

[9] J. R. Garcia, “Análise experimental e numérica de radiers estaqueados executados em solo da região de Campinas/SP,” Ph.D. dissertation, Univ. Estadual de Campinas, 2015.

[10] F. Kuwabara, "An elastic analysis for piled raft foundations in a homogeneous soil," *Soil Found.*, vol. 29, no. 1, pp. 82–92, Mar 1989, http://dx.doi.org/10.3208/sandf1972.29.82.

[11] A. Saeedi Azizkandi, H. Rasouli, and M. H. Baziar, "Load sharing and carrying mechanism of piles in non-connected pile rafts using a numerical approach," *Int. J. Civ. Eng.*, vol. 17, no. 6, pp. 793–808, 2019., http://dx.doi.org/10.1007/s40999-018-0356-2.

[12] P. Clancy and M. F. Randolph, "An approximate analysis procedure for piled raft foundations," *Int. J. Numer. Anal. Methods Geomech.*, vol. 17, no. 12, pp. 849–869, Dec 1993, http://dx.doi.org/10.1002/nag.1610171203.

[13] G. Russo and C. Viggiani, “Factors controlling soil structure interaction for piled rafts,” in *Int. Conf. Soil-Structure Interaction*, Darmstadt University of Technology, 1998, http://dx.doi.org/10.13140/2.1.4035.7125.

[14] R. Katzenbach and D. Choudhury, *Combined Pile-Raft Foundation Guideline*, Darmstadt: Institute and Laboratory of Geotechnics, 2013.

[15] H. Poulos, “Methods of analysis of piled raft foundations,” *Int. Soc. Soil Mech. Geotech. Eng.*, no. July, pp. 46, 2001.

[16] A. Mandolini, G. Russo, and C. Viggiani, “Pile Foundations : Experimental Investigations, Analysis and Design,” in *Proceedings of the 16th International Conference on Soil Mechanics and Geotechnical Engineering: Geotechnology in Harmony with the Global Environment*, Osaka, Japan, 2005, vol. 1, no. 2003, pp. 177–213.

[17] J. Lee, D. Park, D. Park, and K. Park, "Estimation of load-sharing ratios for piled rafts in sands that includes interaction effects," *Comput. Geotech.*, vol. 63, pp. 306–314, Jan 2015, http://dx.doi.org/10.1016/j.compgeo.2014.10.014.

[18] P. Clancy and M. F. Randolph, "Simple design tools for piled raft foundations," *Geotechnique*, vol. 46, no. 2, pp. 313–328, Jun 1996, http://dx.doi.org/10.1680/geot.1996.46.2.313.

[19] O. A. Abdel-Azim, K. Abdel-Rahman, and Y. M. El-Mossallamy, "Numerical investigation of optimized piled raft foundation for high-rise building in Germany," *Innov. Infrastruct. Solut.*, vol. 5, no. 1, pp. 11, Apr 2020., http://dx.doi.org/10.1007/s41062-019-0258-4.

[20] R. Katzenbach, U. Arslan, and C. Moormann, “13. Piled raft foundation projects in Germany,” in *Design applications of raft foundations*, Thomas Telford Publishing, 2000, pp. 323–391.

[21] V. Fioravante, D. Giretti, and M. B. Jamiolkowski, “Physical modelling of piled raft,” in *Deep Foundations on Bored and Auger Piles*, W. F. Van Impe and P. O. Van Impe, Eds. Routledge, 2009.

[22] F. A. De Cock, “Sense and sensitivity of pile load-deformation behaviour,” in *Deep Foundations on Bored and Auger Piles*, W. F. Van Impe and P. O. Van Impe, Eds. 2009.

[23] V. Caputo, “Experimental evidence for the validation of load-settlement predictions,” 2003.

[24] M. W. O’Neill and L. C. Reese, *Behavior of Axially Loaded Shafts in Beaumont Clay, Part Four Design Inferences and Conclusions*, Center for Highway Research, the University of Texas at Austin, 1970.

[25] A. S. Vesic, “*Design of pile fundations: National Cooperative Highway Research Program, Synthesis Highway Practice*,” Report No. 42, Transportation Research Board National Academy of Sciences, 1977.

[26] Q.-Q. Zhang, Z.-M. Zhang, and S.-C. Li, "Investigation into Skin friction of bored pile including influence of soil strength at pile base," *Mar. Georesour. Geotechnol.*, vol. 31, no. 1, pp. 1–16, Jan 2013., http://dx.doi.org/10.1080/1064119X.2011.626506.

[27] D. H. Ardiaca, “*Mohr-Coulomb parameters for modelling of concrete structures*,” *Plaxis Bull.*, pp. 12–15, 2009.

[28] British Standard. *Code of Practice for Foundations Foundations*, BS 8004:1986, 2004.

[29] L. De Sanctis, A. Mandolini, G. Russo, and C. Viggiani, "Some remarks on the optimum design of piled rafts," *Deep Foundations*., vol. 132, no. 12, pp. 405–425, Feb. 2002, http://dx.doi.org/10.1061/40601(256)30.

[30] Y. M. El-Mossallamy, B. Lutz, and R. Duerrwang, "Special aspects related to the behavior of piled raft foundation," *Proc. 17th Int. Conf. Soil Mech. Geotech. Eng. Acad. Pract. Geotech. Eng.*, vol. 2, pp. 1366–1369, 2009, http://dx.doi.org/10.3233/978-1-60750-031-5-1366.

Author contributions: EASO: conceptualization, formal analysis, methodology, writing, review; MOJ: formal analysis, methodology, writing; JRG: funding acquisition, supervision and review.

Editors: José Marcio Calixto, Guilherme Aris Parsekian.

IBRACON Structures and Materials Journal
Revista IBRACON de Estruturas e Materiais
ISSN 1983-4195 ismj.org

ORIGINAL ARTICLE

Evaluation of the reliability of optimized reinforced concrete beams

Avaliação da confiabilidade de vigas otimizadas de concreto armado

Rubens Silva Correia[a]
Giuliana Furtado Franca Bono[a]
Charlei Marcelo Paliga[b]

[a]Universidade Federal de Pernambuco – UFPE, Programa de Pós-Graduação em Engenharia Civil e Ambiental, Caruaru, PE, Brasil
[b]Universidade Federal de Pelotas – UFPel, Faculdade de Arquitetura e Urbanismo, Departamento de Tecnologia da Construção, Pelotas, RS, Brasil

Received 21 April 2021
Accepted 21 January 2022

Abstract: In the present research, the reliability of optimized reinforced concrete beams was evaluated in different design situations. Simply supported beams were optimized to find the dimensions and reinforcements of the cross-section that minimize costs, meeting the criteria of technical codes, through genetic algorithms. For each optimized beam, the reliability index was obtained in relation to the ultimate limit state of flexure with the iHLRF algorithm, considering the uncertainties of the resistance and load models, loads and resistances. It wa s verified that the reliability indexes, in general, were higher than the minimum value of 3.8, recommended by technical codes, in design situations with little live load. Through a parametric study, trends were identified for the reliability index according to the design parameters and characteristics of the beams.

Keywords: beams, reinforced concrete, structural optimization, structural reliability.

Resumo: Na presente pesquisa foi realizada a avaliação da confiabilidade de vigas otimizadas de concreto armado em diferentes situações de projeto. Vigas simplesmente apoiadas foram otimizadas para encontrar as dimensões e armaduras da seção transversal que minimizam os custos, atendendo aos critérios das normas técnicas, por meio dos Algoritmos Genéticos. Para cada viga otimizada, foi obtido o índice de confiabilidade em relação ao estado-limite último de flexão com o algoritmo iHLRF, considerando as incertezas dos modelos da resistência e da solicitação, das cargas e das resistências. Foi verificado que os índices de confiabilidade, de modo geral, foram maiores que o valor mínimo de 3,8, recomendado por códigos normativos, nas situações de projeto com pouca carga variável. Através de um estudo paramétrico, foram identificadas tendências para o índice de confiabilidade em função dos parâmetros de projeto e das características das vigas.

Palavras-chave: vigas, concreto armado, otimização estrutural, confiabilidade estrutural.

How to cite: R. S. Correia, G. F. F. Bono, and C. M. Paliga, "Evaluation of the reliability of optimized reinforced concrete beams," *Rev. IBRACON Estrut. Mater.*, vol. 15, no. 4, e15409, 2022, https://doi.org/10.1590/S1983-41952022000400009

INTRODUCTION

Nowadays several computational programs can be used to design structural projects, simulating structures with a high degree of complexity in a very realistic way, with integrated systems that cover all stages of the project [1]. Despite the various advances that already exist in structural engineering, the procedure for designing structures is still a process of trial and error. In the conventional procedure, the structure is pre-sized, where the dimensions of the structural elements are defined. Structural analysis and structure sizing are then performed. If the safety, construction and serviceability criteria are not met, a new pre-sizing is carried out and the criteria are rechecked. The procedure continues until a viable solution is found. The final solution adopted will not necessarily be the best solution, among all possible.

Corresponding author: Rubens Silva Correia. E-mail: rubens.correia@ufpe.br
Financial support: This research received the financial support of the Coordination for the Improvement of Higher Education Personnel (CAPES).
Conflict of interest: Nothing to declare.
Data Availability: The data that support the findings of this study are openly available in [UFPE Digital Repository] at [https://repositorio.ufpe.br/handle/123456789/39598].

This is an Open Access article distributed under the terms of the Creative Commons Attribution License, which permits unrestricted use, distribution, and reproduction in any medium, provided the original work is properly cited.

To determine the best solution, optimization techniques can be incorporated into the structural design. Mathematically, an optimization problem aims to find variables that minimize a function, meeting the constraints imposed by the problem. Optimization variables are called design variables (describe the system), and the function to be minimized as objective function [2]. In structural design, design variables can be the dimensions of structural elements, and the objective function can minimize the cost for example. Thus, by transforming conventional structural design into an optimization problem, it is possible to find the best possible solution (optimal solution) to minimize (or maximize) some specific objective.

The conventional procedure for designing structures, in addition to being a trial and error process, is also a deterministic procedure. However, the design of structures involves uncertainties associated with the calculation models, loads and materials properties [3]. To cover these uncertainties, a deterministic response of the structure is obtained using safety factors. Therefore, at the end of the project, it is likely that there is an over-designed or under-designed structure, in the face of uncertainties [4].

The ideal approach to dealing with engineering projects involving uncertainties is the stochastic approach. In this approach, the statistical characteristics of variables that have uncertainties are considered in the system analysis procedure. In this way, a system response is obtained through analysis with statistical properties. At the end of the design, there is a robust system, which is safe against uncertainties [4]. To assess the reliability of structures, a stochastic approach is used to "quantify" a safety measure. This measure is known as a reliability index and can be determined through numerical methods.

Several studies were carried out to optimize reinforced concrete beams [5]–[9], with different formulations and methods, but without evaluating reliability. In studies of structural reliability of reinforced concrete beams, the reliability index was evaluated in some design situations [10]–[12]. Other studies presented calibration procedures, based on reliability, of the partial safety factors of technical codes [13].

Therefore, the present work evaluated the structural reliability of reinforced concrete beam optimized in different design situations, through the reliability index.

FORMULATION OF THE OPTIMIZATION PROBLEM

The reinforced concrete beam evaluated, presented in Figure 1, is a simply supported beam subject to a uniformly distributed load formed by the dead load g and live load q, and with span L. The cross-section of the beam was rectangular of width b and height h, with n_t tension bars with diameter $\emptyset_t$ and n_c compressed bars with diameter $\emptyset_c$. The steel of the longitudinal reinforcements was CA-50 and the stirrups was CA-60; the level of the environmental aggressiveness (CAA) was equal to II, with a cover of 30 mm; and the diameters of the vibrator and the large aggregate were equal to 25 mm and 19 mm, respectively.

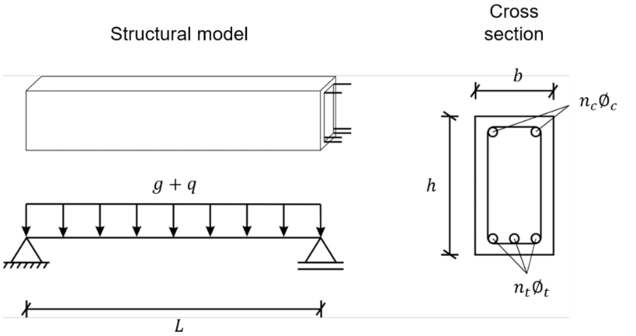

Figure 1. Reinforced concrete beam considered.

To obtain results in different design situations, the values of span (L), total loading ($g + q$), the relationship between live load and total load ($r = \frac{q}{g+q}$) and characteristic compressive strength of concrete (f_{ck}) were varied. The span varied from 3 to 7 m, in increments of 0.5 m. The total loading varied from 10 to 40 kN/m, in increments of 5 kN/m. This values of ($g + q$) do not include the self-weight of the beam. However, the self-weight was considered in the implementations. The r ratio was varied from 0.2 to 0.8, in increments of 0.2. The f_{ck} ranged from 25 to 35 MPa, in increments of 5 MPa. Thus, by combining the values of L, $(g+q)$, r, and f_{ck}, the reinforced concrete beam was optimized for 756 design situations. The following terminology will be used to identify the beams: (V - L - $(g+q)$ - r - f_{ck}).

In the optimization of the reinforced concrete beam in Figure 1, the width (b), the height (h), the number (n_t) and the diameter of the tension bars ($\emptyset_t$), and the number (n_c) and the diameter of the compressed bars ($\emptyset_c$) that compose the cross section were considered as design variables.

The objective function aims to minimize the beam costs (Equation 1), considering the costs of concrete (C_C), steel (C_A) and formwork (C_F):

$$C = C_C + C_A + C_F \tag{1}$$

In the cost of concrete (Equation 2), c_c is unit cost in R\$/m^3. In the cost of steel (Equation 3), the costs of the tension bars, compressed bars, stirrup and skin reinforcement were considered, where $c_{\emptyset_t}$, $c_{\emptyset_c}$, $c_{\emptyset_e}$ and $c_{\emptyset_p}$ are their unit costs, respectively, in R\$/kg. In Equation 3, ρ, c and n_e are the mass density of steel (7850 kg/m^3), the cover and the number of stirrups in the beam, respectively. In the cost of the formworks (Equation 4), c_f it is the unit cost in R\$/m^2.

$$C_C = bhLc_c \tag{2}$$

$$C_A = \left(\frac{\pi{\emptyset_t}^2}{4} L n_t \rho c_{\emptyset_t}\right) + \left(\frac{\pi{\emptyset_c}^2}{4} n_c L \rho c_{\emptyset_c}\right) + \left\{\frac{\pi{\emptyset_e}^2}{4}[2(h+b) - 8c] n_e \rho c_{\emptyset_e}\right\} + \left(\frac{\pi{\emptyset_p}^2}{4} L \rho c_{\emptyset_p}\right) \tag{3}$$

$$C_F = (b + 2h)Lc_f \tag{4}$$

The unit costs of concrete, steel and formwork were extracted from the Sistema Nacional de Pesquisa de Custos e Índices da Construção Civil (SINAPI) [14], from September of 2019 in the state of Pernambuco (Brazil). Table 1 lists the costs of concrete for types C25 to C35, the costs of steel bars for commercial diameters from 5 mm to 25 mm and the cost of the formwork. These unit costs consider, in addition to the material, costs associated with labor in its composition. In the unit cost of the formwork, it was also considered their reuse.

Table 1. Unit costs.

Concrete		
Source	Type	Cost (R$/m³)
94965 - SINAPI PE 09/2019	C25	327.94
94966 - SINAPI PE 09/2019	C30	336.69
(interpolation between C30 and C40)	C35	353.99
CA-50 steel		
Source	Diameter (mm)	Cost (R$/kg)
-	5	8.20
92760 - SINAPI PE 09/2019	6.3	8.20
92761 - SINAPI PE 09/2019	8	8.16
92762 - SINAPI PE 09/2019	10	6.67
92763 - SINAPI PE 09/2019	12.5	6.01
92764 - SINAPI PE 09/2019	16	5.68
92765 - SINAPI PE 09/2019	20	5.25
92766 - SINAPI PE 09/2019	25	5.82
Formwork		
Source		Cost (R$/m²)
92448 - SINAPI PE 09/2019		78.07

In the beam optimization problem (Equations 5 to 21), the constraints are criteria associated to the ultimate and serviceability limit states, details and limitations for the design variables, according to the specifications of NBR 6118 [15]. The variables b, h, n_t and n_c should be limited (Equations 6, 7, 8, 9, 10, 11 and 12). The bending moment (M_{sd}) should be less than or equal to the resistant moment (M_{Rd}) (Equation 13) to ensure safety to the ultimate limit state of flexure. The ratio of the neutral line position to effective depth (x/d) must comply with the limit of 0.45 to ensure good ductility conditions (Equation 14). The design value of the requesting shear force (V_{sd}) should be limited to resistant shear force (V_{Rd2}) to prevent the ruin of compressed concrete diagonals (Equation 15). The final displacement (a_t) and the characteristic crack opening (w) should be limited (Equations 16 and 17). The reinforcement areas (A_s e A'_s) must meet minimum and maximum values (Equations 18 and 19). In the detailing, the distance from the center of gravity of the bars to the center of the farthest bar (a) should be less than 10% of the height (Equation 20) and the spacing of the stirrups (s) must meet a minimum value (Equation 21).

Therefore, the optimization problem aims to find the values of b, h, n_t, $\emptyset_t$, n_c, and $\emptyset_c$ of the cross section (Figure 1) to minimize beam costs (Equation 5), meeting the imposed constraints (Equations 6 to 21). The optimization problem was written as:

Find the vector $\mathbf{x} = \{b, h, n_t, \emptyset_t, n_c, \emptyset_c\}^T$, to minimize the cost:

$$C(\mathbf{x}) = C_C + C_A + C_F \tag{5}$$

Subject to:

$$12 \text{ cm} \leq b \leq 25 \text{ cm} \tag{6}$$

$$25 \text{ cm} \leq h \leq 100 \text{ cm} \tag{7}$$

$$2 \leq n_t, n_c \leq 20 \tag{8}$$

$$\emptyset_t, \emptyset_c = \{5, 6.3, 8, 10, 12.5, 16, 20, 25\} \text{ mm} \tag{9}$$

$$3h \leq L \tag{10}$$

$$n_t \geq n_c \tag{11}$$

$$\emptyset_t \geq \emptyset_c \tag{12}$$

$$M_{sd} \leq M_{Rd} \tag{13}$$

$$\frac{x}{d} \leq 0.45 \tag{14}$$

$$V_{sd} \leq V_{Rd2} \tag{15}$$

$$a_t \leq a_{tlim} = \frac{L}{250} \tag{16}$$

$$w \leq w_{lim} = 0.3 \text{ mm} \tag{17}$$

$$A_s \geq A_{smin} \tag{18}$$

$$(A_s + A'_s) \leq 0.04bh \tag{19}$$

$$a \leq 0.1h \tag{20}$$

$$s \geq s_{min} \tag{21}$$

The optimization problem (Equations 5 to 21) was implemented in MATLAB (version R2016a). Thus, there was a constrained optimization problem that involves discrete variables and non-differentiable functions. In this case, the Genetic Algorithms (GA) of the MATLAB Global Optimization Toolbox [16] were used because it is an appropriate method for these situations [17]. The GA, in fact, are commonly used in the optimization of reinforced concrete beams, as verified in Govindaraj and Ramasamy [6], Alexandre [7], Oliveira [8] and Bezerra [9].

The performance of GA depends mainly on their parameters, such as population size and crossover and mutation rates [18]. Thus, after the implementation of the optimization problem in MATLAB, the parameters of the AG [16] "populationsize", "crossoverfraction" (fraction of individuals produced by the crossover operators) and "elitecount" (fraction of individuals that survive) were calibrated [19], resulting in 1000, 0.7 and 0.05, respectively. After calibration, the implementation of the optimization of reinforced concrete beams was validated through examples of Oliveira [8] and Bezerra [9].

FORMULATION OF THE RELIABILITY PROBLEM

In the evaluation of the reliability for the optimized reinforced concrete beams, the following random variables were considered (Equation 22):

$$X = \{\theta_R, \theta_S, g, q, f_c, f_y\}^T \tag{22}$$

where θ_R is the resistance model error; θ_S is the load model error; g is the dead load; q is the live load; f_c is the compressive strength of concrete and f_y is yield strength of the steel reinforcement. The statistical characteristics of the random variables (probability distribution, mean and standard deviation) are found in Table 2 and were extracted from Scherer et al. [12].

Table 2. Statistical characteristics of $\boldsymbol{X}$.

Variables	Distribuition	Mean (μ)	Standard deviation (σ)
θ_R	Lognormal	1	0.05
θ_S	Lognormal	1	0.05
g	Normal	$1.05g$	0.10μ
q	Gumbel	$\frac{q}{(1+0.35\times 0.25)}$	0.25μ
f_c	Normal	$\frac{f_{ck}}{(1-1.645\times 0.10)}$	0.10μ
f_y	Normal	$\frac{f_{yk}}{(1-1.645\times 0.05)}$	0.05μ

The ultimate limit state considered is related to flexion, being calculated according to Equation 23, by the difference between resistance and load effects. In the portion of the load effects, the bending moments are considered due to the total loading $(g+q)$ and the self-weight of the beam $(\rho_c bh)$, where ρ_c is the specific weight of the reinforced concrete equal to 25 kN/m³. In Equation 23, M is the resistant moment.

$$g(X) = \theta_R M - \theta_S \left[\frac{(g+q)L^2}{8} + \frac{(\rho_c bh)L^2}{8}\right] \tag{23}$$

The random variables θ_R, θ_S, g, q, f_c and f_y are parameters that have uncertainties and were considered in other reliability research of reinforced concrete beams [10]–[12]. The variability of θ_R is due to the approximations of the resistance calculation model, in this case being the model of NBR 6118 [15]. The variable θ_S is related to the inaccuracies of the action model. Loading g is an uncertain value and q varies in space and time. The variability of the strength of f_c concrete is due to the microstructural non-homogeneity of the material, formed by cement slurry and aggregate, and the non-homogeneity of the mixture. And the variability in the strength of f_y steel is a consequence of its production process and bars [20].

Thus, the reliability problem consists in finding the reliability index of the optimized beam, associated with the probability of failure when the resistance is less than the load effects ($g(X) < 0$) in the bending, in the face of the uncertainties of X.

In structural reliability, the probability of failure (Equation 24) is given as the integral of the joint density function of the random variables ($f_X(X)$) over the failure domain ($X|\ g(X) \leq 0$) [20]:

$$p_f = \int_{X|\ g(X)\leq 0} f_X(X)dX \tag{24}$$

Through transformation methods, the reliability index (β) can be associated with p_f by Equation 25 [20]:

$$p_f \cong \Phi(-\beta) \tag{25}$$

where $\Phi(.)$ is the standard normal cumulative distribution function.

To find the reliability index of the optimized beams, the improved algorithm of Hasofer, Lind, Rackwitz and Fiessler, the iHLRF [21], [22], which presents improvements over the original HLRF algorithm, was used. In iHLRF, the step size in the algorithm was adjusted to ensure convergence, presenting better performance than other algorithms [23]. As MATLAB does not have an iHLRF function for reliability analysis, iHLRF was implemented and validated through examples of Scherer et al. [12] and Nogueira and Pinto [11]. The implementation was carried out according to Beck's formulation [20], using the Armijo rule presented in Zhang and Der Kiureghian [21].

RELIABILITY INDEX OF OPTIMIZED BEAMS

After the optimization of reinforced concrete beams for the 756 design situations, varying the parameters L, $(g + q)$, r and f_{ck}, the reliability index β of each optimized beam was determined (V - L - $(g + q)$ - r - f_{ck}).

Figure 2 shows the main effects chart for the reliability index. In the graph, for each parameter L, $(g + q)$, r and f_{ck}, the averages of β are displayed in each parameter value. It was verified a change in β values as L was varied. Similarly, the values of β change with the variation of $(g + q)$. With the variation of the r ratio, a change is also observed in β. The r graph, when compared to the L and $(g + q)$ results, shows a large slope, which indicates a great effect of this parameter in β. On the other hand, the variations f_{ck} do not present significant changes in β, when compared to the changes due to the variations of the other parameters.

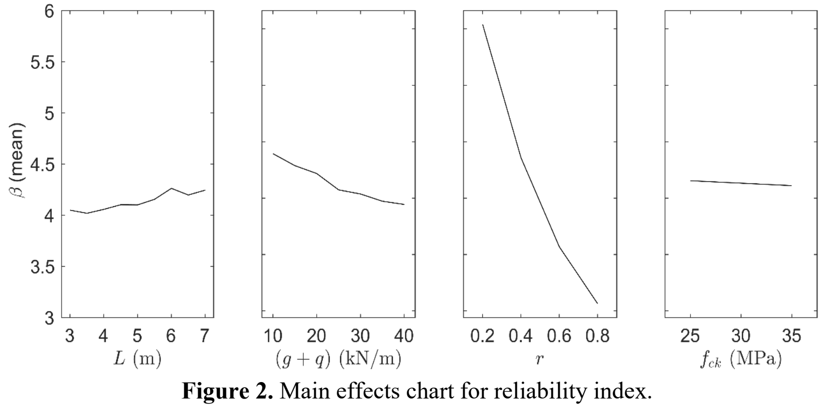

Figure 2. Main effects chart for reliability index.

Figure 3 shows the interaction graph for the reliability index. In the graph, one can observe that the interaction between the parameters L, $(g+q)$, r and f_{ck}, through the averages of the reliability index in each parameter value. It was verified an interaction between L - $(g+q)$, L - r and $(g+q)$ - r, since the lines of the graphs were not parallel. This interaction between the parameters affects the values of β, as observed in Figure 3. The interaction of f_{ck} with the other parameters was less expressive, once that the lines of the graphs were almost parallels.

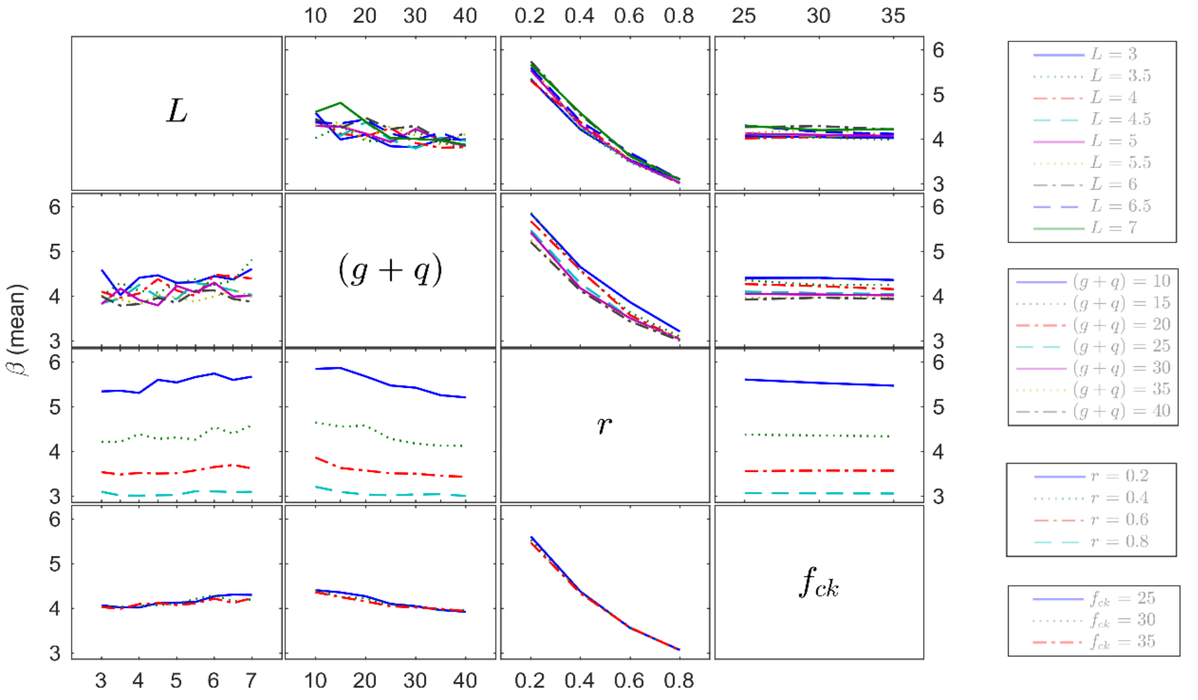

Figure 3. Interaction graph for reliability index.

The interaction and main effects graphs indicate that there was a main effect on the reliability index due to the variation of the L, $(g+q)$ and r parameters, where the most significant effect in β occurs due to variations of r, and that the interactions of f_{ck} with the other parameters has no significant influence on the values of β. The great influence of r on the reliability index of reinforced concrete beams was also observed by Santos et al. [10], Nogueira and Pinto [11] and Scherer et al. [12].

Moreover, to verify whether the previous observations are valid, an ANOVA analysis was performed for the reliability index. The ANOVA is a methodology that allows comparing the means of several groups and determining whether these means are different. This analysis can be done through an indicator called a p-value. A sufficiently small p-value indicates that at least one group mean was significantly different from the other means. It is common to consider the p-value small enough if it is less than 0.05 [24].

The results of ANOVA are presented in Table 3. Since the p-values of L, $(g+q)$ and r were less than 0.05, the mean β values are significantly different due to variation in these parameters. The p-value of f_{ck} was greater than 0.05, indicating that the mean values of β in the variations of f_{ck} were not significantly different. The p-values of the f_{ck} interactions with the other parameters were greater than 0.05, indicating that these interactions were not statistically significant in β. Furthermore, the interaction between L - r was not significant since it presented a p-value greater than 0.05. When analyzing Figure 3 again, it was verified that, in fact, the interaction between L - r was not significant, since the lines of the graph present a certain degree of parallelism.

Table 3. Analysis of Variance (ANOVA) for reliability index.

Parameter	*p*-value
L	0
$(g+q)$	0
r	0
f_{ck}	0.3390
L - $(g+q)$	0
L - r	0.1411
L -f_{ck}	0.9431
$(g+q)$ - r	0.0001
$(g+q)$ -f_{ck}	0.9837
r -f_{ck}	0.7228

Figure 4 shows the surface of β as a function of $(g+q)$ and r. In addition to the interaction $(g+q)$ - r, the interaction L - $(g+q)$ also resulted statistically significant according to the ANOVA. However, this interaction does not appear to result in a trend to β, as observed in Figure 3. In addition, the effect of this interaction was smaller when compared to $(g+q)$ - r. Moreover, there was a well-defined trend of increasing the reliability index as r and $(g+q)$ decrease. The influence of r on the increase β was more significant than the influence of $(g+q)$.

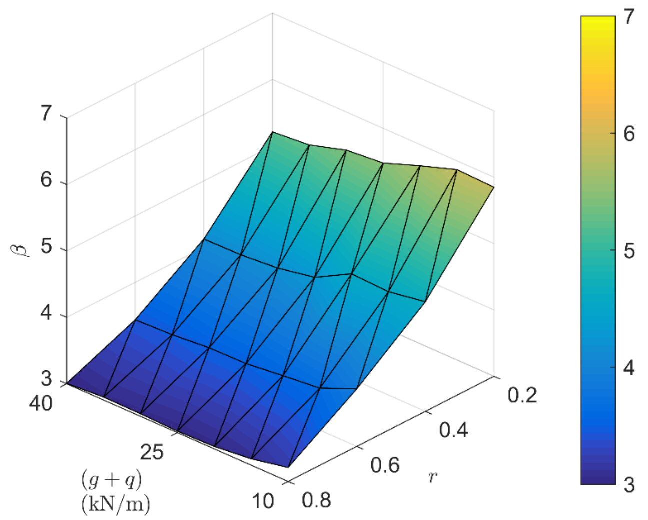

Figure 4. Relationship between reliability index and design parameters.

In addition to the trends for β as a function of the design parameters, the trends as a function of the characteristics of the optimized beams were also investigated. Figure 5 shows the β with the tension reinforcement ratio (ρ_{A_s}), concrete area (A_C), and with the relationships $\frac{h}{L}$ and $\frac{b}{h}$. The behavior is clearly defined by the r ratio, as observed in the previous results. It was not observed a trend of β as a function of ρ_{A_s}, A_C and $\frac{b}{h}$. For the $\frac{h}{L}$ ratio, however, there was a downward trend in the reliability index with the increase of $\frac{h}{L}$. This trend was more evident for low values of r.

In Figure 5, the reliability index equal to 3.8 represents a minimum reliability value suggested by the *fib* 2010 model code [25] for ultimate limit state, considering a representative period of 50 years and failures with average consequences. This target reliability index was also considered in the evaluations of Santos et al. [10], Nogueira and Pinto [11] and Scherer et al. [12]. It was observed that, in general, regardless of the characteristics of the optimized beams, the reliability index resulted less than 3.8 for higher values of r (0.6 and 0.8). Thus, in these situations, optimized beams do not have a minimum reliability index, following the criterion of code *fib* 2010 [25].

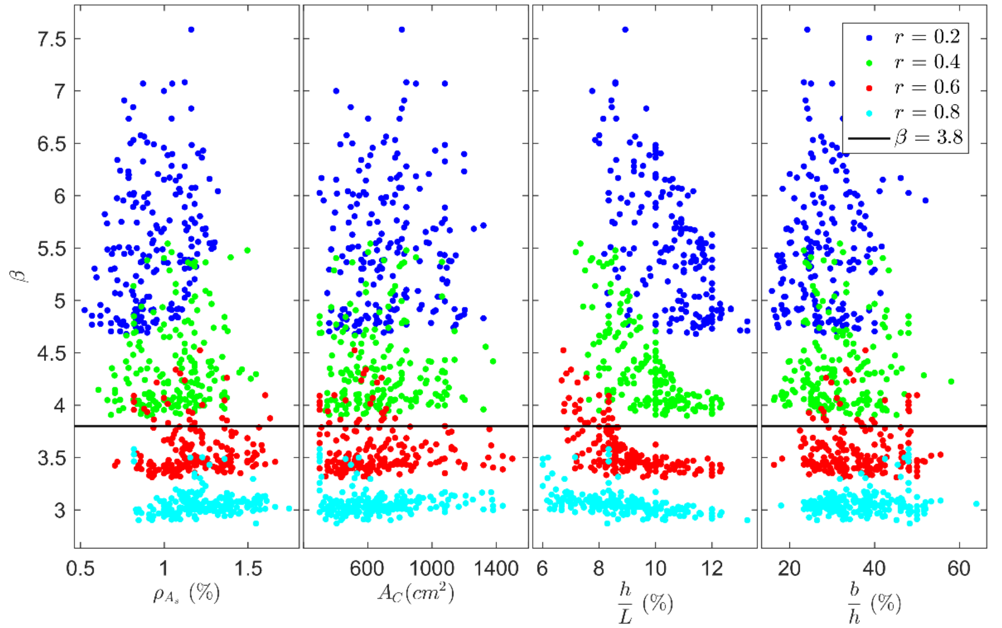

Figure 5. Relationship between reliability index and beam parameters.

Figure 6 shows the reliability indexes as a function of the $\frac{h}{L}$ ratio and the load $(g + q)$. The results in the figure indicate that a tendency of β to decrease with the increase of $\frac{h}{L}$, being it related to $(g + q)$. As the $\frac{h}{L}$ ratio becomes higher, along with $(g + q)$, the reliability index tends to decrease. Thus, optimized beams with high $\frac{h}{L}$ values and subject to a large load tend to have lower reliability indexes.

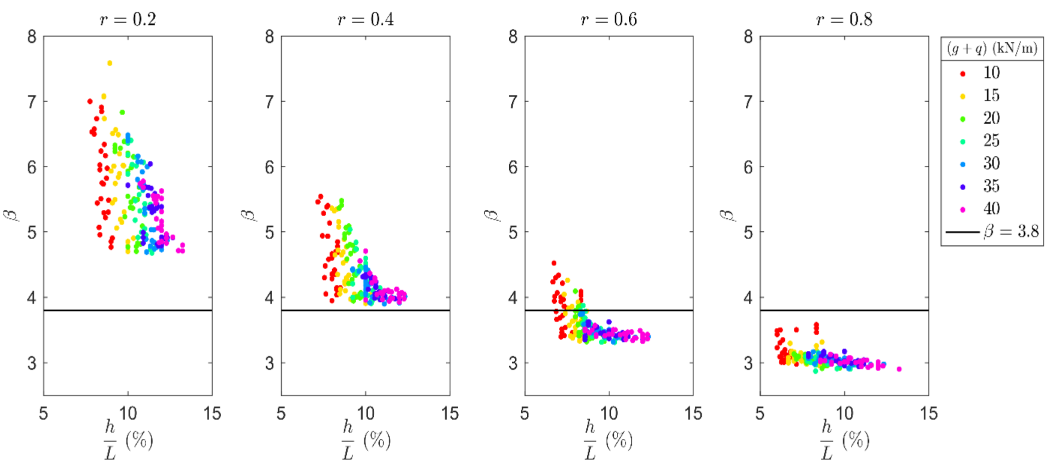

Figure 6. Relationship between the reliability index, $\frac{h}{L}$ and $(g + q)$.

To find a justification for the trend of decrease in the reliability index with the increase of $\frac{h}{L}$ and $(g + q)$, the resistant moment (M_R) and the bending moment (M_S) of the optimized beams were calculated, considering the mean values of the random variables X (Table 2). Through the relationship $\frac{M_R}{M_S}$, it was possible to infer about the resistance and load effects on the beam. Figure 7 shows the reliability indexes as a function of $\frac{h}{L}$ and $\frac{M_R}{M_S}$. A general trend of $\frac{M_R}{M_S}$ to decrease with the increase of $\frac{h}{L}$ was observed, indicating a greater load effect in the beams in these situations. Thus, optimized beams with high $\frac{h}{L}$ values and loading tend to present a higher load effect and, consequently, lower reliability indexes.

A statistical summary of the reliability index of optimized beams is shown in Figure 8. The mean reliability indexes were 4.13. Both the average and median were higher than the minimum index of 3.8. From the 756 indexes obtained, 404 were higher than 3.8, representing 53.44% of the cases.

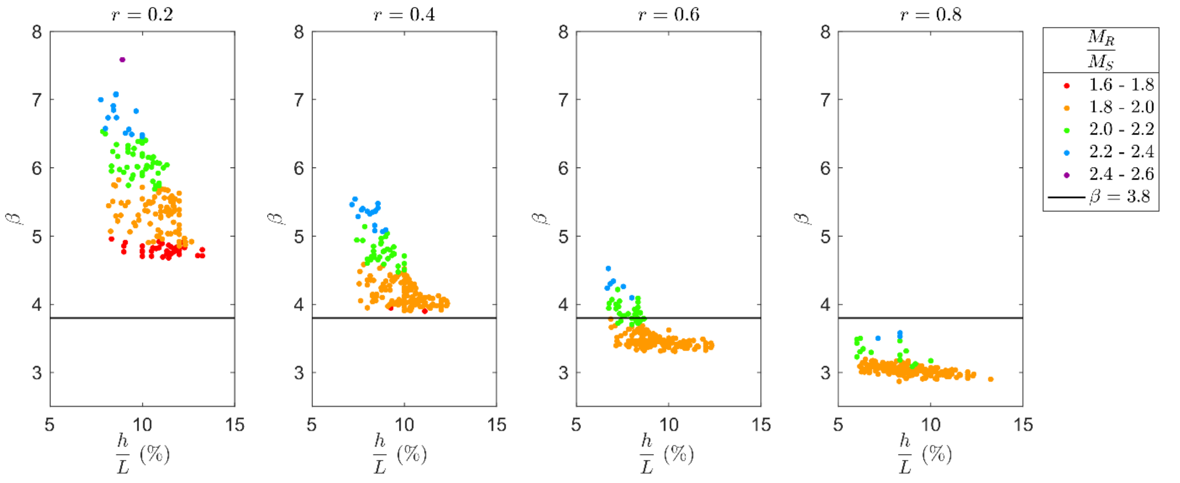

Figure 7. Relationship between reliability index, $\frac{h}{L}$ and $\frac{M_R}{M_S}$.

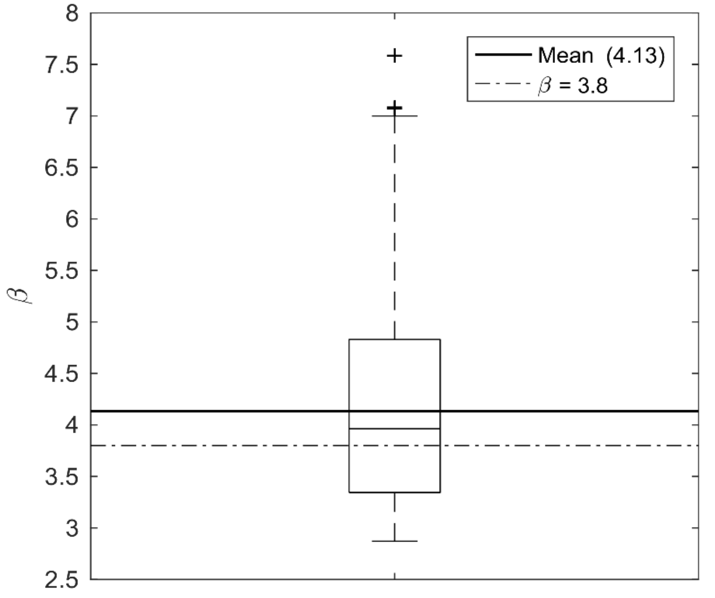

Figure 8. Reliability index variation.

CONCLUSION

Through the stochastic approach it was possible to determine the reliability index of optimized reinforced concrete beams. The reliability index is associated with the probability of failure of the beams in relation to the ultimate limit state of flexure, when uncertainties of the resistance and load models, loads and material strength were considered.

For the various design situations analyzed, it was observed a well-defined trend of the reliability index of optimized beams, as loading and the relationship between loads were changed. As r and $(g + q)$ decrease, the reliability index increases, and this increase is caused mostly by the r ratio. In the design of optimized beams, a small value of r $\left(r = \frac{q}{g+q}\right)$ represents a small portion of live load at total loading. Thus, the observed trend indicates that the reliability index of optimized beams was higher in design situations with small live load. This great influence of r on the reliability index is justified since, among the random variables considered, the live load was the one with the greatest variability in space and time.

While regarding the variation of the span in the design of the optimized beams, it was verified an effect on the reliability index of the beams due to this variation. However, there was no well-defined trend or interaction with the other design parameters. On the other hand, the variations of f_{ck} did not result in significant changes in the reliability index. The analysis of the main effects, interactions graphs and ANOVA indicated no influence of f_{ck}.

The results indicate that there was no trend to the reliability index due to the reinforcement ratio, concrete area and the width/height ratio of optimized beams. However, there was a tendency to decrease the reliability index with the increase in the height/span ratio, depending on the r ratio. This trend is also related to loading, once that the height/span ratios with higher values occur in high loading situations (Figure 6). This behavior was justified by the increased load effects on the beams in these high height/span and load situations (Figure 7). Then, it was possible to affirm that the beams optimized for high loads, and that they have a high height/span ratio, tend to have lower reliability indexes.

The average reliability indexes of the optimized beams was 4.13, being higher than the minimum value recommended by the model code *fib* 2010 [25] that is 3.8. Despite the variations in the reliability index between approximately 3 and 7 (Figure 8), more than half of the indexes obtained (53.44%) were greater than 3.8, indicating an acceptable reliability for the optimized beams in these cases. The beams that presented a reliability index lower than 3.8, in general, were those that were designed with high live load. In these cases, as observed in Figure 6, the beams had reliability indexes lower than acceptable, regardless of their characteristics (reinforcement ratio, concrete area, etc.).

ACKNOWLEDGEMENT

The authors acknowledge the CAPES for their financial support.

REFERENCES

[1] A. Kimura, *Informática Aplicada a Estruturas de Concreto Armado*, 2. ed. São Paulo: Oficina de Textos, 2018.

[2] J. S. Arora, *Introduction to Optimum Design*, 3rd ed. Amsterdam: Elsevier Academic Press, 2012.

[3] R. E. Melchers and A. Beck, *Structural Reliability Analysis and Prediction*, 3rd ed. Hoboken: Wiley, 2018.

[4] S. K. Choi, R. V. Grandhi, and R. A. Canfield, *Reliability-based Structural Design*. Berlin: Springer-Verlag, 2007.

[5] S. Kanagasundaram and B. L. Karihaloo, "Minimum-cost reinforced concrete beams and columns," *Comput. Struc.*, vol. 41, no. 3, pp. 509–518, 1991.

[6] V. Govindaraj and J. V. Ramasamy, "Detailed design of reinforced concrete continuous beams using genetic algorithms," *Comput. Struc.*, vol. 84, pp. 34–48, 2005.

[7] L. J. Alexandre, "Otimização do pré-projeto de vigas de concreto armado utilizando algoritmos genéticos," M.S. thesis, Univ. Fed. Rio de Janeiro, Rio de Janeiro, 2014.

[8] L. F. Oliveira, "Otimização multinivel de vigas de concreto armado via Algoritmos Genéticos," M.S. thesis, Univ. Fed. Ceará, Fortaleza, Brasil, 2014.

[9] L. A. Bezerra, "Emprego de algoritmos genéticos para otimização de vigas de concreto armado," M.S. thesis, Univ. Fed. Pernambuco, Caruaru, 2017.

[10] D. M. Santos, F. R. Stucchi, and A. T. Beck, "Confiabilidade de vigas projetadas de acordo com as normas brasileiras," *IBRACON Struct. Mater. J.*, vol. 7, no. 5, pp. 723–746, 2014.

[11] C. G. Nogueira and M. D. T. Pinto, "Avaliação da variabilidade da segurança de vigas em concreto armado submetidas ao momento fletor considerando os coeficientes parciais de segurança da NBR 6118:2014," *IBRACON Struct. Mater. J.*, vol. 9, no. 5, pp. 682–709, 2016.

[12] M. Scherer, I. B. Morsch, and M. V. Real, "Reliability of reinforced concrete beams designed in accordance with Brazilian code NBR-6118:2014," *IBRACON Struct. Mater. J.*, vol. 12, no. 5, pp. 1086–1125, 2019.

[13] W. C. Santiago, H. M. Kroetz, and A. T. Beck, "Reliability-based calibration of Brazilian structural design codes used in the design of concrete structures," *IBRACON Struct. Mater. J.*, vol. 12, no. 6, pp. 1288–1304, 2019.

[14] Sistema Nacional de Pesquisa de Custos e Índices da Construção Civil – SINAPI. https://www.caixa.gov.br/poder-publico/modernizacao-gestao/sinapi/Paginas/default.aspx (accesed Oct. 14, 2019).

[15] Associação Brasileira de Normas Técnicas, *Projeto de Estruturas de Concreto – Procedimento,* ABNT NBR 6118:2014, 2014.

[16] MathWorks Inc, *Global Optimization Toolbox User's Guide*, 2020.

[17] S. N. Sivanandam and S. N. Deepa, *Introduction to Genetic Algorithms.* Springer-Velag, 2008.

[18] M. Mitchell, *An Introduction to Genetic Algorithms.* Cambridge: MTI Press, 1996.

[19] M. E. V. Matamoros and M. Kumral, "Calibration of genetic algorithm parameters for mining-related optimization problems," *Nat. Resour. Res.*, vol. 28, pp. 443–456, 2019.

[20] A. T. Beck, *Confiabilidade e Segurança das Estruturas.* 1. ed, Rio de Janeiro: Elsevier, 2019.

[21] Y. Zhang and A. Der Kiureghian, "Two improved algorithms for reliability analysis," in *Proc. 6th IFIP WG7.5 Conf. Reliability and Optimization Structural Systems*, R. Rackwitz, G. Augusti, and A. Borri, Eds. Boston: Springer, 1995, pp. 297-304.

[22] B. Sudret and A. Der Kiureghian, *Stochastic Finite Element Methods and Reliability: a State-of-the-art Report*". Berkeley: University of California, 2000.

[23] A. T. Beck, "Computational issues in FORM with uniform random variables," in *10th World Congr. Computational Mechanics*, São Paulo, Brazil, 2012, pp. 1228-1244.

[24] W. L. Martinez and M. Cho, *Statistics in MATLAB®: a primer*. Boca Raton: CRC Press, 2014.

[25] Fédération Internationale Du Béton. *Fib Model Code for Concrete Structures 2010*. Lausanne, Switzerland: Ernst & Son, 2013.

Author contributions: RSC: conceptualization, literature review, methodology, computational implementation, validation, analysis, written, illustration and editing; GFFB: conceptualization, methodology, analysis and review; CMP: conceptualization, methodology, analysis and review.

Editors: Edgar Bacarji, Guilherme Aris Parsekian.

IBRACON Structures and Materials Journal
Revista IBRACON de Estruturas e Materiais
ISSN 1983-4195 ismj.org

ORIGINAL ARTICLE

A method for considering the influence of distinct casting stages in the flexural design of prestressed concrete cross sections

Um método para consideração da influência de moldagens distintas no dimensionamento à flexão de seções transversais de concreto protendido

Eduardo Vicente Wolf Trentini[a]
Guilherme Aris Parsekian[a]
Túlio Nogueira Bittencourt[b]

[a]Universidade Federal de São Carlos – UFSCar, Programa de Pós-graduação em Engenharia Civil, São Carlos, SP, Brasil
[b]Universidade de São Paulo – USP, Escola Politécnica, São Paulo, SP, Brasil

Received 09 September 2021
Accepted 24 January 2022

Abstract: Composite elements are structures of concrete, or other materials, constructed in different casting stages that act jointly under external loads. These elements are used when it is intended to combine the constructive advantages of precast structures with the monolithic behavior of cast-in-place structures. In regular civil engineering applications, such as the construction of a bridge or viaduct, the precast section is used as shoring before casting the slab in place. This process leads to imposed deformations prior to the ultimate limit state and a discontinuity in the specific strain of the composite cross section. This work proposes a methodology to design composite cross sections, built in two casting stages, evaluating the specific strain provided the construction process that can be easily implemented in precise computational routines. From applying the methodology on study-case numerical example, it is observed that the beam casted in two stages presents a factored moment resistance smaller than an identical beam casted in a single stage. However, further investigations should be conducted to assess the extent of this difference.

Keywords: composite sections, construction process, precast, bending, structural design.

Resumo: Elementos compostos são estruturas de concreto, ou outros materiais, executados em moldagens distintas que atuam de maneira conjunta sob ações externas. Esses elementos são utilizados quando se pretende aliar as vantagens construtivas de estruturas pré-moldadas ao comportamento monolítico de estruturas moldadas no local. Em situações comuns na engenharia civil, como a construção de uma ponte ou viaduto, a seção pré-moldada é utilizada como cimbramento para a moldagem no local da laje. Esse processo proporciona deformações prévias ao estado-limite último e descontínuas na seção transversal composta. Este trabalho propõem uma metodologia para dimensionamento de seções compostas, em duas etapas de concretagem, avaliando as deformações proporcionadas pelo processo construtivo que pode ser facilmente implementada em rotinas computacionais precisas. Aplicando a metodologia em um exemplo numérico, é observado que a seção concretada em duas etapas apresenta um momento resistente menor que uma seção idêntica concretada em etapa única. Porém são necessárias mais investigações para avaliar a amplitude desta divergência em outros elementos.

Palavras-chave: seções compostas, processo construtivo, pré-moldado, flexão, dimensionamento.

How to cite: E. V. W. Trentini, G. A. Parsekian, and T. N. Bittencourt, "A method for considering the influence of distinct casting stages in the flexural design of prestressed concrete cross sections," *Rev. IBRACON Estrut. Mater.*, vol. 15, no. 4, e15410, 2022, https://doi.org/10.1590/S1983-41952022000400010

Corresponding author: Eduardo Vicente Wolf Trentini. E-mail: eduardowtrentini@gmail.com
Financial support: None.
Conflict of interest: Nothing to declare.
Data Availability: The data that support the findings of this study are available from the corresponding author, EVWT, upon reasonable request.

This is an Open Access article distributed under the terms of the Creative Commons Attribution License, which permits unrestricted use, distribution, and reproduction in any medium, provided the original work is properly cited.

1 INTRODUCTION

The demand for quality, speed of execution and rationalization of building materials has increased the choice for precast concrete structures. The use of precast elements introduces a repetitive character into the construction process reducing waste and directly reflecting a better productivity of the workforce [1].

To connect the precast elements to the rest of the structure, it is common to cast in place part of the element, creating a monolithic connection. In civil construction these elements are known as pre-beams and pre-slabs and NBR 9062 [2] defines them as composite elements, being: "structures of concrete, or other materials, constructed in different casting stages that act jointly under external loads".

The use of concrete composite elements combines the advantages of precast concrete structures, such as the use of more complex cross sections, reuse of formwork, possible prestress on plant, excellent quality control, reduction of shoring, the monolithic behavior induced by cast in place concrete [3], [4].

The use of composite sections in concrete introduces peculiar situations the structural analysis process. Each influence of the factors below must be checked:

deformations in the precast concrete section prior to the curing of the second stage cast;

different strain resulting from concrete shrinkage and creep, on each stage, due to the difference between materials and casting age, and;

the existence of slip between the interface of the two concrete casts [2].

Regarding occurrence of slip verification between the contact surfaces, many experimental studies were carried out and proposed equations to evaluate the load capacity of the interface to the horizontal shear are available in [5]–[12]. Design codes, such as ACI [13], AASHTO [14] and NBR 9062 [2], include equations to evaluate this capacity. The NBR 9062 [2] prescribes that if the horizontal shear strength is greater than the shear stress load, it can be considered that the composite element presents monolithic behavior, as also observed by [15]–[17].

Different age, rheology, and stress level in each casting stage, causes different volume changes due to shrinkage and creep of the concrete. Since there is a relative strain restriction between the two casting stages, the differential volume variation results in the development of stresses in the section [18]. Models for evaluating the resulting stresses due to differential volume variation are extensively addressed in the literature [19]–[24]. As shown by [25], the creep effect ends up decreasing the tension difference between the precast section and the cast in place section, thus making the stress distribution in the composite cross section more similar to that developed in a single-step casted section. The shrinkage effect is more intense in the first days. Therefore, after the in place casting, the concrete of the second cast shrinks more than the first cast, developing tensile stresses and even cracks that may reduce durability [26]. In bridge construction, the girders usually are joined to the slab in a later cast in place step. This connection occurs in the upper region of the cross section subject to compression in the case of beams demanded by positive bending moment. In this case, the tensile stress mentioned above is beneficial for the analysis of the section in Ultimate Limit State (ULS), therefore, the evaluation of these both effects are not included in the scope of this article assuming that the ULS occurs when the effects of shrinkage and creep have not yet fully developed.

During the construction process, the precast girder is lifted and placed on the supports, and then used as shoring for the cast in place slab. The self-weight load deforms only the girders, once only after the curing of the second casting stage can the additional loads be considered acting on the monolithic composite section. This constructive process results in a cross section that presents a strain, ε, discontinuity along of its z-height due to previous strain imposed to the precast member prior to the slab curing. Figure 1 illustrates the strain and normal stresses of part of a beam, resulting from this construction process. To show the contrast between the developed stresses and strains, in Figure 1 the behavior of beam built within this construction process is compared to that of a beam built in a single casting.

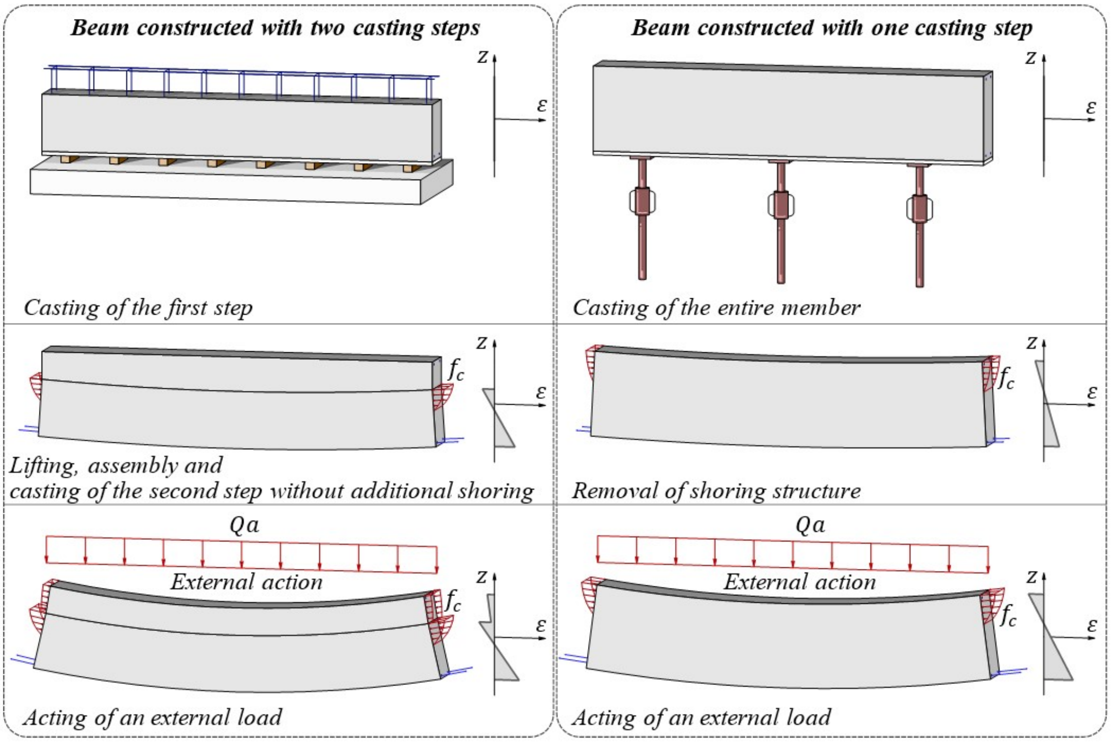

Figure 1. Comparison between construction processes.

The strain discontinuity along the cross section makes the use of conventional design methods unfeasible, since usually continuous strain distribution along the height is assumed. Few works have been developed considering the influence of strain in the precast section when used as shoring for the second casting stage.

In 1955 [27], experimental studies were carried out in which previous prestressing and self-weight strain in the precast section are considered to estimate the stresses, in elastic regime, of composite cast-in-place slab and precast concrete beams, built in two steps. Authors conclude that if the rough interface provides enough friction, the composite cross section can be monolithic considered.

Taha, in 1978 [28], developed a software for the design of composite sections of steel beams and concrete slabs. The permanent strain in the steel section due to the slab casting load were considered, but still in an elastic regime. The design was carried out using the allowable stress method. Dritsos et al. in 1995 [29] reports the efficiency of reinforcing concrete structures by adding a new casting step. The authors considered the slip at the interface between the two casting steps which, in turn, promotes a similar strain discontinuity situation as the construction of non-shored composite cross sections. The equilibrium was evaluated with non-linear constitutive laws for steel and concrete.

Hwang *et al.* in 2015 [30] proposed a method to evaluate the factored moment resistance and the deformation of precast post-tensioned beams, composed with cast-in-place slab and shored. The authors proposed a complex analysis where, in addition to the non-linear behavior of the materials, the existence of slippage at the interface is also considered with a non-linear response. As this method is intended for shored while casting structures, the analysis developed only evaluates the strain discontinuity due to the prestressing of the precast beam before the slab curing, and due to the interface slippage of the two concretes.

This work proposes a method for flexural design, of precast post-tensioned composite concrete sections with cast-in-place slab without additional shoring. This method evaluates the strains in the precast beam, which precede the curing of the concrete of the second casting stage due to prestressing and self-weight, considering the monolithic behavior after curing, neglecting the effects of the differential volume variation between the concrete of the two casting stages.

2 HYPOTHESES OF THE MODEL

To simplify and limit the problem, the following hypotheses are adopted:

1. The beams are long one-dimensional structural elements; thus, the cross sections remain plane after deformation – Bernoulli's theorem.
2. The connection between passive and prestressing reinforcement with concrete is assumed to be perfect. There is no slippage between the elements and the strain of the reinforcement is the same as the concrete in its vicinity.
3. The interaction between the precast beam and the cast-in-place slab is full, that is, there is no slippage at the interface, thus assuming a monolithic behavior. Any variation in curvature or axial deformation that occurs after cure of the second step is the same for the entire cross section. This hypothesis is valid, according to NBR 9062 [2], if the horizontal shear load is less than the interface strength.
4. Prestressing is applied before the cast of the second step.
5. The cast of the second step is carried out without additional shoring, that is, all self-weight including the self-weight of the slab deforms only the precast section.
6. Between the concrete of the two castings, the differential effects of temperature, shrinkage and creep are neglected.

The constitutive law of the materials involved in this analysis are described in NBR 6118:2014 [31] and presented in Figure 2. The constitutive law for compressed concrete has two parts, the first a polynomial curve and the second linear. The stress of the tensioned concrete is neglected. The steel used for passive reinforcement is CA-50 which has an elastic modulus E_s and a factored yield stress f_{yd} defined in [31]. The steel of the prestressing reinforcement is CP-190 RB with modulus of elasticity E_p, factored conventional yield strength f_{pyd} and factored tensile strength f_{ptd} defined in [32]. Both steels have symmetrical behavior

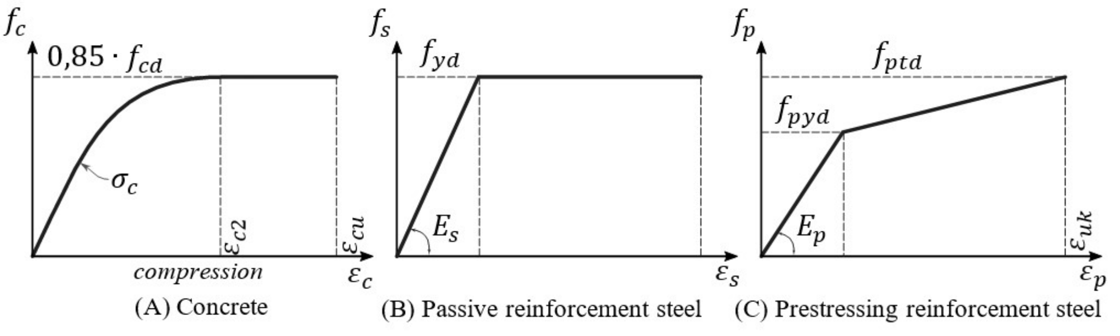

Figure 2. Stress-strain relationship of the materials.

Where σ_c is

$$\sigma_c = 0{,}85 \cdot f_{cd}\left[1 - \left(1 - \frac{\varepsilon_c}{\varepsilon_{c2}}\right)^n\right] \tag{1}$$

where f_{cd}, ε_{c2}, ε_{cu} and n are defined in [31] as a function of the characteristic strength of concrete f_{ck}.

3 EQUILIBRIUM AND COMPATIBILITY EQUATIONS

The internal forces must be in equilibrium with the external forces. In the case of the current structure, the equilibrium must be verified in two situations. The first verification is performed during the casting of the addition on site, which here is called the initial step. Figure 3 illustrates the internal forces and strains of the cross section, when it is submitted to the initial step. This figure also highlights the position of layers A, B, C, and S, which are respectively: surface level between the two castings, finished level of the cast in place addition, level of the beam base and level of the passive reinforcement outermost to the beam.

Checking the equilibrium in the initial step is necessary to evaluate the permanent deformation prior to the slab casting. The strain at layer A, $\varepsilon_{A,i}$, and the strain in the layer S, $\varepsilon_{S,i}$, are the variables chosen to define the curvature and the axial deformation of the beam during the initial step. The strain between the layers A and B are null.

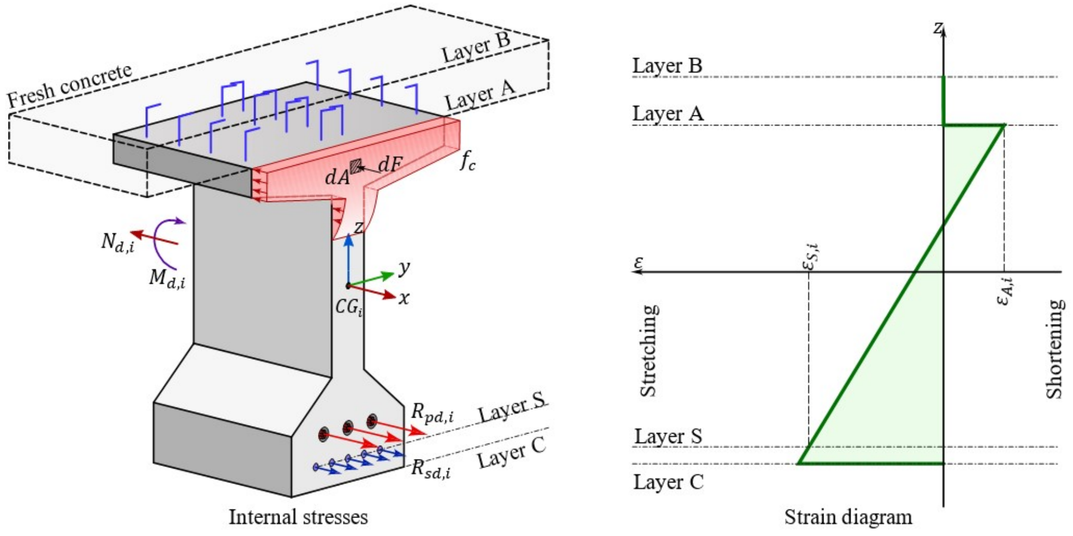

Figure 3. Internal stresses and strain diagram in initial step.

The second equilibrium is developed with the composite section in ULS. This includes the strains on the initial step plus then addition of curvature and axial deformation after the slab casting. This phase is called total step. Figure 4 illustrates internal forces and the strains on the composed cross section, in the total step.

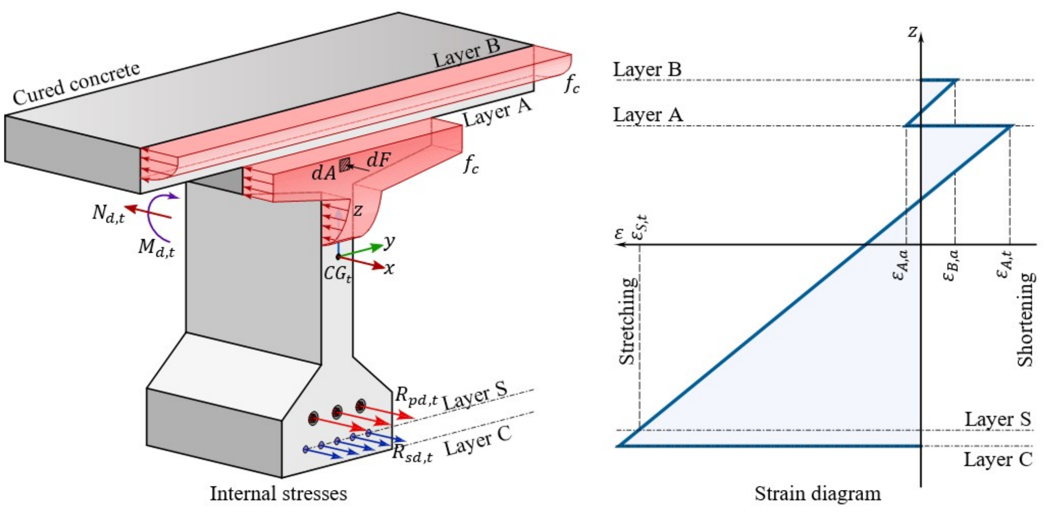

Figure 4. Internal stresses and strain diagram in total step.

The equilibrium equations that apply to the case of symmetrical bending are: (2) Sum of forcer in the x direction, SN; (3) Sum of moments in the y direction, SM. These equations are defined at the point CG, which represents the centroid of the cross section.

$$\sum F_x = 0 \;\therefore\; R_{sd} + R_{pd} + R_{cd} - N_d = 0 \;\rightarrow\; SN = 0 \qquad (2)$$

$$\sum M_y = 0 \therefore M_{sd} + M_{pd} + M_{cd} + M_d = 0 \rightarrow SM = 0 \tag{3}$$

Where: R_{sd} normal reaction of the passive reinforcement, R_{pd} normal reaction of the prestressing reinforcement, R_{cd} normal reaction of the concrete, N_d factored normal force of the member, M_{sd} moment of the reaction of the passive reinforcement, M_{pd} moment of the reaction of the active reinforcement, M_{cd} moment of the reaction of the concrete, M_d factored bending moment of the member. All these moments are defined around the y-axis.

The reactions and moments of the reinforcement are obtained by assuming the constitutive law shown in Figure 2. Assuming perfect bond, the strain of the passive reinforcement is equal to that of the concrete in its vicinity. The strain of the prestressing reinforcement is the sum of the pre-strain of the steel, ε_{pre}, with the strain of the adjacent concrete.

The contribution of concrete in the internal equilibrium is analyzed by highlighting the infinitesimal element of area dA, considering that an infinitesimal force dF is exerted on it. Since dF is function of the concrete stress f_c, where $dF = f_c \cdot dA$, the R_{cd} and M_{cd} are then written as:

$$R_{cd} = \int_A \mathrm{d}F \therefore R_{cd} = \int_A f_c \cdot \mathrm{d}A, \tag{4}$$

$$M_{cd} = \int_A z \cdot \mathrm{d}F \therefore M_{cd} = \int_A z \cdot f_c \cdot \mathrm{d}A. \tag{5}$$

The integrals of the Equations 4 and 5 can be solved by one of two processes: analytical integration or numerical integration by discretizing the area into small elements.

Numerical integration is versatile in terms of allowing to consider different constitutive laws. On the other hand, the quality of the response is related to the number of elements used, and this alternative has a higher computational cost. The computational cost is an inconvenience that can make the use of this alternative unfeasible when incorporated in iterative processes.

Analytical integration presents a negligible computational cost when compared to numerical integration, and its answer is precise within the approximations of the mathematical model. Thus, the integrals of Equations 4 and 5 are here analytically evaluated.

3.1 Analytical integral of concrete stresses

The methodology for evaluating the axial reaction R_{cd} and the moment M_{cd} by analytical integration, used here, was developed by Silva and Carvalho in 2019 [33], for the NBR 6118:2014 constitutive law of the concrete.

The method is applied to cross sections described in polygonal form, which have nodes at the vertices and at transition points of the constitutive relation. The transition points of the constitutive relation occur where the section deformation is null, or equal to ε_{c2} or equal to ε_{cu}.

With the polygonal defined, the cross section is subdivided into trapezoids, A_l, contained between the z-axis and the lines that define the perimeter of the cross section. Figure 5 illustrates one of these trapezoids contained between the line l and the z-axis.

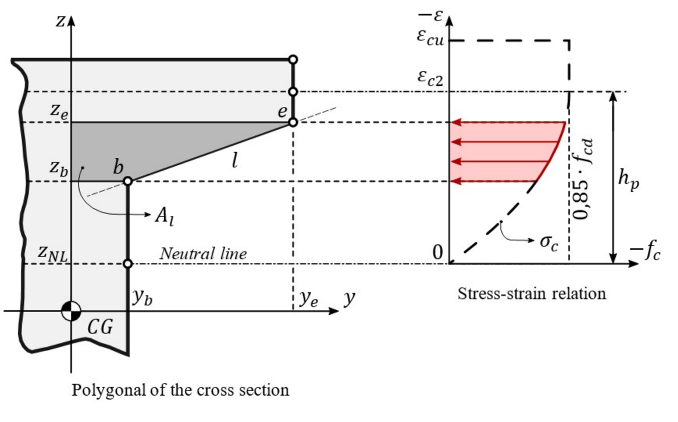

Figure 5. Subdivision of the cross section into trapezoids.

The contribution of concrete in the equilibrium is evaluated with the Equations 6, 7, 13 and 14 as shown in [33].

For the polynomial part of the constitutive relation, σ_c of Equation 1, that is, strains smaller than zero and larger than ε_{c2}.

$$R_{cd} = \sum_{Pol}\left(-0{,}85 \cdot f_{cd} \cdot \left(-\frac{h_p \cdot \left(\frac{z_{NL}+h_p-z}{h_p}\right)^{n_1} \cdot \left(c_1 \cdot n_2 + c_2 \cdot \left(h_p + z_{NL} + n \cdot z + z\right)\right)}{n_1 \cdot n_2} - c_1 \cdot z - \frac{c_2 \cdot z^2}{2}\right)\right)\Bigg|_b^e \quad (6)$$

and

$$M_{cd} = \sum_{Pol}\left(\frac{0{,}85 \cdot f_{cd}}{6 \cdot n_1 \cdot n_2 \cdot n_3} \cdot \left(3 \cdot c_1 \cdot \left(n_1 \cdot n_2 \cdot n_3 \cdot z^2 + 2 \cdot h_p \cdot \left(\frac{z_{NL}+h_p-z}{h_p}\right)^{n_1} \cdot \left(\left(h_p + z_{NL}\right) \cdot n_3 + n_1 \cdot n_3 \cdot z\right)\right) + 2 \cdot c_2 \cdot \left(n_1 \cdot n_2 \cdot n_3 \cdot z^3 + 3 \cdot h_p \cdot \left(\frac{z_{NL}+h_p-z}{h_p}\right)^{n_1} \cdot \left(2 \cdot {z_{NL}}^2 + 2 \cdot {h_p}^2 + 2 \cdot h_p \cdot n_1 \cdot z + n_1 \cdot n_2 \cdot z^2 + 2 \cdot z_{NL} \cdot \left(2 \cdot h_p + n_1 \cdot z\right)\right)\right)\right)\right)\Bigg|_b^e \quad (7)$$

where z is the coordinate of the polygonal node, sometimes of node b, sometimes of node e; z_{LN} the coordinate of the neutral line; h_p the height of the polynomial part of the constitutive relationship, highlighted in Figure 5; c_1 and c_2 are the constants of the equation of the line l of y as a function of z; and n_1, n_2 e n_3 are terms depending on the degree of the polynomial of the constitutive relation. The constants of line l and the terms as a function of the exponent of the constitutive relationship are determined with

$$c_1 = \frac{z_b \cdot y_e - z_e \cdot y_b}{z_b - z_e} \text{ and } c_2 = \frac{y_b - y_e}{z_b - z_e} \quad (8) \text{ and } (9)$$

$$n_1 = n + 1, n_2 = n + 2 \text{ and } n_3 = n + 3 \quad (10), (11) \text{ and } (12)$$

where n is defined in [31] as function of f_{ck}.

For the part of the constitutive relation where the stress is constant, that is, specific strains smaller than ε_{c2} and larger than ε_{cu}.

$$R_{cd} = \sum_{Polygonal}\left(0{,}85 \cdot f_{cd} \cdot \left(c_1 \cdot z + \frac{c_2 \cdot z^2}{2}\right)\right)\Bigg|_b^e \quad (13)$$

and

$$M_{cd} = \sum_{Polygonal}\left(0{,}85 \cdot f_{cd} \cdot \left(\frac{c_1 \cdot z^2}{2} + \frac{c_2 \cdot z^3}{3}\right)\right)\Bigg|_b^e \quad (14)$$

In the analyses, the reinforcement area is not subtracted from the concrete cross section area.

3.2 Strain in the cross section during the construction steps and in ULS

The equilibrium equations are a function of the cross-sectional strains. As the member is in equilibrium, these equations can be used to determine the deformations in the cross section.

Assuming that the cross sections remain flat after the loading action, the deformations then vary linearly in relation to height. Thus, in a conventional cross section (consisting of a single casting step), the cross-sectional strains are completely determined by knowing the strain of a pair of points with known height. In the case of a cross section of the type analyzed in this work, the deformation of the initial step is defined by the deformations in the following regions:

- $\varepsilon_{A,i}$ – strain at the layer A, in initial step;
- $\varepsilon_{S,i}$ – strain at the layer S, in initial step;
- with the strains between layers A and B being null.

The strains in the total step are defined by the strain in the following regions:

- $\varepsilon_{A,t}$ – strain at the layer A, in total step;
- $\varepsilon_{S,t}$ – strain at the layer S, in total step;
- $\varepsilon_{B,a}$ – strain at the layer B in additional and total step;
- $\varepsilon_{A,a}$ – strain at the layer A in additional and total step.

These strains are illustrated in Figures 3 and 4.

The evolution of strains in the cross section throughout the steps of the construction process is shown in Figure 6. With the composed section, admitting full interaction, the section behaves in a monolithic manner and the strain present in the total step are equal to the strain of the initial step plus strain developed in the additional step.

The additional step is a *virtual* step that represents the addition of curvature and axial deformation, which occurs in the composed beam, between the initial step and the total step. For the newly formed composite beam, Bernoulli's hypothesis is also true, thus the addition of strain, as a function of height, is linear, and is valid for the entire cross section. Adding the strain of the additional step to the already developed strain in the initial step, the strain of the total step of the cross section is obtained.

The strains in the additional step are defined by the strain in the following regions:

- $\varepsilon_{B,a}$ – strain at the layer B, in additional step;
- $\varepsilon_{S,a}$ – strain at the layer S, in additional step;

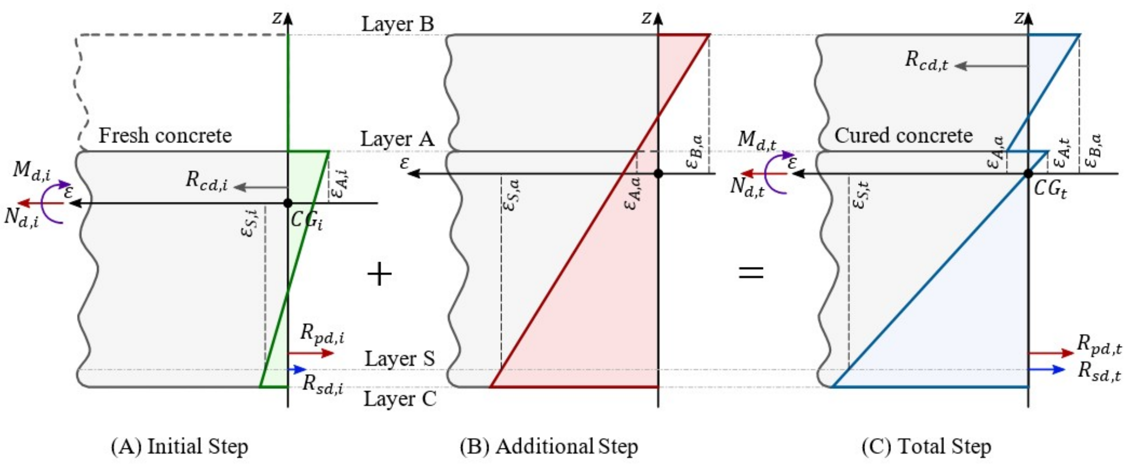

Figure 6. Evolution of strain in defined steps.

Having defined the three steps, the following relations between the strains are now written:

$$\varepsilon_{A,t} = \varepsilon_{A,i} + \varepsilon_{A,a} \tag{15}$$

$$\varepsilon_{S,t} = \varepsilon_{S,i} + \varepsilon_{S,a} \tag{16}$$

where $\varepsilon_{A,a}$ is the strain at the layer A in additional step given by:

$$\varepsilon_{A,a} = \varepsilon_{B,a} + \kappa_a \cdot (z_B - z_A), \tag{17}$$

where κ_a is the curvature of the additional step calculated by the equation:

$$\kappa_a = \frac{\varepsilon_{S,a} - \varepsilon_{B,a}}{z_B - z_S}, \tag{18}$$

where z_j is the z coordinate of the layer j.
Note that now, using relations (15), (16), (17) and (18), all the strains of the problem are determined if the deformations $\varepsilon_{A,i}$, $\varepsilon_{S,i}$, $\varepsilon_{B,a}$ and $\varepsilon_{S,a}$ are known.
Writing a system of equations with (2) and (3), for the initial step, it is possible to determine the strains $\varepsilon_{A,i}$ e $\varepsilon_{S,i}$. This process is called *determination of the strains in initial step* and is described in item 4 of this work. Once these strains are known, the strains domains of the additional step that promote ULS in the composite section are then defined, a process described in item 5. Once the strains domains are known, the process for evaluate the factored moment resistance for the composite cross section is described in item 6 and the design method is presented in item 7.

4 DETERMINATION OF THE STRAINS IN INITIAL STEP

The initial step is defined as the instant immediately after the cast in place addition. In this situation, the addition concrete is fresh, therefore, it accommodates the strains and does not offer participation in the $R_{cd,i}$ e $M_{cd,i}$. The pre-strain, necessary to determine the prestressing force, must be calculated with the prestressing losses of the current instant. Furthermore, the factored internal forces $N_{d,i}$ and $M_{d,i}$, are determined with the loads at this moment: self-weight of the precast section and self-weight of the cast in place addition.

To evaluate the moment resistance of the cross section, it is first necessary to evaluate the strains $\varepsilon_{A,i}$ and $\varepsilon_{S,i}$ that occur in the initial step. The NBR 6118:2014 allows to assume that the stress-strain relationship of concrete is linear if the stress is less than 50% of the compressive strength of concrete. To overcome this limitation, the non-linear constitutive relationship for the concrete in bending shown in Figure 2 will be assumed [31].

Usually at least the strain at one point in the cross section is known. This does not apply to the current situation since the strains $\varepsilon_{A,i}$ e $\varepsilon_{S,i}$ can assume any values within their limits. The problem requires the evaluation of strains in the initial step for arbitrary bending moment. Thus, the problem consists of the solution of the nonlinear system, written by applying Equations 2 and 3 in the initial step, with two variables to be evaluated, namely $\varepsilon_{A,i}$ e $\varepsilon_{S,i}$. The evaluation of Equations 2 and 3 presupposes a defined problem, that is, the concrete cross section as well as the position, area, and pre-strain, $\varepsilon_{pré,i}$, of the reinforcements must be known.

To solve the system, the use of the damped Newton-Raphson method is proposed. This method consists of an iterative process to search for the root of a function $f(x_n)$, nonlinear, where the tangent $f'(x_n)$ of the current iteration n is used to estimate the next candidate solution x_{n+1}.

$$x_{n+1} = x_n - \alpha \cdot \frac{f(x_n)}{f'(x_n)} \tag{19}$$

Since the function of the problem is a vector function, the damped Newton-Raphson method is written as

$$\boldsymbol{x}_{n+1} = \boldsymbol{x}_n - \alpha \cdot \boldsymbol{J}_{\boldsymbol{f}(\boldsymbol{x}_n)}{}^{-1} \cdot \boldsymbol{f}(\boldsymbol{x}_n), \tag{20}$$

where $\boldsymbol{J}_{\boldsymbol{f}(\boldsymbol{x}_n)}$ is the Jacobian matrix defined on the vector function $\boldsymbol{f}(\boldsymbol{x}_n)$.
For this problem, the Equation 20 is rewritten as:

$$\begin{Bmatrix}\varepsilon_{A,i}\\ \varepsilon_{S,i}\end{Bmatrix}_{n+1} = \begin{Bmatrix}\varepsilon_{A,i}\\ \varepsilon_{S,i}\end{Bmatrix}_{n} - \alpha \cdot \begin{bmatrix}\frac{\partial SN(\varepsilon_{A,i},\varepsilon_{S,i})}{\partial \varepsilon_{A,i}} & \frac{\partial SN(\varepsilon_{A,i},\varepsilon_{S,i})}{\partial \varepsilon_{S,i}}\\ \frac{\partial SM(\varepsilon_{A,i},\varepsilon_{S,i})}{\partial \varepsilon_{A,i}} & \frac{\partial SM(\varepsilon_{A,i},\varepsilon_{S,i})}{\partial \varepsilon_{S,i}}\end{bmatrix}_n^{-1} \cdot \begin{Bmatrix}SN(\varepsilon_{A,i},\varepsilon_{S,i})\\ SM(\varepsilon_{A,i},\varepsilon_{S,i})\end{Bmatrix}_n \tag{21}$$

The term α is the damping factor determined as follows:

1. For $\alpha = 1$, evaluate $\left\|\begin{Bmatrix}SN\\ SM\end{Bmatrix}_n\right\|_p$ and $\left\|\begin{Bmatrix}SN\\ SM\end{Bmatrix}_{n+1}\right\|_p$;
2. Check if $\left\|\begin{Bmatrix}SN\\ SM\end{Bmatrix}_{n+1}\right\|_p < \left\|\begin{Bmatrix}SN\\ SM\end{Bmatrix}_n\right\|_p$;
3. if 2 is true, $\begin{Bmatrix}\varepsilon_{A,i}\\ \varepsilon_{S,i}\end{Bmatrix}_{n+1}$ is accepted as a new iteration;
4. if 2 is false, $\alpha \leftarrow \frac{\alpha}{2}$ and the process is repeated from 2.

Figure 7 graphically shows the problem-solving strategy, which iteratively, the deformations will be approaching the roots of equations.

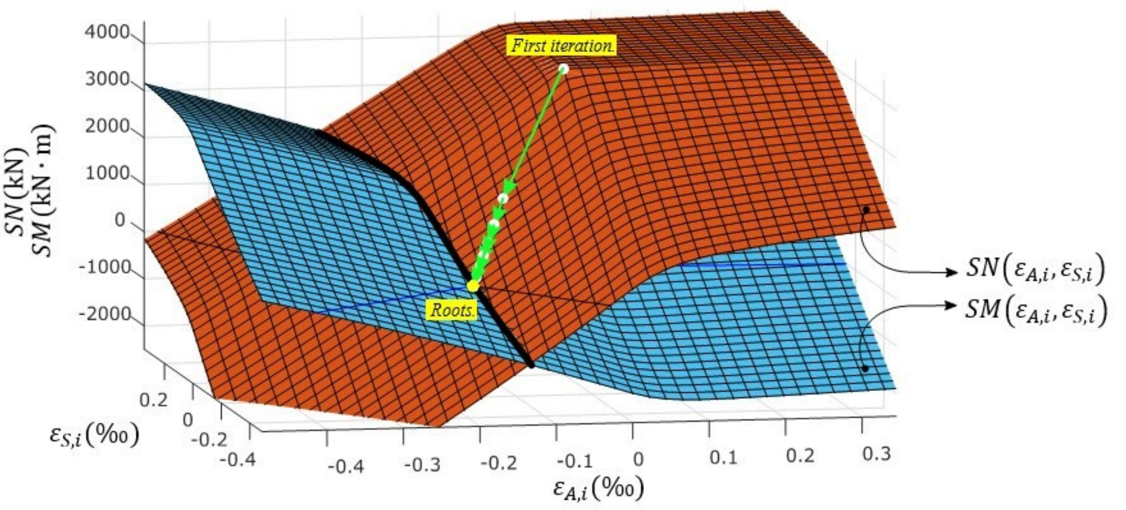

Figure 7. Problem of determination the strains in the initial step.

The Jacobian matrix requires the evaluation of partial derivatives of the SN and SM functions. These derivatives are approximated using central finite differences resulting in Equations 22 to 25. This technique approximates the tangent slope of the function, at the point of interest, by the slope of a line formed by two points on the function, distant h from each other.

$$\frac{\partial SN(\varepsilon_{A,i},\varepsilon_{S,i})}{\partial \varepsilon_{A,i}} \cong \frac{SN(\varepsilon_{A,i}+h,\varepsilon_{S,i})-SN(\varepsilon_{A,i}-h,\varepsilon_{S,i})}{2\cdot h} \tag{22}$$

$$\frac{\partial SN(\varepsilon_{A,i},\varepsilon_{S,i})}{\partial \varepsilon_{S,i}} \cong \frac{SN(\varepsilon_{A,i},\varepsilon_{S,i}+h)-SN(\varepsilon_{A,i},\varepsilon_{S,i}-h)}{2\cdot h} \tag{23}$$

$$\frac{\partial SM(\varepsilon_{A,i},\varepsilon_{S,i})}{\partial \varepsilon_{A,i}} \cong \frac{SM(\varepsilon_{A,i}+h,\varepsilon_{S,i})-SM(\varepsilon_{A,i}-h,\varepsilon_{S,i})}{2\cdot h} \tag{24}$$

$$\frac{\partial SM(\varepsilon_{A,i},\varepsilon_{S,i})}{\partial \varepsilon_{S,i}} \cong \frac{SM(\varepsilon_{A,i},\varepsilon_{S,i}+h)-SM(\varepsilon_{A,i},\varepsilon_{S,i}-h)}{2\cdot h} \quad (25)$$

The Newton-Raphson method is repeated until the stopping criterion defined in Equation 26 is reached.

$$\left\| \begin{Bmatrix} SN \\ SM \end{Bmatrix}_n \right\|_p < \xi_1 \quad (26)$$

where ξ_1 is the error admitted for the vector function.
In the examples in this article, it is admitted $\xi_1 = 10^{-2}$ when evaluating SN and SM in kN and in kN · m, respectively. The distance h for evaluating the partial derivatives was adopted equal to 10^{-3} for the first iteration and 10^{-9} for the other iterations, using *double-precision*. The first iteration starts from the strains $\varepsilon_{A,i} = 0$ and $\varepsilon_{S,i} = 0$.

5 DERMINATION OF THE ULS REGIONS OF COMPOSITE CROSS SECTIONS

ULS strain domains can be defined. In this work, the concept of domain is replaced by Santos [34] proposal. Santos proposes the grouping of one or more ULS domains in regions that present the same rupture mechanism.

In composite sections, the ULS can be characterized by the individual or combined state of three situations:

- conventional failure due to excessive plastic strain of the passive reinforcement, $\varepsilon_{S,t} = \varepsilon_{su}$, where $\varepsilon_{su} = 10$ ‰ [31], region 3;
- conventional failure by limit-shortening of concrete in the cast in place addition, $\varepsilon_{B,t} = \varepsilon_{cu}$, region 2B;
- conventional failure by limit-shortening of concrete of the precast section, $\varepsilon_{A,t} = \varepsilon_{cu}$, region 2A.

Figure 8 illustrates the deformation of the composite cross section, in ULS, exemplifying the characteristic rupture of each strain region.

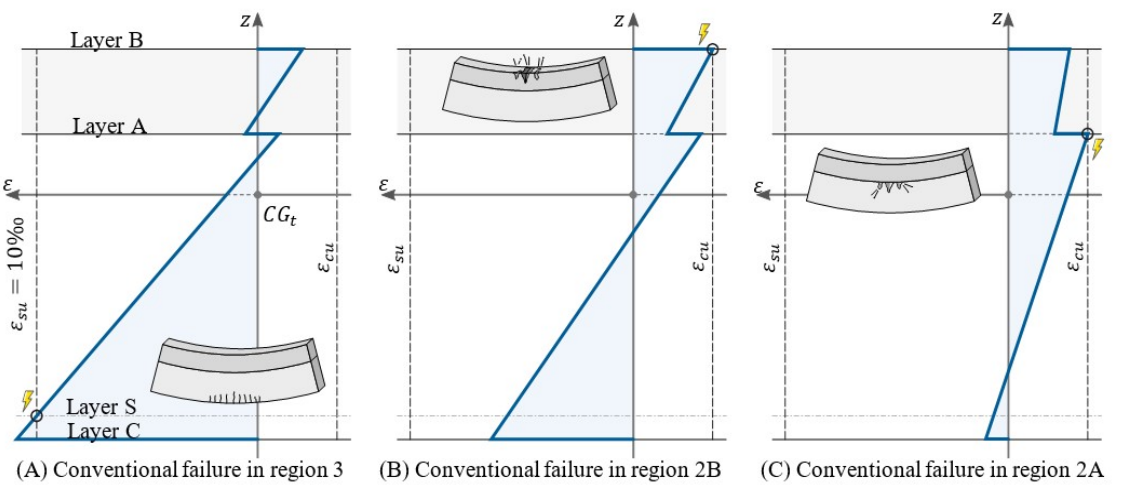

Figure 8. Deformation of the composite cross section in ULS in the total step.

A cross section, depending on its resulting strains in the initial step, can present three possible trajectories of ULS regions. A trajectory is understood as the sequence in which the regions are presented, analyzing the deformations in ULS, when the normal force N_d assumes values in decreasing order from the maximum to the minimum allowed.

Thus, the trajectory of ULS regions is determined by evaluating the level of strain value $\varepsilon_{A,i}$ in relation to the limits $\varepsilon_{A,i,23B}$ and $\varepsilon_{A,i,12B}$, thus classifying the precast cross section in one of three categories:

- lightly compressed precast section, when $\varepsilon_{A,i} > \varepsilon_{A,i,12B}$, with ULS region trajectory from 3 to 2B;

- moderately compressed precast section, when $\varepsilon_{A,i,23B} < \varepsilon_{A,i} \leq \varepsilon_{A,i,12B}$, with ULS region trajectory from 3 to 2B to 2A;
- heavily compressed precast section, when $\varepsilon_{A,i} \leq \varepsilon_{A,i,23B}$, with ULS region trajectory from 3 to 2A.

The limits $\varepsilon_{A,i,23B}$ and $\varepsilon_{A,i,12B}$ are determined by Equations 27 and 28 as a function of the strains obtained in the initial step.

$$\varepsilon_{A,i,12B} = \left(\varepsilon_{cu} - \varepsilon_{C,t,min} + \varepsilon_{C,i}\right) \cdot \frac{z_B - z_A}{z_B - z_C} \tag{27}$$

$$\varepsilon_{A,i,23B} = \left(\varepsilon_{cu} - \varepsilon_{yu} + \varepsilon_{S,i}\ \right) \cdot \frac{z_B - z_A}{z_B - z_S} \tag{28}$$

where ε_{su} is the maximum strain allowed in the passive reinforcement, $\varepsilon_{C,t,min}$ the strain at layer C of the boundary between regions 1 and 2, being $\varepsilon_{C,t,min} = 0$, and $\varepsilon_{C,i}$ the strain at layer C of the initial step given by:

$$\varepsilon_{C,i} = \varepsilon_{A,i} + \kappa_i \cdot (z_A - z_C), \tag{29}$$

where κ_i is the curvature of the initial step evaluated by the equation:

$$\kappa_i = \frac{\varepsilon_{S,i} - \varepsilon_{A,i}}{z_A - z_S}. \tag{30}$$

Region 1 is not of interest to this work as it exceeds the limits of x/d for beams of item 14.6.4.3 of NBR 6118 [31].

The strain regions in ULS for the composite section are defined in relation to the strains of the additional step. Figure 9 represents the strain regions in ULS for composite beams with lightly, moderately and heavily compressed precast section.

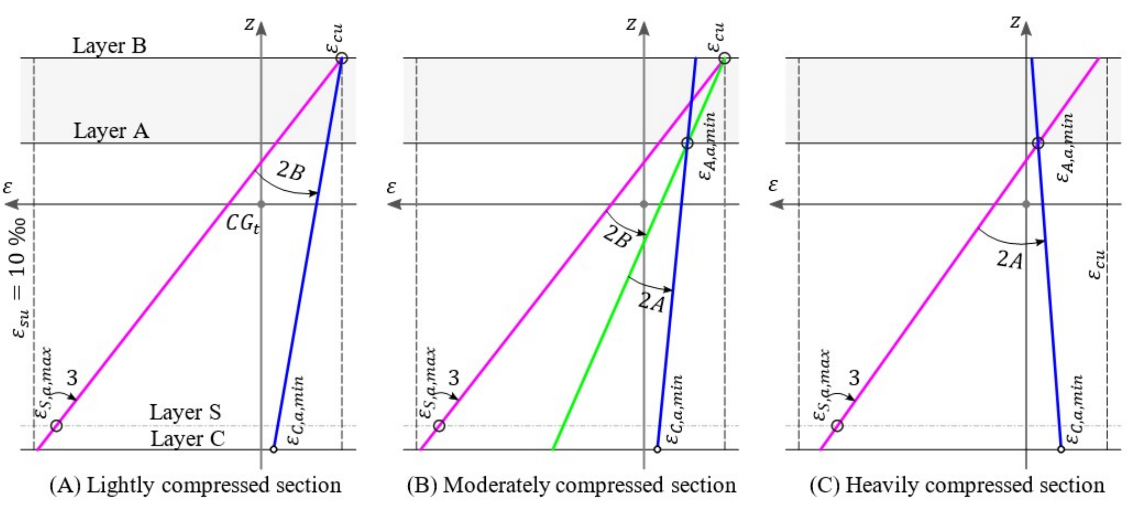

Figure 9. Strain regions in ULS in the additional step.

Each strain region in ULS is defined by a strain group of that have the same value at a certain level of the cross section. Each region has a limited curvature as a function of the compression level of the precast section.

In Figure 9, $\varepsilon_{A,a,min}$, $\varepsilon_{S,a,max}$ and $\varepsilon_{C,a,min}$ are the strains in the additional step, which provides that the strains in the total step are respectively equal ε_{cu}, ε_{su} and $\varepsilon_{C,t,min}$ at the layers A, S and C. These are defined with

$$\varepsilon_{A,a,min} = \varepsilon_{cu} - \varepsilon_{A,i} \tag{31}$$

$$\varepsilon_{S,a,max} = \varepsilon_{su} - \varepsilon_{S,i} \tag{32}$$

$$\varepsilon_{C,a,min} = \varepsilon_{C,t,min} - \varepsilon_{C,i}. \tag{33}$$

Knowing the limits of the strain regions in ULS, it is possible to evaluate in which region the solution of a defined problem is located. This region is obtained by evaluating the sign of the SN function when the strain in the additional step is equal to the limit between adjacent regions. Observing the behavior of the signal of this function, it is then possible to evaluate the region in which Equation 2 is satisfied, which is the region where the curvature and axial deformation solution to the problem is found.

6 DETERMINATION OF FACTORED MOMENT RESISTANCE FOR THE COMPOSITE CROSS SECTION

For a defined problem, that is, where the cross section and the characteristics of the reinforcements are known, it is now possible to determine the factored moment resistance M_{Rd} of the composite section. Having determined the region in which the ULS deformation is located, the problem boils down to looking, within the solution space contained in the defined region, for the curvature that determines the root of the Equation 2.

The root can be obtained by several iterative numerical methods such as the bisection method, the false position method, the secant method or even the Newton-Raphson method already discussed here. As it is necessary that the solution process does not exceed the limits of the evaluated region and as Equation 2, as it is evaluated here, is not derivable, the false position method becomes the most suitable within the considered methods.

The false position method fetches the root of the function $f(x)$ contained in a known initial range $[a_0, b_0]$, where iteratively the search range is reduced so that the root of the function is still contained in the new range $[a_k, b_k]$. The new range is defined in iteration k by

$$c_k = b_k - \frac{f(b_k)\cdot(b_k - a_k)}{f(b_k) - f(a_k)} \tag{34}$$

where c_k is the root of the secant that passes through the points $[a_k, f(a_k)]$ and $[b_k, f(b_k)]$. Once c_k is determined, the response interval is reduced by making $a_{k+1} = c_k$ and $b_{k+1} = b_k$, if $f(a_k)$ and $f(c_k)$ have the same sign, otherwise, $a_{k+1} = a_k$ and $b_{k+1} = c_k$.

Figure 10 illustrates the solution strategy of the false position method, assuming linear behavior for the function in the assigned solution interval, and successively shortens this interval until it reaches a stopping criterion such

$$f(c_k) < \xi_2 \tag{35}$$

where ξ_2 is the error allowed for the function $f(x)$ in this process.

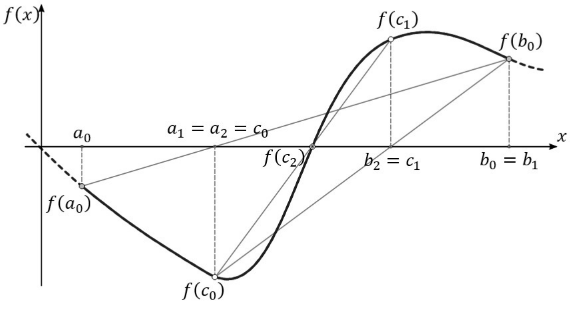

Figure 10. Solution strategy of the false position method.

To define the deformation in ULS using the false position method, the function $f(x)$ assumes Equation 2 written in the total step, the variable x is the curvature of the additional step κ_a and the search interval $[a_0, b_0]$ is defined as the limiting curvatures of the strain region in ULS for the section in question $[\kappa_{a,min}, \kappa_{a,max}]$.

Once the additional step strains are defined, the moment M_d that satisfies Equation 3 written in total step is the factored moment resistance M_{Rd} of the composite cross section.

7 DESIGN METHOD OF COMPOSITE CROSS SECTION

The factored moment resistance evaluation process, described in item 6, requires a complete definition of the problem, including the area and position of the reinforcement. For design, it is necessary to organize the problem to determine the amount of passive reinforcement needed so that the composite section can withstand the acting factored moment M_{Sd}.

Using the processes described in items 4, 5 and 6 to determine the M_{Rd} it is possible to use the false position method to determine the area of passive reinforcement that satisfies the design equation

$$M_{Rd} - M_{Sd} = 0. \tag{36}$$

To design the passive reinforcement area, using the false position method, the function $f(x)$ assumes Equation 36, the independent variable x is the passive reinforcement area A_s and the search interval $[a_0, b_0]$ is defined as the assumed minimum and maximum reinforcement areas for this cross section $[A_{s,min}, A_{s,max}]$.

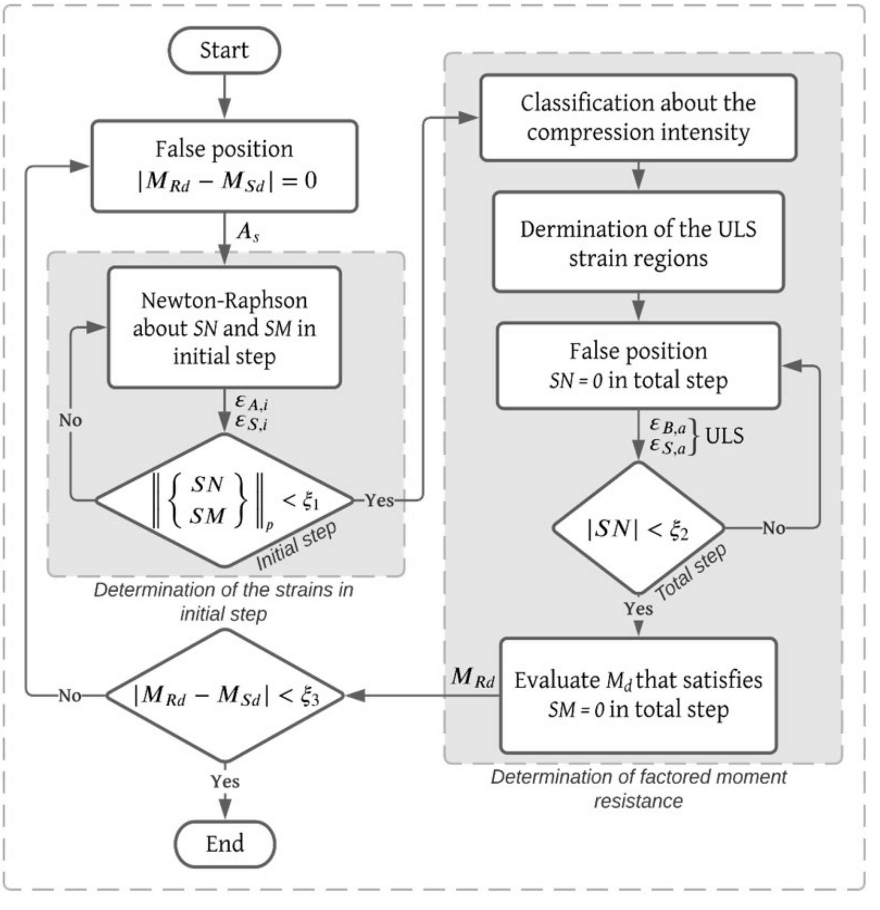

Figure 11. Flowchart of the composite section design process.

During the design process, summarized in Figure 11, the SM function is evaluated for different areas of passive reinforcement. The discretization procedure of the reinforcement elements in the cross section is presented in the next item, 7.1, since the positioning of these elements is necessary for the evaluation of Equation 3.

7.1 Discretization model of reinforcement elements with continuous variation

The reinforcements are positioned in the cross section in layers that must respect the horizontal and vertical spacing of [31]. Furthermore, as this is a real problem, the number of rebars is defined by an integer number. The problem written with an amount of reinforcement defined by an integer, presents a discontinuous relationship between reinforcement area and moment resistance. This discontinuity makes it difficult to use numerical methods to determine the answer to the design problem.

To promote a continuous relationship between A_s and M_{Rd}, the discretization of the individual elements representing the steel rebars is replaced here by q rectangular elements. These elements have the sum of their areas equivalent to A_s, they are equally spaced and arranged in a reinforced region of the cross section that estimates the real positioning of the discrete rebars

The reinforced region is defined by the dimensions b and h, where b is the displacement of the axis of the outermost reinforcement and h the axis of the highest reinforcement layer in the cross section. Dimensions b and h are determined by a linear function in relation to A_s obtained from the extreme values b_{min}, h_{min}, b_{max} e h_{max}, established by the actual positioning of the minimum and maximum reinforcement in the cross section, Figure 12.

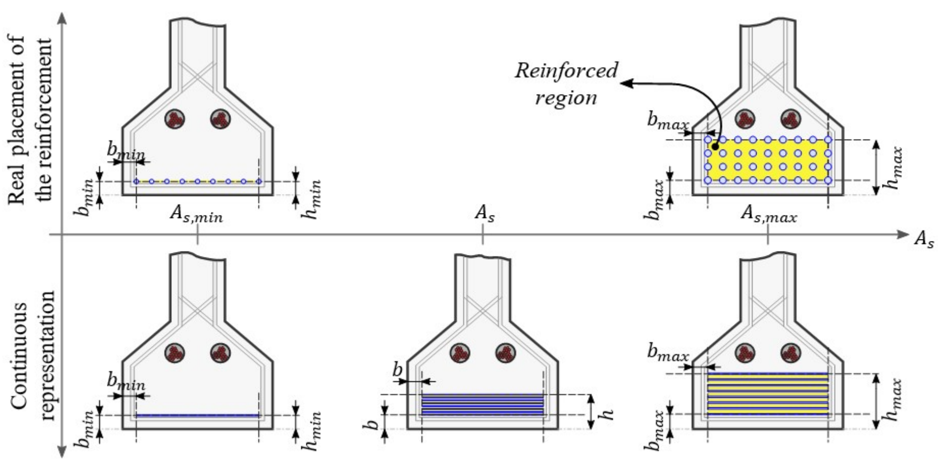

Figure 12. Real positioning and continuous representation of passive reinforcement.

The use of rectangular elements makes the relationship between A_s and M_{Rd} continuous but introduces a difference in the position of the resulting R_{sd}, in relation to the real positioning of the passive reinforcement rebars. Thus, at the end of the process, the factored moment resistance of the beam must be verified with the real positioning of the reinforcement rebars.

8 EXAMPLES

The method proposed here to design composite cross sections was implemented in a routine in *MATLAB*. This routine was then used to develop the following examples.

8.1 Comparison with the experimental results

In order to roughly estimate the influence of the simplifying hypothesis of the model, the ultimate moment evaluated by this methodology will be compared with the experimental results obtained by [35] and [36]. In their work, two full-scale reinforced concrete beams were tested to failure in bending. These beams were casted in two steps, with the precast section being loaded prior to the second casting, simulating the effect investigated in this paper.

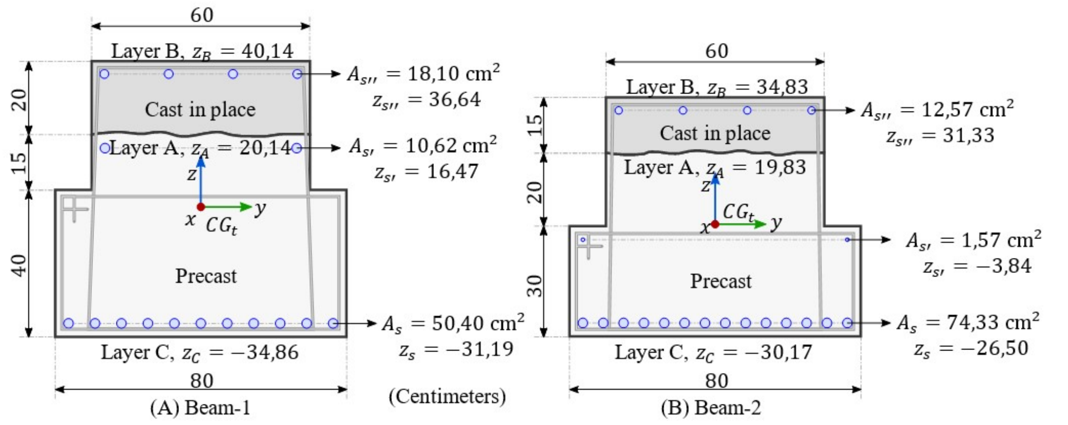

Figure 13. Cross-section of beam-1 and beam-2.

The cross sections of the tested beams are shown in Figure 13. Table 1 shows the estimated strength of the concrete of the beams measured by the strength of the cylindrical specimens at different ages coincident with the test steps. The yielding stress of the steel reinforcement, obtained from tensile tests on samples extracted from the rebars, is $f_y = 490\ \mathrm{MPa}$. The bending moment acting on the precasted beam in the initial step is $M_i = 531\ \mathrm{kN \cdot m}$ for the beam-1 and $M_i = 385\ \mathrm{kN \cdot m}$ for the beam-2, according to [35] and [36].

Table 1. Strength of the cylindrical specimens at different ages.

	First cast - initial step	First cast - total step	Second cast - total step
	$f_{c,i}$ (MPa)	$f_{c,t}$ (MPa)	$f_{c,t}$ (MPa)
Beam-1	51	59	32
Beam-2	66	68	25

Removing the effect of the Rüsch coefficient from the concrete constitutive relationship and using the strength safety factor $\gamma_c = \gamma_s = 1$ the ultimate moment of beam-1 and beam-2 is estimated as shown in Table 2. Figures 14 and 15 show the strains of the cross section, as well as the resulting forces in equilibrium in the initial, additional and total steps evaluation of the ultimate moment of beam-1 and beam-2, respectively.

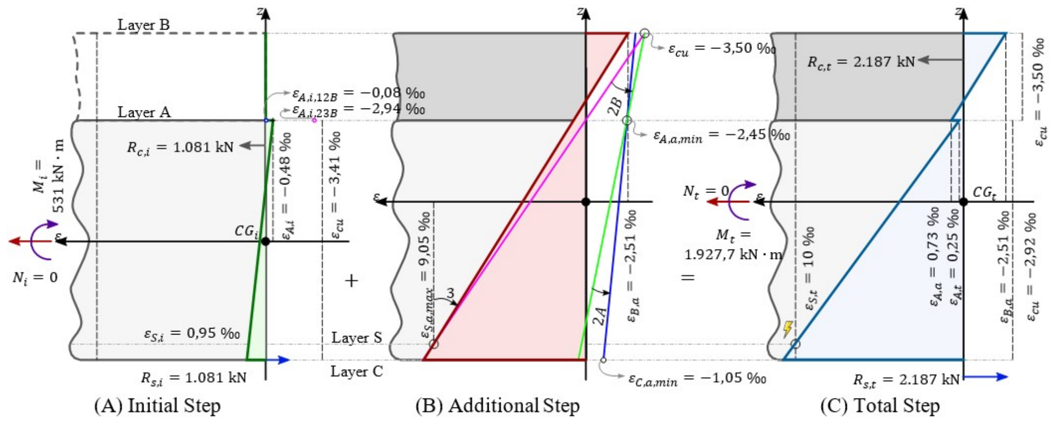

Figure 14. Strain diagram in ULS for the beam-1.

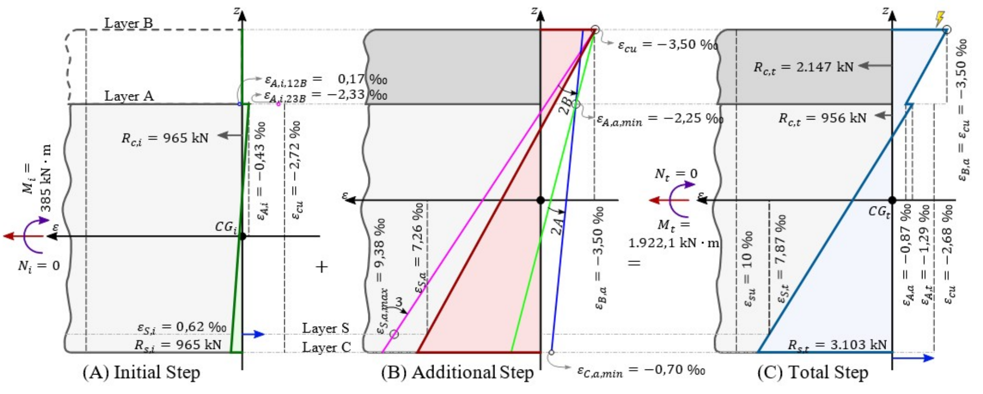

Figure 15. Strain diagram in ULS for the beam-2.

Table 2. Summary of test and estimated ultimate moment.

	Ultimate moment in total step M_t (kN · m)		Error (%)
	Experimental [35] and [36]	**Estimated by this work**	
Beam-1	1953,5	1927,7 (limited by the steel strain equal to 10 ‰)	1,3
Beam-2	2346,2	1922,1 (limited by the concrete strain equal to 3,5 ‰)	18,1

The differences shown in Table 2 can be explained by the simplifications of the proposed model. The constitutive relationship used for the concrete limits the maximum strain to ε_{cu}, in the experiment, it is likely that the maximum strain of the concrete was higher. This limitation hinders the development of larger reactions of compressed concrete close to layer A because the curvature is limited by the maximum deformation in layer B. This effect is more pronounced in beam-2 because, in this beam, the failure was characterized by the maximum strain of the concrete of the layer B.

8.2 Numerical Example

To evaluate the differences introduced in the design when a cross section is casted in a single step and in two steps, it is proposed the design of the cross section in Figure 16. In this example the factored moment in the precast section when the second step is being casted is 15.792 kN · m, and the factored moment resistance in ULS of composite beam need to be 42.658 kN · m.

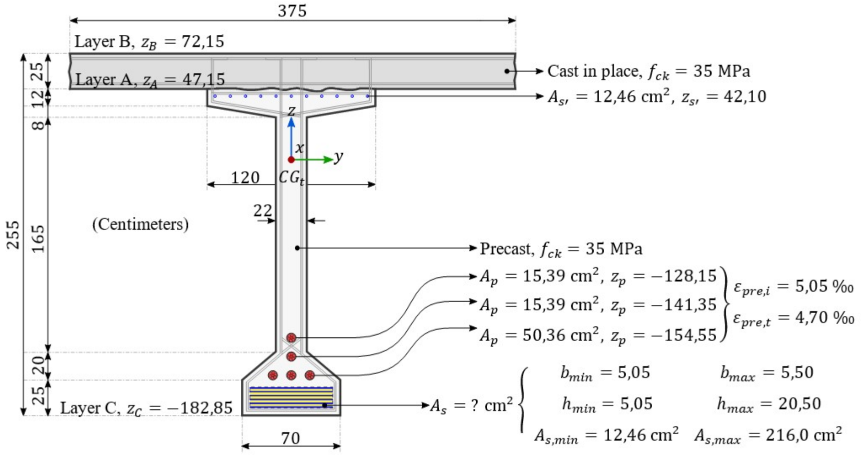

Figure 16. Proposed beam for numerical example.

Figures 17 and 18 show the strains in the ULS, as well the resulting forces in equilibrium in the cross section when the beam in Figure 16 is design considering single-step and two-step casting, respectively.

Developing the design of the beam assuming that the entire beam is casted in a single step, $177{,}1\ \text{cm}^2$ of passive reinforcement area is needed.

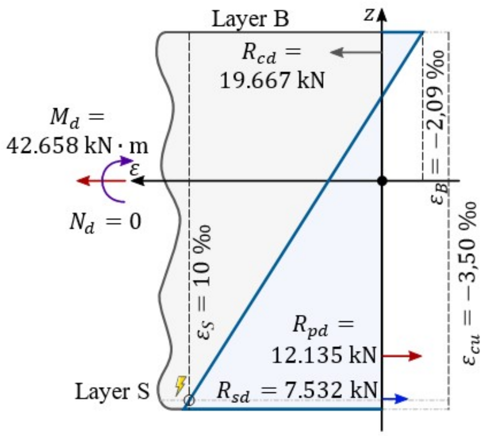

Figure 17. Strain diagram in ULS for the example assuming casting in single step. $A_s = 177{,}1\ \text{cm}^2$.

In contrast, if the beam in Figure 16 is built by two casting steps, with the precast beam not being shored during the second casting step, the design results in a $189{,}0\ \text{cm}^2$ of passive reinforcement area.

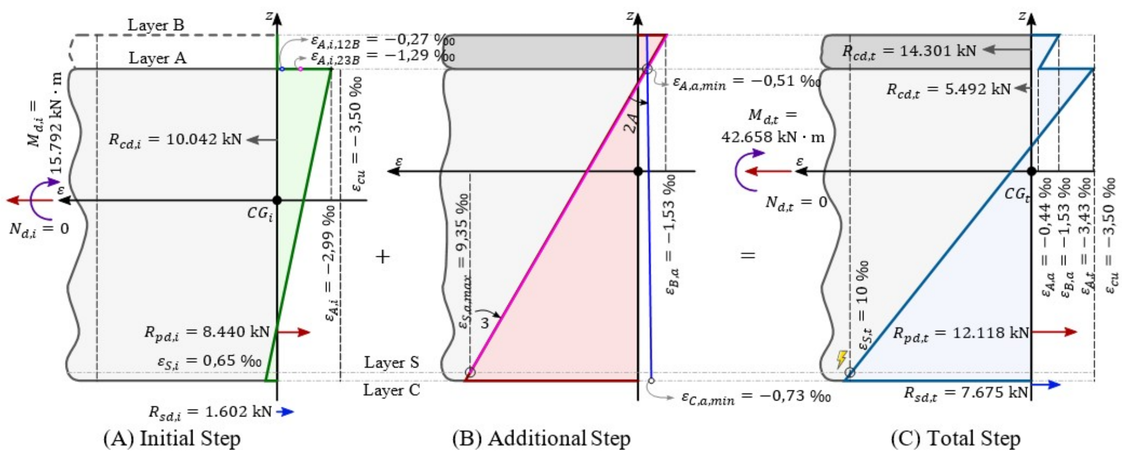

Figure 18. Strain diagram in ULS for the example assuming two casting steps. $A_s = 189{,}0\ \text{cm}^2$.

Analyzing the two designs, it is observed that 6,7% more passive reinforcement is required, when the beam is built in two casting steps, in relation to de construction in a single cast.

Using the same reinforcement area, $A_s = 189{,}0\ \text{cm}^2$, it is possible to evaluate and compare the factored moment resistance of the beam in Figure 16, considering the construction in single casting step and in two casting steps. Evaluating the beam constructed in a single step, the factored moment resistance is $43.963\ \text{kN} \cdot \text{m}$. When the factored moment resistance is evaluated considering two casting steps, it is equal to $42.658\ \text{kN} \cdot \text{m}$. For the example in

Figure 16, the beam with two casting stages provides a factored resistance moment 3,0% lower than the beam with a single casting step with the same reinforcement area.

9. CONCLUSIONS

Here it is proposed a methodology to design prestressed sections constructed in two casting steps, built without additional shoring, where the strain discontinuity in the cross section, introduced by the construction process, is considered.

The proposed design process consists of iteratively varying the area of passive reinforcement until the factored moment resistance is equal to the requested factored moment. Initially the strains in the precast section are evaluated and, in sequence, the strains in ULS that satisfy the equilibrium and compatibility equations are found.

The damped Newton-Raphson method for evaluating the deformations in the initial step proved to be efficient and numerically stable. The false position method, here used to satisfy the equilibrium and the design equation, is sufficiently efficient and necessary because the search need to be developed within the validity limits of the equations, different from the Newton Raphson method, which does not respect the boundary conditions.

Also, within the solutions adopted to make the method viable, the discretization of the reinforcement elements with continuous variation allowed the solution of the design equation using iterative numerical processes seamlessly.

With all the solutions proposed here, this method can be easily implemented in computational routines for verification and design of composite elements with precision.

Regarding the comparison of the experimental results, the accuracy of the model is high when the failure is characterized by the limit strain of the reinforcement, and lower when the limit strain occurs in concrete. It should be noted that this divergence is due to a simplification of the constitutive relationship of the NBR 6118:2014 and that the estimated resistance is lower than that measured in the test. To obtain an ultimate moment with better experimental and theoretical fitting a more realistic concrete constitutive law is recommended.

The numerical example results show that the section built in two steps, resulted in a moment resistance 3,0% lower in relation to the verification considering a single casting step. These results may vary when compared to other cross sections, different ratios between the height of each cast stage, different strain in the precast section and different prestressing level. To evaluate the relation between each of these variables in the factored moment resistance further investigation is needed.

For a better understanding of the extent of the effects investigated here, it is very important that more experimental tests of concrete beams casted in two stages with higher loading level in the precast section are carried out due to the lack of tests like this in the literature. It is also proposed that future investigations evaluate experimentally and numerically the effects of time-dependent strain, such as shrinkage and creep, in the moment resistance of concrete composite cross sections.

ACKNOWLEDGEMENTS

This study was financed in part by the Coordenação de Aperfeiçoamento de Pessoal de Nível Superior – Brasil (CAPES) – Finance Code 001.

REFERENCES

[1] R. Tomek, "Advantages of precast concrete in highway infrastructure construction," *Procedia Eng.*, vol. 196, pp. 176–180, 2017, http://dx.doi.org/10.1016/j.proeng.2017.07.188.

[2] Associação Brasileira de Normas Técnicas, *Projeto e Execução de Estruturas de Concreto Pré-Moldado*, ABNT NBR 9062:2017, 2017.

[3] T. I. Campbell, V. K. R. Kodur, S. M. R. Lopes, J. Harrop, and A. E. Gamble, "Study of moment redistribution in prestressed concrete beams," *J. Struct. Eng.*, vol. 125, no. 3, pp. 351–352, Mar 1999, http://dx.doi.org/10.1061/(ASCE)0733-9445(1999)125:3(351).

[4] A. A. Yee and D. Hon, "Structural and economic benefits of precast/prestressed concrete construction," *PCI J.*, vol. 46, no. 4, pp. 34–42, 2001.

[5] J. C. Saemann and G. W. Washa, "Horizontal shear connections between precast beams and cast-in-place slabs," *ACI J. Proc.*, vol. 17, no. 3, 1964, http://dx.doi.org/10.14359/7832.

[6] A. H. Mattock, *Shear Transfer Under Monotonic Loading, Across an Interface Between Concretes Cast at Different Times*. Seattle: Washington Univ., 1976. [Online]. Available: https://ntrl.ntis.gov/NTRL/dashboard/searchResults/titleDetail/PB275257.xhtml

[7] J. Wairaven, J. Frenay, and A. Pruijssers, "Influence of concrete strength and load history on the shear friction capacity of concrete members," *PCI J.*, vol. 32, no. 1, pp. 66–84, Jan 1987, http://dx.doi.org/10.15554/pcij.01011987.66.84.

[8] R. E. Loov and A. K. Patnaik, "Horizontal shear strength of composite concrete beams with a rough interface," *PCI J.*, vol. 39, no. 1, pp. 48–69, 1994, http://dx.doi.org/10.15554/pcij.01011994.48.69.

[9] A. K. Patnaik, "Behavior of composite concrete beams with smooth interface," *J. Struct. Eng.*, vol. 127, no. 4, pp. 359–366, Apr 2001, http://dx.doi.org/10.1061/(ASCE)0733-9445(2001)127:4(359).

[10] L. F. Kahn and A. Slapkus, "Interface shear in high strength composite T-beams," *PCI J.*, vol. 49, no. 4, pp. 102–110, 2004, http://dx.doi.org/10.15554/pcij.07012004.102.110.

[11] M. A. Mansur, T. Vinayagam, and K.-H. Tan, "Shear transfer across a crack in reinforced high-strength concrete," *J. Mater. Civ. Eng.*, vol. 20, no. 4, pp. 294–302, Apr 2008, http://dx.doi.org/10.1061/(ASCE)0899-1561(2008)20:4(294).

[12] A. A. Semendary, W. K. Hamid, E. P. Steinberg, and I. Khoury, "Shear friction performance between high strength concrete (HSC) and ultra high performance concrete (UHPC) for bridge connection applications," *Eng. Struct.*, vol. 205, pp. 110–122, 2020, http://dx.doi.org/10.1016/j.engstruct.2019.110122.

[13] American Concrete Institute, *Building Code Requirements for Structural Concrete*, ACI 318-19, 2019.

[14] American Association of State Highway and Transportation Officials, *AASHTO Bridge Design Specifications*, 9th ed. Washington: AASHTO, 2020.

[15] J. P. R. Dantas, "Investigação experimental da fadiga em lajes de pontes armadas com barras ou telas soldadas," M.S. thesis, Esc. Politéc., Univ. São Paulo, São Paulo, 2010.

[16] P. S. P. Cavalcanti, "Investigação experimental da fadiga ao cisalhamento em lajes de pontes com pré-lajes," M.S. thesis, Esc. Politéc., Univ. São Paulo, São Paulo, 2011.

[17] E. C. Caixeta, "Investigação experimental da fadiga em lajes de pontes com ou sem pré-lajes," M.S. thesis, Esc. Politéc., Univ. São Paulo, São Paulo, 2010.

[18] S. A. Kristiawan, "Evaluation of models for estimating shrinkage stress in patch repair system," *Int. J. Concr. Struct. Mater.*, vol. 6, no. 4, pp. 221–230, 2012, http://dx.doi.org/10.1007/s40069-012-0023-y.

[19] H. W. Birkeland, "Differential shrinkage in composite beams," *ACI J. Proc.*, vol. 56, no. 5, pp. 1123–1136, 1960, http://dx.doi.org/10.14359/8133.

[20] D. E. Branson, "Time-dependent effects in composite concrete beams," *ACI J. Proc.*, vol. 61, no. 2, pp. 213–230, 1964, http://dx.doi.org/10.14359/7776.

[21] Y. Yuan and M. Marosszeky, "Restrained shrinkage in repaired reinforced concrete elements," *Mater. Struct.*, vol. 27, no. 7, pp. 375–382, Aug 1994, http://dx.doi.org/10.1007/BF02473440.

[22] J. Silfwerbrand, "Stresses and strains in composite concrete beams subjected to differential shrinkage," *ACI Struct. J.*, vol. 94, no. 4, pp. 347–353, 1997, http://dx.doi.org/10.14359/485.

[23] Y. Yuan, G. Li, and Y. Cai, "Modeling for prediction of restrained shrinkage effect in concrete repair," *Cement Concr. Res.*, vol. 33, no. 3, pp. 347–352, Mar 2003, http://dx.doi.org/10.1016/S0008-8846(02)00960-2.

[24] J. Zhou, G. Ye, E. Schlangen, and K. van Breugel, "Modelling of stresses and strains in bonded concrete overlays subjected to differential volume changes," *Theor. Appl. Fract. Mech.*, vol. 49, no. 2, pp. 199–205, 2008, http://dx.doi.org/10.1016/j.tafmec.2007.11.006.

[25] S. Sullivan, "Construction and behavior of precast bridge deck panel systems," Ph.D. dissertation, Virginia Tech, Blacksburg, 2007.

[26] H. Beushausen and M. G. Alexander, "Localised strain and stress in bonded concrete overlays subjected to differential shrinkage," *Mater. Struct.*, vol. 40, no. 2, pp. 189–199, Jan 2007, http://dx.doi.org/10.1617/s11527-006-9130-z.

[27] R. H. Evans and A. S. Parker, "Behavior of prestressed concrete composite beams," *ACI J. Proc.*, vol. 51, no. 5, pp. 861–878, 1955, http://dx.doi.org/10.14359/11721.

[28] N. M. Taha, *A Microcomputer Program for the Design of Composite Beam*. Cairo: Cairo Univ., 1978.

[29] S. Dritsos, K. Pilakoutas, and E. Kotsira, "Effectiveness of flexural strengthening of RC members," *Constr. Build. Mater.*, vol. 9, no. 3, pp. 165–171, Jun 1995, http://dx.doi.org/10.1016/0950-0618(95)00010-D.

[30] J.-W. Hwang, J.-H. Kwak, and H.-G. Kwak, "Finite-element model to evaluate nonlinear behavior of posttensioned composite beams with partial shear connection," *J. Struct. Eng.*, vol. 141, no. 8, pp. 04014205, Aug 2015, http://dx.doi.org/10.1061/(ASCE)ST.1943-541X.0001174.

[31] Associação Brasileira de Normas Técnicas, *Projeto de Estruturas de Concreto – Procedimento*, ABNT NBR 6118:2014, 2014.

[32] Associação Brasileira de Normas Técnicas, *Cordoalhas de Aço para Estruturas de Concreto Protendido – Especificação*, ABNT NBR 7483:2020, 2020.

[33] L. M. Silva and R. C. Carvalho "Análise de seções transversais de concreto armado e protendido sujeitas a flexão oblíqua composta em estados-limites último e de serviço por integração analítica," *Rev. Sul-Am. Eng. Estrut.*, vol. 16, no. 2, pp. 76–97, 2019, http://dx.doi.org/10.5335/rsaee.v16i2.8482.

[34] L. M. Santos, *Sub-Rotinas Básicas do Dimensionamento de Concreto Armado*, 1a ed. São Paulo: Thot, 1994.

[35] C. Mazzotti and N. Buratti, "A design oriented fibre-based model for simulating the long-term behaviour of RC beams: Application to beams cast in different stages," *J. Build. Eng.*, vol. 44, pp. 103176, Dec 2021, http://dx.doi.org/10.1016/j.jobe.2021.103176.

[36] M. Bottoni, C. Mazzotti, and M. Savoia, "Long-term experimental tests on precast beams completed with cast in situ concrete," *Eur. J. Environ. Civ. Eng.*, vol. 13, no. 6, pp. 727–744, 2009, http://dx.doi.org/10.1080/19648189.2009.9693148.

Author contributions: EVWT: conceptualization, development of the computational algorithm, data analysis, writing and translation; GAP and TNB: supervision, revision, translation.

Editors: Leandro Trautwein, Antônio Carlos dos Santos